



**HAL**  
open science

# Structure and spin dynamics of a metal complex studied by synchrotron radiation

Victoria Kabanova

► **To cite this version:**

Victoria Kabanova. Structure and spin dynamics of a metal complex studied by synchrotron radiation. Materials Science [cond-mat.mtrl-sci]. Université Grenoble Alpes [2020-..], 2020. English. NNT : 2020GRALY062 . tel-03276783

**HAL Id: tel-03276783**

**<https://theses.hal.science/tel-03276783>**

Submitted on 2 Jul 2021

**HAL** is a multi-disciplinary open access archive for the deposit and dissemination of scientific research documents, whether they are published or not. The documents may come from teaching and research institutions in France or abroad, or from public or private research centers.

L'archive ouverte pluridisciplinaire **HAL**, est destinée au dépôt et à la diffusion de documents scientifiques de niveau recherche, publiés ou non, émanant des établissements d'enseignement et de recherche français ou étrangers, des laboratoires publics ou privés.

## THÈSE

Pour obtenir le grade de

### DOCTEUR DE L'UNIVERSITÉ GRENOBLE ALPES

Spécialité : Physique de la Matière Condensée et du Rayonnement

Arrêté ministériel : 25 mai 2016

Présentée par

### Victoria KABANOVA

Thèse dirigée par **Michael WULFF**  
et codirigée par **Sakura PASCARELLI**, European Synchrotron  
Radiation Facility

préparée au sein du **Laboratoire European Synchrotron  
Radiation Facility**  
dans l'**École Doctorale Physique**

### Structure et dynamique de spin d'un complexe métallique étudié par rayonnement synchrotron

### Structure and spin dynamics of a metal complex studied by synchrotron radiation

Thèse soutenue publiquement le **18 décembre 2020**,  
devant le jury composé de :

**Monsieur ANTON PLECH**

DOCTEUR EN SCIENCES - HDR, INSTITUT DE TECH. KARLSRUHE -  
ALLEMAGNE, Rapporteur

**Monsieur KRISTOFFER HALDRUP**

DOCTEUR EN SCIENCES - EQUIVALENCE HDR, UNIVERSITE  
TECHNIQUE DU DANEMARK, Rapporteur

**Madame FREDERIQUE LOISEAU**

PROFESSEUR DES UNIVERSITES, UNIVERSITE GRENOBLE ALPES,  
Présidente

**Monsieur MACIEJ LORENC**

DIRECTEUR DE RECHERCHE, CNRS DELEGATION BRETAGNE PAYS  
DE LOIRE, Examineur

**Monsieur ERIC COLLET**

PROFESSEUR DES UNIVERSITES, UNIVERSITE RENNES 1,  
Examineur





# CONTENTS

---

---

<b>Acknowledgements</b>	<b>vi</b>
<b>Résumé de la thèse</b>	<b>xi</b>
<b>1 Introduction</b>	<b>1</b>
1.1 Pump-probe technique . . . . .	2
1.2 Photoreactions in molecules . . . . .	3
1.3 Time and length scales in photochemistry. . . . .	3
1.4 Information from ultrafast probes . . . . .	5
1.5 Time-resolved work from ESRF: historical perspective . . . . .	7
1.5.1 Laue diffraction studies of CO dissociation in MbCO . . . . .	8
<b>2 Probing Molecular Structure in Solution with X-rays</b>	<b>11</b>
2.1 Scattering from an electron . . . . .	11
2.2 Scattering from an atom . . . . .	12
2.2.1 Elastic scattering . . . . .	12
2.2.2 Compton scattering . . . . .	13
2.3 Scattering from a molecule . . . . .	15
2.3.1 Scattering from CCl <sub>4</sub> . . . . .	16
2.3.2 Debye limits . . . . .	16
2.3.3 Debye functions for [Fe(phen) <sub>3</sub> ] <sup>2+</sup> from DFT . . . . .	17
2.4 Scattering from a solution . . . . .	19
2.4.1 Atom-atom distribution functions $g_{\alpha\beta}$ . . . . .	19
2.4.2 Liquid structure factor $S(q)$ . . . . .	20
2.4.3 Time-resolved scattering $dS(q,t)$ . . . . .	21
2.4.4 Solvent hydrodynamics . . . . .	23
2.5 Scattered intensity on the detector . . . . .	27
2.5.1 Transmission of a liquid sheet . . . . .	29
2.5.2 Detector sensitivity . . . . .	30
2.5.3 Solid angle of a pixel . . . . .	30
2.5.4 Water intensity from a single pulse . . . . .	31
2.6 X-ray Emission Spectroscopy . . . . .	32
2.6.1 K $\alpha$ emission line . . . . .	33
2.6.2 K $\beta$ emission line . . . . .	34
2.6.3 Valence-to-core emission . . . . .	34
<b>3 Instrumentation</b>	<b>37</b>
3.1 Synchrotron radiation . . . . .	37
3.1.1 Accelerator complex . . . . .	38
3.1.2 X-ray sources . . . . .	39
3.1.3 Bunch structures at the ESRF . . . . .	41
3.2 ID09 beamline . . . . .	42
3.2.1 Undulators . . . . .	43
3.2.2 Chopper system . . . . .	45
3.2.3 Heatload choppers . . . . .	45
3.2.4 High-speed chopper . . . . .	48
3.2.5 Mirrors . . . . .	49
3.2.6 Multilayer monochromators . . . . .	56

3.2.7	Sample environment . . . . .	57
3.2.8	Detectors . . . . .	60
3.2.9	Laser/X-ray timing . . . . .	64
3.2.10	Laser system . . . . .	65
3.3	XES Spectrometers on ID09 . . . . .	65
3.3.1	Johann spectrometer . . . . .	66
3.3.2	Von Hámos spectrometer . . . . .	67
3.3.3	Von Hámos commissioning . . . . .	78
<b>4</b>	<b>WAXS and XES experiments on <math>[\text{Fe}(\text{phen})_3]^{2+}</math> in water</b>	<b>87</b>
4.1	Structure and photocycle of $[\text{Fe}(\text{phen})_3]^{2+}$ . . . . .	89
4.1.1	Ligand field splitting . . . . .	90
4.1.2	Photo-excitation . . . . .	92
4.2	Laser excitation . . . . .	94
4.3	Sample delivery . . . . .	96
4.4	Beamline configuration . . . . .	96
4.5	WAXS measurements . . . . .	98
4.6	Dye measurements . . . . .	100
4.7	WAXS scaling . . . . .	101
4.8	Solvent heating . . . . .	102
4.8.1	Direct water heating . . . . .	105
4.8.2	Sequential excitations . . . . .	105
4.8.3	Ligand excitation . . . . .	107
4.9	LS and HS structures of $[\text{Fe}(\text{phen})_3]^{2+}$ . . . . .	108
4.10	MD simulations of cage terms . . . . .	110
4.11	Lifetime measurements with Johann Spectrometer . . . . .	112
4.12	Spin state detection with von Hámos Spectrometer . . . . .	115
	<b>Conclusions</b>	<b>122</b>
<b>A</b>	<b>3d emission energies</b>	<b>123</b>
<b>B</b>	<b>DFT structure coordinates</b>	<b>125</b>
<b>C</b>	<b>Transition optical absorption spectroscopy (TOAS) measurements</b>	<b>135</b>
<b>D</b>	<b>Simulations of single-pulse Laue diffraction from proteins with radiation from synchrotron and XFEL sources</b>	<b>137</b>
D.1	Introduction . . . . .	137
D.2	Myoglobin structure . . . . .	138
D.3	Diffraction pattern predictions . . . . .	140
D.4	Serial Laue crystallography experiments on ID09 . . . . .	147
	<b>Bibliography</b>	<b>153</b>

# ACKNOWLEDGEMENTS

---

---

I would like to express my deep gratitude for having worked at the ESRF as a PhD student on beamline ID09 in the Complex Systems & Biomedical Sciences Group under the supervision of Michael Wulff. The ESRF is a wonderful institute with so many talented people from all over the world. It has been very inspiring to learn about new science from the many events that I attended like the student days out, group days out, science days, workshops and user meetings. The wide range of scientific and technical knowledge at the ESRF is truly impressive and will leave a lasting impression on me.

As a PhD student financed by the EU grant XPROBE directed by Beatrice Vallone, La Sapienza Rome, I was seconded for two weeks in 2016 to the Paul Scherrer Institute in Villigen in the group headed by Gebhard Schertler. I wish to thank him and his junior colleagues Elena Lesca and Niranjana Varma for their warm welcome and for having introduced me to crystallisation of biological membranes. Likewise I also spent a two weeks at the University of Rennes under the supervision of Marco Cammarata who helped me analysing the scattering data in my thesis. His great insight and efficiency are greatly appreciated.

Our collaboration with Qingyu Kong at the SOLEIL Synchrotron was essential for the project. Qingyu provided MD simulations of the DFT calculated structures of  $[\text{Fe}(\text{phen})_3]^{2+}$  which greatly facilitated the interpretation of the scattering and spectroscopy data. I would like to thank him most warmly for his kindness and help and for always being available.

The DFT structures were provided by Latévi Max Lawson Daku at the University of Geneva. His calculations were essential for quantifying the change in structure in the photo cycle of  $[\text{Fe}(\text{phen})_3]^{2+}$ .

As for the experiments on the beamline I wish to thank Sophie Canton for having introduced me to spin-crossover systems and for providing new metal complexes and reference samples. I really appreciate her great experience and friendship. I would also like to thank Dmitry Khakhulin for his help during an experiment at the FXE beamline at the EuXFEL in Hamburg and for very instructive discussions.

The present thesis would not have been possible without the support from my beamline colleagues who guided me so well in operating the beamline and analysing the data. I sincerely wish to thank Denis Leshchev for his enthusiastic and energetic help in my first experiment on the  $\text{Ru}_3(\text{CO})_{12}$  complex. I am also indebted to Martin Nors Pedersen, Norman Kretzschmar, Matteo Levantino and Mathias Sander for their great help and friendship during my stay at ESRF. A very special thank you to Mathias Sander for having organized a laser experiment at the University of Potsdam that provided unique insight in the photo physics of  $[\text{Fe}(\text{phen})_3]^{2+}$ .

The solution samples were prepared in the PSCM labs and I would like to thank Diego Pontoni and Pierre Lloria for their great help and wonderful company.

In the analysis of the spectroscopy data I received great help from Marius Retegan who calculated the emission spectra for  $[\text{Fe}(\text{phen})_3]^{2+}$  and helped with the interpretation. I really appreciate his reports and the time that he spent with me. Likewise I would like to thank

Christoph Sahle, Sara Lafuerza and Pieter Glatzel for instructing us in the theory and practice of emission spectroscopy and Martina Sandroni for her advice about metal complexes. The crystal analysers were made by Roberto Verbeni and I would like to thank for his excellent work.

My thesis progress was followed by Narayan Theyencheri, Kristina Kvashnina and Sakura Pascarelli with Sakura being the formal co-supervisor. I am really grateful for their kind advice and support.

Finally I would like to thank Michael Wulff most warmly for his never failing support and guidance in my work and daily life. I am greatly inspired by his enthusiasm and love for science and for the events that he organised during weekends for the beamline.

Victoria Kabanova

# RÉSUMÉ DE LA THÈSE

---

---

Cette thèse de doctorat intitulé «structure et dynamique de spin d'un complexe métallique étudié par rayonnement synchrotron» décrit une étude expérimentale du complexe métallique  $[\text{Fe}^{\text{II}}(\text{phen})_3]^{2+}$  en solution par la diffusion des rayons X résolue en temps et la spectroscopie d'émission, dont l'objectif est de surveiller les changements structuraux et de spin au cours du photocycle du complexe. Dans l'état photo-excité du complexe, un électron de l'orbitale 3d est transféré au ligand pour une fraction de picoseconde. Après ce "transfert de charge métal - ligand" (MLCT, *Metal-to-Ligand Charge Transfer*), l'électron revient au métal dans un état haut spin (HS) quasi-stable. Le photocycle se termine par un retour à l'état bas spin (BS), l'état fondamental, qui s'effectue en 725 ps. La structure et la rotation de l'état HS ont été mesurées par la diffusion de rayons X pulsés et la spectroscopie d'émission avec une résolution temporelle de 100 picoseconde. Les expériences ont été réalisées sur la ligne de lumière ID09 à l'ESRF – The European Synchrotron, à Grenoble, sous la direction de Michael Wulff et la co-tutelle de Sakura Pascarelli. Cette thèse de doctorat a été financée grâce à la subvention Horizon 2020 XPROBE (no 637295).

Le premier chapitre de la thèse donne un contexte scientifique et historique à ce travail, et commence par décrire l'importance de visualiser à l'aide de courtes impulsions de rayons X la façon dont les atomes se déplacent au cours de réactions chimiques et transformations. Ahmed Zewail a reçu le prix Nobel de chimie en 1999 pour avoir inventé la femtochimie, qui consiste à 'filmer' les atomes et molécules en action avec une résolution à la femtoseconde par spectroscopie optique et diffraction électronique. Par spectroscopie optique, Zewail et ses collègues ont surveillé la création et l'annihilation des liaisons chimiques, l'isomérisation et le transfert d'électrons avec la résolution femtoseconde, l'échelle de temps primaire en chimie. Le travail optique de Zewail s'est limité à l'étude de transitions énergétiques dans les molécules, lui permettant ainsi qu'à de nombreux scientifiques de mesurer *quand* les événements chimiques se produisent et *combien de temps* cela prend.

La spectroscopie optique ne permet pas de voir où les atomes se déplacent réellement dans l'espace. Dans les réactions en phase gazeuse, la diffraction des électrons a fourni le premier aperçu de la façon dont les atomes se réarrangent dans les molécules photosensibles simples. L'utilisation de rayons X pour des études structurales de molécules et de protéines a commencé avec l'inauguration de l'installation européenne de rayonnement synchrotron ESRF en septembre 1994, et a permis aux chercheurs de visualiser les réactions induites par photons avec une résolution de temps de 100 picosecondes. L'inauguration en 2009 du premier laser à électrons libres à Stanford, le LCLS, a constitué une avancée majeure dans le domaine. Il fournit des impulsions femtoseconde très intenses pour un large éventail d'applications dans de nombreux domaines de la science.

Des expériences ultrarapides sont effectuées à l'aide d'un faisceau laser "pompe" et d'un faisceau de rayons X "sonde". Résoudre les événements sur une échelle de temps allant de la pico à la femtoseconde requiert des intensités et des charges thermiques très élevées.

Dans l'expérience optique & rayons X de pompe-sonde, des impulsions laser courtes excitent l'échantillon à un temps zéro (excitation et synchronisation sont combinées) et d'intenses impulsions X permettent de sonder l'échantillon avec un délai qui peut être varié. Les clichés successifs obtenus en incrémentant progressivement ce délai produisent un "film" de l'évolution de l'échantillon en temps réel. La résolution de temps est limitée par les longueurs d'impulsion laser et de rayons X; dans ce travail, cette limite est fixée par l'impulsion de rayons X de 100 ps du synchrotron.

Les premières études réalisées avec des impulsions uniques de rayons X à l'ESRF ont concerné la dissociation de l'iode à l'intérieur d'une cage de solvant observée par diffusion de rayons X et la dissociation du C=O dans la myoglobine par diffraction de Laue à partir d'un cristal. Dans le cas de l'iode, le solvant capte les atomes d'iode dissociés; la plupart d'entre eux se recombinaient avec le même partenaire dans la cage sur l'échelle de temps de la picoseconde. Dans le cas de la myoglobine, en revanche, la dissociation génère un changement structural dans la protéine qui empêche le C=O de se recombinaison geminate qui est essentielle pour l'absorption et la libération du dioxygène dans les globules rouges. La limite de résolution temporelle des expériences de rayons X a été repoussée à 100 fs à XFELS en 2009. La contraction de la liaison Au-Au dans le trimère  $[\text{Au}(\text{CN})_2^-]_3$ , dont le temps caractéristique est de seulement 1.6 ps, a été observée par diffusion femtoseconde des rayons X à SACLA à SPring8, par le groupe de Ihee à KAIST.

Dans le chapitre deux «Sonder la structure moléculaire en solution avec des rayons X», la théorie de la diffusion des rayons X est mentionnée à commencer par le cas d'un électron libre suivi de la diffusion d'un atome avec des électrons  $Z$ . La diffusion de Debye à partir de molécules orientées au hasard est ensuite présentée, soulignant que lorsque la structure moléculaire est connue, le modèle de diffusion est facilement calculé. L'inverse n'est pas vrai puisque l'on mesure l'intensité diffusée, et donc l'information de phase est manquante. Les données doivent être modélisées par une structure modèle pour obtenir des informations 3D sur la position des atomes dans la molécule. La formule de Debye suppose que les atomes sont sphériques et que les électrons partagés dans les liaisons sont négligés, des approximations qui s'avèrent justifiées dans la pratique. L'amplitude de Debye  $S(q)$  est examinée dans la limite des grands  $q$  (magnitude du vecteur d'onde) au-dessus de  $10 \text{ \AA}^{-1}$ ; elle se rapproche asymptotiquement la diffusion par des atomes libres. Dans la pratique, il est important d'avoir accès à la plage de  $q$  élevée au-dessus de  $10 \text{ \AA}^{-1}$  pour mettre à l'échelle la diffusion totale rapportée à la diffusion atomique de la stœchiométrie de la solution, c'est-à-dire le soluté dilué et le solvant «*bulk*».

La diffusion Compton inélastique, qui n'apporte pas d'information structurale, domine la diffusion totale à grands  $q$  et doit être prise en compte lors de la mise à l'échelle de la diffusion, et donc aussi la mise à l'échelle de la diffusion différentielle induite par le laser. L'effet Compton est décrit: photon incident  $\rightarrow$  électron éjecté & photon diffusé. Le décalage énergétique du photon est calculé par rapport à l'angle de diffusion d'un faisceau monochromatique et rose à 15 keV. Pour le faisceau rose, l'énergie Compton sur le détecteur 2D Rayonix varie de 13,0 à 15,0 keV. Il est montré plus tard dans le chapitre, que 60% des photons diffusés par l'eau le sont par effet Compton!

La théorie de la diffusion discutée jusqu'à présent se limite aux atomes et molécules libres. Lorsqu'un soluté comme  $[\text{Fe}(\text{phen})_3]^{2+}$  est dissous dans un solvant, la position des atomes est décrite par des fonctions statistiques de corrélation inter-atomiques  $g_{\alpha\beta}(r)$  les indices  $\alpha$  et  $\beta$  correspondent au type d'atome dans la solution. Ces fonctions ont une plage intramoléculaire – dans la molécule de soluté – où les positions de l'atome sont (quasi) fixes et une plage intermoléculaire où la distribution est étalée en raison de mouvement diffus. Les fonctions  $g_{\alpha\beta}(r)$  ne peuvent être mesurées directement que pour les liquides mono-atomiques comme

Li et Na, mais elles peuvent être simulées pour des liquides complexes par la dynamique moléculaire puis comparées aux expériences. La fonction de diffusion  $S(q)$  s'exprime comme une intégrale dans l'espace de  $g_{\alpha\beta}(r)$ . À titre d'exemple,  $S(q)$  est calculé pour l'eau à partir de données MD basées sur le modèle TIP4P. Les fonctions de diffusion partielle pour les paires spécifiques dans l'eau, O..O, H..H et H..O. sont également calculées.

À partir des fonctions  $g_{\alpha\beta}(r)$  pour l'eau, la diffusion d'un film d'eau de 0,36 mm d'épaisseur est calculée pour une seule impulsion de rayons X avec  $1,0 \times 10^9$  ph/pulse à 18 keV. L'intensité calculée par pixel comprend des corrections pour la polarisation linéaire du faisceau, l'absorption dans l'eau et l'écran de phosphore de la caméra CCD ainsi que l'angle solide des pixels pour une distance de détecteur d'échantillon de 40 mm. Le détecteur reçoit  $4,1 \times 10^6$  ph/impulsion et  $2,7 \times 10^6$  sont détectés. Les photons sont intégrés sur la gamme de  $q$  0-10  $\text{\AA}^{-1}$ . Le calcul est en excellent accord avec l'intensité mesurée, ce qui permet de valider que le  $dS(q)$  de l'excitation laser est mesuré et mise à l'échelle correctement.

Comme mentionné précédemment, l'inversion des données expérimentales  $S(q)$  pour revenir à  $g_{\alpha\beta}(r)$  est impossible à partir de simples mesures d'intensité et la seule façon d'inférer des informations spatiales réelles est de comparer les données de diffusion avec un modèle. Les modèles DFT des structures à bas et haut spins de  $[\text{Fe}(\text{phen})_3]^{2+}$  ont été générés par Latévi Max Lawson Daku à l'Université de Genève et les structures ont été insérées dans une simulation de dynamique moléculaire en présence d'eau. Les fonctions  $S(q)$  ont ensuite été calculées par la fonction de Debye généralisée et comparées à des expériences. La principale conclusion est que les liaisons Fe-N dans l'état HS s'allongent de 0,19  $\text{\AA}$ , ce qui a pour effet d'élargir le complexe.

Malgré la simplicité du modèle de Debye pour un gaz moléculaire, il est instructif d'examiner son comportement pour les cas suivants : la contraction et l'expansion des liaisons, leur formation et dissociation. Dans le cas de l'expansion des liaisons, par exemple, la diffusion à petits  $q$  est positive, et négative dans le cas de la contraction. Lorsqu'un lien est rompu, la diffusion dans la direction du faisceau direct est négative et vice versa pour la formation de liaisons. Avec ces règles de base, une première impression des tendances d'une réaction peut être obtenue. Ceci est plus tard utilisé pour déduire que le rayon de cage se contracte par 0.3  $\text{\AA}$  dans l'état HS où les liaisons sont allongées!

Une caractéristique essentielle de la diffusion des rayons X par les liquides, qu'il s'agisse de la diffusion totale ou différentielle, est qu'elle sonde toutes les distributions atome-atome dans l'échantillon, y compris celle du solvant 'bulk'. Quand une molécule de soluté change de structure, elle change d'énergie et l'excès d'énergie est dissipé dans le solvant. La température du solvant augmente et le signal thermique doit être inclus dans l'analyse. Sur les échelles de temps courtes, 0,1-10 ns, la hausse de température est adiabatique et isochore. Plus tard, de 10 ns à 1  $\mu\text{s}$ , la pression excessive est libérée par expansion et la température de l'échantillon s'homogénéise mais à une température plus élevée. La diffusion thermique est déterminée lors d'une deuxième expérience avec un colorant qui absorbe le rayonnement laser comme point chaud sans aucun changement de structure. La réponse de l'eau a été mesurée de cette façon et l'échelle de température calibrée par rapport au modèle d'eau TIP4P.

Dans la théorie hydrodynamique développée par Savo Bratos et Rodolphe Vuilleumier, le liquide est supposé être en équilibre thermique local. L'expression pour le refroidissement des points chauds dans un liquide de Landau et Lifshitz est examinée pour la concentration de soluté utilisée dans cette deuxième expérience dans l'eau. Le calcul montre que la distance moyenne soluté-soluté pour une concentration de 2,1 mM de  $[\text{Fe}(\text{phen})_3]^{2+}$  excité est de 92  $\text{\AA}$  et que l'onde thermique prend 82 ps pour se déplacer de 46  $\text{\AA}$  (temps de mi-parcours). La température est uniforme localement, mais aux échelles de longueur plus longues, la température est fonction du profil laser et du coefficient d'atténuation dans le film d'eau. S'il existe

de petites variations de température à l'échelle du nm, elles sont aplanies par l'impulsion à rayons X de 100 ps. Enfin, un diagramme de phase hydrodynamique est calculé avec la voie de réaction de  $[\text{Fe}(\text{phen})_3]^{2+}$  en fonction de la densité, de la température et de la pression dans le cas de l'eau et de l'acétonitrile.

La dernière section du chapitre 2 est un résumé de ce que l'on peut apprendre de la spectroscopie par émission de rayons X (XES). Les spécifications des lignes  $K\alpha$ ,  $K\beta$  et valence-à-noyau (VtC, Valence-to-Core) sont présentées : intensité, spin et sensibilité au ligand. Le changement induit par laser dans les lignes  $K\beta$  est le marqueur le plus sensible de l'état de rotation et les différences spectrales peuvent être prédites avec le programme Crispy® développé par Marius Retegan à l'ESRF.

Dans le chapitre 3, le synchrotron ESRF et la ligne de faisceau ID09 sont décrits en mettant l'accent sur les caractéristiques importantes pour les expériences à impulsion unique. Ainsi, le disque à roue dentée permettant de hacher le faisceau («chopper») a besoin d'un espace de temps de  $\pm 176$  ns pour isoler les photons produits par paquets d'électrons uniques, ce qui est possible dans les modes de l'anneau de stockage  $7/8 + 1$ , 4-paquets et 16-paquets. Le mode uniforme avec 992 paquets séparés par 2,84 ns est inutilisable pour l'expérience d'impulsion uniques mais demeure très utile pour hacher des impulsions microsecondes avec une intensité élevée. Le nouveau miroir de mise au point produit par Thales a été installé dans la dernière année de ce projet de thèse et j'ai participé à sa mise en opération, ce qui m'a permis d'approfondir mes connaissances en optique de rayons X. Le miroir est cylindrique dans la direction longitudinale et fléchi mécaniquement pour adopter une forme toroïdale. La forme du miroir a été examinée en scannant la position verticale de celui-ci avec un faisceau fixe très fin. En surveillant la position réfléchi du faisceau à 10 mètres en aval, la pente locale a été déduite de la position du faisceau réfléchi. Le rayon de courbure a été trouvé en parfait accord avec la position du miroir par rapport à la source et la mise au point. En outre, les erreurs de polissage ont été déterminées et utilisées dans le traçage des rayons pour vérifier la cohérence avec la mise au point mesurée. Le meilleur foyer de l'ancienne source ESRF était  $40 \times 60 \mu\text{m}(\text{H}) \times \mu\text{m}(\text{V})$ .

Le nouveau détecteur Rayonix a été installé au début de mon doctorat et la grande surface de son phosphore,  $170 \times 170 \text{ mm}^2$ , sa lecture rapide et son faible courant d'obscurité ont étendu la gamme de  $q$  utilisable à  $10.6 \text{ \AA}^{-1}$  dans les expériences à 18 keV. La linéarité et le courant d'obscurité ont été mesurés : la non-linéarité devient importante au-dessus de 40 000 points/pixel (lecture de 16 bits) et les temps d'exposition jusqu'à 100 s sont essentiellement exempts de bruit.

Le laser femtoseconde et le laser TOPAS OPA sont décrits, y compris la synchronisation à l'horloge RF. L'activation de l'impulsion laser peut être variée avec une résolution de 11 ps et les fluctuations entre rayons X et laser sont de 2-3 ps (moyenne quadratique).

Les spectromètres Johann (JS) et Von Hamos (VH) pour XES sont également décrits en mettant l'accent sur VH puisqu'il a été utilisé pour la première fois pour mon projet de doctorat. Je décris comment la fluorescence  $4\pi$  est concentrée par les analyseurs cylindriques dans une ligne d'énergie dispersive. L'intensité du détecteur Maxipix est calculée à partir de l'acceptation énergétique des analyseurs ( $dE/E$ ) et de leurs angles solides. Le taux de comptage de  $K\beta$  est faible, généralement 0,01 ph/pulse/analyseur, et l'échantillon a été exposé pendant 1 heure par délai pour obtenir un bon rapport signal-sur-bruit.

Les expériences WAXS et XES sont décrites et analysées au chapitre 4. Le niveau  $3d$  10 fois dégénéré est séparé par le champ du ligand en deux états,  $t_{2g}$  et  $e_g$ , qui peuvent accueillir des électrons dans un état  $S = 0$  (BS) et un état  $S = 2$  (HS) à plus haute énergie. Après la photo-excitation en MLCT, l'électron transféré retourne à l'état HS centré sur le métal en environ 300 fs pour ensuite revenir à l'état BS par désintégration non radiative en 725 ps.

Pour les applications pratiques des cellules solaires, l'état MLCT du  $[\text{Fe}(\text{phen})_3]^{2+}$  a une durée de vie très courte car il est déstabilisé par les bandes d'énergie inférieures des états triplet et quintet qui accélèrent la désintégration par le croisement des systèmes. Cependant, grâce à un choix approprié de ligands, la division des ligands peut être augmentée de sorte que les croisements de courbes et les croisements entre systèmes sont bloqués. Dans le complexe Fe carbène  $[\text{Fe}(\text{btz})_3]^{2+}$ , la durée de vie de la MLCT est de 538 ps, suffisamment longue pour que l'électron du ligand pénètre dans le semi-conducteur  $\text{TiO}_2$  d'une cellule solaire.

Le changement de structure dans la transition BS  $\rightarrow$  HS a été mesuré par diffusion de rayons X aux grands angles (WAXS) avec une résolution temporelle de 100 ps. L'échantillon était excité avec des impulsions de 1,2 ps à 400 nm et la structure sondée par des impulsions de rayons X à 18 keV (monochromatisées par un multicouche Ru de 2,1%) avec un décalage de 100 ps. La séquence pompe-sonde a été répétée à 1 kHz et les impulsions de rayons X ont été isolées avec un *chopper* à la même fréquence. La diffusion a été enregistrée par le détecteur Rayonix HS170 couvrant la gamme de  $q$  0-10,6  $\text{\AA}^{-1}$ . Les courbes d'intensité radiale des images laser ON et laser OFF ont été mises à l'échelle de la cellule unitaire de solution dans la limite des grands  $q$  à partir de laquelle les courbes  $dS(q, t)$  ont été calculées pour 10 retards de -100 ps à 2 ns. Les courbes  $dS(q, t)$  sont des instantanés de 100 ps du changement structurel moyen pour toutes les paires d'atomes dans l'échantillon au moment  $t$ . Sur de courtes échelles de temps  $t < 10$  ns, le solvant est chauffé adiabatiquement à volume constant. Ce processus a dans l'espace réciproque ( $q$ ) une signature unique qui est proportionnelle à la hausse de température. La réponse thermique de l'eau a été mesurée dans un mélange colorant/eau. Ce colorant fonctionne comme absorbeur de photons et chauffe le solvant sans aucun changement structurel mesurable dans la molécule de colorant. Les données WAXS sont compatibles avec les structures BS et HS simulées par DFT avec une durée de vie HS de 725 ps. Le changement du rayon de la cage est déduit des données à petits  $q$ . La cage se contracte de 0,3  $\text{\AA}$  dans l'état HS ce qui est surprenant puisque la distance Fe-N est plus longue de 0,19  $\text{\AA}$  dans cet état à haut spin.

La durée de vie de l'état HS a été observée par XES en temps résolu à partir de la ligne  $K\beta$  à 7058 eV. Le spectromètre Johann, qui observait une seule énergie à la fois, a été utilisé pour les mesures de durée de vie en raison de sa sensibilité élevée aux petits changements d'intensité. XES est spécifique à l'atome et ne génère pas de bruit de fond de sorte que cette technique est parfaite pour étudier des changements de population en fonction du temps.

La ligne spectrale  $K\beta$  a été mesurée avec le nouveau spectromètre von Hamos et comparée aux simulations Crispy<sup>®</sup>. Les simulations confirment, sans ambiguïté, que l'état 725 ps est le quintet HS  $S = 2$ . Des émissions de VtC très faibles ont également été observées (100 fois plus faibles que  $K\beta$ ).

En combinant la plus grande brillance de la nouvelle source ESB de l'ESRF, l'utilisation de 16 analyseurs et d'autres améliorations possibles, le taux de comptage XES peut être augmenté d'au moins un ordre de grandeur. Cela devrait permettre de mesurer les changements subtils dans les spectres VtC et ainsi sonder les électrons du ligand connecté au métal.



# INTRODUCTION

---

---

Science has always been driven by the desire to understand how nature works. In order to understand how physical, chemical and biological systems function, it is crucial to know their structures, i.e the geometrical arrangements of atoms at the atomic level, and to follow how they evolve as a function of time. After the discovery of X-rays by Wilhelm Conrad Röntgen in 1895 it is now possible to determine the static structures of materials, at atomic resolution, by diffraction using conventional lab sources. With the advent of 3<sup>rd</sup> and 4<sup>th</sup> generation synchrotron sources like the ESRF and more recently the Extremely Bright Source (EBS) in Grenoble, very intense undulator beams are now allowing to perform time resolved experiments based on single X-ray pulses in areas from imaging, diffraction and spectroscopy with 100 picosecond time resolution. The ultimate X-ray sources for time-resolved experiments are Free Electron Lasers, the LCLS in Stanford (US), SwissFEL in Villigen (CH) and the European XFEL in Schenefeld (DE) for example, where the SASE effect produces 100 femtosecond pulses that allow to examine processes on the primary chemical time scale of bond formation and breakage, electron transfer, isomerisation processes etc.

For a full understanding of a process it is not enough to know the static structure of the system at the starting and end-points of the process. It is essential to follow how the structure changes during the process in order to understand the underlying mechanism. Various processes in nature occur on very different time scales spanning orders of magnitude in time, from attoseconds to seconds and beyond so it is very important to have experimental techniques for all these time scales. The motions in large scale systems, e.g. muscle contraction or large amplitude motions in proteins like changes in tertiary and quaternary structure in heme proteins happen on the millisecond time scale [1]. These processes can be studied with time-resolved X-ray techniques based on millisecond shutter controlled exposures of detectors. For smaller molecular systems, the time scales of structural changes are much faster. At the extreme, chemical reactions and elementary chemical processes that happen on the atomic length scale, such as bond breakage/formation or molecular vibrations and rotations, occur on the time scale of femtoseconds. To get a feel for the time scale for primary chemical reactions, changes in molecular structure propagate at the speed of sound, typically 1000 m/s, which corresponds to 100 fs per Å. Another example is the vibration time of diatomic molecules like H<sub>2</sub> and I<sub>2</sub> with oscillation periods of 10 fs and 156 fs respectively in their ground states. The femtosecond time scale became accessible with ultrafast lasers in the 1980 and the Nobel Prize was awarded to Ahmed H. Zewail in 1999 for filming of the formation and annihilation of molecules by femtosecond optical absorption spectroscopy. Moreover, Gerard Mourou from Ecole Polytechnique was awarded the Nobel Prize in Physics in 2019 for the development of the so-called chirped-pulse-amplification technique that allows to amplify femtosecond pulses

a million times and make them useful for pump-probe experiments at synchrotrons for example [2], [3].

The beauty of optical spectroscopy is that it allows to measure *when* bonds are broken or formed and to measure binding and dissociation energies. Due to the long wavelengths of optical light however, 300-600 nm, there is no structural information in optical absorption data on the atomic length scale.

Third generation synchrotrons like the European Synchrotron Radiation Facility are producing intense 100 picosecond pulses. As we have seen, these X-ray pulses are too long for probing the primary steps in reactions but perfect for slower secondary structure determination. With the advent of Free Electron Lasers like the LCLS, SwissFEL and EuXFEL, short and very intense X-ray pulses are now available for structural studies with femtosecond time resolution.

## 1.1 Pump-probe technique

As mentioned above, it is now possible to study very fast processes in real time by stroboscopic pump-probe techniques. In this project we primarily used laser/X-ray pump-probe and to some extent, laser/laser pump-probe to test a hypothesis. The optical pulse, the laser pump, initiates a structural change in the sample and defines time zero. The second pulse (laser or X-ray probe) arrives after a certain controlled time delay and probes the properties of the system at that particular delay. The time delay between the pump and probe pulses can be changed electronically or optically and the system is probed at different stages in the photo-induced reaction. The continuous process is thus broken up into a series of snapshots which can be stitched together afterwards into a molecular movie. The pump-probe principle is shown in figure 1.1.

Because of the finite pulse lengths of the pump and probe pulses, the observed processes are smeared on the movie. The instrumental time resolution of a pump-probe experiment is given by the convolution of the two pulse lengths and the uncertainty in the time delay, the jitter between them:

$$\Delta t = \sqrt{\Delta t_{pump}^2 + \Delta t_{probe}^2 + \Delta t_{delay}^2}.$$

The pump-probe parameters on beamline ID09 at the ESRF are  $\Delta t_{pump} = 1.2$  ps,  $\Delta t_{probe} = 100$  ps and  $\Delta t_{delay} = 2$  ps. As the X-ray pulse length dominates, the instrument resolution is 100 ps (FWHM).

At present, femtosecond resolution is achieved routinely in pump-probe experiments at X-ray free electron lasers (XFELs) in serial Laue crystallography [4], in wide-angle solution scattering [5] and in X-ray absorption and emission spectroscopy [6] [7]. Laser pulses can be shortened to sub-fs, but commercial laser systems typically generate 25-100 fs pulses. For the X-ray pulses, a typical length of an X-ray pulse from an XFEL is 10–100 fs. Pulses from synchrotrons are 100 ps long and that sets the limit of the temporal resolution of synchrotron pump-probe experiments.

It should be noted that the frequency of the X-ray wavefront is given by  $c = \nu \times \lambda$ , where  $c$  is the speed of light,  $\nu$  the frequency and  $\lambda$  the wavelength. For 1 Å radiation for example, the frequency is  $3 \cdot 10^{18}$  Hz, which corresponds to the oscillation period of  $0.33 \cdot 10^{-18}$  s, i.e. sub-attoseconds. Therefore, X-rays can potentially resolve vibrations in molecules at  $\sim 10^{15}$  Hz if the electron bunch emitting the X-ray pulse is sufficiently short.

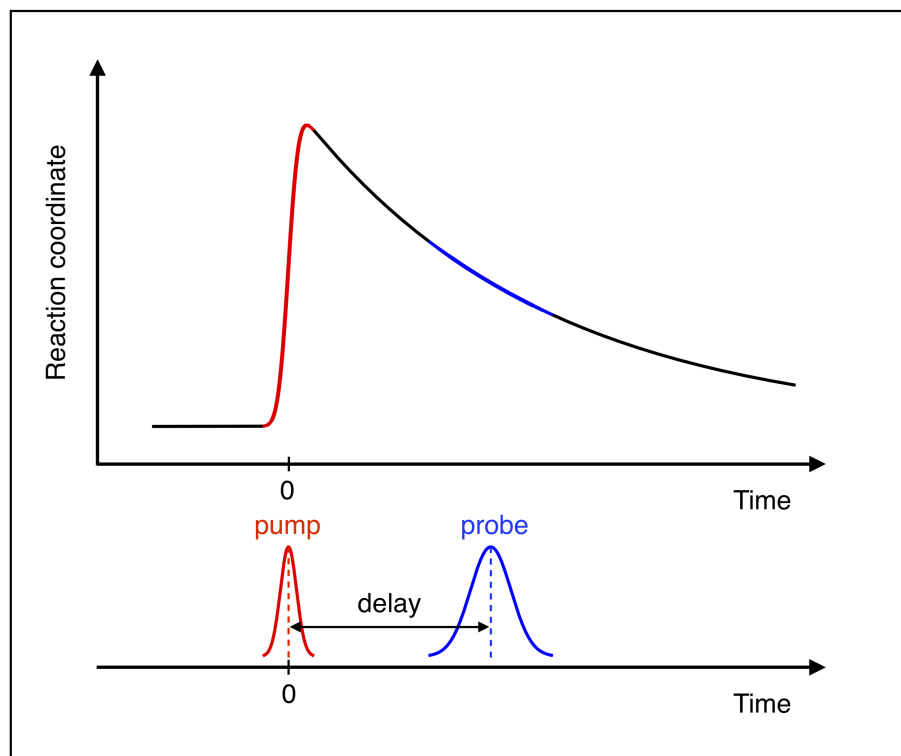


**Figure 1.1:** Pump-probe principle. The pump triggers the structural change and defines time zero of the process. The starting accuracy is given by the duration of the pump pulse. The evolving structure is probed by a delayed X-ray or laser pulse and the signal is recorded on a detector. Many pump-probe pulses are needed to get a high signal to noise ratio, typically thousands of pulses.

## 1.2 Photoreactions in molecules

A variety of physical and chemical processes can be initiated by a laser pulse. The photoexcitation of a molecule, from the absorption of a laser pulse, brings the molecule to an excited state of higher energy. That can lead to:

- Bond breakage/formation (e.g.  $I_2$  dissociation, [8])
- Isomerisation (e.g. trans-cis isomerisation in PYP, [9])
- Electron transfer (e.g. DMABN, [10], donor-acceptor bimetallic complexes, RuCo [11])

The optical photon can also indirectly trigger a reaction by causing a temperature change in the system or releasing a chemical from a caged compound to start an association reaction [12].

## 1.3 Time and length scales in photochemistry.

The molecular system can be described by its potential energy as a function of its configuration, e.g. the positions of all the atoms in the molecule. This function is a complex multi-dimensional potential energy surface with potential wells (local minima) and barriers between them. The valleys correspond to low-energy metastable states and the saddle points between them to transient states. The energy needed to overcome the potential barrier is the energy needed to drive the transition between metastable states.

In the simplest case of diatomic molecules like  $\text{H}_2$ ,  $\text{Br}_2$  and  $\text{I}_2$ , the potential energy depends only on the distance between the two atoms, and the potential energy is represented by a curve. The potential energy for  $\text{I}_2$  is shown in figure 1.2 for the ground and low energy excited states. At large atom-atom separation, the force is attractive and driving the atoms closer together towards the potential minimum. At short distances, repulsive forces dominate. The minimum in the potential is the equilibrium bond length. The classical and quantum description of the energy levels, oscillation amplitudes and frequencies are described in detail in Slater's paper in [13]. The energy of the molecule is quantised in discrete vibrational levels. At room temperature, the ground state vibration level is essentially 100% occupied. In gas phase iodine, the ground state bond length is 2.666 Å. The oscillation frequency is  $6.41 \cdot 10^{12}$  Hz (156 fs) and the mean amplitude of the vibration 0.05 Å [14].

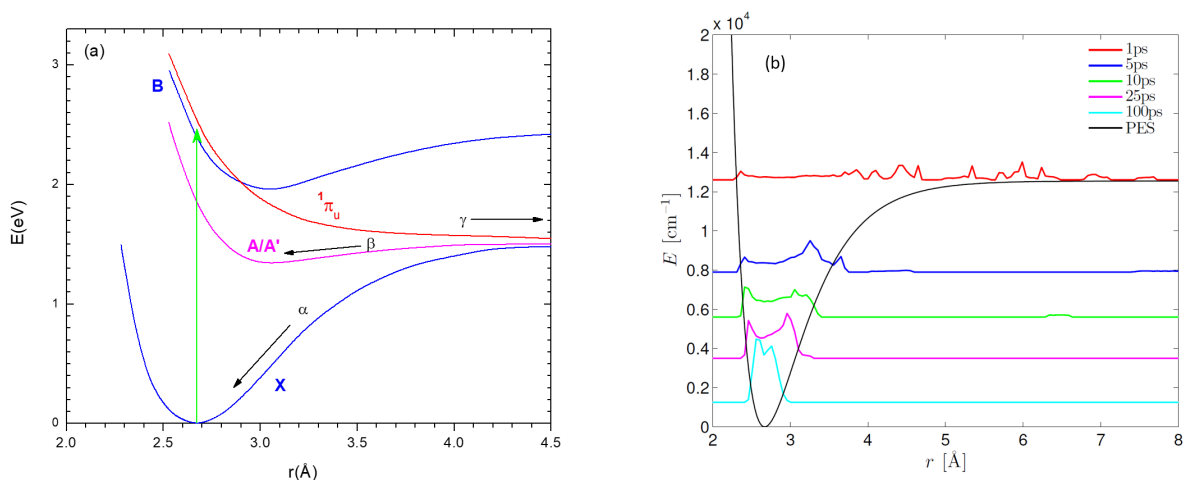


**Figure 1.2:** Ground and excited state potentials for  $\text{I}_2$  in solution. (a) The X-potential is approximated by a Morse Potential. Following the Franck-Condon principle, an ultrashort green laser pulse excites  $\text{I}_2$  vertically to the repulsive antibonding  $\pi$  and B potential. In the pursuing expansion along  $\pi$ , the atoms collide with the solvent cage in 300 fs. 65% of the I atoms recombine in the cage, 20% recombine in the 2.7 ns A/A' state and 15% escape the cage. The recombination is random and phase coherence is lost after the first cage collision. (b) Molecular dynamics simulations by Klaus Moeller, DTU, Lyngby, Denmark, private communication. It shows the distribution of distances  $g_{I-I}(r)$  vs time in the vibrational cooling of  $\text{I}_2$  in liquid  $\text{CCl}_4$ . The red curve at 1 ps is very broad and has a low amplitude (difficult to measure). The distribution sharpens at later times as  $\text{I}_2$  is cooled by the solvent.

The recombination of  $\text{I}_2$  in liquid  $\text{CCl}_4$  was the first prototype chemical reaction studied with pulsed X-rays from a synchrotron [8], [15]. The key finding is that when a molecule changes structure, the change in energy is dissipated in the solvent. On the fast time scale 0-10 ns that leads to an adiabatic temperature rise in the solvent followed by thermal expansion driven by the pressure gradient from the laser beam profile. The scattering signal from the change in solvent structure has to be included in the analysis. Secondly, the scattered signal from the solute is the weighted sum of the scattering from pairs of atoms in the molecule. We will discuss the details later when isolating the structural signal from the high spin state of  $[\text{Fe}(\text{phen})_3]^{2+}$  from the water background.

## 1.4 Information from ultrafast probes

By optical pump-probe techniques it is possible to follow, in real time, the dynamics of elementary chemical processes like bond breakage, formation, isomerisation etc. Optical lasers generate radiation with wavelengths in 350-800 nm range, which corresponds to photon energies of several eV. This also is the typical energy needed to overcome the potential energy barrier between metastable states of a chemical system. Thus the absorption, emission or scattering of optical light probing transient states give information about the potential energy surfaces of the system.

Knowing the potential energy landscape of a molecule (or rather the energy transitions) can be used to deduce the excited state structure in the simple case of diatomic dissociation, where the potential energy can be predicted quite well. With the increase in complexity of the system, it quickly becomes very difficult to model the potential due to the large number of degrees of freedom, and more direct structural information is needed. This information is probed more directly by X-ray diffraction and scattering since the wavelength is matching interatomic distances in molecules, crystals and solids.

The advent of 3<sup>rd</sup> generation X-ray sources made it possible to use short X-ray wavelength  $\sim 1 \text{ \AA}$  to probe structures at atomic resolution. The high brilliance and the pulsed nature of synchrotron sources made it possible to expose the sample with trains of single X-ray pulses and achieve 100 ps time resolution in optical/X-ray pump-probe techniques like diffraction, scattering, spectroscopy and imaging. It is now possible to probe the dynamics of excited states of matter with X-rays in both space and in time. The pioneering picosecond time resolved X-ray experiments using optical/X-ray pump-probe were performed at the ESRF in 1994 by Michael Wulff, Dominique Bourgois, Keith Moffat and their colleagues [16]. Time-resolved Laue diffraction from the myoglobin complex MbCO produced a film in 3D showing the motion of the CO after dissociation from Fe triggered by a 635 nm 7.5 nanosecond laser pulse. It was shown that after dissociation, CO is trapped in a cavity above the Fe where it stays for 10 ns. It also revealed the Fe motion out of the heme plane in response to the change in Fe coordination from 7 to 6 after dissociation. This pioneering work on wild type sperm whale myoglobin was followed by studies of mutants [17], [18] and the results will be reviewed in section 1.5.1.

The power of diffraction and scattering is that the interference from different atoms probes distances between pairs of atoms, i.e. the structure of the material. Structural changes are driven by electronic changes in the molecule, the switching from a bonding to antibonding state for example. X-ray absorption techniques like XANES, EXAFS and XES are probing the electronic states of the system under study. The pioneering spectroscopy work was done by Lin Chen in 2001 at the APS synchrotron at Argonne where she studied ligand ( $L_2$ ) dissociation in the Ni complex NiTPP- $L_2$  in solution by time resolved XANES spectroscopy. She identified a transient dissociated structure from the change in shape of the XANES spectrum. [19]. This work was followed by another XANES study of the transient structure of  $[\text{Ru}(\text{bpy})_3]^{2+}$  at the  $L_3$  and  $L_2$  absorption edges performed by the group of Majed Chergui in Lausanne. The experiment showed the presence of a charge transfer excited state with a lifetime of 300 ns. This work was done at the ALS synchrotron in Berkeley. The change in oxidation state of the central Ru atom, from 2+ to 3+, was unambiguously determined [20].

X-ray absorption is element-specific and allows to monitor electronic changes on an atom without interference from solvent heating. Zooming in selectively on a specific transition metal is an important complement to scattering and, as we will see later, perfect for measuring changes in excited state populations without interference from hydrodynamics in the solvent. We used X-ray emission spectroscopy to study the  $[\text{Fe}(\text{phen})_3]^{2+}$  complex since XES can be

done with a fixed incident beam energy as long as this energy is above the ionisation threshold of the transition metal.

The advent of XFELs made it possible to obtain even shorter X-ray pulses due to the SASE effect and achieve femtosecond time resolution. One of the first scattering experiments probing a chemical reaction in solution was performed by Hyotcherl Ihee, KAIST Korea and Shin-ichi Adachi, KEK, using the SACLA Free electron laser at SPring-8 [21]. They studied the formation of a gold trimer  $[\text{Au}(\text{CN})_2^-]_3$  by X-ray scattering. In the ground state, the Au atoms in three molecules are weakly bound by van der Waals interactions. Upon photoactivation, an Au electron is excited to a bonding orbital leading to formation of covalent Au-Au bonds with a linear geometry with 500 fs lifetime. The Au bonds shorten in a second 1.6 ps step. Finally, this linear conformation combines with  $\text{Au}(\text{CN})_2^-$  in 3 ns to form a tetramer. The reaction is shown in figure 1.3.

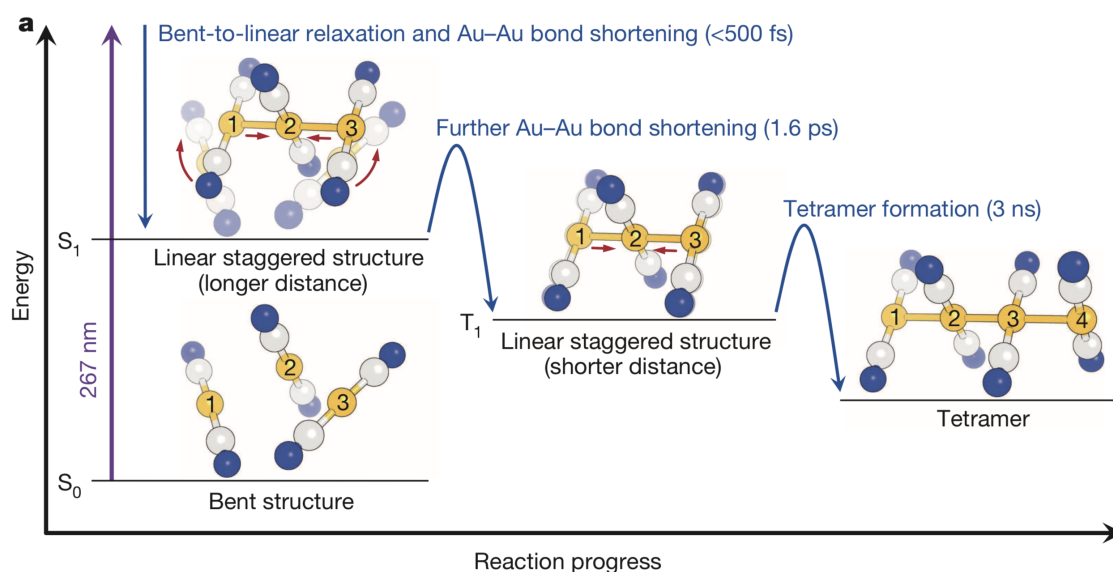


**Figure 1.3:** Pioneering solution phase scattering experiment from an XFEL by the Ihee and Adachi groups. The formation of a covalent bond between three Au atoms in  $[\text{Au}(\text{CN})_2^-]_3$  is monitored using 100 fs pulses at 15 keV with  $10^{12}$  ph/pulse in a 0.6% BW. [21]

The first X-ray spectroscopy experiment from an XFEL was reported by H. Lemke and M. Cammarata and co-workers in 2013 [6]. They performed a XANES study of the spin-crossover complex  $[\text{Fe}(\text{bpy})_3]^{2+}$  in a 50 mM aqueous solution using 100 fs pulses from the LCLS. The position of the Fe absorption edge depends on the Fe-N distance from which they deduced that the switch from the low-spin (LS) to the high-spin (HS) state takes 160 fs. The HS state subsequently decays to the LS state in 650 ps. The experiment was done with fluorescence detection and the white beam was monochromatised with a diamond monochromator. The K-edge was scanned over 45 eV, the spectral width of the white beam. The main challenge was timing drift which could be up to 100 fs per hour. That problem was later solved by time stamping the X-ray pulses followed by sorting them according to their delay [22], which allows to fully exploit the short pulse from an XFEL in time-resolved experiments.

A unique feature of XFEL radiation is the "diffraction before destruction" principle, which is central to serial crystallography. Even if the strong electric field ionises the absorbing atoms in a Coulomb explosion, the diffraction pattern is recorded before the crystal disintegrates. This hypothesis was tested on photosystem II (PS II) in a combined diffraction and XES experiment by Kern et al. in 2013 at the LCLS. They monitored changes in the  $K\beta_{1,3}$  line from Mn with a von Hámos spectrometer similar to the one used in this work.  $K\beta_{1,3}$  is sensitive

to the oxidation and spin state of the transition metal. The experiment, which is not time-resolved, showed that ultrashort XFEL pulses can record the structure of PS II microcrystals at room temperature without radiation damage of the central  $\text{Mn}_4\text{CaO}_5$  cluster.

In spite of the higher intense and shorter pulse from XFELs, synchrotrons will continue to play an important role for studies in the time range from 100 ps to seconds due to the higher beam stability and the wider available energy range. It is also important that users can get more beamtime so that the best experimental parameters can be found.

## 1.5 Time-resolved work from ESRF: historical perspective

The European Synchrotron, ESRF, was the first third-generation synchrotron light source built worldwide. The construction started in 1988 in Grenoble, France, and the commissioning of the first eight beamlines started in March 1993. Beamline ID09 was the fourth beamline to receive beam after ID11, ID13 and ID10. It was a white beam station for Laue diffraction and high pressure experiments and the X-rays were produced by a 44-pole wiggler that produced white beam from 5-50 keV (W70,  $K_{max} = 5.0$  at 20 mm gap). The thinking at the time was that protein structures could be obtained from single shot Laue images from a broadband wiggler source. The short exposure would limit radiation damage. However, the Laue images were overcrowded with spots and only very good crystals, free from mosaic spread, produced good images. Cryo cooling of protein crystals and collecting the data with the rotation method in a monochromatic beam was far more efficient. Michael Wulff, Dominique Bourgeois and Thomas Ursby therefore decided to use the intense white beam for time-resolved experiments from smaller protein crystals, MbCO, PYP and Br for example, where the crystals produced sharp Laue images. In collaboration with Keith Moffat's group at the University of Chicago, a prototype chopper was built that could isolate *one* pulse from the ESRF single bunch mode which has a revolution time of 2.82  $\mu\text{s}$ . The first successful MbCO data were collected in September 1994 using a 7.5 ns laser borrowed from Michel Roth at the IBS. The time resolution was limited by the laser in the first MbCO and PYP experiments. A femtosecond laser was installed in 1998 which was financed by the machine division. The deal was to use the laser to trigger a jitter-free streak camera, built in collaboration with Gerard Mourou, to measure the temporal X-ray profile very precisely, and to also use it for experiments in diffraction from solid surfaces.

It was very difficult to trigger protein crystals efficiently with the very short 100 fs pulse and various optical schemes were used to stretch the pulse to 1-2 ps to lower the peak intensity of the pulse by a factor of 10-20. The first 100 ps time-resolved Laue film was published in Science in 2003 by Friedrich Schotte, Philip Anfinrud (NIH) and the beamline team [17].

The first single-pulse Laue experiments were done with the focused beam from a broad band wiggler, the W70. The wiggler was later replaced by a U17 in-vacuum undulator. The U17 spectrum is concentrated in a 2-4% bandwidth around the fundamental which can be varied from 15 to 20 keV. In addition, a new high speed chopper from KFA Jülich could isolate single pulses, very reliably, at 1000 Hz, which opened up experiments with flowing samples. Exchanging the sample between pulses eliminates radiation damage from the laser/X-ray beams and overheating the sample.

## 1.5.1 Laue diffraction studies of CO dissociation in MbCO

Myoglobin has always served as a benchmark for many studies of protein structure and dynamics. It is the building block of hemoglobin that transports O<sub>2</sub> in blood cells from the lungs to muscles. It has a globular structure with six helices surrounding the protein active site: the heme. The heme is a porphyrin moiety with an Fe atom in the centre that binds and releases oxygen depending on the protein conformation.

The myoglobin structure was solved in 1958 by John Kendrew [23]. It was the first protein structure that was solved by X-ray crystallography. But the mechanisms of oxygen trapping and release needed to be studied by time-resolved techniques. Such biological processes happen on the time scale of fs to milliseconds. The first studies of the ligand dissociation and recombination were carried out in solution using optical spectroscopy and supported by molecular dynamics simulations (MD). The early X-ray studies were limited to millisecond time resolution., i.e. insufficient to monitor the CO and O<sub>2</sub> photocycle in photolysis experiments. The fast protein structural changes were studied indirectly by manipulating the proteins chemically or physically, for example, by trapping the reaction intermediates by lowering the temperature [24], [25].

Laue crystallography has boosted the temporal resolution in structure determination from the use of single pulse exposures from synchrotrons. This technique differs from monochromatic diffraction, where the crystal is rotated to sample  $k$ -space as much as possible. When a polychromatic X-ray pulse diffracts from a single crystal with random orientation, the reflections between the Ewald sphere spanned by  $E_{min}$  and  $E_{max}$  satisfy Bragg's law. As a result, many more reflections appear on the detector compared with a monochromatic experiment. For the monoclinic myoglobin crystals used by Srajer et al, the crystals were rotated in steps of 3° per exposure, from 0 to 180°, and 16 images were accumulated before detector readout. For each time delay, 50 000 intensities  $I(hkl)$  were measured. When the initial structure is known, the excited state can be deduced from a difference Fourier transform of  $\Delta I(hkl)$ .

As mentioned above, the ESRF was first to take advantage of the pulsed structure of X-ray sources by recording single-pulse Laue diffraction with sub-ns temporal resolution. In the first years, the ID09 chopper system allowed for single X-ray pulse isolation if the pulses were separated by  $\sim 2 \mu s$  [26], which was only possible when the storage ring was operated in single-bunch mode. In this filling mode, the bunch charge is 10 mA and the pulse duration 150 ps. To initiate photoreactions in the first Laue experiments, the beamline used a Nd:YAG pumped dye laser with 7.5 ns pulses running at 10 Hz.

The pump-probe repetition rate was slow ( $< 0.1$  Hz) to allow the photocycle for return to the initial state and to reduce heating the crystal. The pump wavelength 635 nm was chosen to make sure that the optical density OD of the crystals was low, around 0.1, so that only 10% of the laser pulse was absorbed. As a result, gradients in the excitation profile are small which would otherwise deform the crystals. Carbon monoxide ligand (CO) was used instead of diatomic oxygen (O<sub>2</sub>) because of its stronger Fe binding which prevents water from the mother liquor from binding to Fe [17].

The nanosecond myoglobin study showed that 1 ns after CO dissociation, the shortest probed time delay, CO is occupying a small cavity next to Fe where it stays for about 70 ns. The heme plane is slightly tilted from the motion of Fe atom out of the plane in the opposite (proximal) direction. The change in conformation is hindering CO from rebinding immediately. Direct recombination is called geminate recombination which, unlike for I<sub>2</sub> in solution, is blocked by the reorganisation in the heme structure. It is fascinating that without this conformational change, the release of O<sub>2</sub> in blood cells could not happen, which is fundamental for respiration in humans and mammals.

At later time delays, the detached CO migrates to escape the protein via the so-called Xe1 internal pocket – one of the four hydrophobic cavities known from the studies of Xe binding to myoglobin under pressure [27]. The kinetic study of the CO population in these two docking sites determined the half-lives of 70 ns and 10  $\mu$ s, respectively.

Because the distal heme site is hosting the CO ligand at early time delays after dissociation, the protein function is most likely influenced by the amino acid side chains surrounding the binding site. The L29F mutant of Mb(CO), where leucine Leu was substituted by phenylalanine, showed 1000 times faster dynamics. The experiment was performed on ID09 with 150 ps time resolution, and color difference electron density maps were used to track the structural changes [17]. The CO migration path was studied in detail together with its correlations with side chain motions. The Fourier difference map of the L29F mutant after 100 ps is shown in figure 1.4. The difference is contoured at  $\pm 3\sigma$  and overlaid on the initial structure in white. Negative changes are shown in red, positive in blue. Note how blue and red pockets are positioned side by side from the vectorial translocation of atoms and residues. The CO docking site is populated first and, as a result, the CO hole is partly filled by the distal histidine His64. The heme doming and the heme tilting is shown by the arrows.

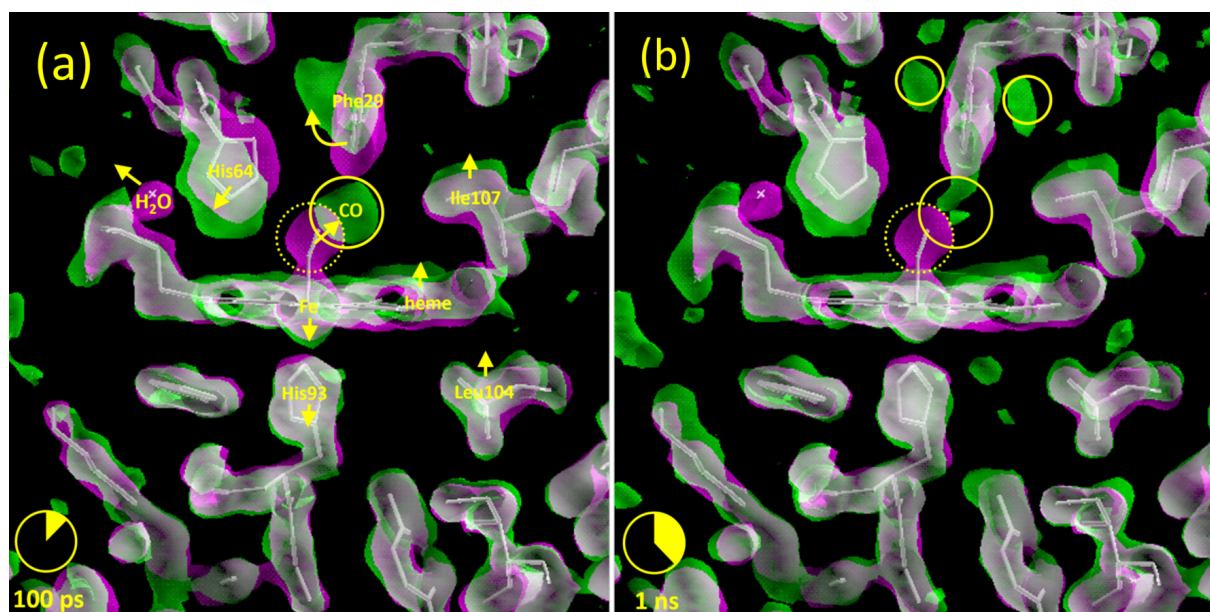


**Figure 1.4:** CO dissociation in the L29F mutant of myoglobin MbCO. The image shows the change in electron density, laser ON – laser OFF, 100 ps after CO dissociation from Fe. Negative and positive densities are shown in red and blue, respectively. The ground state structure is shown in white. The figure shows the changes near Fe but changes could be measured to the edge of the unit cell. (Courtesy Friedrich Schotte).



---

# PROBING MOLECULAR STRUCTURE IN SOLUTION WITH X-RAYS

---

When X-rays interact with a sample they are either absorbed or scattered by the atoms and molecules in the sample. X-rays are electromagnetic waves and the electric field accelerate the electrons in the illuminated atoms. According to the classical electromagnetic theory, an accelerated charge radiates, and this secondary radiation is the scattered radiation. X-ray scattering can be divided into elastic scattering and inelastic scattering. At large distances the former is a spherical wave with the same frequency as the primary beam. The latter, also called Compton scattering, produces scattered radiation with a longer wavelength plus a free electron.

In the present thesis we will examine the change in the structure, induced by a short laser pulse, of  $[\text{Fe}(\text{phen})_3]^{2+}$  diluted in water and acetonitrile. The scattering data will be compared to the structures predicted by Density Functional Theory (DFT) calculations.

To prepare for the analysis, I will briefly present the simplest results from scattering theory starting with free electrons, atoms and molecules. The scattering from a liquid or a liquid solution is more complicated since the liquid structure is statistic and described by atom-atom distribution function  $g_{\alpha\beta}(r)$  where  $r$  is the distance between  $\alpha$  and  $\beta$  type of atoms. In this case the scattering is calculated by the Zernike equation as shown below.

In brief, the solute scattering can be calculated by the Debye function when the atomic positions are known. The solvent scattering, in contrast, cannot be calculated numerically since the positions fluctuate in the liquid, in space and time. The solvent scattering is either measured, taken from tables in the literature, or simulated by molecular dynamics (MD). With recent advances in MD, it is now possible to simulate dilute solutions which requires tracking the positions of all the atoms in more than 4000 solvent molecules and in one or a few solutes. This allows to calculate the solvent structure around the solute, the cage, which is important in the following.

Finally a comprehensive account of the theory of X-ray scattering is given in B. E. Warren's book "X-ray Diffraction", Dover Publishing from 1969 [28].

## 2.1 Scattering from an electron

For a free electron, the scattered intensity into the space angle  $d\Omega$  is given by:

$$I = I_0 r_e^2 \cdot P \cdot d\Omega,$$

where

$$r_e = \frac{e^2}{m_e c^2} = 2.82 \cdot 10^{-15} \text{cm}$$

is the classical electron radius.  $I_0$  is the incident intensity (ph/m<sup>2</sup>/s) and  $P$  is the polarisation factor. Let's define the coordinate system as shown in figure 2.1. For linearly polarised X-rays along the  $y$  axis  $P$  is the projection of the incoming field onto the plane perpendicular to the direction of the detector as:

$$P(\theta, \phi) = \sin^2 \chi = 1 - \cos^2 \chi = 1 - \sin^2 \theta \sin^2 \phi,$$

where  $\theta$  and  $\phi$  are the polar angles towards the detector. The space angle is:

$$d\Omega = \sin \theta d\theta d\phi,$$

where  $d\theta$  and  $d\phi$  are the acceptance angles of the detector. The scattered intensity on a detector pixel therefore decreases with distance as  $1/R^2$ , where  $R$  is the distance to the detector.

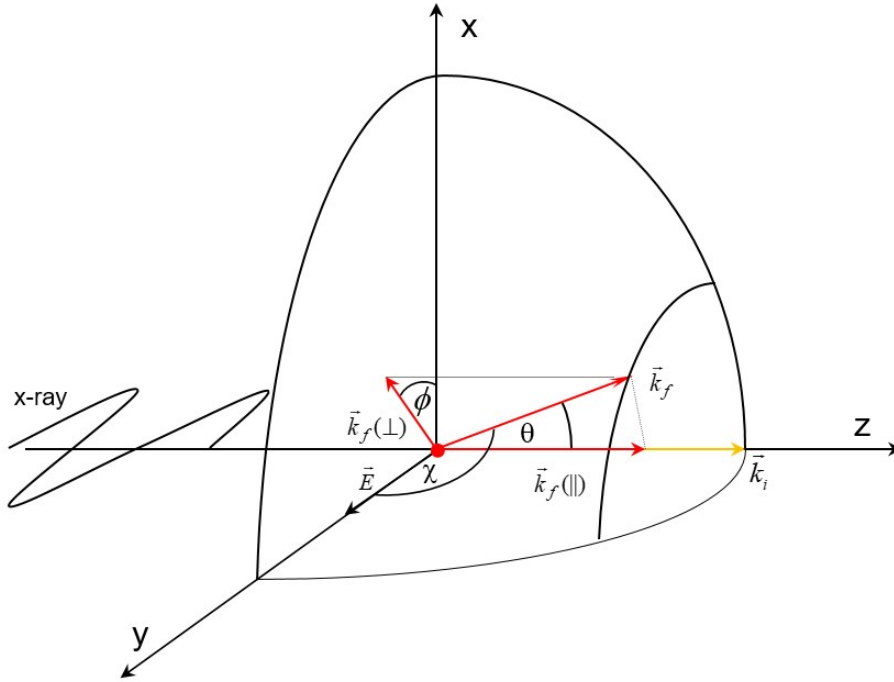


**Figure 2.1:** Polar coordinates of the incident (yellow) and scattered (red) beam for a linearly polarised incident beam. The electric field of the incident and scattered beam is confined to the plane perpendicular to the propagation. The intensity of the scattered beam in the  $y$  direction is 0 due to the polarisation.

## 2.2 Scattering from an atom

### 2.2.1 Elastic scattering

The scattering from an atom is proportional to the sine-Fourier transform of the electron density:

$$f(q) = \int_0^\infty 4\pi r^2 \rho(r) \frac{\sin(qr)}{qr} dr,$$

where  $q$  is the scalar momentum transfer  $q = \frac{4\pi \sin(\theta/2)}{\lambda}$  and  $\rho(r)$  the radial electron density of the atom and  $\theta$  the scattering angle (note that in Warren's book the scattering angle is  $2\theta$ ).

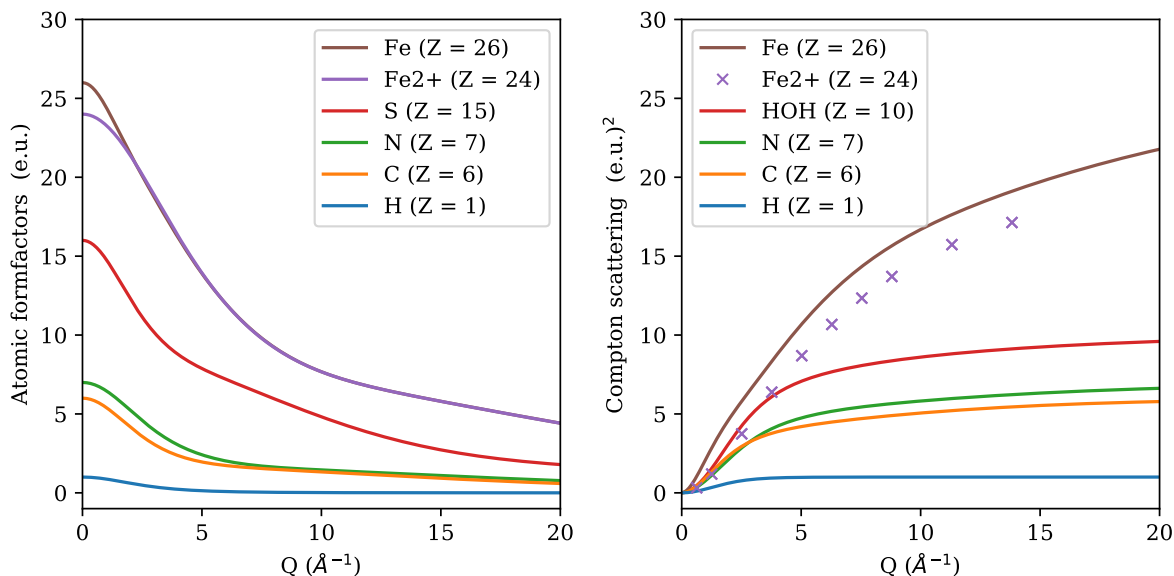


**Figure 2.2:** (a) Atomic formfactors for selected elements. The intensity of the scattered radiation is proportional to the square of the atomic formfactor  $f^2(q)$ . The intensity scales as  $Z^2$  for the forward scattering at  $q = 0$ . Hydrogen atoms are essentially invisible with a forward intensity of 1 as compared to 36 for C. (b) Compton intensity for the atoms in  $[\text{Fe}(\text{phen})_3]^{2+}$  and water. The high  $q$  part of the total scattering is dominated by Compton scattering that approaches  $Z$  in the high  $q$  limit, see also figure 2.21.

The limit  $\lim_{q \rightarrow 0} \frac{\sin qr}{qr} = 1$  gives the forward scattering for an atom with  $Z$  electrons:

$$f(0) = \int_0^\infty 4\pi r^2 \rho(r) dr = Z.$$

In practice atomic form factors are calculated from tabulated coefficients:

$$f(q) = \sum_{i=1}^4 a_i \exp\left(-b_i \left(\frac{q}{4\pi}\right)^2\right) + c, \quad (2.1)$$

where the 9 parameters  $a_i, b_i, c$  are listed in the International Tables for Crystallography. The formfactors for atoms in  $[\text{Fe}(\text{phen})_3]^{2+}$  ( $\text{Fe}^{2+}(\text{N}_2\text{C}_{12}\text{H}_8)_3$ ) are shown in figure 2.2(a). The scattered intensity from a free atom is:

$$I(q) = I_0 r_e^2 \cdot f^2(q) \cdot P d\Omega.$$

## 2.2.2 Compton scattering

In Compton scattering, a photon is scattered inelastically by an atom producing a scattered photon at lower energy (red-shifted) and a free electron. The process is described as "photon in  $\rightarrow$  photon and electron out". The process is shown schematically in figure 2.3. The wavelength  $\lambda'$  of the scattered photon is:

$$\lambda' = \lambda + (1 - \cos \theta) \frac{h}{m_0 c},$$

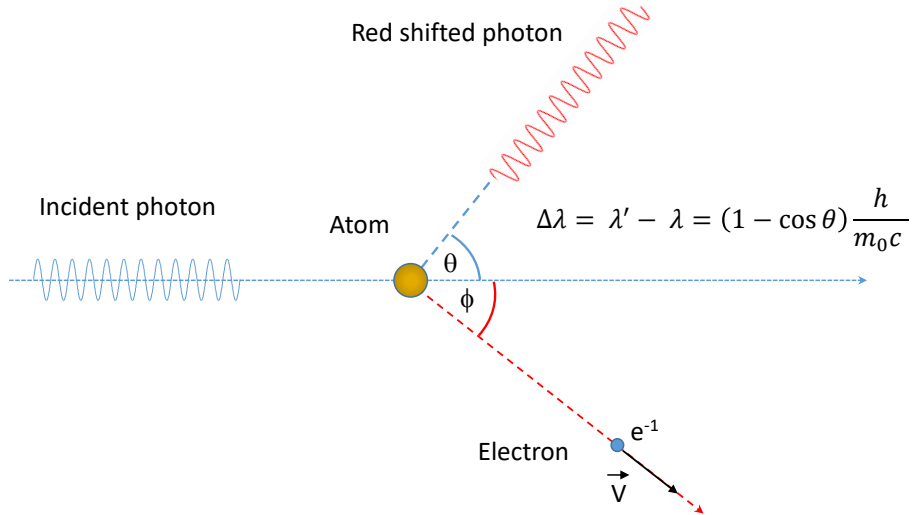


**Figure 2.3:** Compton scattering of a photon by an atom results in a red-shifted photon and a free electron. The polarisation factor is the same as for elastic scattering.

with  $\theta$  being the scattering angle,  $m_0$  the electron rest mass,  $c$  the speed of light, and  $h$  is Planck's constant. The energy shift is shown in figure 2.4 for 15 keV radiation, the peak energy of the U17 undulator at 6 mm gap, as a function of scattering angle between  $0 - 90^\circ$ . At  $90^\circ$  the shift is 0.43 keV. In pink beam experiments, the low energy tail of the U17 widens the shift into a band of energies. To be specific, we are also plotting the Compton energy for an incident photon at 13.3 keV, the energy at the 10% level of the U17, see figure 2.4(a). For completeness we show the U17 spectrum in figure 2.4(b).

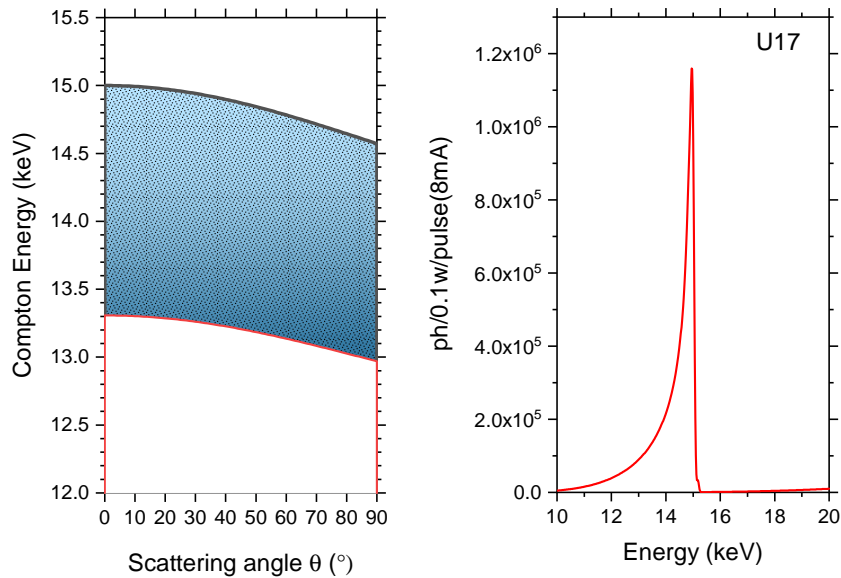


**Figure 2.4:** (a) Energy range of Compton photons from the U17 pink beam as a function of scattering angle. The curve on the upper edge is the Compton energy produced by 15 keV and the lower edge is for 13.3 keV. (b) Spectrum of the U17 undulator from one 8 mA pulse in the storage ring. The integral flux is  $1.7 \cdot 10^9$  ph/pulse (XOP/urgent).

The intensity of Compton scattering can be approximated by the following formula:

$$S_{inel}(s) = \left[ Z - \frac{f^2(s)}{Z} \right] \times \{1 - M [\exp(-Ks) - \exp(-Ls)]\},$$

with

$$s = \frac{\sin(\theta/2)}{\lambda} = \frac{q}{4\pi}.$$

$K$ ,  $L$  and  $M$  are coefficients published in [29] for atomic numbers  $Z$  from 2 to 36 and for  $\text{H}_2\text{O}$  and in [30] for heavier elements  $Z = 20$  to 95. The polarisation factor for Compton scattering is the same as for elastic scattering. The Compton intensity is shown for some elements in figure 2.2(b). For one atom it is:

$$I_{inel}(q) = I_0 r_e^2 \cdot S_{inel}(q) \cdot P d\Omega.$$

The intensity increases with  $q$  and converges towards  $Z$  at high  $q$ . In contrast,  $f^2(q)$  decreases at high  $q$  and is nearly 0 at  $11 \text{ \AA}^{-1}$ , the limit for the WAXS experiments in this project. The Compton intensity is important for normalising the total scattering. We will discuss the normalisation in details later.

## 2.3 Scattering from a molecule

The calculation of the scattering from a molecule involves two steps. First, the scattering from one molecule is calculated, with the interference from the atoms in the molecule. The intensity is derived in B.E Warren's book [28]. In electron units the result is:

$$S(\mathbf{q}) = \sum_m f_m e^{i\mathbf{q}\cdot\mathbf{r}_m} \sum_n f_n e^{-i\mathbf{q}\cdot\mathbf{r}_n} = \sum_m \sum_n f_m f_n e^{i\mathbf{q}\cdot\mathbf{r}_{mn}}, \quad (2.2)$$

where  $\mathbf{r}_{mn} = \mathbf{r}_m - \mathbf{r}_n$  are interatomic vectors. For a random ensemble of molecules, isotropic averaging gives the scattering for a non interacting gas of molecules. Then we obtain the so-called Debye function for the elastic scattering intensity from disordered molecules:

$$S(q) = \sum_{m,n} f_m f_n \frac{\sin qr_{mn}}{qr_{mn}}. \quad (2.3)$$

This important equation is the Debye function for molecular scattering. It is the sum of formfactor products for all pairs of atoms in the molecule. Note that nearest neighbour pairs dominate the intensity. For a given atom-atom pair, the pair intensity is proportional to the product  $Z_1 \cdot Z_2$ . In a metal complex with low- $Z$  atoms surrounding the metal, the sensitivity to the change in bond length to the metal is amplified by  $Z_1 \cdot Z_2$  and the short distance  $r_{12}$ . It should be stressed that when the molecular structure is known, the Debye function is calculated by this simple formula.

The scattered intensity from a molecule is:

$$I(q) = I_0 r_e^2 \cdot S(q) \cdot P d\Omega.$$

In the formfactor description, atoms are assumed to be round. The electron density in bonds is only indirectly included via the bond lengths. The scattering can also be calculated from first principle quantum chemistry calculations like Gaussian but the changes are very small compared to the Debye expression.

### 2.3.1 Scattering from CCl<sub>4</sub>

As an example let's calculate the total scattering intensity from a carbon tetrachloride gas. In the tetrahedral CCl<sub>4</sub> molecule with the bond length  $r_{C-Cl} = 1.7670 \text{ \AA}$ , the distance between chlorine atoms is  $r_{Cl-Cl} = \sqrt{8/3} r_{C-Cl} = 2.8855 \text{ \AA}$ . The elastic scattering intensity is expressed by

$$S(q) = f_C \left( f_C + 4f_{Cl} \frac{\sin qr_{C-Cl}}{qr_{C-Cl}} \right) + 4f_{Cl} \left( f_{Cl} + f_C \frac{\sin qr_{C-Cl}}{qr_{C-Cl}} + 3f_{Cl} \frac{\sin qr_{Cl-Cl}}{qr_{Cl-Cl}} \right).$$

As Compton scattering is an atomic property independent of molecular structure, it is calculated as the sum of the individual intensities for one carbon and four chlorine atoms. After reorganising the terms in  $S^{el}$ , the total scattering in electron units for one CCl<sub>4</sub> molecule is:

$$S_{tot}(q) = f_C^2 + 4f_{Cl}^2 + 8f_C f_{Cl} \frac{\sin qr_{C-Cl}}{qr_{C-Cl}} + 12f_{Cl}^2 \frac{\sin qr_{Cl-Cl}}{qr_{Cl-Cl}} + S_C^{inel} + 4S_{Cl}^{inel}.$$

The calculated scattering intensities are shown in figure 2.5.

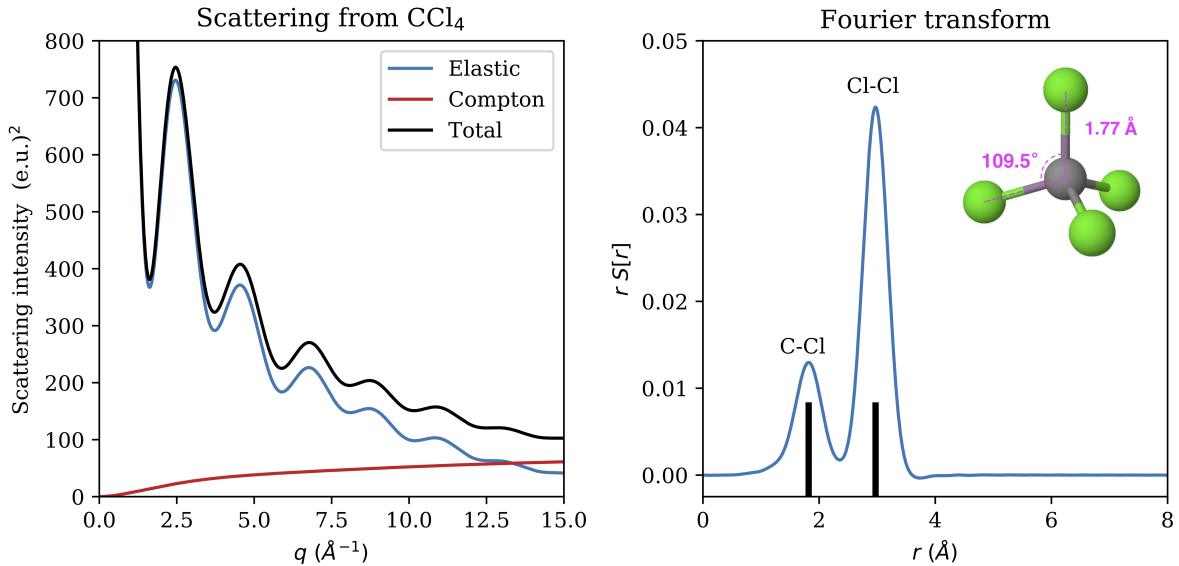


**Figure 2.5:** Debye intensity for gas phase CCl<sub>4</sub>. The Compton scattering is shown in red, gas scattering in blue and the sum in black. The intensity at  $q = 0$  is  $(6 + 4 \cdot 17)^2 = 5476 \text{ (e.u.)}^2/\text{CCl}_4$ . The sine-Fourier transform, the radial electron density, is shown on the right. The tetrahedral CCl<sub>4</sub> structure is shown in the inset.

### 2.3.2 Debye limits

Having derived the Debye and Compton scattering intensities for gas molecules and CCl<sub>4</sub> as an example, let's examine these functions in the low and high  $q$  limits.

The limit  $q = 0$  gives the total forward scattering (behind the beamstop). The intensity in electron units per molecule is

$$S(q = 0) = \lim_{q \rightarrow 0} \sum_{m,n} f_m f_n \frac{\sin qr_{mn}}{qr_{mn}} = \sum_{m,n} f_m f_n = \left( \sum_n f_n \right)^2 = Z^2,$$

where  $Z$  is the total number of electrons in a molecule. For a molecule containing  $N_\alpha$  atoms of species  $\alpha$  with  $Z_\alpha$  electrons

$$Z = \sum_{\alpha} N_{\alpha} Z_{\alpha}.$$

At values of  $q$  typically above  $8 \text{ \AA}^{-1}$ , the oscillations caused by the term  $\sin(qr_{mn})/qr_{mn}$  in the Debye function decrease quickly. The interference is very weak, and the elastic scattering converges asymptotically to that of free atoms in the high  $q$  limit. It can be shown by decomposing equation 2.3 into diagonal and off-diagonal contributions:

$$S(q) = \sum_{m,n} f_m f_n \frac{\sin qr_{mn}}{qr_{mn}} = \sum_n f_n^2 + \sum_{m \neq n} f_m f_n \frac{\sin qr_{mn}}{qr_{mn}} \xrightarrow{q \rightarrow \infty} \sum_n f_n^2.$$

Thus, the Debye scattering intensity decreases with  $q$ , whereas Compton scattering increases with  $q$ , which is also seen in figure 2.5. The high  $q$  limit of  $S(q)$  is used for normalising the scattering curves as discussed in more details in the following sections.

### 2.3.3 Debye functions for $[\text{Fe}(\text{phen})_3]^{2+}$ from DFT

The atomic positions for the LS and HS state of  $[\text{Fe}(\text{phen})_3]^{2+}$  were calculated by DFT by Latévi Max Lawson Daku at the Chemistry Faculty at the University of Geneva. The stoichiometry of the complex is  $\text{Fe}^{2+}(\text{N}_2\text{C}_{12}\text{H}_8)_3$ , i.e. it has 67 atoms per molecule including hydrogens. Recall that the scattering will amplify the six Fe-N bonds due to the high  $Z$  of Fe, 26, and the short Fe-N distances of  $1.99 \text{ \AA}$  in the LS state. The structures are shown in figure 2.6.

Two LS and five HS structures were optimised. The LS structure was first constrained to have  $D_3$  point group symmetry, where all six Fe-N distances are forced equal, and with the three phenantroline ligands in orthogonal planes. In this geometry, the angles between the ligand central axes are  $120^\circ$ . The angles between the opposite Fe-N bonds are  $175.6^\circ \neq 180^\circ$ . The structure deviates slightly from octahedral symmetry due to steric hindrance of the ligands. The second optimisation of the LS structure did not constrain the Fe-N distances nor their angles ( $C_1$  point group symmetry).

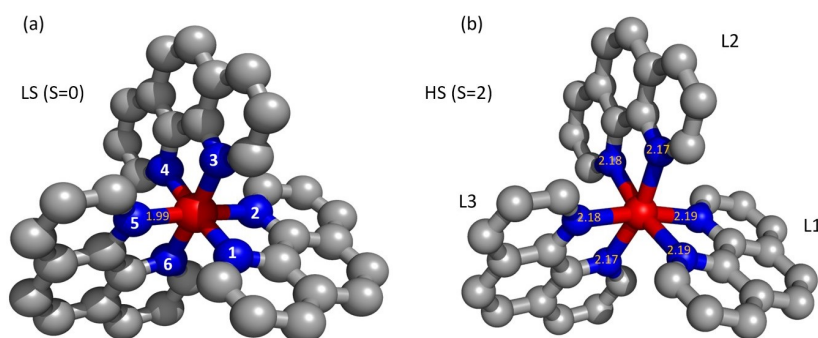


**Figure 2.6:**  $[\text{Fe}(\text{phen})_3]^{2+}$  structures in the LS (a) and HS state (b).  $\text{Fe}^{2+}$  is red, N blue and C grey (H atoms are omitted).  $\text{Fe}^{2+}$  has the configuration  $[\text{Ar}]3d^6$ . In the LS state Fe-N distances are  $1.99 \text{ \AA}$ , the ligand planes are orthogonal and their centre-axes form  $120^\circ$  angles. In the HS state the Fe-N distances increase by  $\sim 0.20 \text{ \AA}$  and the structure is distorted. The ligand angles between the centre-lines deviate slightly from  $120^\circ$ .

The HS structure was calculated with five sets of constraints: two structures with  $D_3$  point symmetry, two structures with  $C_2$  point symmetry, and finally one with  $C_1$  point symmetry. The resulting atomic positions  $(x, y, z)$  are listed in Appendix B for the optimised structures. The values of the refined Fe-N distances and angles are also presented in table B.1 in the Appendix. The Debye functions for the best structures are shown in figure 2.7(a) together with the difference (b).

The conversion from  $S(q)$  to the radial density  $S[r]$  in space for the LS and HS states is shown in figure 2.7(c). The sine-Fourier transform will be discussed later, see equation

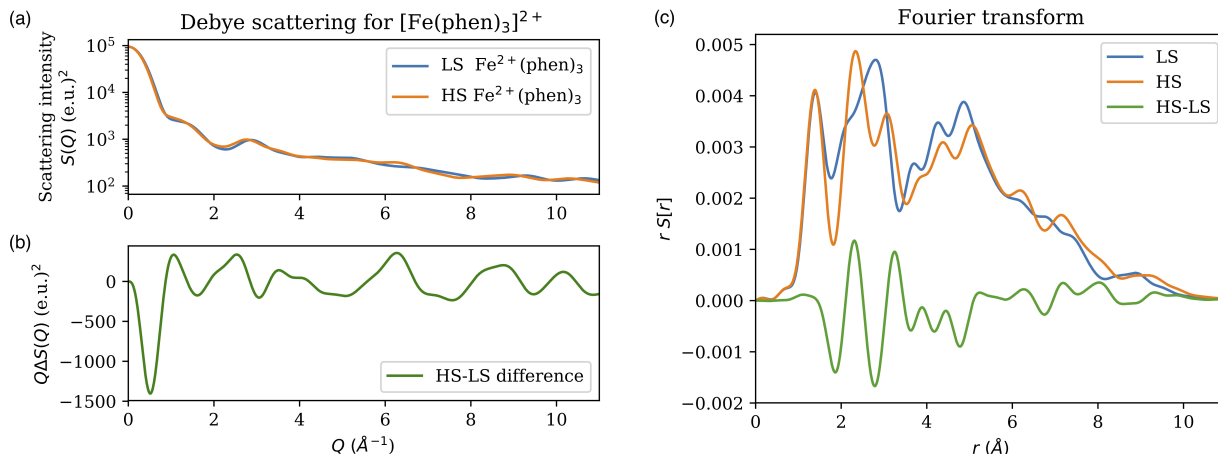


**Figure 2.7:** Scattering functions for  $[\text{Fe}(\text{phen})_3]^{2+}$  in the gas phase calculated from DFT coordinates. (a) Debye functions for the LS and HS structures. The  $q$  range is the one used in the experiment. The forward scattering is the same for the two structures. (b) Difference HS-LS scattering. The function is negative at low  $q$  due to the increase in the Fe-N bond length, from 1.99 to 2.18  $\text{\AA}$ . (c) The Fourier transform of the HS and LS structures to  $r$  space. The HS-LS curve has a local minimum at 1.87  $\text{\AA}$  and a maximum at 2.29  $\text{\AA}$  from the elongation of the Fe-N bond. The minima/maxima differ slightly from the true bond lengths due to the size of the atoms (atomic formfactors) and interference with other pairs.

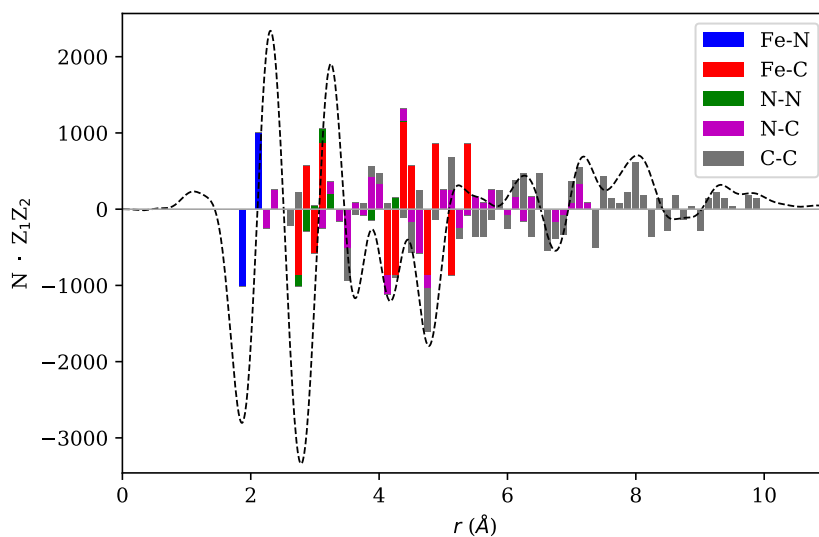


**Figure 2.8:** Fourier transform of the HS-LS difference from DFT (broken curve) and the difference histogram calculated from the changes in pair distances multiplied by their  $Z$  product. Pairs with hydrogen are omitted.

2.5. We can get a clearer understanding of the difference Fourier transform  $dS[r]$  by listing the different atom-atom pairs Fe-N, Fe-C, N-N etc. and plot them vs pair distances, see figure 2.8. The amplitude in this histogram is the scattering power  $Z_i \cdot Z_j \times$  multiplicity. The difference in the position of the peaks and valleys of the Fourier transform  $S[r]$  compared to the histogram shows the importance of fitting the experimental data against a model and to use data with the widest possible  $q$  range to discriminate between models.

## 2.4 Scattering from a solution

### 2.4.1 Atom-atom distribution functions $g_{\alpha\beta}$

The structure of disordered media like amorphous solids and liquids can only be described statistically from the distribution of atom-atom distances. Although the atomic positions change with time, spatial correlations exist which are known as short-range order. Measuring these correlations can give a lot of insight into the structure of a liquid.

The statistical approach to describe the structure of a liquid is based on the  $g(r)$  function, the so-called radial distribution function (RDF). It is defined as the probability of finding an atom at a distance  $r$  from another atom. Consider first the simple case of a liquid with only one type of atoms like liquid Li or Na. For the definition of the radial distribution function, we randomly choose one atom at the origin. The number of atoms in a spherical layer at a distance  $r$  from the origin is  $dN(r)$ . The radial density is then  $\rho(r) = dN(r)/(4\pi r^2 dr)$ . The radial distribution function is defined by  $g(r) = \rho(r)/\rho_0$  where  $\rho_0$  is the average density of the liquid.

When the liquid contains more than one type of atoms, we introduce the partial radial

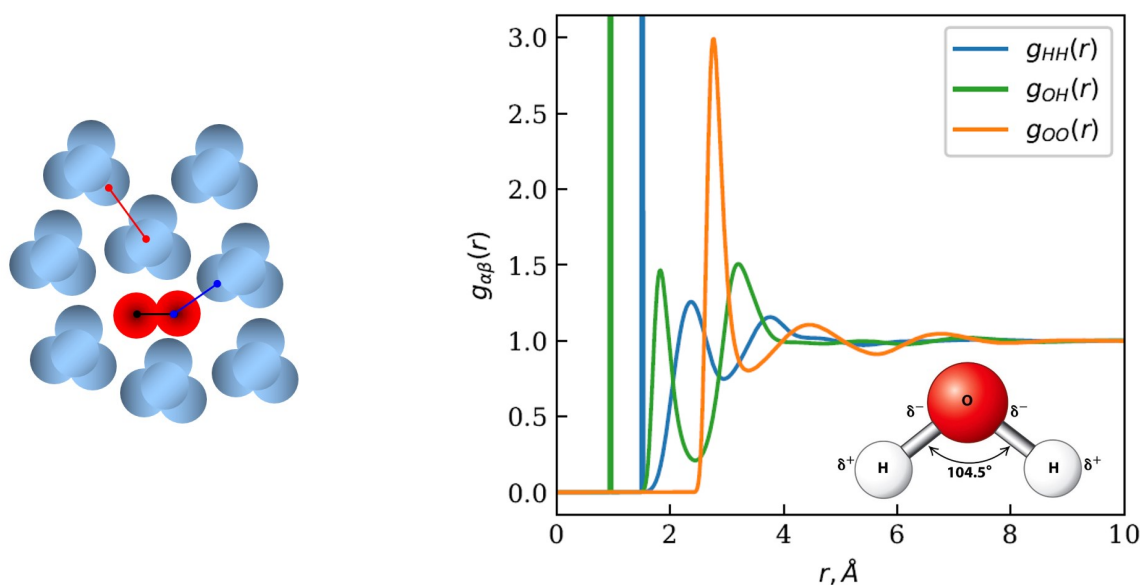


**Figure 2.9:** (a) Atom-atom pairs contributing to the radial distribution functions  $g_{\alpha\beta}(r)$  in a solution. The solute and solvent molecules are shown in red and blue, respectively. The black line is a fixed distance inside the solute, the blue is a solute-solvent distance and the red is a solvent-solvent distance. Blue and red distances fluctuate. The  $g_{\alpha\beta}$  functions are simulated by MD from which the scattering function  $S(q)$  can be calculated. (b) Atom-atom functions for liquid H<sub>2</sub>O from MD. The insert shows the H<sub>2</sub>O molecule. The  $g_{OO}$  peaks at 2.77 Å, which is a measure of the distance between H<sub>2</sub>O molecules.

distribution function  $g_{\alpha\beta}(r)$ . Let's choose an atom of species  $\alpha$  at the origin and define the radial density of species  $\beta$  as  $\rho_{\alpha\beta}(r) = dN_{\beta}(r)/(4\pi r^2 dr)$ . If the total number of  $\beta$  atoms in the sample volume  $V$  is  $N_{\beta}$  then the average density of the species  $\beta$  in the sample is  $\rho_{0\beta} = N_{\beta}/V$ . The probability of finding an atom  $\beta$  at a distance  $r$  from an atom of species  $\alpha$  is  $g_{\alpha\beta}(r) = \rho_{\alpha\beta}(r)/\rho_{0\beta}$ .

At very short distances  $r$  there is no probability to find another atom as the interatomic distance is shorter than the atomic radius, thus the radial distribution function is zero. At intermediate distances  $g(r)$  exhibits distinct peaks for short interatomic distances (about 2-3 coordination shells) but then dampen and broaden out as  $r$  increases, while  $g(r)$  approaches 1 at large  $r$  as the density tends to its average value. The definition of the  $g_{\alpha\beta}$  functions for a solution is shown in figure 2.9(a). The MD simulated  $g_{\alpha\beta}$  functions for pure water are shown in figure 2.9(b). The simulation was done in collaboration with Qingyu Kong, SOLEIL Synchrotron, Palaiseau. The MD uses 4096 molecules in a 49.6 Å cubic box. The position of the atoms is tracked for 1.2 ns in steps of 0.5 fs. At each step, the distances are recorded. The intramolecular distances are  $r_{OH} = 0.958$  Å and  $r_{HH} = 1.515$  Å and the angle between the O–H bonds is 104.5°. The O–O function peaks at 2.77 Å, the radius of the first coordination shell. The 2<sup>nd</sup> and 3<sup>rd</sup> shells are also visible.

The ultimate goal of a time-resolved structure experiment is to measure  $g_{\alpha\beta}(t)$  on the time scale of the structural changes of a solute. In MD the liquid is assumed to be in thermal equilibrium which is inconsistent with tracking structural changes. But as we will show later, the solvent thermalises excited molecules very quickly and the temperature become locally homogeneous in less than 100 ps, which is compatible with the X-ray pulse length. For the work presented here, we can safely assume that the solvent is in quasi thermal equilibrium.

The change in the scattering from water induced by a small temperature rise from the change in structure of the solute will be studied later.

## 2.4.2 Liquid structure factor $S(q)$

As mentioned above, in a liquid the atomic positions change continuously and the Debye formalism for gas phase molecules can not be used to calculate the scattering function. Warren provides the following expression for the scattered intensity based on the  $g_{\alpha\beta}$  functions:

$$S(q) = \sum_{\alpha,\beta} f_{\alpha}(q)f_{\beta}(q) \left( N_{\alpha}\delta_{\alpha\beta} + \frac{N_{\alpha}N_{\beta}}{V} \int_0^{\infty} g_{\alpha\beta}(r) \frac{\sin(qr)}{qr} 4\pi r^2 dr \right) = \sum_{\alpha,\beta} I_{\alpha\beta}(q).$$

The above function is referred to as the Zernike equation in the literature.  $N_{\alpha}$  is the number of atoms of kind  $\alpha$ ,  $V$  is the volume and  $\delta_{\alpha\beta}$  is the Kronecker delta function ( $\delta_{\alpha\alpha} = 1$ ,  $\delta_{\alpha\beta} = 0$  for  $\alpha \neq \beta$ ). By analogy, the correlations between atoms of types  $\alpha$  and  $\beta$  define the partial liquid structure factor is:

$$S_{\alpha\beta}(q) = \frac{I_{\alpha\beta}(q)}{N_{\alpha}f_{\alpha}(q)f_{\beta}(q)} = \delta_{\alpha\beta} + \frac{N_{\beta}}{V} \int_0^{\infty} g_{\alpha\beta}(r) \frac{\sin(qr)}{qr} 4\pi r^2 dr.$$

From  $N_{\beta}/V = \rho_{0\beta}$  and slightly rearranging the last expression we get

$$S_{\alpha\beta}(q) = \delta_{\alpha\beta} + \frac{4\pi\rho_{0\beta}}{q} \int_0^{\infty} r g_{\alpha\beta}(r) \sin(qr) dr. \quad (2.4)$$

The total and partial scattering for water are shown in figure 2.10.

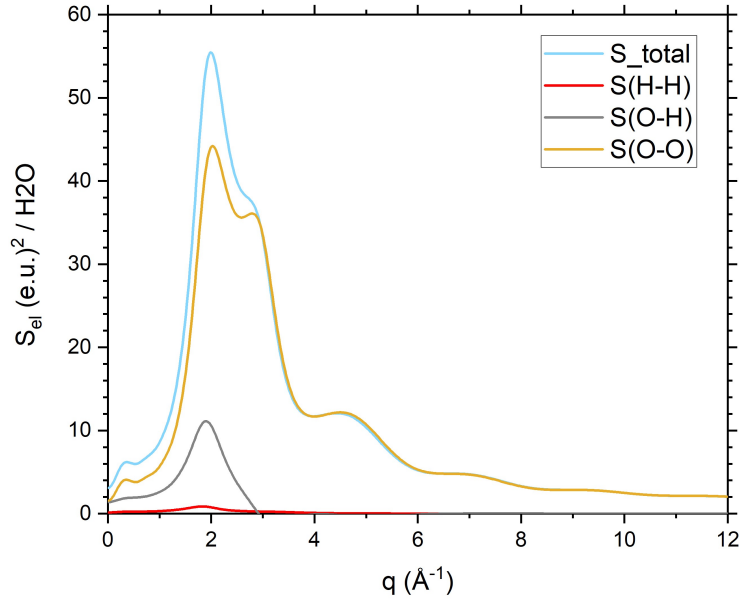


**Figure 2.10:** Elastic scattering from one H<sub>2</sub>O molecule calculated from the  $g_{\alpha\beta}(r)$  functions in figure 2.9. The partial contributions are also shown. The scattering is dominated by  $g_{OO}$ .

### 2.4.3 Time-resolved scattering $dS(\mathbf{q}, t)$

In the previous sections the Debye function was derived for gas molecules and it was shown how the scattering from a liquid is expressed from  $g_{\alpha\beta}$  via the Zernike equation. In a time-resolved experiment, the change in scattering  $dS(q)$  is measured:

$$dS(q, t) = S_{ON}(q, t) - S_{OFF}(q),$$

where  $S_{ON}(q, t)$  is the laser excited solution and  $S_{OFF}(q, t)$  is the non excited reference. In practice the non excited part is acquired with a negative time delay, usually -3 ns, to minimise the effect of the slight deformation of the jet produced by the laser. Before subtraction, the scattering is normalised to one unit-cell-molecule representing the stoichiometry of the solute/solvent ratio. The scaling is done in a high  $q$  interval, typically between 6 – 8 Å<sup>-1</sup>. The range has to be so wide that residual weak oscillations from the solute average to zero in the difference.

Since  $dS(q)$  is difficult to interpret geometrically, Savo Bratos and Rodolphe Vuillemier define a radial Fourier transform  $dS[r]$  as:

$$dS[r, t] = \frac{1}{2\pi^2 r} \int_0^\infty dq \left[ \sum_{\mu \neq \nu} f_\mu(q) f_\nu(q) \right]^{-1} q dS(q, t) \sin(qr). \quad (2.5)$$

The denominator, i.e. the off-diagonal formfactor products, is called the sharpening function. It compensates for the broadening of atom-atom distances from the atomic formfactors. It does not transform  $dS[r]$  to a series of Dirac functions but the peaks and valleys are sharpened a bit. Following a convention proposed by Savo Bratos, the real-space function  $S$  is written with a square bracket,  $S[r]$ , to distinguish it from the base function  $S(q)$ .

To aid the interpretation of the experimental data from [Fe(phen)<sub>3</sub>]<sup>2+</sup>, we will simulate the signals from four generic reactions for a diatomic molecule:

- (i) Bond contraction
- (ii) Bond expansion
- (iii) Bond breakage
- (iv) Bond formation

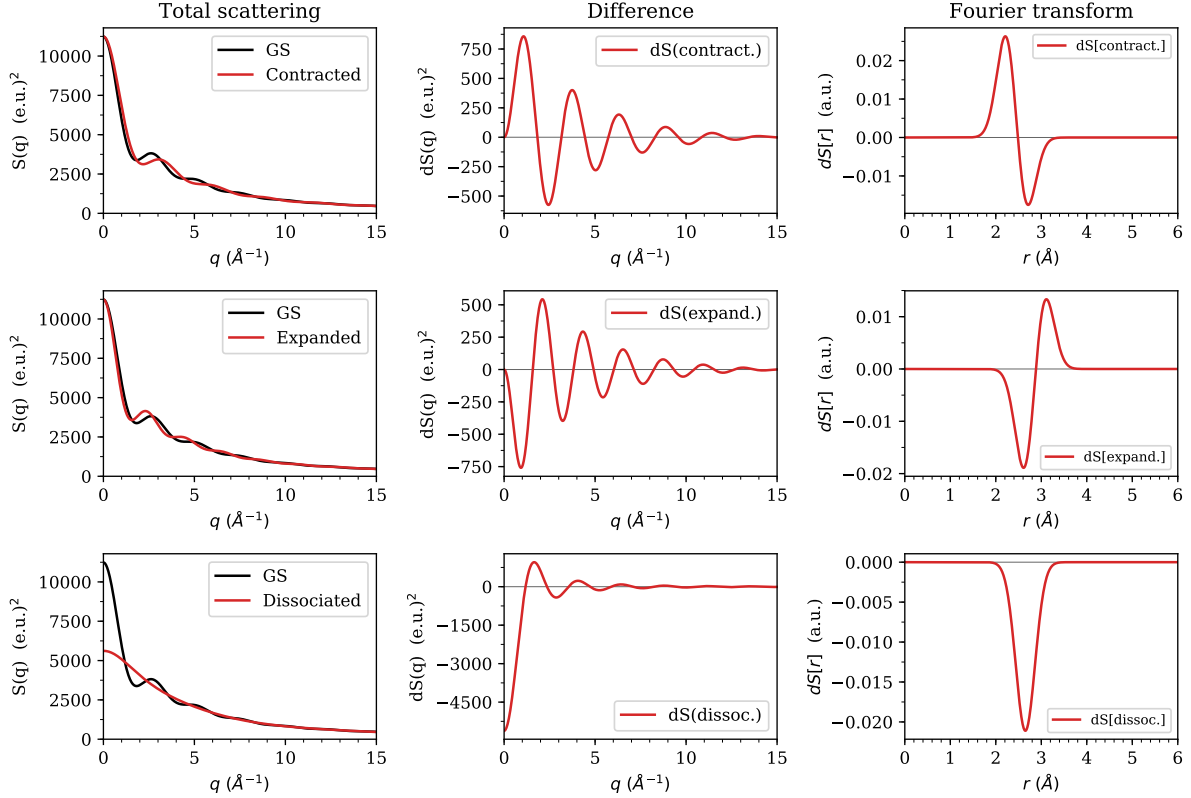


**Figure 2.11:** Fingerprinting atom-atom bonds in diatomic molecules. The top panel shows a 15% contraction of the I-I bond in I<sub>2</sub>, and the middle panel a 15% expansion. In the bottom panel, the molecule is dissociated into two atoms infinitely apart. For the reverse reaction, bond formation, the  $y$  scale of the  $dS(q)$  and  $dS[r]$  plots is inverted.

The Debye function for a diatomic molecule with two identical atoms separated by  $r_0$  is

$$S(q) = 2f^2(q) \left( 1 + \frac{\sin(qr_0)}{qr_0} \right).$$

When the atom-atom distance changes from  $r_0$  to  $r_1$ , we get:

$$dS(q) = 2f^2(q) \left( \frac{\sin(qr_1)}{qr_1} - \frac{\sin(qr_0)}{qr_0} \right)$$

The functions  $S(q)$ ,  $dS(q)$  and  $dS[r]$  are shown in figure 2.11 for I atoms. The top panel shows  $S(q)$  for ground state (GS) I<sub>2</sub> with a bond length 2.667 Å and for a 15% contracted bond of 2.267 Å. The difference  $dS(q) = S_{contract} - S_{GS}$  is shown in the middle. Note that  $dS(q=0)$  is 0 since the number of electrons in the molecule is constant.  $dS[r]$  is shown on the outer right. The creation peak is at 2.246 Å and the depletion peak at 2.671 Å. The width of the peaks is determined primarily by the size of iodine and to a lesser extent by the  $q$  range (0–30 Å<sup>-1</sup>). In the middle panel, the scattering from a 15% expanded I<sub>2</sub> with a 3.067 Å bond is shown. This case corresponds to the A/A' state in iodine. The depletion peak is at 2.650

Å and the creation peak at 3.060 Å. The bottom panel shows the dissociation  $I_2 \rightarrow 2I$  with atoms infinitely apart. The forward scattering is negative (positive for association), which is an important signature in experiments. The inverse reaction, bond formation  $2I \rightarrow I_2$ , is difficult to synchronise for an ensemble of atoms unless the atoms are trapped in a solvation cage. The simulation uses a wide  $q$  range, 0 – 30 Å<sup>-1</sup>, to get well defined peaks and as a result, the peak positions in  $dS[r]$  are close to the input bond lengths. For very small changes in a bond length, the creation/annihilation peaks tend to reduce the difference signal. For very small changes  $dr$ ,  $dS[r]$  is the differential  $-dS' \cdot dr$ . The *amplitude* of the measured signal is proportional to  $dr$ .<sup>1</sup> That makes it difficult to distinguish changes in population from changes in bond length. Usually though, structural changes in single molecules happen extremely fast, on the sub-picosecond time scale, which can not be resolved with synchrotron radiation. We will discuss this issue later in determining the cage radius of  $[\text{Fe}(\text{phen})_3]^{2+}$ .

In an experiment, the  $q$  range is typically 0 – 10 Å<sup>-1</sup> and that produces weak artifact oscillations and small shifts in the peak position of  $dS[r]$ . They can be reduced by multiplying  $dS(q)$  by a convergence factor  $\exp(-\alpha q^2)$  with  $\alpha$  around 0.015 Å<sup>2</sup>. In any event, the bond lengths are determined from fitting to a model. With large molecules like  $[\text{Fe}(\text{phen})_3]^{2+}$ ,  $dS[r]$  is showing the trends for the nearest neighbours only. We will discuss this in the next section.

#### 2.4.4 Solvent hydrodynamics

During a chemical reaction in solution, the solvent changes temperature and density from energy transitions in the solutes. This parasitic solvent signal has to be removed reliably to get the true signal from the new solutes and their solvent cages. The solvent signal is often dominating the solute signal, especially for low- $Z$  solutes like  $[\text{Fe}(\text{phen})_3]^{2+}$ , so the correction has to be done carefully. The hydrodynamic theory for X-ray scattering was developed by Savo Bratos and Rodolphe Vuilleumier, Université Jussieu, Paris, in 2006 in collaboration with the ID09 team [31]. A systematic study of the relevant solvent parameters for common solvents was later published by Kasper Kjær et al. in 2013 based on measurements from ID09 [32]. In these measurements, the temperature rise is produced by a laser absorbing dye for which the change in the dye structure can be neglected (see below). The laser is exciting vibrational and rotational motions in the dye molecule without producing any structural change after 100 ps. The theory and the dye method are now well understood and widely used at synchrotrons and XFELs. Below we will briefly describe the theory that is relevant for determining the HS structure of  $[\text{Fe}(\text{phen})_3]^{2+}$ .

The hydrodynamic Bratos theory assumes that the solvent is in local thermal equilibrium. That implies that the solvent around hot excited solutes cools very fast so that the temperature is homogeneous between excited solutes on time scales beyond 100 ps, the time resolution of the experiment. On the macroscopic length scale, on the other hand, the temperature is varying due to the intensity profile of the laser beam, longitudinally and transversely. If the laser excitation is not generating turbulence in the liquid sheet, the signal is the spatial average of the probed sample.

The time it takes for the solvent temperature to become locally uniform can be calculated from the classical theory of heat conduction in a liquid. In Landau and Lifshitz's book "Fluid Mechanics", Pergamon Press, §51, p 192 [33], the cooling of a hot point is given as a function of distance  $r$  and time  $t$ . They derive the equation:

$$T(r, t) = \text{const} \cdot \frac{1}{8(\pi\chi t)^2} \exp(-r^2/4\chi t),$$

---

<sup>1</sup>The shape of  $-dS'[r]$  can not be interpreted as a simple displacement.

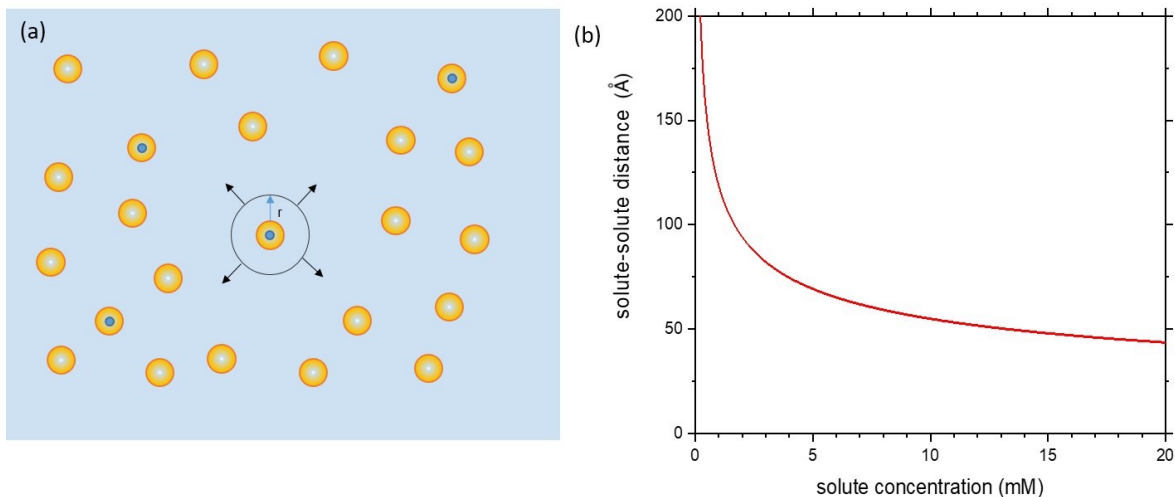


**Figure 2.12:** (a) Cooling of excited solutes by the solvent. The front of the temperature wave is indicated by a black circle.  $[\text{Fe}(\text{phen})_3]^{2+}$  solutes are shown in yellow, excited solutes are indicated with blue centres, and the solvent medium is blue. (b) Solute-solute distance as a function of concentration.

where  $\chi$  is the thermometric conductivity

$$\chi = \frac{\kappa}{\rho C_P},$$

$\kappa$  the thermal conductivity ( $\text{J s}^{-1} \text{m}^{-1} \text{K}^{-1}$ ),  $\rho$  the density ( $\text{g m}^{-3}$ ) and  $C_P$  the heat capacity at constant pressure ( $\text{J g}^{-1} \text{K}^{-1}$ ). After a time  $t$ , the wavefront is at the distance  $r$ :

$$r = \sqrt{\chi t},$$

and propagates at the speed:

$$v = \sqrt{\frac{\chi}{4t}}.$$

The parameters for water are listed in table 2.1.

$\chi$ ( $\text{m}^2 \text{s}^{-1}$ )	$\kappa$ ( $\text{J s}^{-1} \text{m}^{-1} \text{K}^{-1}$ )	$\rho$ ( $\text{g m}^{-3}$ )	$C_P$ ( $\text{J g}^{-1} \text{K}^{-1}$ )	$C_V$ ( $\text{J g}^{-1} \text{K}^{-1}$ )
$1.452 \cdot 10^{-7}$	0.607	$1.0 \cdot 10^{-6}$	4.18	4.14

**Table 2.1:** Thermal conductivity parameters for water at 20°C.

A schematic of excited and non excited  $[\text{Fe}(\text{phen})_3]^{2+}$  solutes is shown in figure 2.12(a) together with a plot of the nearest-neighbour distance as a function of concentration (b). The distance is calculated with solutes in a cubic lattice. With a 2.1 mM excited state concentration, the nearest excited-neighbour-distance is 92 Å on average.

The temperature profile  $\Delta T(r, t)$  is shown in figure 2.13(a) for 10, 25, 50 and 100 ps. At early times, the high local solvent temperature is cooling down as the heat wave propagates into the bulk by thermal diffusion. The position of the wavefront is shown in figure 2.13(b) for the inflection point of the wavefront. The wavefronts from 2.1 mM excited  $[\text{Fe}(\text{phen})_3]^{2+}$  merge at the mid-point  $92/2 = 46$  Å in 82 ps. After that time, the solution is in local thermal equilibrium. As the time resolution is 100 ps, the remaining temperature inhomogeneities

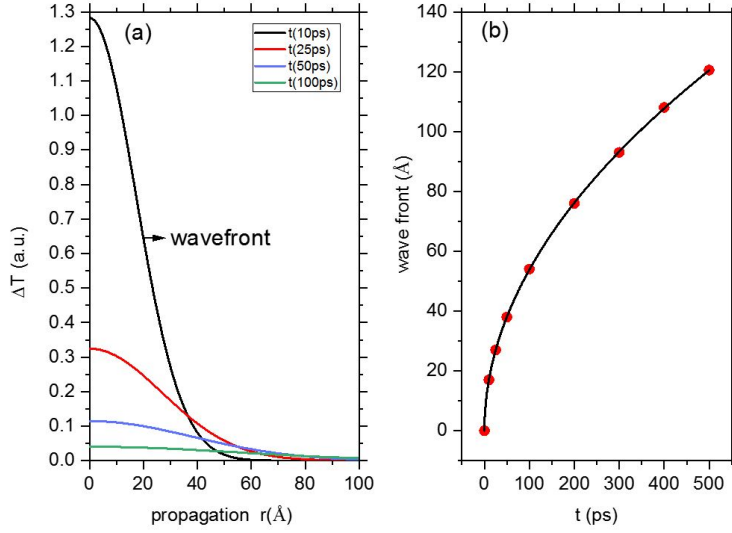


**Figure 2.13:** (a) Temperature profile around an excited solute in water as a function of time after excitation. (b) Wavefront vs time for 10, 25, 50 and 100 ps. When wavefronts from nearest neighbours meet, the solvent is in local thermal equilibrium. The speed of the wave is 19.1 m/s after 100 ps.

after 82 ps are averaged out by the X-ray pulse. Note that the speed of the wavefront at 100 ps is 19.1 m/s, which is much slower than the speed of sound in water, 1480 m/s. It is also useful to estimate the time it takes for the macroscopic sample to thermalise. For a circular laser beam with a 0.1 mm radius, the wavefront from the centre passes that radius after 0.26 s. On that time scale, the laser energy is diffusing out of the X-ray volume.

For a solvent in thermal equilibrium,  $S(q)$  is a function of the thermodynamic variables  $T$ ,  $P$  and  $\rho$ . From the equation of state of the liquid, the pressure is a function of  $T$  and  $\rho$  (see below); the function is therefore reduced to  $S(q, T, \rho)$ . For a weak initial temperature rise, the change in solvent scattering can be approximated by the differential:

$$dS(q, t) = \left. \frac{\partial S(q)}{\partial T} \right|_{\rho} \Delta T(t) + \left. \frac{\partial S(q)}{\partial \rho} \right|_T \Delta \rho(t).$$

The derivative  $\left. \frac{\partial S(q)}{\partial T} \right|_{\rho}$  is the response to a 1 K temperature rise at constant density (or constant volume), the important term for the early time correction. The second term,  $\left. \frac{\partial S(q)}{\partial \rho} \right|_T$ , is the change from a unit change  $\delta\rho$  at constant temperature. When the solvent is excited transiently by the dye,

$$dS(q, 100 \text{ ps}) = \left. \frac{\partial S(q)}{\partial T} \right|_{\rho}(q) \cdot \Delta T(100 \text{ ps}).$$

The second term, the density change becomes important at later times, after  $\sim 100$  ns, when thermal expansion sets in. The expansion is driven by the pressure gradient from the radial laser intensity. For a  $\varnothing$  0.2 mm laser beam, the pressure gradient propagates at the speed of sound, i.e. 1480 m/s in water, and reaches the edge of the beam in 68 ns. In practice, the scattering is measured after 1  $\mu$ s to make sure that the expansion has stopped and that the pressure is back to ambient. From the conservation of energy, the temperatures jumps are related as

$$C_V \Delta T(100\text{ps}) = C_P \Delta T(1\mu\text{s}),$$

where  $C_V$  and  $C_P$  are the heat capacities at constant volume and constant pressure. The short and long time differential are related as:

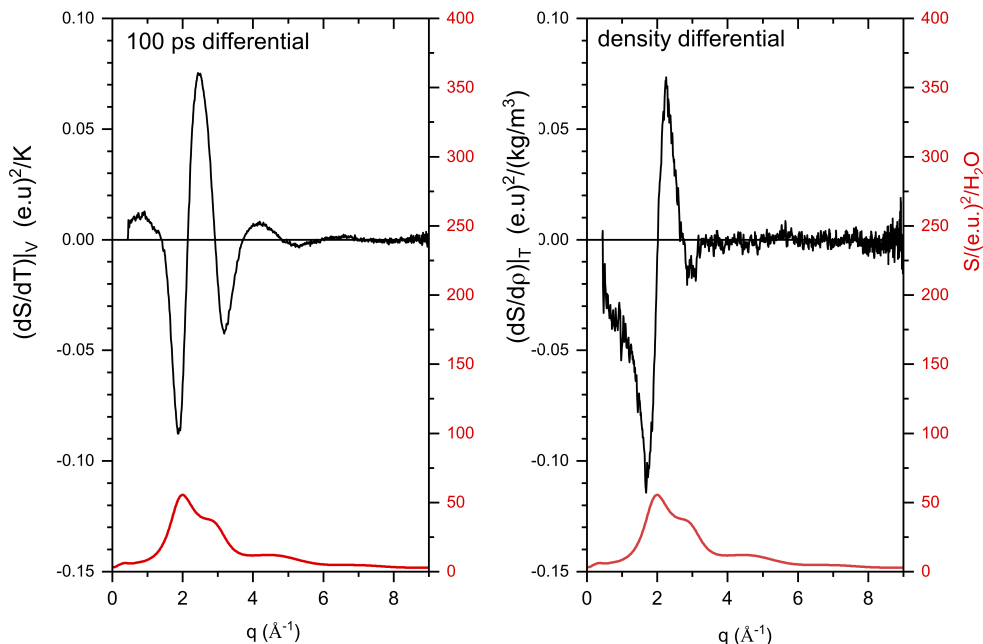


**Figure 2.14:** Solvent differentials for water measured with the dye  $C_{16}H_{18}BrN_3$  excited at 400 nm with the 1.2 ps pulses from the ID09 laser. The amplitudes are scaled to the MD simulation by Marco Cammarata. The (non excited) water scattering is shown in red below.

$$\left. \frac{\partial S(q)}{\partial \rho} \right|_T \Delta \rho(1 \mu s) = dS(1 \mu s) - \frac{C_V}{C_P} dS(100 \text{ ps}).$$

Following the approach in Kasper Kjær's paper, the differentials were measured using the bromine dye  $C_{16}H_{18}BrN_3$  to transfer heat to the solvent from the absorbed laser photons. The dye was dissolved at 10 mM with an OD of 0.5 at the excitation wavelength 400 nm.

As for the calibration of the differentials for water, the adiabatic temperature rise at 100 ps was first estimated from the absorbed laser energy divided by  $C_V$  and the result checked against the TIP4P MD simulation by Marco Cammarata (PhD thesis "Time resolved X-ray scattering as a tool to study transient species in solution", University of Palermo, December 2006) [34]. Marco calculated the differentials from MD simulations at two temperatures at constant volume and simulations for two densities at constant temperature. The measured and scaled differentials are shown in figure 2.14. They were measured with the 2.1% Ru multilayer beam that was used in the  $[Fe(phen)_3]^{2+}$  experiments. The water scattering is shown below. As for the 100 ps differential, the oscillation is produced by a broadening of the water peak at higher temperatures from the increase in O-O dispersion. For the density differential, the increase in density leads to a smaller O-O distances and the water peak shifts to higher  $q$ .

It is interesting to track the hydrodynamic parameters during the thermal cycle of the solvent in the dye experiment. The change in pressure is

$$\Delta P = (1/\rho\chi_T)\Delta\rho + (\alpha_P/\chi_T)\Delta T,$$

where  $\chi_T$  is the isothermal compressibility. The thermodynamic cycle for a 10 mM dye excitation at 400 nm is shown in figure 2.15 for water and acetonitrile. Note the vertical temperature and pressure rise at constant density in the time interval 0.1-10 ns (a). After 10 ns, the solvent expands for 70 ns while the pressure returns to ambient. After the expansion, the temperature is lowered by the factor  $C_V/C_P$  (close to 1 for water). Finally, the solvent

returns to the initial state in 0.3 s as the excess heat diffuses away. The diagram for acetonitrile is shown for comparison. Note the decrease in temperature after the expansion, the normal case for solvents except water.

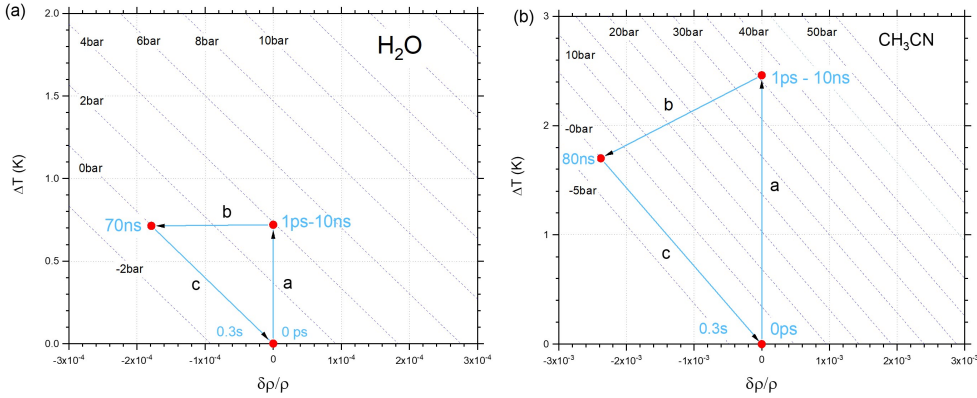


**Figure 2.15:** Hydrodynamic presentation of the solvent heating cycle. The isobars are shown as inclined broken lines. (a) Water cycle produced by 400 nm excitation of 10 mM  $\text{C}_{16}\text{H}_{18}\text{BrN}_3$  dye. (b) Similar cycle for acetonitrile. Note the temperature drop in the expansion phase b, which is greater than for water (the incremental pressure under 10 m of water is 1 bar).

## 2.5 Scattered intensity on the detector

Now that the angular dependence of elastic and Compton scattering is known, we will calculate the intensity on a 2D detector. The incident undulator beam is linearly polarised and the detector is flat and centred on the beam. The intensity in a pixel will be calculated and corrected for the flatness of the detector so that all pixels have the same distance and solid angle from the sample. The distance of these "virtual pixels" is  $\text{det}x$ , i.e. the pixel distance in the forward direction.

To calculate the intensity on each pixel one needs to know the scattered intensity per solid angle and the space angle of the pixels. The direction to a pixel is expressed in the polar coordinates shown in figure 2.16. The incident beam is a plane wave propagating along the  $Z$ -axis with an electric field  $\mathbf{E}_0$  parallel to the  $Y$ -axis,  $\mathbf{E}_0 = E_0(0, 1, 0)$ . The linearly polarised incident beam  $\mathbf{k}_i$  and the scattered beam  $\mathbf{k}_f$  are shown in figure 2.16.

We will now consider the scattering in the  $(\theta, \phi)$  direction along the unit vector  $\mathbf{s}$ :

$$\mathbf{s} = (\sin \theta \cos \phi, \sin \theta \sin \phi, \cos \theta).$$

The differential cross section for elastic scattering from a free electron at the origin is:

$$\frac{d\sigma}{d\Omega} = r_0^2 \sin^2 \chi = r_0^2 P(\theta, \phi),$$

where  $d\Omega = \sin \theta d\theta d\phi$  is the solid angle,  $r_0$  is the classical electron radius,  $\chi$  is the angle between the scattered direction and the incident polarisation.  $P(\theta, \phi)$  is the polarisation factor, i.e. the projection of  $\mathbf{E}_0$  onto the plane perpendicular to the direction of the scattered beam. The angle  $\chi$  is obtained from:

$$\cos \chi = \frac{\mathbf{E}_0 \cdot \mathbf{s}}{|E_0|} = \sin \theta \sin \phi.$$

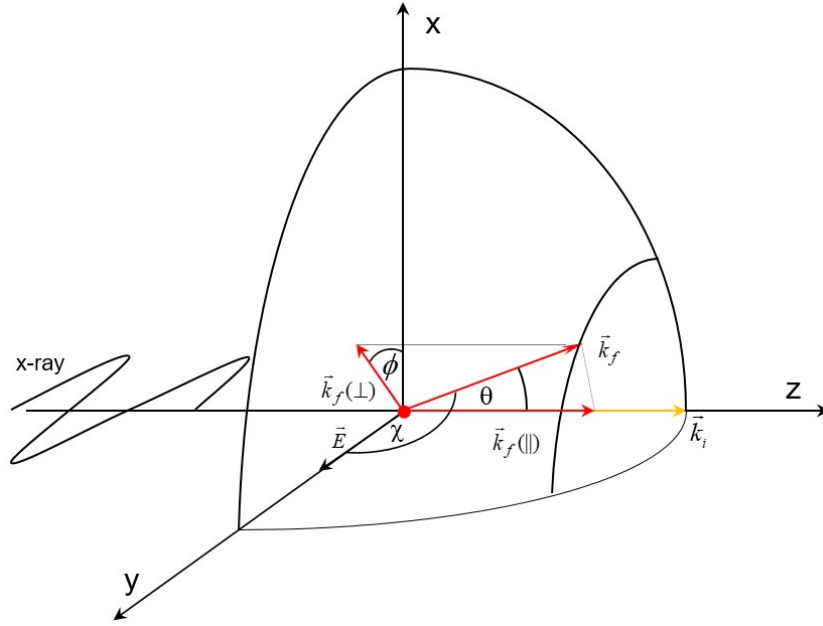


**Figure 2.16:** Polar coordinates of the incident (yellow) and scattered (red) beam. The electric field of the incident and scattered beam is confined to the plane perpendicular to the propagation. The scattered intensity, elastic and inelastic, is zero in the  $y$  direction (polarisation hole).

The amplitude in the plane perpendicular to the scattered beam is:

$$E_{\perp} = E_0 \sin \chi.$$

The intensity is proportional to  $E_{\perp}^2$  which is reduced by the geometric polarisation factor:

$$P(\theta, \phi) = \sin^2 \chi = 1 - \cos^2 \chi = 1 - \sin^2 \theta \sin^2 \phi.$$

In the two principal planes we get:

$$P(\theta, \phi) = \begin{cases} 1 & \text{in the vertical plane } (x, z); \\ \cos^2 \theta & \text{in the horizontal plane } (y, z). \end{cases}$$

If the incoming X-ray beam has the intensity  $I_0$  in photons/m<sup>2</sup>/s, the scattered intensity from a free electron is:

$$\frac{dn_2(\theta, \phi)}{d\Omega} = I_0 \frac{d\sigma(\theta, \phi)}{d\Omega} = I_0 r_0^2 (1 - \sin^2 \theta \sin^2 \phi).$$

Note that this expression does not contain any form factor as we consider an infinitely small free electron. Integration over  $\phi$  gives the radial intensity:

$$\frac{dn_1(\theta)}{d\theta} = 2\pi I_0 r_0^2 \left( \frac{1 + \cos^2 \theta}{2} \right).$$

The average polarisation is shown in figure 2.20(a). Integrating over  $\theta$  we obtain the total intensity scattered into  $4\pi$ :

$$n_0 = \frac{3\pi}{2} I_0 r_0^2.$$

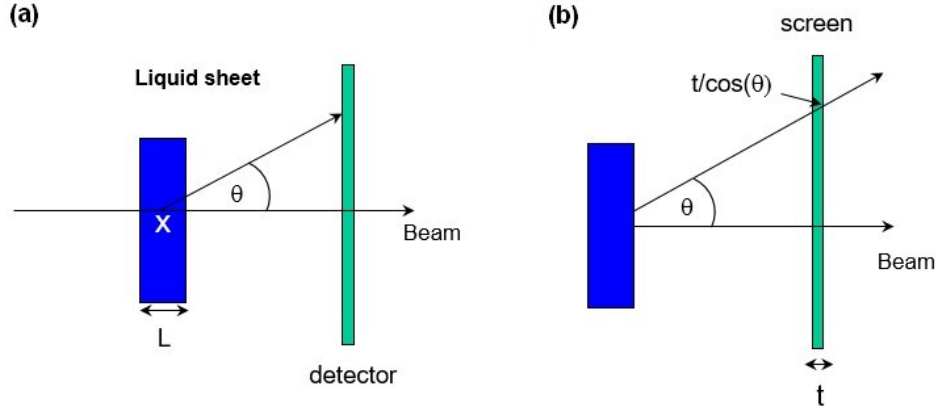


**Figure 2.17:** (a) Liquid sheet transmission. The scattered beam is attenuated by absorption in the sheet which increases with angle. (b) The absorption in the phosphor screen in the detector increases at high angles from the increase in thickness in the scattered beam direction.

The angular resolved cross section for a free electron is readily generalised to a liquid with scattering functions  $S^{el}$  and  $S^{inel}$  as:

$$\frac{dn_2(\theta, \phi)}{d\Omega} = I_0 r_0^2 T(\theta) D_{phosphor}(\theta) P(\theta, \phi) \sum_{i \in V} (S_i^{el}(q) + S_i^{inel}(q)), \quad (2.6)$$

where the sum is over molecules in the exposed volume.

In the above formula we have included the sample transmission from photoelectric absorption and the detector sensitivity  $D_{phosphor}$  from the finite absorption in the phosphor screen that converts X-ray photons to visible light. The space angle  $\delta\Omega$  is the solid angle of a pixel on the detector (see later).

### 2.5.1 Transmission of a liquid sheet

Let's first calculate the transmission for a flat liquid sheet as a function of scattering angle  $\theta$  and the sheet thickness  $L$ . The beam geometry is shown in figure 2.17(a). The intensity of an X-ray beam transmitted through a sample of thickness  $L$  is given by Beer-Lambert's law:

$$I_T = I_0 e^{-\mu L},$$

where  $I_0$  is the incoming intensity,  $I_T$  is the transmitted X-ray intensity,  $\mu = \mu(E)$  is the absorption coefficient of the solution. The transmission through the sample is defined as  $T = I_T/I_0$ . If we consider the scattering in the  $\theta$  direction from position  $x$  inside the sheet (figure 2.17(a)), the transmission is:

$$T(\theta, L) = \frac{1}{L} \int_0^L e^{-\mu x} e^{-\mu(L-x)/\cos\theta} dx,$$

$$T(\theta, L) = \frac{1}{\mu L} \left( \frac{\cos\theta}{1 - \cos\theta} \right) [e^{-\mu L} - e^{-\mu L/\cos\theta}].$$

The calculated transmission for water and liquid  $\text{CCl}_4$  is shown in figure 2.18(a).

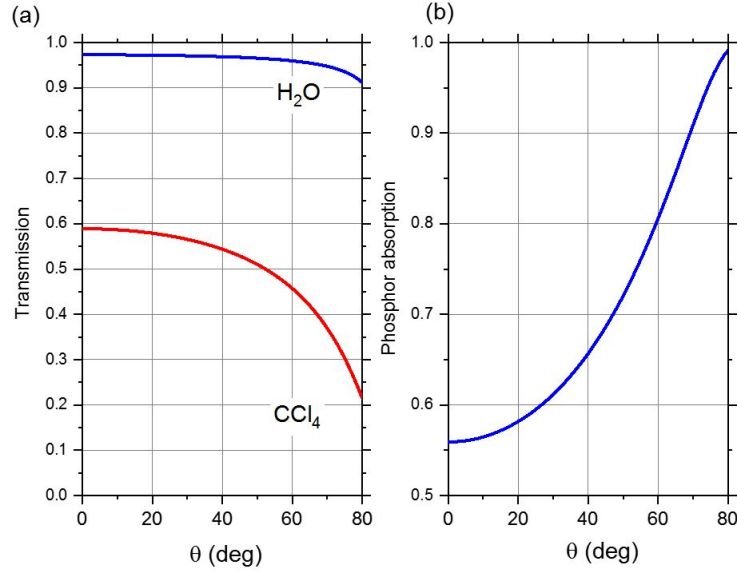


**Figure 2.18:** (a) Transmission in a 0.36 mm thick sheet of water. The high- $Z$  liquid  $\text{CCl}_4$  is also shown. The X-ray energy is 18 keV. (b) Phosphor absorption vs scattering angle. The phosphor in the Rayonix MX170 is 40  $\mu\text{m}$  thick and the absorption coefficient  $\mu$  is 20.5  $\text{mm}^{-1}$  at 18 keV. The useful angular range in WAXS is 0 – 65°.

## 2.5.2 Detector sensitivity

The absorption in a phosphor screen of thickness  $t$  depends on the incidence angle of the scattering. It is readily calculated from the thickness of the screen as shown in figure 2.17(b). The absorption is

$$D_{\text{phosphor}}(\theta) = 1 - e^{-\mu(\lambda)t/\cos\theta},$$

where  $\mu$  is the absorption coefficient of the phosphor. The phosphor is 40  $\mu\text{m}$  thick  $\text{Gd}_2\text{O}_2\text{S:Tb}$  sheet with an absorption coefficient of 20.5  $\text{mm}^{-1}$  at 18 keV. The absorption at zero angle is 56% at 18 keV as shown in figure 2.18(b).

## 2.5.3 Solid angle of a pixel

Let's now determine the space angle for a pixel element on a flat detector. Consider the scattering recorded on a flat detector at a distance  $d$  from the sample. The radiation scattered at an angle  $\theta$  is recorded by a pixel element of size  $dl \times dl$ . This pixel has the solid angle  $d\Omega$ :

$$d\Omega = \left(\frac{\cos\theta}{d}\right)^2 \cos\theta (dl)^2 = \frac{\cos^3\theta}{d^2} (dl)^2, \quad (2.7)$$

as illustrated in figure 2.19(a). Summing up the azimuthal pixels gives the ring area  $dA$  and number of pixels  $N_P$  (figure 2.19(b)) expressed as:

$$dA = 2\pi d \tan\theta dl, \quad N_P = \frac{2\pi d \tan\theta}{dl}.$$

Let's calculate  $N_P$  at the inner edge of the square 170  $\times$  170  $\text{mm}^2$  detector for a sample-detector distance  $d$  of 40 mm. The pixel size is 0.088 mm,  $\theta = 64.8^\circ$  which gives  $N_P = 6069$  pixels. With that many pixels collecting the weak signal near the edge of the detector, the readout noise and dark current have to be very low to get a reliable signal. The CCD sensor in the Rayonix is cooled to 80 K to minimise thermal noise.

The solid angle of a pixel and the azimuthally averaged polarisation are shown in figure 2.20. The solid angle is normalised to 1 at  $\theta = 0$  for clarity.

### 2.5.4 Water intensity from a single pulse

We will now calculate the pixel intensity from water from one 18 keV pulse from the U17 undulator. The beam dimension is  $0.04 \times 0.06 \text{ mm}^2$  and the pulse intensity  $1.0 \cdot 10^9 \text{ ph/pulse}$ . The beam is considered monochromatic. The water sample is delivered by a 0.36 mm thick jet and the Rayonix detector is 40 mm from the jet.

The pixel intensity  $I_P$  is here calculated as the azimuthally averaged pixel intensity:

$$I_P(\theta) = I_0 r_0^2 T_{sheet}(\theta) D_{phosphor}(\theta) \left( \frac{1 + \cos^2 \theta}{2} \right) \sum_{i \in V} (S_i^{el}(q) + S_i^{inel}(q)) d\Omega,$$

where  $d\Omega$  is the solid angle of a pixel on the detector. The scattering functions for water are shown in figure 2.21 and the parameters are listed in table 2.2. The water scattering function will be discussed in more detail in the next section.

In the simulation, a 0.36 mm thick water sheet is exposed to a single X-ray pulse with  $1.0 \cdot 10^9$  photons at 18 keV. That is the typical intensity of a pink pulse from the U17 undulator at 8.6 mm gap. The cross section of the incident beam is  $0.04 \times 0.06 \text{ mm}^2$  and  $2.89 \cdot 10^{16}$   $\text{H}_2\text{O}$  molecules are exposed to the beam. The Rayonix MX170 detector is 40 mm from the sample and centred on the primary beam. The non scattered radiation is stopped by a Tungsten beamstop with a 1.6 mm diameter. The input parameters are summarized in table 2.2.

The maximum detected intensity on the liquid peak of water has 12.85 ph/pixel/pulse (figure 2.22). At this count rate, with multiple photons in a pixel per pulse, the detector has to accumulate the signal, as in the Rayonix detector where the charge in the CCD is accumulated during the pulse. The simulation predicts that the intensity on the liquid peak in a 1 s exposure at 1 kHz is 12850 counts in close agreement with the experiments.

The detector used for XES, the Maxipix  $5 \times 1$ , is photon counting which is perfect for very low count rates in XES where the full detector receives  $< 0.1$  photon per pulse. With such low count rates, photon counting is perfect: noise free detection, perfect linearity and a very high dynamic range.

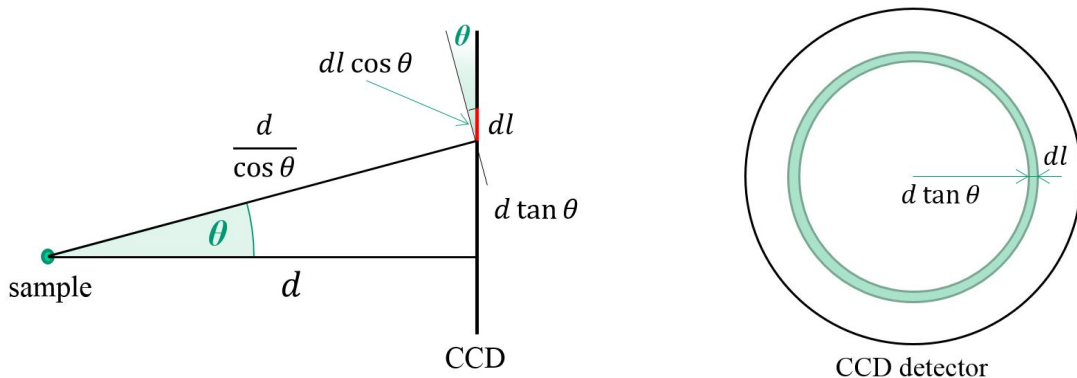


**Figure 2.19:** (a) Solid angle of a pixel on a flat detector. (b) Azimuthal averaging of the intensity in a ring.

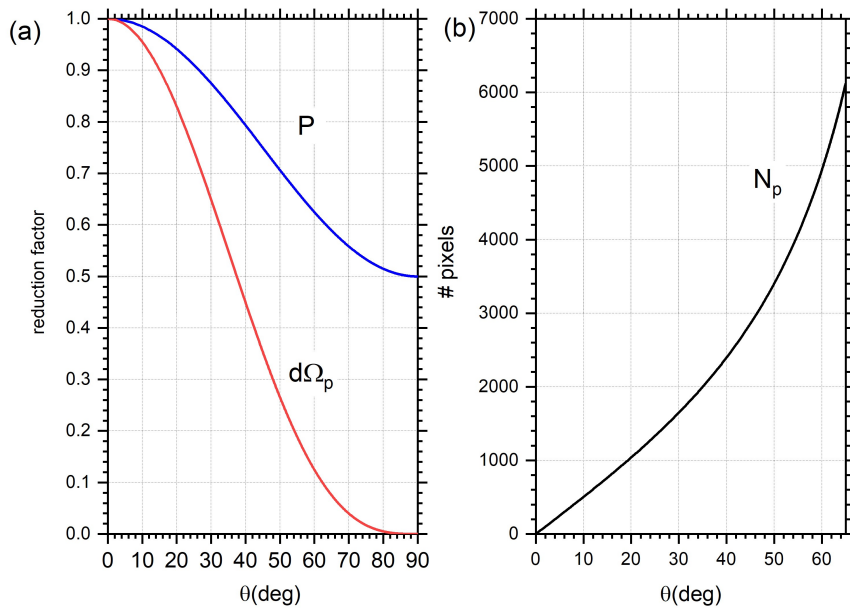


**Figure 2.20:** (a) The polarisation factor, azimuthally averaged, is shown in blue. The solid angle of a pixel vs scattering angle for a flat detector is shown in red. It is normalised to 1 at  $0^\circ$ . (b) Number of pixels in the azimuthal pixel ring for 0.088 mm pixels 40 mm from the sample.

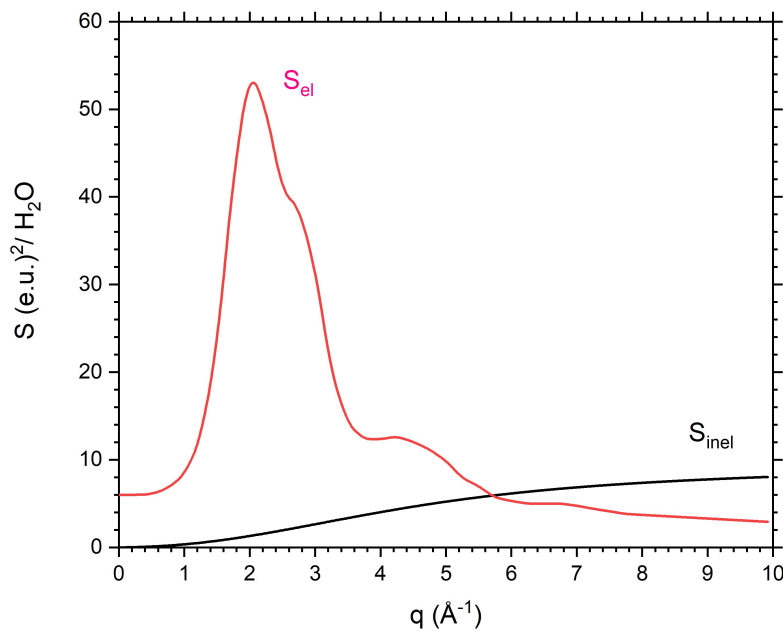


**Figure 2.21:** Elastic and inelastic Compton scattering for water at  $20^\circ\text{C}$  [35]. Scattering at  $q > 6 \text{ \AA}^{-1}$  is dominated by Compton scattering.

## 2.6 X-ray Emission Spectroscopy

We will now briefly mention the main XES features that were used to interpret the data from  $[\text{Fe}(\text{phen})_3]^{2+}$ . For a detailed review of X-ray spectroscopies the reader is referred to the comprehensive review article by Majed Chergui and Eric Collet [36]. When a core hole is

<b>Beam</b>		
Energy	18.0	keV
Wavelength	0.689	Å
Beam size H	0.040	mm
Beam size V	0.060	mm
Pulse intensity	$1 \cdot 10^9$	ph/pulse
$I_0$	$4.17 \cdot 10^{11}$	ph/mm <sup>2</sup> /pulse
<b>Sample</b>		
Volume (w × h × d)	$0.04 \times 0.06 \times 0.36$	mm <sup>3</sup>
H <sub>2</sub> O in sample	$2.89 \cdot 10^{16}$	
<b>Rayonix Detector</b>		
Detector distance	40	mm
Pixel size	0.088	mm
Pixel array	$2032 \times 2032$	
Angular range	0.0 – 65.9	deg
Photons on detector	$4.1 \cdot 10^6$	ph/pulse
Photons detected	$2.7 \cdot 10^6$	ph/pulse
Scattering ratio	$4.1 \cdot 10^{-3}$	

**Table 2.2:** Water simulation parameters. Note that only 1:244 of the incident photons hit the detector.

created by ionising X-rays, the core hole is filled in less than 1 fs by an electron from a higher energy level. The excess energy is released by the emission of an X-ray photon or an Auger electron. For the K edge of Fe, 34% are emitted as photons, 66% as Auger electrons. The emission is labelled by the shell of the core hole, i.e. K, L, M and N for  $n = 1, 2, 3$  and 4 core holes, respectively. In the  $[\text{Fe}(\text{phen})_3]^{2+}$  project, we used the  $\text{K}\beta$  emission due to its high spin sensitivity. In addition,  $\text{K}\beta$  emission is readily produced from the absorption of X-rays from the U17 undulator above the K edge at 7112 eV. The K edge has the added advantage that the experiments can be done in a helium atmosphere rather than in vacuum.

The K emission has three principal components,  $\text{K}\alpha$ ,  $\text{K}\beta$  and valence-to-core (VtC) as described below. The electronic transitions are shown in figure 2.23(a) and the spectra of  $\text{K}\alpha$  and  $\text{K}\beta$  lines are shown in figure 2.23(b,c) for  $[\text{Fe}(\text{terpy})_2]^{2+}$ .

### 2.6.1 $\text{K}\alpha$ emission line

$\text{K}\alpha$  emission is produced by the  $2p \rightarrow 1s$  transition which is split by the spin-orbit coupling into  $2p_{1/2}$  and  $2p_{3/2}$  levels. The  $2p_{1/2} \rightarrow 1s$  transition is called  $\text{K}\alpha_2$  and the  $2p_{3/2} \rightarrow 1s$  is called  $\text{K}\alpha_1$ . The  $\text{K}\alpha_2$  line is lowest in energy. The intensity ratio  $\text{K}\alpha_2 : \text{K}\alpha_1$  is 1:2 due to the 2- and 4-fold degeneracy of the  $2p_{1/2}$  and  $2p_{3/2}$  levels. The FWHM of the  $\text{K}\alpha_1$  line is proportional to the total spin but usually the  $\text{K}\beta$  lines are used to monitor spin changes in spite of the lower intensity. The  $2p$  hole is filled by a higher energy electron with the emission of a UV photon.

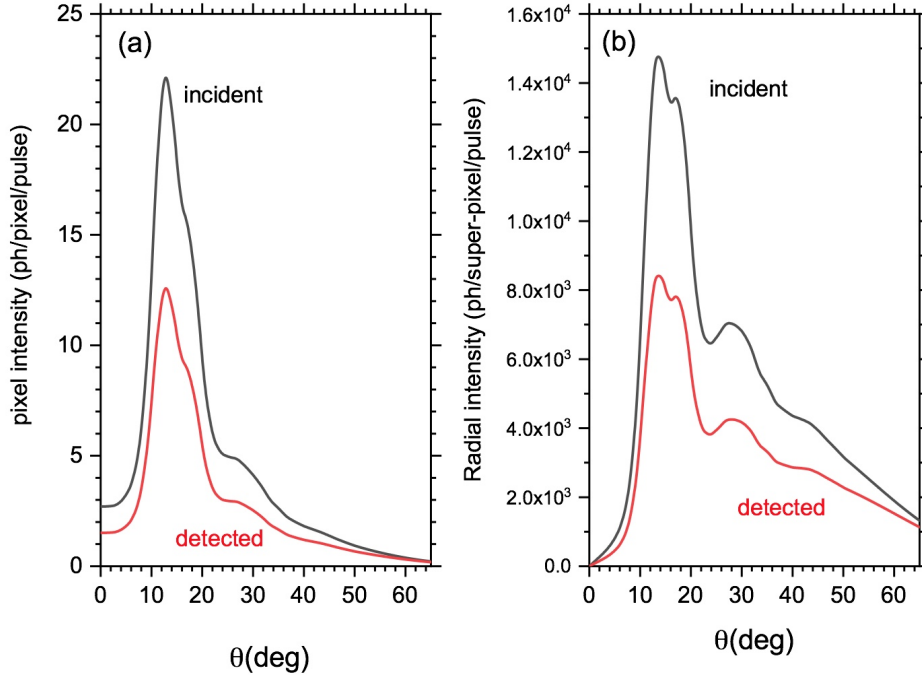


**Figure 2.22:** (a) Intensity in a pixel from a 0.36 mm thick sheet of water from a single pulse at 18 keV with  $1 \cdot 10^9$  ph/pulse. The pixel intensity is the azimuthal average. The incident and detected counts are shown in black and red, respectively. (b) The intensities are summed azimuthally into superpixels. The integral shows that  $4.1 \cdot 10^6$  photons per pulse are scattered onto the detector of which 65% are detected. 60% of the detected photons are Compton scattered!

## 2.6.2 $K\beta$ emission line

$K\beta$  emission is produced by the  $3p \rightarrow 1s$  transition which is split into  $K\beta_{1,3}$  and  $K\beta'$ . The splitting is proportional to the total spin of the metal. That makes  $K\beta$  an excellent marker of the spin state [38]. In Fe, the intensity of the  $K\beta$  lines is seven times weaker than  $K\alpha$  due to the lower overlap between the  $3p$  and  $1s$  orbitals in  $K\beta$ .

## 2.6.3 Valence-to-core emission

The  $3d \rightarrow 1s$  valence-to-core (VtC) transitions  $K\beta''$  and  $K\beta_{2,5}$  are 2-3 orders of magnitude weaker than  $K\beta$ . In the present study, VtC is allowed due to the weak hybridisation of the  $3d$  electrons with the  $2p$  electrons in the Fe-N bond which gives some  $2p$  character to the  $3d$  electrons [39]. Valence-to-core is spin sensitive since it probes the  $3d$  electrons directly including ligand hybridisation. VtC is sensitive to the ligand environment including their number and distance [40]. The weakness of VtC makes it difficult to measure the spectrum with 100 ps resolution due to the long exposure times that are needed when the pump-probe experiment runs at 1 kHz. In the near future the experiments could be done with MHz pump-probe technology which should greatly improve the data quality as already demonstrated at the APS on beamline Sector 7 [41].

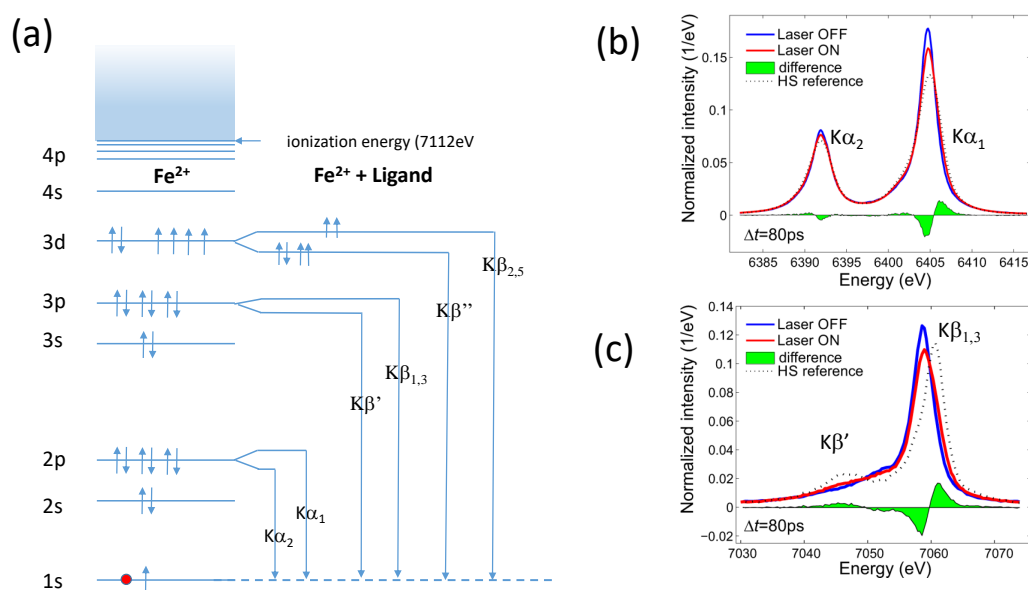


**Figure 2.23:** (a) The transitions in  $\text{Fe}^{2+}$  are shown on the left. On the right, the levels are shown in the ligand field for the HS state ( $S = 2$ ). The 3d level is split and the total spin is  $S = 2$ . The 3d spin sensitivity of  $K\beta$  is due to the exchange interaction with the 3p hole. (b)  $K\alpha$  lines for  $[\text{Fe}(\text{terpy})_2]^{2+}$  measured with a Johann spectrometer with a Ge(440) spherical analyser. The HS-LS difference is shown in green. (c)  $K\beta$  lines in the LS and HS states. The  $K\beta'$  and  $K\beta_{1,3}$  splitting probes the spin of the 3d level from the ligand field. The amplitude of the green HS-LS curve shows that the 15 mM concentrated sample is 40% excited.  $[\text{Fe}(\text{terpy})_2]^{2+}$  data from György Vankó et al. [37].



# INSTRUMENTATION

## 3.1 Synchrotron radiation

In synchrotron light sources electrons are circulating in a closed orbit close to the speed of light. Their trajectory is deflected by strong magnetic fields produced by dipole magnets and at each turning point X-rays are emitted due to the acceleration of the electrons. According to classical electromagnetic theory, an accelerated charge radiates and the power emitted by a particle of charge  $q$  and acceleration  $a$  is given by Larmor's formula:

$$P = \frac{2q^2 a^2}{3c^3},$$

where  $c$  is the speed of light. Figure 3.1(a) shows the radiation from a dipole for an electron accelerated to a small velocity  $v \ll c$ . A relativistic charge radiates in a narrow forward cone with the aperture  $\theta = 1/\gamma$  as shown in figure 3.1(b).  $\gamma$  is the relativistic factor  $\gamma = 1/\sqrt{1 - \beta^2} = E/m_e c^2$  and  $\beta = v/c$ .

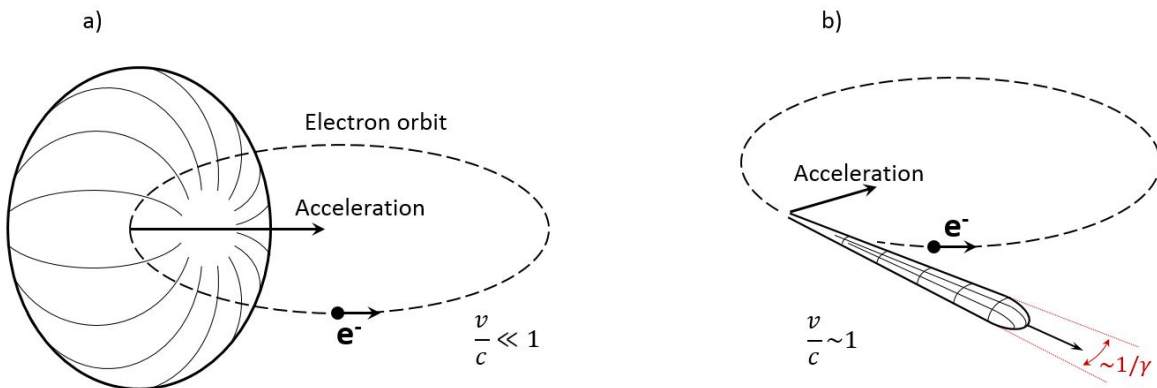


**Figure 3.1:** (a) Radiation from a non relativistic electron. (b) Radiation from a relativistic electron. The radiation is tangential to the orbit with an opening angle  $\sim 1/\gamma$  (85  $\mu$ rad for 6 GeV).

The ESRF is the most intense and brilliant 3<sup>rd</sup> generation synchrotron sources worldwide. It operates at 6.03 GeV, which corresponds to  $\gamma = 11800$ . At this energy, a single electron emits an X-ray beam with a 85  $\mu$ rad divergence, which is therefore the vertical divergence of ESRF bending magnet beamlines.

The electron beam has a finite root mean square size  $\sigma_{y,z}$  and angular divergence  $\sigma'_{y,z}$ . An important parameter of a synchrotron source is the emittance, the source size  $\times$  divergence. For a synchrotron source it is calculated from the electron and photon parameters:

$$\varepsilon_{y,z} = \sqrt{\sigma_{y,z}^2 + \sigma_R^2} \cdot \sqrt{\sigma'_{y,z}{}^2 + \sigma'_R{}^2},$$

where  $\sigma_{y,z}$  and  $\sigma'_{y,z}$  are the electron beam size and divergence and  $\sigma_R$  and  $\sigma'_R$  are the photon source size and divergence. The emittance of the electron beam is constant, which means that the electron beam can be focused at the expense of divergence by quadrupole magnets in front of the straight section for undulators or wigglers.

### 3.1.1 Accelerator complex

A simplified accelerator complex is shown in figure 3.2. The electrons are accelerated in three steps as follows:

#### Linac

First bunches of electrons are produced at 10 Hz by an electron gun. The bunches are accelerated by radio frequency (RF) cavities in a linear accelerator, the so-called Linac. The

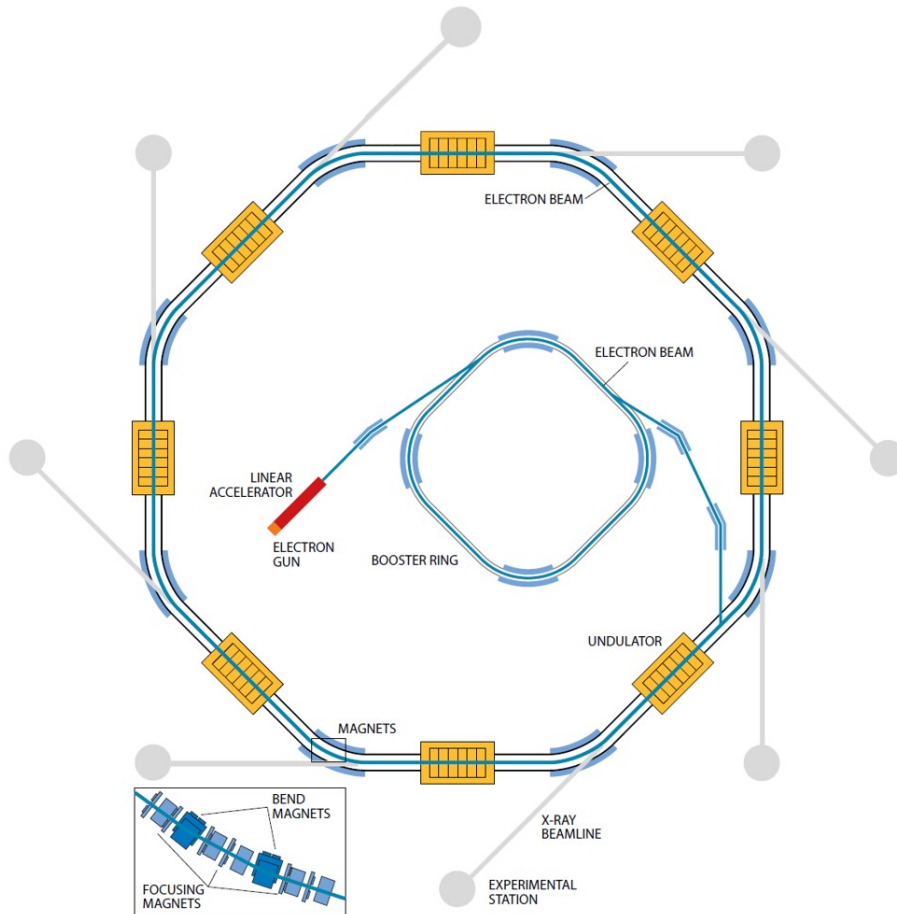


**Figure 3.2:** Simplified schematics of the linac, booster and storage ring with 8 undulator straight sections. The beamlines from the undulators are also shown. Adapted from M. Altarelli et al. [42].

RF cavities produce an alternating electromagnetic field parallel to the electron beam to efficiently accelerate the electrons. At the end of the Linac the electron energy reaches 200 MeV energy before entering the booster synchrotron.

## Booster

In this part of the accelerator, the electrons continue to be accelerated up to 6.03 GeV and are kept in a 281 m long circular orbit by bending magnets. As the electrons gain energy, the magnetic field in the bending magnets is increased synchronously in order to maintain a constant orbit. (Synchrotrons were given their name for this reason).

## Storage ring

When the 6.03 GeV energy is reached in the booster, the electrons are transferred to the 844 m long storage ring where they are guided into a closed orbit by 32 bending magnets. Each bending magnet has one 0.85 T and one 0.4 T electromagnets, and that combined deflect the electron beam by  $11.25^\circ$ . As electrons lose energy due to X-ray emission, the RF cavities in the storage ring keep the energy constant at 6.03 GeV. Without the compensating RF acceleration, stochastic energy losses to synchrotron radiation would broaden the energy distribution of the electrons. Electrons with lower energies are deflected slightly more by the magnetic field and will slowly drift towards the centre of the synchrotron. Each of the 32 straight sections has quadrupole and sextupole magnets to focus the electron beam constrained by the constant emittance.

The storage ring is kept under ultra-high vacuum ( $\sim 10^{-9}$  mbar). Eventually some electrons are deflected in collisions with residual molecules. As a result, the current in the storage ring slowly decreases. The lifetime is typically 10-50 hours depending on the filling mode of the storage ring. For this reason additional electrons are injected 2-4 times per day. More recently the storage ring current is maintained constant by injecting electrons in top-up mode with injections every 20 minutes. The top-up mode was a real benefit for the experiments in my thesis: the beam intensity is high all the time and more importantly, the beam position is very stable since the temperature of the optics is constant.

### 3.1.2 X-ray sources

The ESRF has 44 beamlines based on different X-ray sources: bending magnets (BM) and insertion devices (ID). BM beamlines use the radiation from the bending magnets that are guiding the electrons in the storage ring; ID beamlines use insertion devices, undulators and wigglers, in the middle of the straight sections of the storage ring. Each straight section has 2-3 insertion devices in the middle. These X-ray sources produce much higher intensity than the bending magnets. They consist of periodic arrays of dipole magnets (figure 3.4). The electrons are deflected by alternating vertical magnetic fields that produce a sinusoidal trajectory. The X-rays are emitted at each turn as shown in figure 3.4.

Insertion devices are characterised by their deflection parameter  $K$  which depends on the magnetic field  $B$  and period  $\lambda_u$  of the magnets:

$$K = \frac{eB\lambda_u}{2\pi m_e c} = 0.934 \lambda_u[\text{cm}] B[\text{T}].$$

If  $0 < K < 1$ , the amplitude of the sinusoidal motion is small and the X-rays emitted by a single electron from the tops of the orbit interfere constructively. Such an insertion

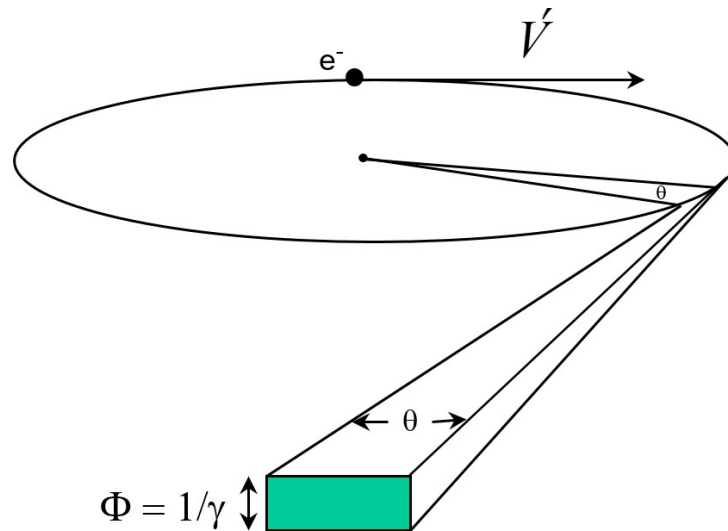


**Figure 3.3:** Synchrotron emission from a circular orbit. The front-end of bending magnet beamlines limits the horizontal radiation to 6 mrad. That radiation is emitted by a 0.85 T and a 0.40 T dipole magnets. By suitable alignment of the beamline aperture, the two beams can be separated.

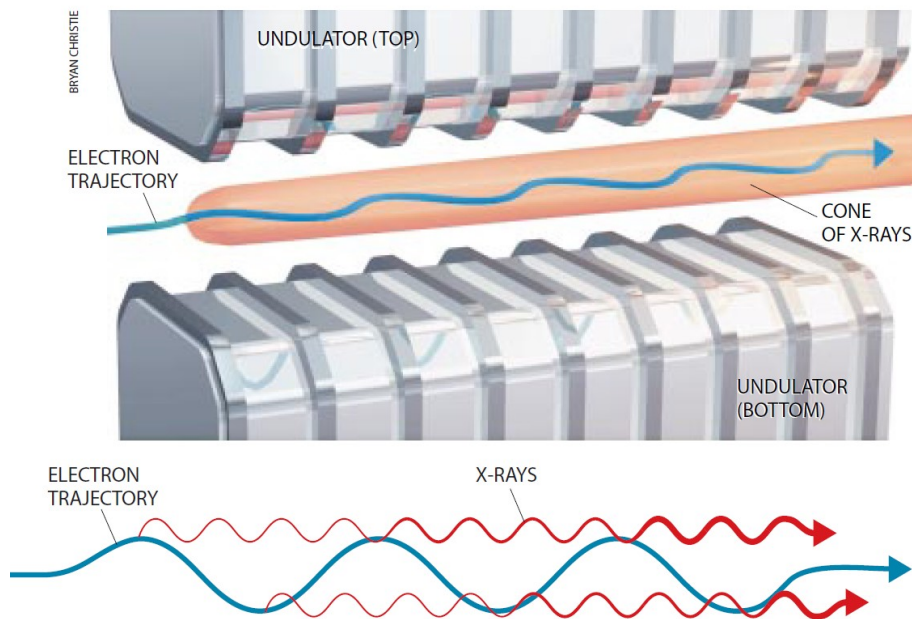


**Figure 3.4:** Undulator radiation. The radiation from in-line tops in the orbit interferes and the intensity is amplified by  $N^2$ , where  $N$  is the number of periods in the magnetic array. The interference is a single-electron effect. At the highest magnetic field of 0.85 T of the U17 undulator, the amplitude of the orbit is  $0.19 \mu\text{m}$ , much smaller than the  $120 \mu\text{m}$  horizontal source size. (From [42]).

device is called an undulator. It has an energy spectrum with intense narrow bands, and its intensity  $I_U$  scales as  $I_U \propto N^2 I_{BM}$  where  $I_{BM}$  is the intensity from the bending magnets in the sinusoidal orbit and  $N$  is the number of magnetic periods.

If  $K \gg 1$ , the amplitude of the sinusoidal orbit is large and the X-rays emitted at the turning points sum up with random phase. The insertion device is called a wiggler and it

has a broad spectrum similar to that of a bending magnet with an increase in intensity by a factor of  $N$ .

Most experiments in my thesis were done on ID09 using the U17 undulator with the parameters presented in table 3.1. The source will be described later in this chapter.

### 3.1.3 Bunch structures at the ESRF

The electrons in the 844 m storage ring rotate close to the speed of light with a rotation time of  $2.817 \mu\text{s}$  corresponding to an orbit frequency of 355.0 kHz. The RF cavities frequency is 352.2 MHz, the 992<sup>nd</sup> harmonic of the orbit frequency. Thus, the storage ring can be filled with up to 992 equidistant electron bunches and this filling pattern is called the uniform mode. The bunches are separated by 2.84 ns and each time a bunch passes an insertion device, an X-ray pulse is emitted.

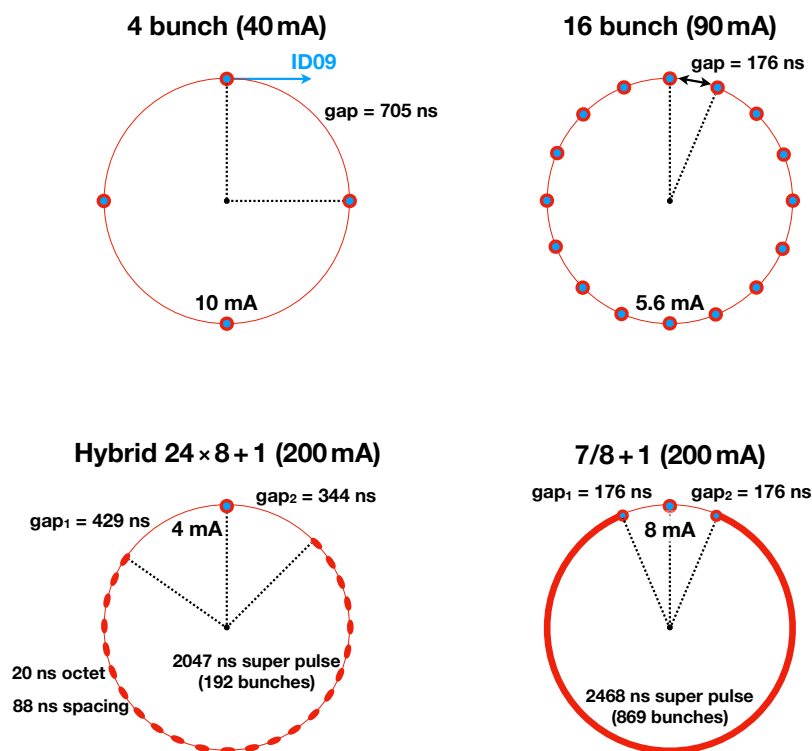


**Figure 3.5:** ESRF filling patterns for single-pulse experiments. The  $7/8 + 1$  mode is the default mode used 70% of the time. The total current is 200 mA with 8 mA in the single bunch. (Courtesy Michael Wulff).

In order to achieve the highest possible time resolution at a synchrotron source, which is determined by the 100 picosecond long flash from a single bunch, it is necessary to isolate the X-ray pulse mechanically by a chopper. For the ID09 chopper to isolate a single pulse, the pulses have to be separated by at least 150 ns. Therefore, in order to make time-resolved experiments feasible most of the time, the synchrotron often uses diluted filling patterns with 176 ns between the bunches or longer, e.g. the 4-bunch, 16-bunch,  $7/8 + 1$  and hybrid modes. The ESRF filling patterns are shown in figure 3.5.

The single pulse chopper on ID09, called the high-speed chopper, rotates at 986.3 Hz and can select single bunch X-ray pulses every  $\sim 1$  ms, which is much lower than the orbit frequency. This makes time-resolved experiments "photon hungry", and the single bunch current becomes an important parameter. Due to instabilities in the bunch, the single bunch current decays faster than the total current in the  $7/8 + 1$  mode. The recently introduced top-up mode has significantly improved this situation.

The time resolution of a laser pump/X-ray probe experiment is limited by the duration of the pump and probe pulses and by the uncertainty in the delay between them. Typically in a synchrotron experiment the X-ray pulse is significantly longer than the 1.2 ps laser pump pulse and the jitter in the time delay (2 ps). The time resolution is then essentially given by the X-ray pulse length:

$$\Delta\tau = \sqrt{\Delta\tau_{laser}^2 + \Delta\tau_{X-ray}^2 + \Delta\tau_{delay}^2} \approx \Delta\tau_{X-ray}.$$

A higher bunch charge is bigger in space and produces a longer X-ray pulse. Figure 3.6 shows the single pulse temporal profiles and the FWHM pulse length as a function of the bunch current, as measured by a streak camera.

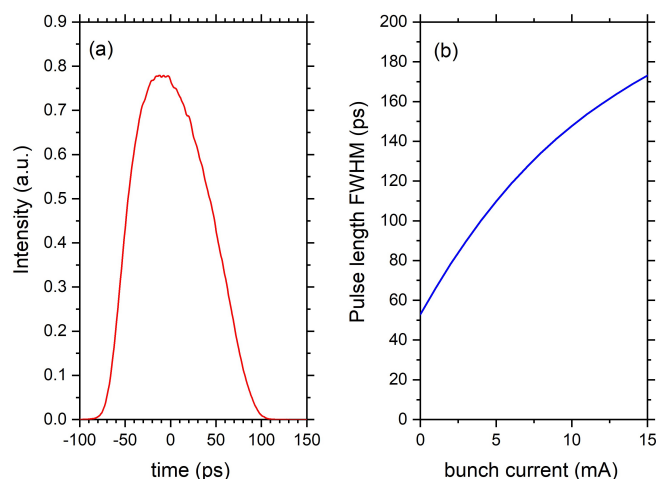


**Figure 3.6:** Temporal pulse profile and length. (a) Pulse profile from a 5 mA bunch. The FWHM is 110 ps. The asymmetric profile is caused by mirror charges in the vacuum vessel. (b) Pulse length vs bunch current. The charge in a 10 mA bunch at ESRF is 28.2 nC.

## 3.2 ID09 beamline

ID09 is a time-resolved pump-probe beamline with an option for pink-beam experiments. The beamline has choppers that can isolate single non-attenuated X-ray pulses from the synchrotron. For this purpose a unique chopper system is used to isolate intense 100 ps long X-ray pulses at 1 kHz. The beamline has two Class 4 lasers with tunable wavelengths: a 1 kHz picosecond laser and a 10 Hz nanosecond laser.

The current layout of the beamline is shown in figure 3.7. The beamline has three hutches: one optics hutch OH and two experimental hutches EH1 and EH2. The main components described in this chapter are: the two undulators U17 and U27, the focusing mirror, the

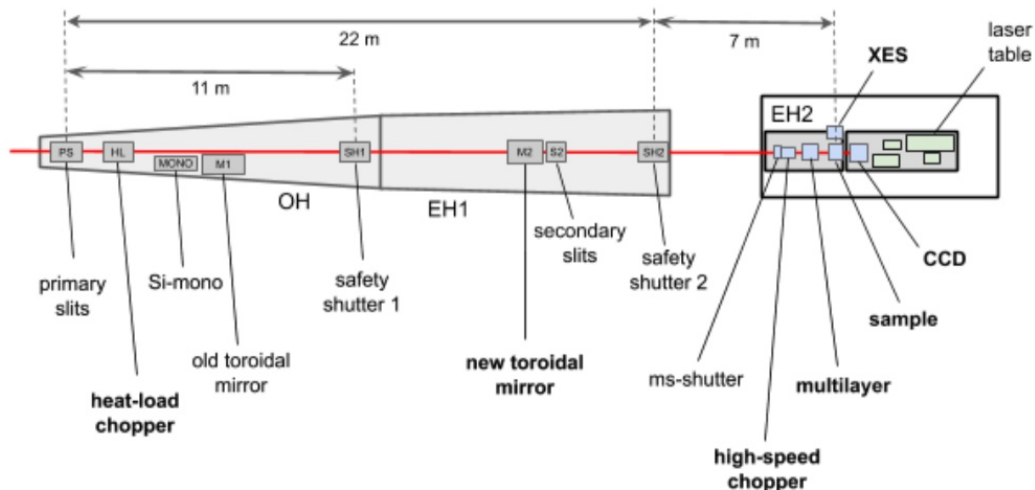


**Figure 3.7:** Layout of ID09. The main elements in the optics hutch (OH), experimental hutch 1 (EH1) and experimental hutch 2 (EH2) are shown.

chopper system, the ms-shutter, the multilayer monochromator, the goniometer, the CCD detector, two X-ray emission spectrometers and the two lasers.

### 3.2.1 Undulators

ID09 has two undulators: the in-vacuum U17 and in-air U27 undulator. To shift the spectrum of an undulator in energy and intensity, the magnetic field of the undulator can be tuned by changing the distance (gap) of the magnets to the electron beam. The advantage of in-vacuum undulators, where the magnets are placed in the vacuum chamber of the electron beam, is the possibility to significantly reduce the magnetic gap down to 6 mm whereby the magnetic field increases. It allows to produce a higher photon flux and a larger accessible energy range. The spectra of the U17 and U27 measured with the monochromator at different gap values are presented in figure 3.8 and the parameters are summarised in table 3.1.

	Period (mm)	Length (mm)	Poles	Gap min (mm)	$B_{max}$ (T)	$K_{max}$	$E_f$ (keV)	Total power (W/200 mA)
U17 <sub>invac</sub>	17	2000	234	6.0	0.52	0.83	15.0	215
U27 <sub>in-air</sub>	27	1600	118	11.0	0.46	1.17	7.6	131

**Table 3.1:** Undulator parameters on ID09 as of 2019. The power is calculated for a  $5 \times 0.5 \text{ mm}^2$  (H×V) slit at 27 m from the source. Absorption in beamline windows is neglected.

#### U17 undulator

The U17 is a 2 meter long in-vacuum undulator with a magnetic period of 17 mm. It has 234 pairs of NdFeB magnets that produce a sinusoidal vertical field. The gap can be closed to 6 mm which gives up to  $9.3 \cdot 10^9$  photons/pulse at the sample at 15 keV. The fundamental energy can be tuned between 15-20 keV (figure 3.8). The U17 produces up to 400 W of power at 200 mA.

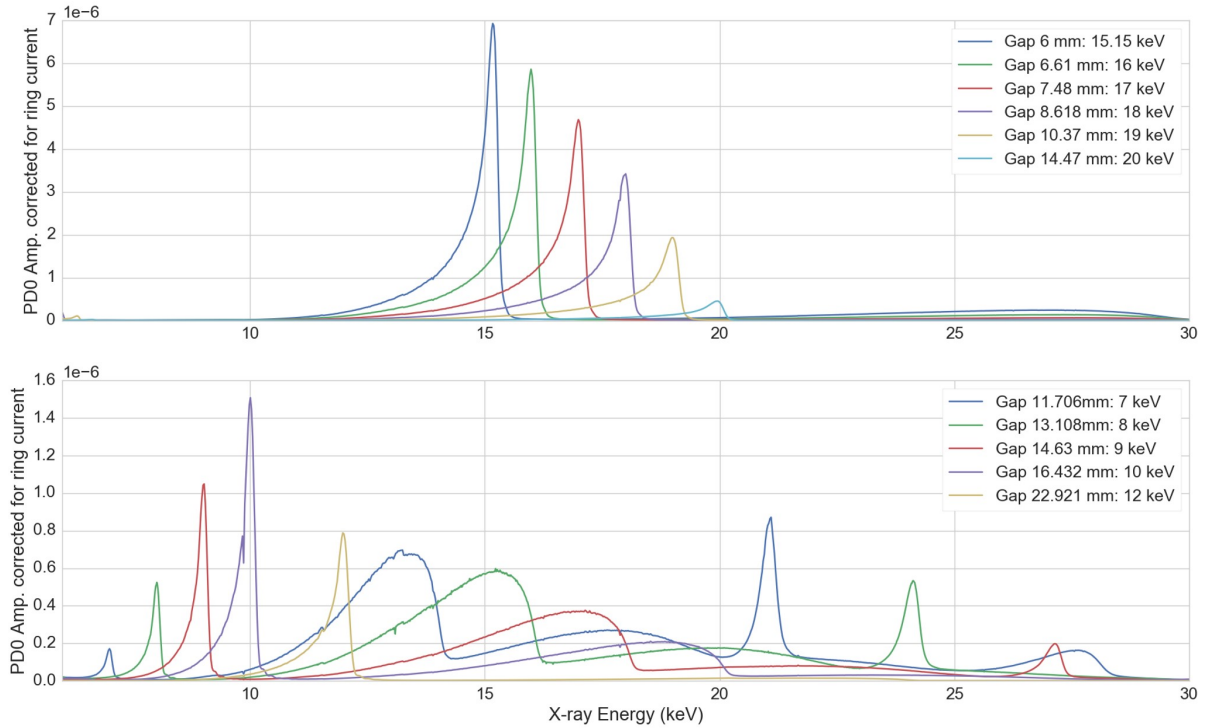


**Figure 3.8:** U17 and U27 spectra measured with the Si(111) monochromator for different gaps using the photodiode pd1 in EH2. The opening of the primary slits is  $0.5 \times 0.5 \text{ mm}^2$  and the incidence angle of the Pt coated toroidal mirror is 2.608 mrad. At that angle, the mirror kills radiation above 28 keV. The two undulators complement each other in energy. Note the striking 5-fold gain in intensity from the U17 in-vacuum undulator.

As mentioned before, the electron beam size and divergence vary at different points of the storage ring. Odd ID straight sections receive a more focused but more divergent electron beam than those in the even straight sections. These parameters are important for the spectrum produced by an insertion device. The cost of having a small source is lower brightness and vice versa. The electron beam rms size and divergence for ID09 are given in table 3.2.

Undulators generate radiation at specific harmonics seen as sharp peaks in the spectrum. Different harmonics have different angular distribution and the spectrum transmitted through the slits depends on the opening. The primary slits on ID09 are 27 m downstream the source (U17) and are usually set to  $7 \times 0.7 \text{ mm}^2$  (H×V). The mirror focuses the beam and rejects higher harmonics.

The U17 spectra at the primary slit were modelled with the XOP software [43]. The intensity in ph/s/0.1%BW is shown in figure 3.9 for the fundamental energies  $E_f = 15$  and

rms source size ( $\mu\text{m}$ )		rms divergence ( $\mu\text{rad}$ )	
$\sigma_H$	$\sigma_V$	$\sigma_{H'}$	$\sigma_{V'}$
59	8.3	90	3.0

**Table 3.2:** Source size and divergence of the electron beam on ID09 (ESRF). The FWHM is  $2.355 \cdot \sigma$ .

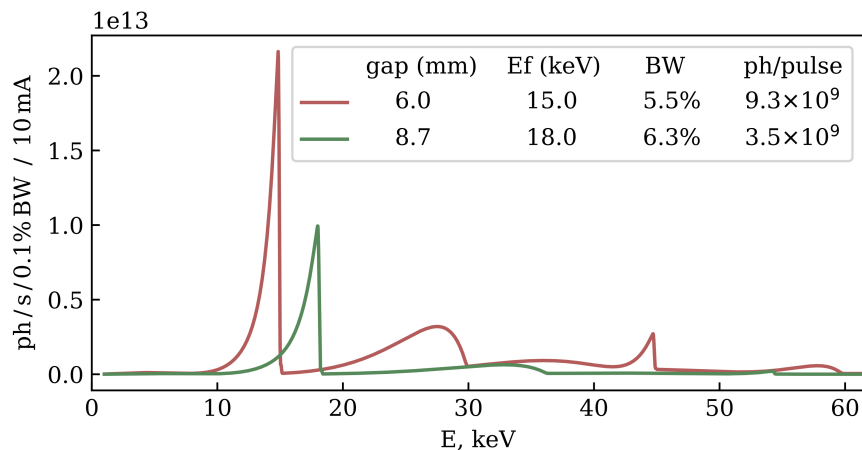


**Figure 3.9:** U17 spectra calculated by XOP for fundamental energies of  $E_f = 15$  and  $18$  keV. The opening of the primary slits is  $7 \times 0.7$  mm<sup>2</sup> and the synchrotron current  $10$  mA.

$18$  keV. The deflection parameters  $K$  are  $K=0.83$  and  $K=0.55$  at gap  $6.0$  mm and  $8.7$  mm, respectively.

The first harmonic of the undulator has a truncated Lorentzian line shape with a FWHM of  $5\%$ . The rising edge at low energies is due to the red shift from photons off-axis: as the electron beam in the straight section is focused into a small spot, the divergence increases and photons are emitted with a larger angular spread.

### 3.2.2 Chopper system

Single-pulse pump-probe experiments are photon hungry and whenever possible they are done without monochromator. The pink beam is focused by the toroidal mirror on the high-speed chopper in EH2 which needs a very small beam to isolate single X-ray pulses. The power from a non-attenuated undulator beam would damage the high-speed chopper. So the power on the high-speed chopper has to be reduced by a pre-chopper, the so-called heatload chopper. The function of the heatload chopper is to reduce the power to about  $10\%$  after the chopper. This is done by chopping the beam, after the primary slits, into  $40 - 80$   $\mu\text{s}$  pulses with a repetition frequency of  $986.3$  Hz.

The maximum repetition rate of a pump-probe experiment on ID09 is now  $\sim 1$  kHz and will be increased to  $\sim 3$  kHz in the near future. The CCD detector for scattering and diffraction is continuously exposed until  $\sim 10 - 50\%$  saturation and then read out after  $\sim 1000$  single-pulse exposures. To gate the CCD detector and to expose the sample only during the CCD exposure, the millisecond shutter is used. Single pulse isolation is divided into three steps as shown in figure 3.10. The heatload and high-speed chopper will be discussed in the following sections.

### 3.2.3 Heatload choppers

During my PhD studies two heatload choppers with different geometries were used on ID09.

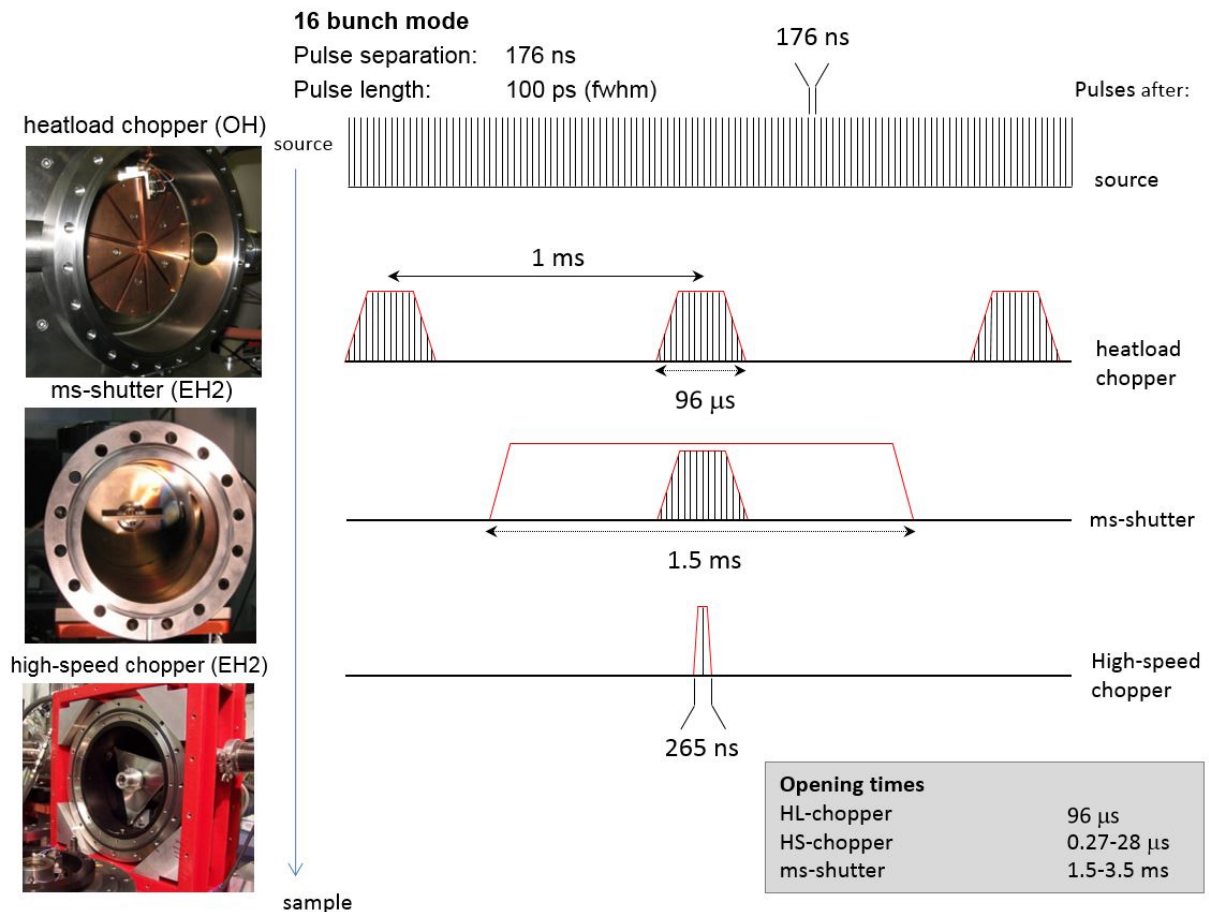


**Figure 3.10:** Synchronisation of the choppers and the ms shutter for a single shot experiment in 16-bunch mode (courtesy Michael Wulff).

### Eybert heatload chopper

The first generation heatload chopper was installed in 2012. It is a water-cooled in-vacuum chopper that can take heatloads up to 400 W and reduce the power to 8.5% after the chopper. The chopper design and photos are shown in figures 3.10 and 3.11. The 150 mm diameter copper disk is rotating inside a vacuum chamber with the rotation axis perpendicular to the beam. The rotor has seven tunnels through the centre and rotates at 70.445 Hz. The beam is then transmitted at 986.23 Hz. The chopper produces a trapezoidal close-open-close window as shown in figure 3.12. The baseline and topline of the transmission can be calculated from the geometry and the rotation speed. The pulse is 96.4 μs long (baseline) with the beam in the tunnel centre.

The chopper has a SmCo magnet glued on the disk and there is a pickup coil to synchronize the rotation to the RF clock. This chopper was designed by Laurent Eybert, the beamline engineer, in 2006. Table 3.3 summarises the chopper characteristics.

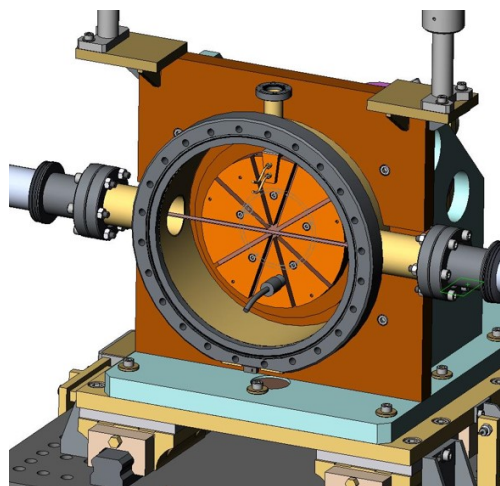


Figure 3.11: Eybert heatload chopper.

Disk radius:	75 mm
Rot. frequency:	70.445 Hz
X-ray frequency:	986.23 Hz
Seven tunnels	
Tunnel height:	3.2 mm
Open time (baseline):	96.4 $\mu$ s
Open time (topline):	75.3 $\mu$ s
Transmission:	8.5%

Table 3.3: Heatload chopper parameters.

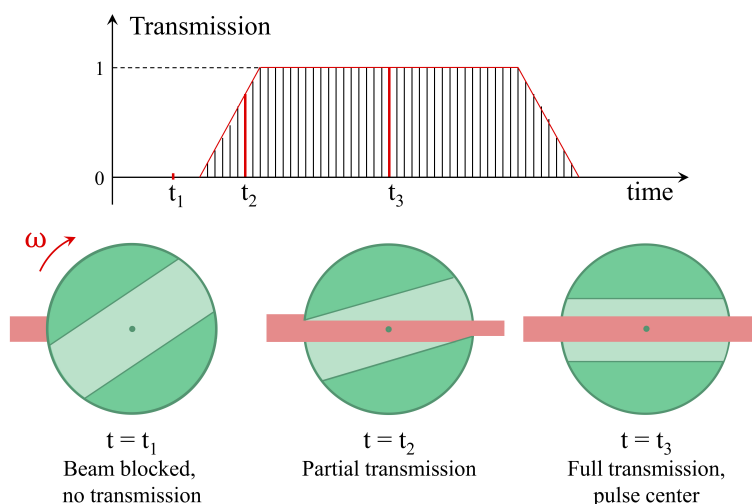
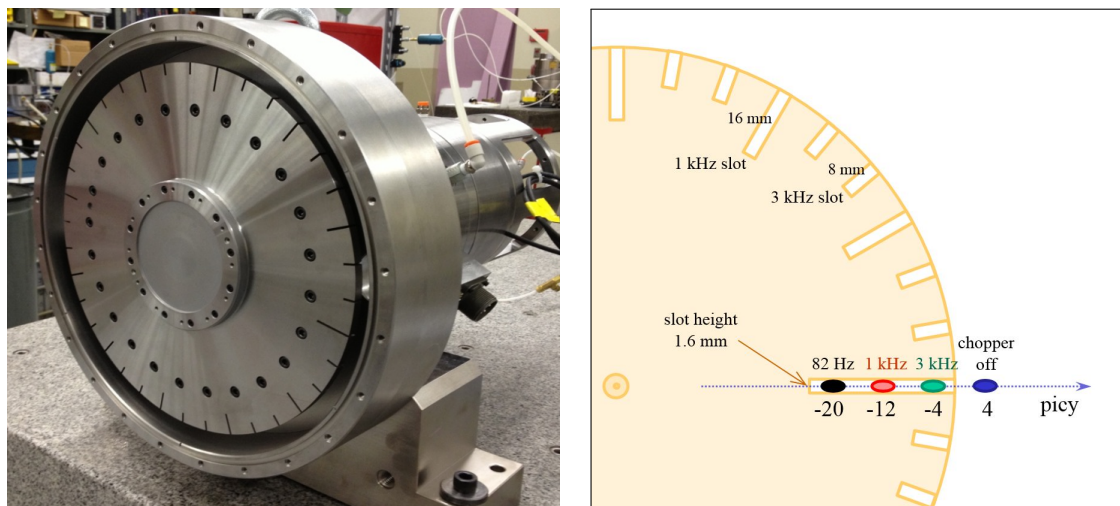


Figure 3.12: Pulse shape from a chopper in a high frequency beam (top). The opening cycle of the heatload chopper (bottom).

### PIC chopper

The second heatload chopper used in this work was made by the American company "Professional Instruments Company" (PIC) and installed in 2013. It uses air bearings and direct cooling and can handle  $\sim 500$  W of white beam.

The PIC chopper is shown in figure 3.13. The design is different: the rotor is a flat disk with a 275 mm diameter and a thickness of 7.6 mm and the rotation axis is parallel to the beam. The disk rotates at 82.19 Hz and has 3 sets of slots on the rim. The chopper can be displaced horizontally and produce 1, 12 or 36 openings per revolution. These regimes correspond to 82.19 Hz, 986.3 Hz and 2958.9 Hz repetition rates of the probe pulses. The opening of the 1.2 mm high slot is 37  $\mu$ s (baseline). Table 3.4 shows the power transmission of the PIC chopper in different modes.



**Figure 3.13:** (a) The PIC chopper. (b) Rotor with the three types of slots along the rim.

picy (mm)	Slots per turn	Frequency (Hz)	Transmission
-20	1	82.19	0.22%
-12	12	986.23	2.4%
-4	36	2958.68	6.9%
4	Chopper off		100%

**Table 3.4:** Pulse frequencies and beam transmission for the different slots in the rotor. picy is the horizontal position relative to the beam.

The rotor is in vacuum with a pressure of  $5 \cdot 10^{-3}$  mbar. The disk rotates in air bearings with a  $7 \mu\text{m}$  cylindrical jacket of air at 7 bar between the bearing and rotation axis. The rotation of the floating disk has nearly no friction and is thus very stable: the rotation jitter is 25 ns (rms).

The chopper is water-cooled through the rotation axis by a water feedthrough. This is possible due to the high pressure of the air bearing. Water is injected directly into the disk and the high pressure in the air bearing prevents water from leaking into the vacuum chamber.

### 3.2.4 High-speed chopper

The high-speed chopper is the crucial element of the beamline. It rotates at 986.3 Hz and can isolate single 100 ps long X-ray pulses or produce longer 0.27-28  $\mu\text{s}$  macro pulses at this frequency. The high-speed chopper and the rotor are shown in figures 3.10 and 3.14. The rotor is an equilateral triangle made of Ti with a small tunnel and a step cut along one of the three edges. The rotation axis is perpendicular to the beam. In single-pulse isolation mode the chopper tunnel is centred on the X-ray beam. The beam is transmitted when the tunnel is parallel to the beam. The tunnel is 126  $\mu\text{m}$  high which produces a 265 ns pulse (baseline). This allows to isolate single X-ray pulses separated by  $265/2 = 132.5$  ns or more. The default pulse separation in ESRF timing modes is 176 ns (figure 3.5).

When 100 ps time resolution is not needed in a pump-probe experiment, longer macro pulses can be made with a gain in pulse intensity. For this, the chopper is shifted horizontally

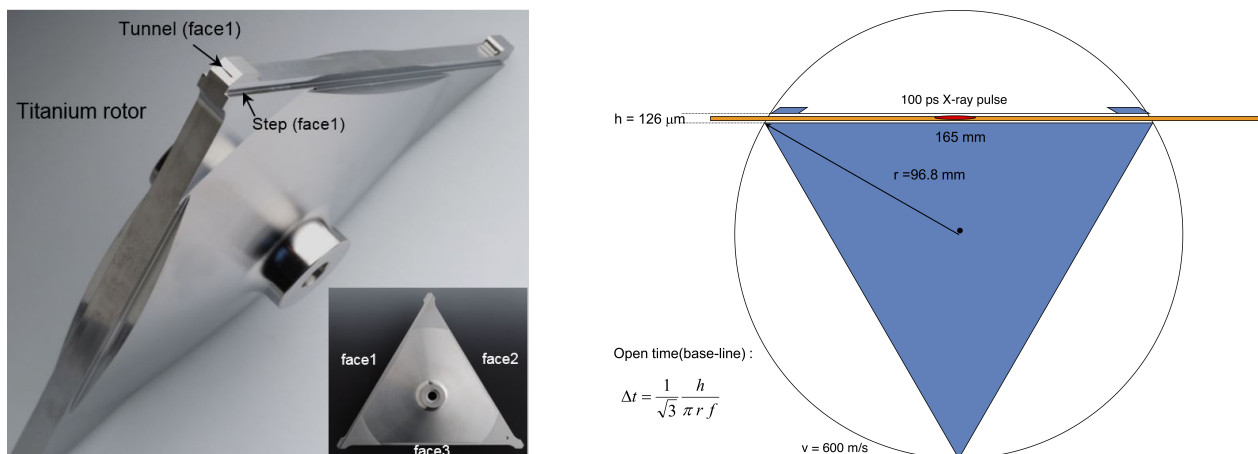


**Figure 3.14:** (a) Rotor of the high-speed chopper. (b) Vertical cross section of the rotor with the slits that define the tunnel. The 100 ps X-ray pulse is shown in the middle. The tangential speed is 600 m/s.

(chopy) with respect to the beam, so that the beam passes above the step (see figure 3.14(a)). The pulse length can be varied by adjusting the chopper height (*chopz*). In the  $7/8 + 1$  bunch mode the single bunch current is 8 mA, whereas a  $1 \mu\text{s}$  pulse integrates 58 mA, i. e. 7 times higher.

The rotor is placed in vacuum and rotates in magnetic bearings at supersonic speed, which causes deformation of the rotor. The tangential speed of the triangle tips is 600 m/s, which leads to tip elongation in the course of rotation. The magnetic bearings provide a very stable rotation with a jitter of 2 ns.

The 100 ps long pulse corresponds to a 30 mm long "needle" travelling at the speed of light. The chopper rotation is much slower and the chopper tunnel is seen as standing still when the X-ray pulse is passing through. The chopper phase is very important for the tunnel to be exactly parallel to the X-ray beam when the pulse is transmitted. In case of a slight de-phasing, the tunnel height would seem smaller for the X-ray pulse. By scanning the tunnel height it is possible to adjust the phase of the TTL synchronisation signal in steps of 2.8 ns until the FWHM of the scan is  $126 \mu\text{m}$ .

### 3.2.5 Mirrors

#### Old Seso mirror (M1)

In the first part of my project, the beam was focused by the toroidal mirror made by Seso. The mirror was installed in 2001 and was used until 2018. It is a 1 m long single crystal of Si cut into a cylindrical shape with a 71.6 mm radius. The mirror is suspended in 3 points and the design is such that gravity bends the mirror longitudinally into a parabola with a radius of curvature of 9.9 km. The resulting difference in height between the central part and the edges is  $8 \mu\text{m}$ .

The mirror surface is coated with a thin layer of platinum. The incidence angle is 2.608 mrad and the cutoff 28 keV. The mirror rejects the higher harmonics of the undulator. The mirror reflectivity was modelled with XOP as shown in figure 3.15 together with the incoming and transmitted spectra. The input parameters to calculate the transmission are: Pt coating with the density of  $16.731 \text{ g/cm}^2$  (79% of the bulk material density); absorption in 1 mm C filter from 3 diamond windows and a 0.2 mm Be window.

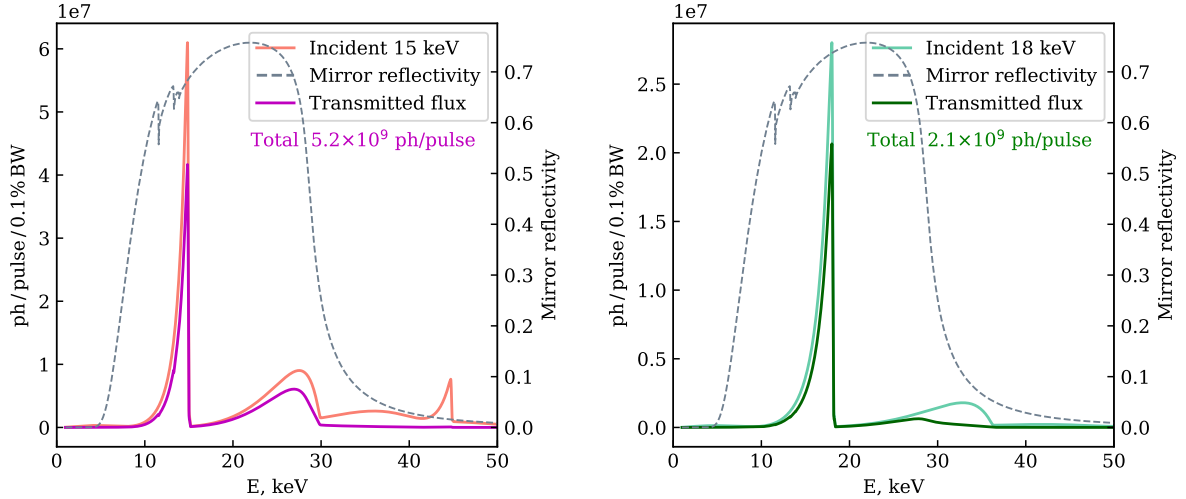


**Figure 3.15:** U17 spectra for 15 and 18 keV operation with and without the reflectivity of the Pt mirror at 2.608 mrad incidence angle. The intensity is shown in photons per pulse (10 mA). Note that at 15 keV the second harmonic is not fully rejected by the mirror; the multilayers are needed to get a clean spectrum at 15 keV.

The mirror is in the optics hutch 33 m ( $p$ ) from the source. It focuses the beam into a  $100 \times 60 \mu\text{m}^2$  spot (H $\times$ V FWHM) at the sample 23 m ( $q$ ) downstream in EH2. The demagnification factor is  $M = q/p = 0.70$ . The mirror curvature is adjusted by a "central-force" that pushes the mirror from below to optimise the focus.

The mirror receives the beam after the heatload chopper and has to withstand about 10% of the full power, 22 W for the U17, of which 20% is absorbed. The cooling system should therefore cool 4.4 W without geometrical distortions. The mirror is made of Si because of its high thermal conductivity in order to minimise shape deformation caused by thermal gradients. On each side of the mirror there are channels filled with liquid InGa with very high thermal conductivity. Water-cooled copper tubes are immersed into the channels to cool the mirror from the side. Then the heat is forced to flow out laterally, not in depth, which minimises longitudinal bending.

### New Thales mirror (M2)

The Thales mirror was installed in EH1 in March 2018. It is a Si mirror with a 600 m long optical surface coated with Pd. When the incidence angle is 2.45 mrad, the cutoff energy is 23 keV. The cylindrical mirror, which has a sagittal radius of 46.07 mm, is bent into a toroid by a standard push-pull bender below the mirror. It bends the mirror longitudinally to a 7.8 km meridional radius.

The vacuum vessel for the mirror is mounted on a very stable hexapod that controls the position and incidence angle. A photo of the mirror taken from the installation is shown in figure 3.16. A massive copper block, the "toboggan", is installed to protect the mirror edge from being hit by the white beam. The cooling principle is the same as for the old Seso mirror. One can see the Cu tubes in the InGa channels along the mirror.

The mirror is placed in EH1 44.45 m ( $p$ ) from the source and 11.79 m ( $q$ ) from the sample. The demagnification  $M = q/p$  is 0.27, which gives a smaller focus than the Seso mirror. The



**Figure 3.16:** (a) Thales mirror in the vacuum vessel in the course of installation in EH1. (b) Polychromatic focus on a YAG screen in front of the sample. The beam dimensions are  $40 \times 60 \mu\text{mH} \times \mu\text{mV}$ .

mirror parameters are related by the focusing equations:

$$r_s = \frac{2pq \sin \theta}{(p + q)},$$

$$R_m = \frac{2pq}{(p + q) \sin \theta},$$

where  $r_s$  and  $R_m$  are the sagittal and meridional radii and  $\theta$  is the incidence angle. The new mirror position is closer to the sample, and the focus is smaller and more stable. The demagnification factor is 0.27 and the polychromatic beam is focused to  $40 \times 60 \mu\text{m}^2$  (H×V). The beam profile at the sample is shown in figure 3.16(b). The beam shape is asymmetric with a diffuse tail below the centre. This is due to spherical aberrations from the (large) horizontal divergence of the beam. The new EBS beam should focus to a round spot of  $25 \times 25 \mu\text{m}^2$  free of aberrations but vertically broadened by the slope error of the mirror.

### Thales mirror commissioning

The new mirror received first beam in May 2018 and I participated in the commissioning. During the commissioning, the focusing was optimised by tweaking the mirror incidence angle and the meridional curvature. The beam stability and the mirror slope error were also measured. Two pairs of slits (horizontal and vertical) were installed at the sample to measure the focus. The mirror incidence angle and meridional radius were optimised to give the best focus, which was measured to  $40 \times 60 \mu\text{m}^2$  (H×V). The optimal incidence angle is 2.451 mrad and the optimal  $R_m = 7.6 \text{ km}$  in agreement with the focusing equation.

The beam stability was also examined by recording a video and analysing the frames. The beam is fluctuating by  $\pm 0.2 \mu\text{m}$  in the horizontal and  $\pm 2 \mu\text{m}$  in the vertical (peak-to-peak). The large vertical amplitude is from vibrations in the floor.

The slope error was measured in the ESRF optics laboratory upon the mirror delivery. The commissioning allowed to re-measure the slope error *in operando* by a simple procedure. I will now describe how we measured the curvature and slope error of the mirror. It is done by measuring the position of the reflected beam, as the mirror is scanned vertically in a small incident beam. When the mirror is displaced vertically, the beam is walking along the length

and probing the local incidence angle. The vertical beam position is measured by a wire monitor 9.4 m from the mirror. The long distance makes the measurements very sensitive. Prior to the measurements, the cylindrical mirror was bent into a toroid and the bending adjusted to give the sharpest focus at the sample 11.7 m downstream. Is the bending radius  $R_m$  consistent with the optical equations? Is the mirror surface spherical along the 600 mm mirror? Can the slope error from polishing imperfections explain the measured focus of  $40 \times 60 \mu\text{m}^2$  (H×V)? The mirror parameters are shown in table 3.5.

The beamline (BL) and mirror coordinate systems are shown in figure 3.17 for a flat mirror inclined at  $\theta_0$ . Note how the deflection point, or take-off point of the beam moves upstream when the mirror is shifted upward. That also shifts the reflected beam upward. The mirror height  $m_z$  is zero when the beam is in the centre of the mirror. We probed the surface in 30 small footprints along the length. For the 600 mm long mirror and the incidence angle 2.45 mrad, the vertical cross section is 1.47 mm. The corresponding step size in  $m_z$  is therefore  $1.47/30 = 0.049$  mm. The vertical beam size at the mirror was then adjusted to 0.49 mm by the primary slit (pvg).

We will now derive the formulae that allow to measure the mirror surface with high precision. Let's consider a flat mirror inclined  $\theta_0$  with respect to the beam. The vertical position of the mirror,  $m_z$ , is zero when the beam hits the centre of the mirror. The reflected beam is deflected by  $2\theta_0$  relative to the incident beam. The position of the deflected beam,  $\text{posz}_0$ , is measured at the distance  $d_0$  from the centre of the mirror. The height of the central reflected beam is:

$$\text{posz}_0 = 2\theta_0 d_0.$$

When the mirror is shifted vertically by  $m_z$ , the take-off point moves upstream in the mirror coordinate system, see figure 3.17(b). The take-off point in the mirror system is:

$$x_D = -m_z/\theta_0.$$

The distance to the wire monitor is:

$$d = d_0 + m_z/\theta_0.$$

Therefore, for a flat mirror the position on the wire monitor is:

$$\text{posz} = 2\theta_0 (d_0 + m_z/\theta_0) = \text{posz}_0 + 2m_z.$$

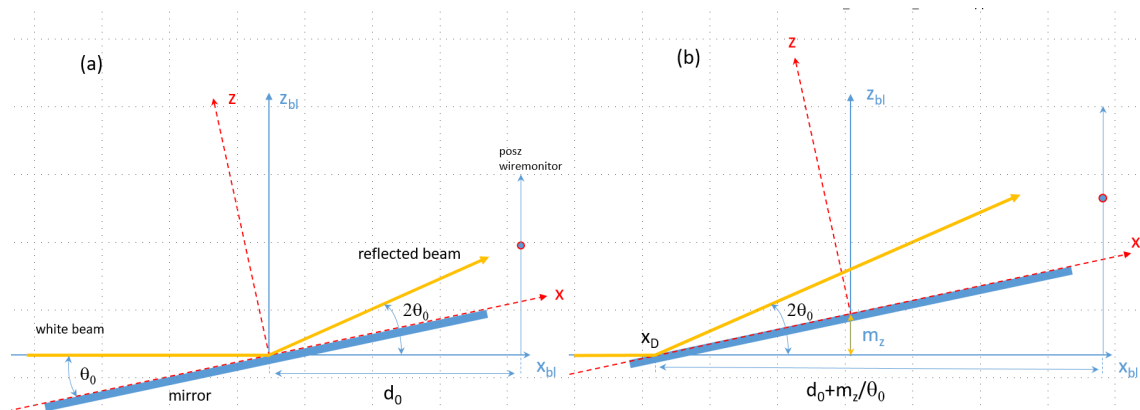


**Figure 3.17:** (a) Flat mirror in the centre of the incident beam (vertical plane,  $m_z = 0$ ). The incidence angle is  $\theta_0$ . The beam is deflected  $2\theta_0$  from the primary beam. The beam position is measured at a distance  $d_0$ . The beamline and mirror coordinate systems  $(x_{BL}, z_{BL})$  and  $(x, z)$  are also defined. (b) Beam geometry with the mirror shifted by  $m_z$ . The deflection point  $x_D$  moves upstream. The reflected beam is shifted up by  $2m_z$ . The distance to the wire monitor is  $d_0 + m_z/\theta_0$ .

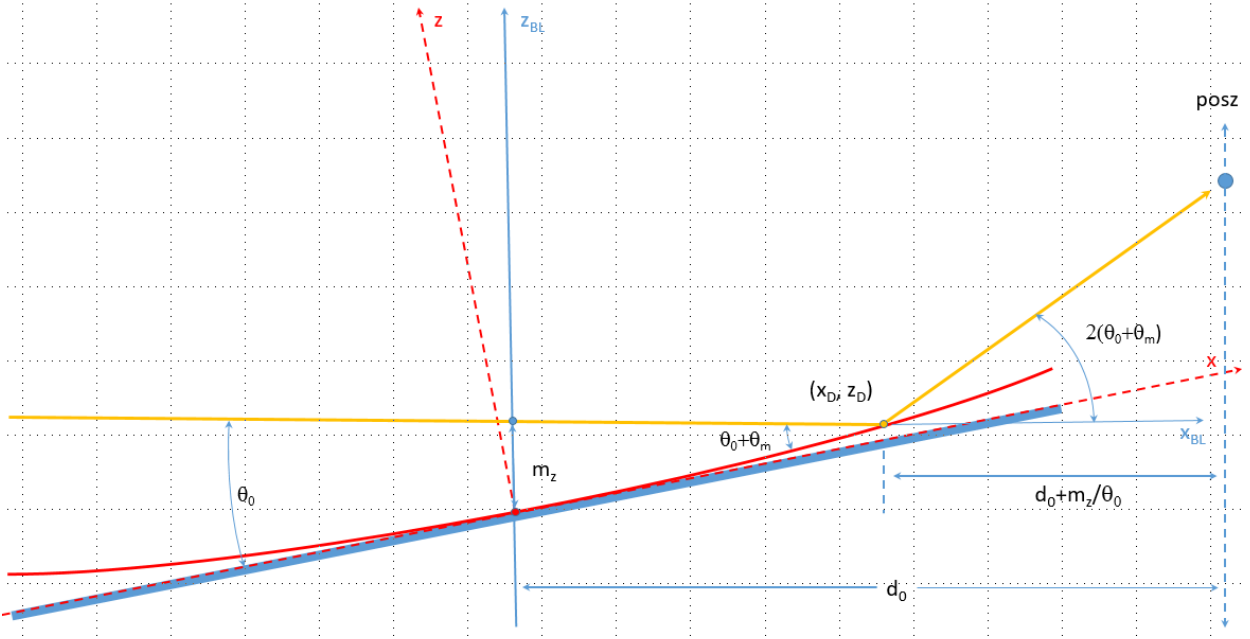


**Figure 3.18:** The spherical mirror surface is shown in red. The deflection point  $(x_D, z_D)$  and take-off angle  $2(\theta_0 + \theta_m)$  is also shown.  $\theta_m$  is the incidence angle in the mirror system. For a large radius  $R_m$ , the wire monitor is approximately  $d_0 + m_z/\theta_0$  from the deflection point ( $< 0.8\%$  error).

So a plot of  $\text{posz}$  vs  $m_z$  is a straight line with a slope  $\alpha = 2$  and intercepting the  $Z$ -axis in  $\text{posz}_0$ .

If the  $(m_z, \text{posz})$  plot deviates from being linear, the incidence angle at the take-off point  $x = -m_z/\theta_0$  is different from the flat mirror case. Denoting the height difference:

$$\delta z = \text{posz}_{\text{exp}} - \text{posz}_{\text{flat}},$$

the change in the local mirror angle is:

$$\delta\theta = \delta z / (2d) = \delta z / [2(d_0 + m_z/\theta_0)].$$

A plot of  $(x, \delta\theta)$  reveals the slope error, i.e. the deviation from a flat surface. The quality of the surface depends on the polishing, bender and mirror support. State of the art slope errors for a short mirror is  $< 0.3 \mu\text{rad}$  (rms), which is achieved by combining mechanical polishing with ion beam polishing. The latter requires that the surface bumps are known from optical measurement with a long trace profiler (LTP).

The figure error of the surface is obtained from the cumulative integral:

$$\delta h(x) = \int_{l_{\min}}^x \delta\theta dx,$$

where  $l_{\min}$  is the upstream extremity of the mirror. The profile of the surface is calculated from

$$h(x) = \int_{l_{\min}}^x (\theta + \delta\theta) dx.$$

The next step is to model a spherical mirror with a radius of curvature  $R_m$ . We will derive an expression for  $\text{posz}$ , as a function of  $m_z$ , which will be fitted to the measured data. That fit will determine  $R_m$  and the distance to the wire monitor. The spherical mirror is shown in

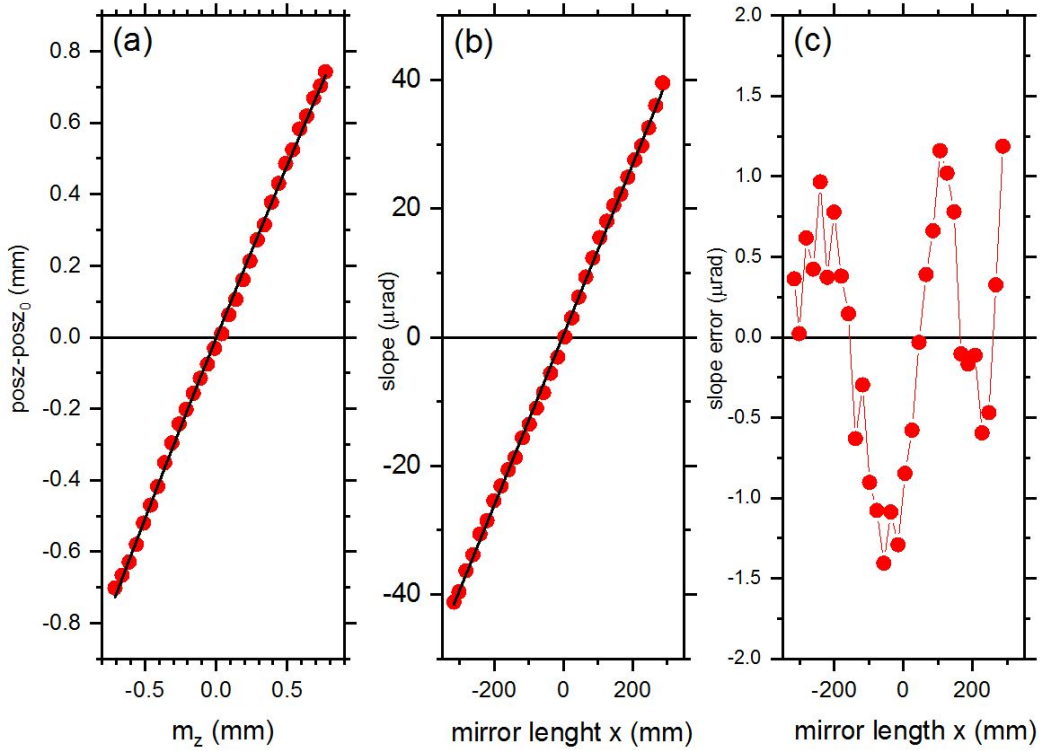


**Figure 3.19:** (a) Position of the reflected beam as a function of  $m_z$ .  $\text{posz}_0$  is the position of the central ray. The black line shows the fit for a spherical surface with  $R_m = 7.57$  km. (b) Local mirror slope deduced from the data in (a). (c) Slope error deduced from the residuals of the slope fit in (b).

figure 3.18. In the mirror system  $(x, z)$ , the meridional circle is positioned at  $(x, z) = (0, R_m)$  and described by:

$$x^2 + (z - R_m)^2 = R_m^2.$$

The  $z$  vs  $x$  function is:

$$z = R_m - \sqrt{R_m^2 - x^2} \approx \frac{1}{2R_m} x^2.$$

The slope of the spherical mirror is:

$$z' = \frac{dz}{dx} = \frac{x}{R_m}.$$

The tricky part is to determine the take-off point  $(x_D, z_D)$  of the beam for the parabolic surface. In the mirror system  $(x, z)$ , the incident beam is given by the straight line

$$z = -\tan \theta_0 x - m_z.$$

The intercept with the parabola is obtained from the expression of the roots of a second order polynomial:

$$x_D = \left( \sqrt{\theta_0^2 - \frac{2m_z}{R_m}} - \theta_0 \right) R_m \approx \frac{-m_z}{\theta_0}.$$

The error in the approximation is greatest at the end-points of the mirror where it is  $< 0.8\%$ . Note that the deflection point is essentially the same as for a flat mirror. That is due to the fact that  $R_m$  is much larger than the length of the mirror. The take-off height is

$$z_D = \frac{1}{2R_m} x_D^2 \approx \frac{1}{2R_m} \frac{m_z}{\theta_0}.$$

Note that the  $z_{BL}$  coordinate of  $z_D$  is  $z_{BL} = 0$  since the height of the incoming beam defines the zero in the BL system. The local mirror slope at the deflection point  $(x_D, z_D)$  is:

$$\theta_m \cong \frac{x_D}{R_m} = -\frac{m_z}{R_m \theta_0}.$$

The total incidence angle for a given  $m_z$  is:

$$\theta = \theta_0 + \theta_m = \theta_0 - \frac{m_z}{R_m \theta_0}.$$

The distance to the wire monitor is:

$$d = d_0 - x_D = d_0 + \frac{m_z}{\theta_0},$$

and the position of the beam:

$$\text{posz} = 2\theta \cdot d = 2 \left( \theta_0 - \frac{m_z}{R_m \theta_0} \right) \cdot \left( d_0 + \frac{m_z}{\theta_0} \right) = 2\theta_0 d_0 + 2 \left( 1 - \frac{d_0}{R_m \theta_0} \right) m_z - \frac{1}{R_m \theta_0^2} m_z^2.$$

The above equation shows that  $\text{posz}$  is a second order polynomial in  $m_z$ . The coefficients can be estimated from table 3.5. The first and second terms are  $\sim 0.980$  and  $\sim 0.022$ , respectively. The measured data  $\text{posz}_{\text{exp}} = \text{posz} - \text{posz}_0$  is shown in figure 3.19(a).  $\text{posz}_0$  is the position of the central ray, i.e.  $d_0 \theta_0$ . In the  $(m_z, \text{posz})$  fit,  $\theta_0$  and  $d_0$  were fixed at  $2.45 \cdot 10^{-3}$  and 9369 mm, respectively. That gives  $R_m = 7.57 \pm 0.05$  km. This result agrees with the optical equation for focusing in the meridional direction:

$$R_m = \frac{2pq}{(p+q) \sin \theta},$$

which gives  $R_m = 7.60$  km. That shows the validity of the approach.

$p$ (mm)	$q$ (mm)	$M$ (mm)	$\theta_0$ (mrad)	$r_s$ (mm)	$R_m$ (km)	$d_0$ (mm)	$\text{posz}_0$ (mm)
44540	11789	0.265	2.450	46.07	7.543	9369	45.01

**Table 3.5:** Parameters for the Thales Toroidal mirror on ID09 (ESRF).

The local mirror angle is determined from the  $\text{posz}$  data as:

$$\theta_m = \frac{\text{posz}}{2(d_0 + \frac{m_z}{\theta_0})} - \theta_0,$$

and the result is shown in figure 3.19(b). The deviation from a straight line is ascribed to the slope error from the polishing and to a lesser extent, errors in the mirror bending. The slope error is shown in figure 3.19(c). The rms slope error is  $\alpha_s = 0.69 \mu\text{rad}$  over the full length  $-300 < x < 300$  mm of the mirror, which is greater than the  $0.5 \mu\text{rad}$  quoted in the technical specifications. The surface and figure error are shown in figure 3.20. The focus size  $F_z$  can be approximated by:

$$F_z = \sqrt{(\alpha p)^2 + (MS_z)^2}.$$

With  $\alpha = 0.69 \mu\text{rad}$  (rms),  $p = 11789$  mm,  $M = 0.265$  and  $S_z = 0.085$  mm (rms), we get  $F_z = 0.016$  mm (rms) or  $F_z = 0.039$  mm (FWHM). Experimentally we find 0.060 mm with the full beam (phg 5, pvg 0.5). The larger measured value is from spherical aberrations since the toroidal shape deviates from a perfect ellipsoid.

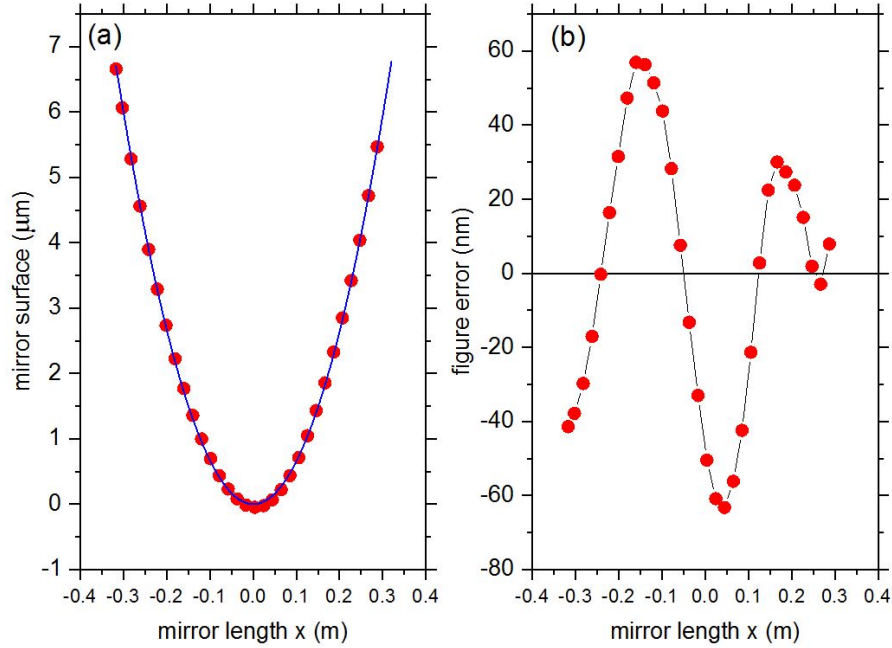


**Figure 3.20:** (a) Mirror surface from the integral of the measured slopes. The solid line is the surface for a spherical mirror with  $R_m = 7.57$  km. (b) Deviation from the spherical surface, i.e. the figure error.

### 3.2.6 Multilayer monochromators

Si monochromators select energies in a rather narrow bandwidth, e.g.  $\Delta E/E = 1.4 \cdot 10^{-4}$  for Si(111). High energy resolution comes at the cost of X-ray intensity, so many photons are rejected by the Si monochromator. As high pulse intensity is very important for pump-probe experiments, they are sometimes done with the pink beam without any monochromator. The pink spectrum is rather sharp but asymmetric with a long tail at low energies (figure 3.21). Moreover the second harmonic is not fully rejected by the mirror reflectivity. It is a drawback for wide angle X-ray scattering experiments because of the uncertainty in the  $q$  definition and the energy dependence of the detector response and absorption in the sample. The scattering at a given  $2\theta$  angle comes from different wavelengths so that high- $q$  oscillations in the scattering signal are dampened.

15 keV (U17, harm 1)	ph/pulse
Pink, 5% bw	2.7E+09
Ru, 3.2% bw	4.3E+08
Si(111), 0.014% bw	5.9E+06

**Table 3.6:** Pulse intensities for the beam modes on ID09 (5 mA per bunch).

Multilayer monochromators are made by the deposition of alternating layers of two materials, which creates interfaces that act like interatomic planes in a Bragg crystal. The  $d$  spacing of the structure is typically a few nm. The larger lattice spacing means that fewer planes are activated by the incoming beam before extinction. As a result, the bandwidth is larger than for a Si crystal. The intensity gain can be up to 2 orders of magnitude.

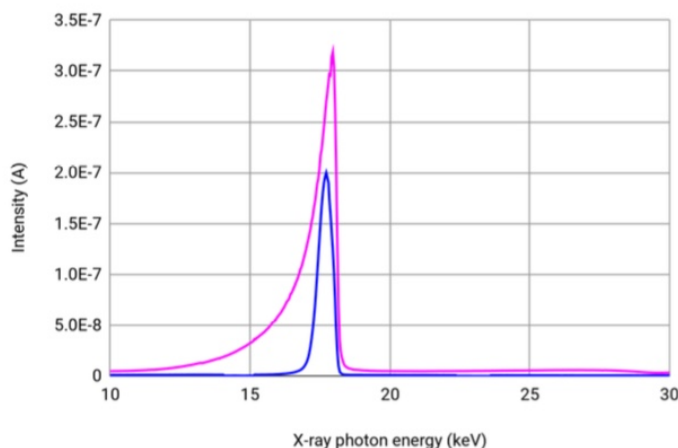


**Figure 3.21:** U17 spectrum (pink) and the ruthenium multilayer spectrum (blue). The spectra were measured with a channel-cut monochromator on the diffractometer. The symmetric Ru spectrum is important for TR-WAXS since the central energy and  $q$  scale are well defined. This is particularly important for high  $q$ -range experiments where the asymmetry of the pink beam smears out the  $q$  definition. Finally the multilayer kills the second harmonic by destructive interference.

In addition to the Si(111) and Ge(111) channel cut monochromators, ID09 has a double-crystal multilayer monochromator. The Si substrates have two stripes of different coatings which can be moved into the beam by a horizontal translation. The multilayer parameters are summarised in table 3.7. The Ru multilayers were used in this work for 18-19 keV. The coating is composed of  $[\text{Ru}/\text{B}_4\text{C}]_{60}$  and produces a 1.9% pseudo-gaussian spectrum (figure 3.21). The flux is reduced after the ML by a factor of about 5, compared to 460 for Si(111). The spectrum transmitted by the ML is almost symmetric with a  $\sim 2\%$  BW, which does not smear out the  $q$  definition in scattering and it does not reduce the amplitude of high- $q$  oscillations.

Name	Composition	$d$ (Å)	dE/E (%)	E-range (keV)
Ruthenium	$[\text{Ru}/\text{B}_4\text{C}]_{60}$	40.4	1.89	11.4–21.0
Tungsten	$[\text{W}/\text{B}_4\text{C}]_{100}$	26.0	1.55	20.2–27.5

**Table 3.7:** Multilayer compositions and bandwidths. The Ru multilayer has 60 layers, the W one has 100.

### 3.2.7 Sample environment

#### Huber goniometer

Most of the beamline elements are motorised and the stepper motors are controlled by the ICEPAP controllers developed at the ESRF. The motor positions are driven from SPEC, the C-based control software for beamlines. The beamline coordinates are assigned as follows: the  $x$  axis is directed along the X-ray beam; the  $y$  axis is horizontal with the positive direction outwards the storage ring; the  $z$  axis is directed upwards. The goniometer from Huber has three translation axes `gonx`, `gony` and `gonz` and one rotation axis `hphi` ( $y$ ). A sample can

be mounted on the goniometer using a goniometer head, which has the two complementary rotational axes ( $x, z$ ) adjusted manually in the range  $\pm 20^\circ$ .

One of the challenges in a time-resolved pump-probe experiment is to overlap the X-ray beam, sample and laser at the same point. In order to find the X-ray position ( $y, z$ ), a sharp needle is mounted parallel to the  $y$  axis with the tip in the centre of rotation. The approximate X-ray beam position is known, and the tip is first scanned across the beam and centred vertically, then horizontally. The needle position is monitored with a Basler camera on the microscope and the beam position is marked with a cross-hair.

### Liquid jet

For solution experiments the liquid sample needs to be flown through a nozzle that creates a laminar flow. The sample is taken from a bottle by a pump, flushed through the nozzle and then returned to the bottle. For reversible reactions, the sample is circulated in a closed loop and returned to the same bottle. The nozzle is mounted on a circular chamber with kapton windows preventing evaporation and splashing. The jet system is shown in figure 3.22.

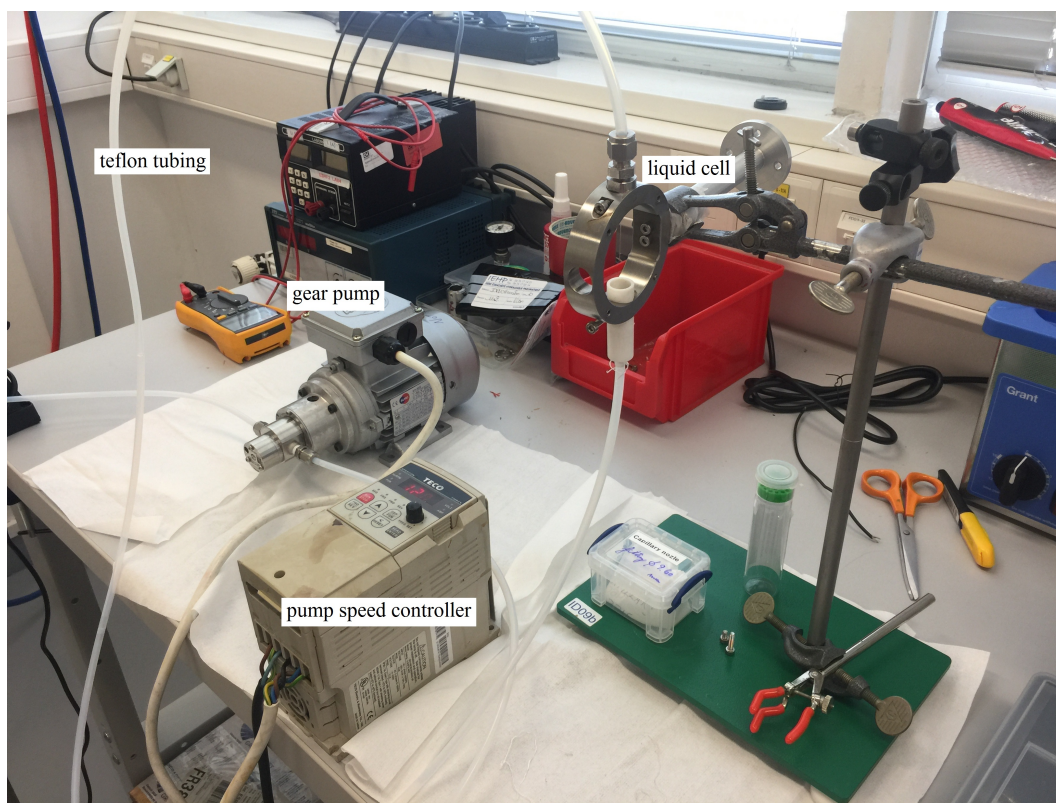


**Figure 3.22:** Liquid jet with the Fluid-o-Tech rotary pump and the jet holder (liquid cell).

Two pumps were used for the experiments in this thesis. The first is the peristaltic pump from BioBlock. In this pump a soft Si tubing is squeezed between rotating elements that push the liquid mechanically through.

The second pump, used in most experiments in the thesis, is the magnet rotary pump from Fluid-o-Tech. The liquid is pumped by a magnetic head to which teflon tubing is attached with Swagelok connectors. The advantage over the peristaltic pump is pulsation-free pumping and the possibility to use teflon tubing which is more resistant to toxic chemicals.

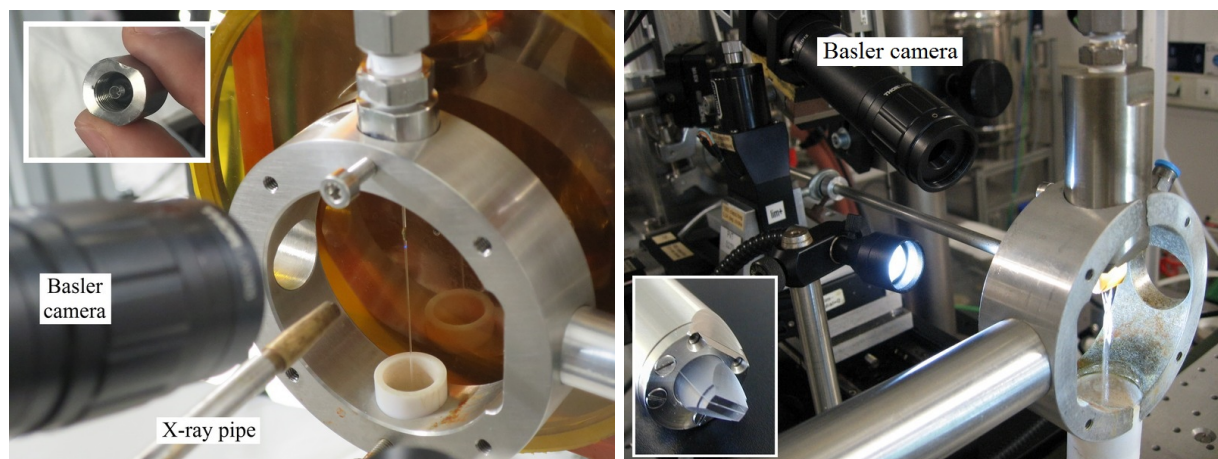


**Figure 3.23:** (a) Liquid cell mount with a capillary nozzle. (b) Liquid cell with the Swiss nozzle (Kyburz) producing a  $360\ \mu\text{m}$  flat jet.

Two types of nozzles were used in the experiments: the capillary nozzle producing a cylindrical jet and the sapphire nozzle producing a flat jet. Both nozzles can be attached to the tubing with Swagelok connectors.

The capillary nozzle consists of a cylindrical stainless steel holder with a circular hole where a capillary can be put through. Two rubber O-rings are put around the thick part of the capillary before screwing the nozzle onto the tubing (figure 3.23(a)). Glass capillaries are more flexible than quartz ones and are preferable as the nozzle can be tightened enough to provide a good sealing without breaking the capillary. The nozzle is assembled each time with a new capillary and the liquid jet diameter can be chosen according to the needs of the experiment. However, the capillary's inner diameter varies and might be slightly different from specified and has to be verified with an optical microscope. The cylindrical jet has some drawbacks. One issue is the laser focusing inside the jet, which might create problems defining the actual power density. For a certain number of liquids (e.g. cyclohexane), the focusing effect is so strong that the sample starts evaporating even at low laser pulse energies.

The sapphire nozzle is fabricated as a  $360\ \mu\text{m}$ -thick slit made from two parallel sapphire crystals (figure 3.23(b)). The very smooth surface of the crystals provides a laminar flow. The advantage of the flat jet from the nozzle is that it is free from laser focusing. The flat surface is also preferential for emission spectroscopy experiments, where the flat jet is put at  $45^\circ$  to the X-ray beam. Such a geometry is optimised for increasing the X-ray emission intensity in the direction of the crystal analysers. One of the drawbacks of the sapphire nozzle is that it is expensive and has to be cleaned regularly. Also, as the cross section of the flat jet is much bigger because of its width, the gear pump needs to operate at a higher speed in order to provide the same flow speed as for a cylindrical jet. As the magnetic pump heads wear out, the jet flow is sometimes too slow even at the maximum speed of the pump.

The jet flow speed is important for high repetition rate pump-probe experiments as the sample has to be refreshed between the successive pump events. Let's calculate some numbers for the flow speed estimation. If the laser vertical spot size is  $300\ \mu\text{m}$  and the experiment repetition rate 1 kHz, the sample volume has to move down by at least  $300\ \mu\text{m}$  in 1 ms, which corresponds to the flow speed of 0.3 m/s. In order to estimate the flow speed  $v$  it is possible to measure how many ml of liquid are flown through the nozzle with a cross section  $S$  in a certain time  $t$ :

$$V[\text{ml}] = S[\text{mm}^2] \cdot v[\text{m/s}] \cdot t[\text{s}].$$

For example, if 25 ml of solution is pumped through a 0.5 mm capillary jet in 30 s, the speed

can be calculated as  $v = V/St = 25/0.25\pi \cdot 30 \approx 1$  m/s. The numbers given in this example are the common values used in the experiment.

### 3.2.8 Detectors

ID09 is currently using three detectors: the Rayonix MX170-HS for X-ray diffraction and scattering, the Ketek AXAS M2 Si drift diode (SDD) for XES in Johann geometry and the Maxipix detector for XES in the von Hámos setup.

#### Rayonix MX170-HS

Time-resolved difference scattering is very weak compared with the total scattering. Typically 1000-10000 single-pulse exposures are acquired at 986.3 Hz and then the detector is read out. So in order to provide enough counts in one image and resolve small differences between images, the exposure time is typically 1 – 10 s. The detector therefore has to have low dark current and readout noise.

It is needless to say that a large detection area is beneficial for recording the scattered intensity up to high  $q$ , typically  $8 - 12 \text{ \AA}^{-1}$ . The intensity in a pixel varies by  $\sim 3$  orders of magnitude in the liquid peak area and at high  $Q$ . For this reason the detector has to have a high dynamic range and very low noise.

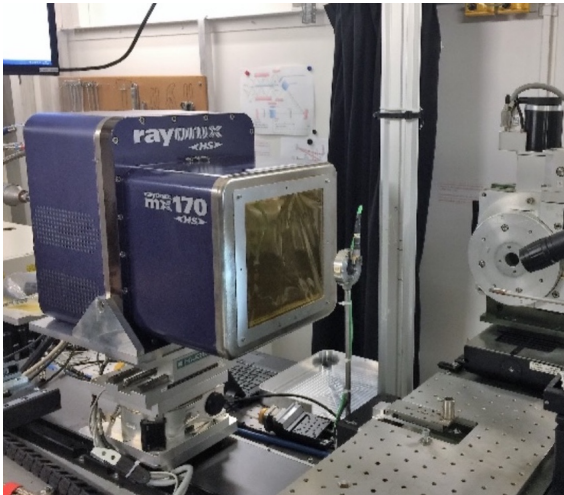


**Figure 3.24:** Rayonix 170HS on the translation stage detx (Feb 2016).

Parameters	Rayonix 170 HS
Detection area (mm <sup>2</sup> )	170 × 170
CCD area (mm <sup>2</sup> )	58 × 58
Number of pixels	3840 × 3840
Pixel size: Phosphor (μm)	44.3
Point-spread-function (μm; FWHM)	100
Dark current (ADU/pixel/s)	0.003
Readout noise (electron/pixel; rms)	4.0
Dynamic range (ADC)	16 bit
Software offset	10
Readout time 1 × 1 binning (s)	0.40
Readout time 2 × 2 binning (s)	0.10
Logfile (reading motors and diodes)	0.2
Dead time 2 × 2 binning (s/image)	0.7

**Table 3.8:** Rayonix parameters.

The Rayonix MX170-HS was installed in February 2016 and was used in all scattering experiments in this thesis. It is a phosphor based CCD detector with a large  $170 \times 170 \text{ mm}^2$  detection area. The detection area is a  $40 \text{ μm}$ -thick phosphor screen protected by a polymer-coated Be window from light in the hutch. The screen is made of  $\text{Gd}_2\text{O}_2\text{S}$  with Tb impurities that acts like a scintillator. The main emission line of  $\text{Gd}_2\text{O}_2\text{S}:\text{Tb}$  is at 544 nm. When X-rays hit the phosphor screen, the X-ray signal is converted to an optical image which is guided by  $2 \times 2$  fiber optic tapers to 4 CCD chips that are read out in parallel. The CCD sensors have  $3840 \times 3840$  pixels which can be binned from  $1 \times 1$  to  $10 \times 10$ . The detector is usually operated in  $2 \times 2$  binning, which corresponds to a pixel size of  $88.54 \text{ μm}$  on the phosphor screen.

When an X-ray photon hits the screen, the green light created in the screen spreads into a round spot with a finite size. This response function defines the detector spatial resolution

and is called the point spread function (PSF). In the standard  $2 \times 2$  binning mode, the Rayonix has a PSF of  $100 \mu\text{m}$ .

The Rayonix is an integrating detector. As opposed to photon-counting detectors, it can not discriminate X-ray photons with different energies, but at this price it has a higher dynamic range, which is essential for high count rate experiments, e.g. time-resolved solution scattering or single-pulse Laue diffraction, where the intensity in one pixel can exceed  $10^4$  photons per pulse. The Rayonix dynamic range is 16-bit, and one pixel saturates at  $2^{16} = 65536$  ADU (analogue-to-digital units). The analogue-to-digital conversion ratio is 1.1 ADU / incident X-ray at 18 keV. The linearity is shown in figure 3.25(a), which suggests that the Rayonix should only be exposed to  $\lesssim 60\%$  of the saturation level. The phosphor screen detection quantum efficiency (DQE) is  $\sim 0.6$  at 18 keV, meaning that the photon is detected with a 60% likelihood. The DQE as a function of X-ray incident energy is shown in figure 3.25(b).

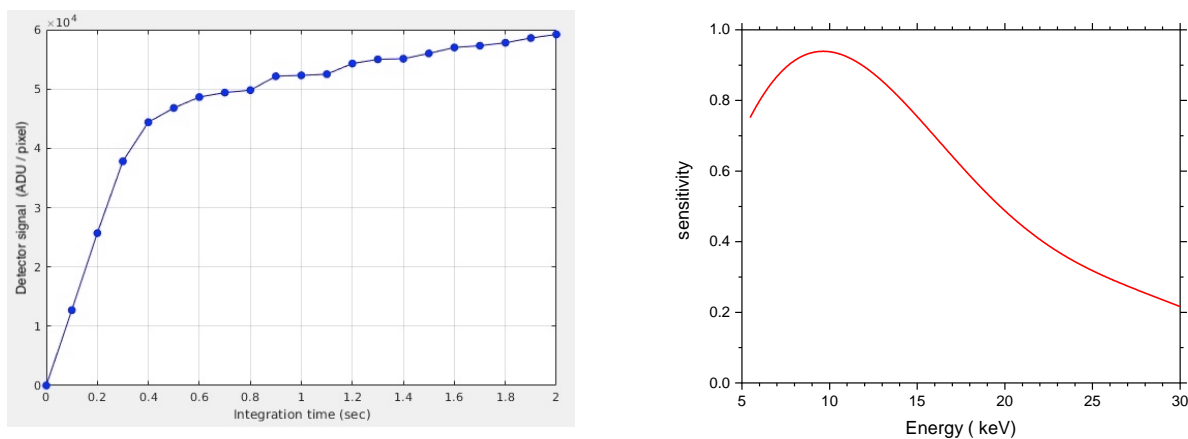


**Figure 3.25:** (a) Linearity check of the Rayonix detector. Above 40000 cts/pixel, the detector starts to saturate. (b) Sensitivity of the  $40 \mu\text{m}$   $\text{Gd}_2\text{O}_2\text{S:Tb}$  phosphor screen vs energy. At low energies the sensitivity is reduced by absorption in the detector window and by readout noise.

The `detx` translation stage allows to move the Rayonix as close as  $d = 35 \text{ mm}$  from the sample. When the detection area is centred on the incident beam and thus on the scattering pattern, the radius of the inscribed and circumscribed circle is  $85 \text{ mm}$  and  $120 \text{ mm}$ , respectively. At the minimum sample-to-detector distance, the scattering can be recorded up to  $\theta_{in} = 67.6^\circ$  at the detector edge and  $\theta_{out} = 73.7^\circ$  in the corners of the detector. At  $18 \text{ keV}$  the corresponding  $q = 4\pi \sin(\theta/2)/\lambda$  values are  $10.15 \text{ \AA}^{-1}$  and  $10.94 \text{ \AA}^{-1}$ , respectively. Having high  $q$  data allows to see more details in the scattering difference and to normalise laser ON and laser OFF images more accurately before subtraction for isolating the laser induced part.

The two  $q$  ranges are given to distinguish the data recorded with different statistics. There are less pixels in the corner regions and that data will have bigger error bars. The pixel intensity decreases because of the structure factor and the smaller solid angle per pixel for higher scattering angles. Within the inscribed scattering cone this is partially compensated by the increase in the number of pixels contributing to the azimuthal averaging at higher angles.

The CCDs are cooled to  $-80^\circ\text{C}$  by a closed loop compressor. In comparison with the FReLoN detector, the Rayonix has a higher frame rate ( $10 \text{ Hz}$  vs.  $1.85 \text{ Hz}$  in  $2 \times 2$  binning), a lower dark current which can be neglected for up to tens of seconds due to the cryo cooling.

Higher acquisition frame rates up to 100 Hz can be achieved by increasing the binning to  $10 \times 10$ . Usually the detector is used in a  $2 \times 2$  binning mode in time-resolved experiments.

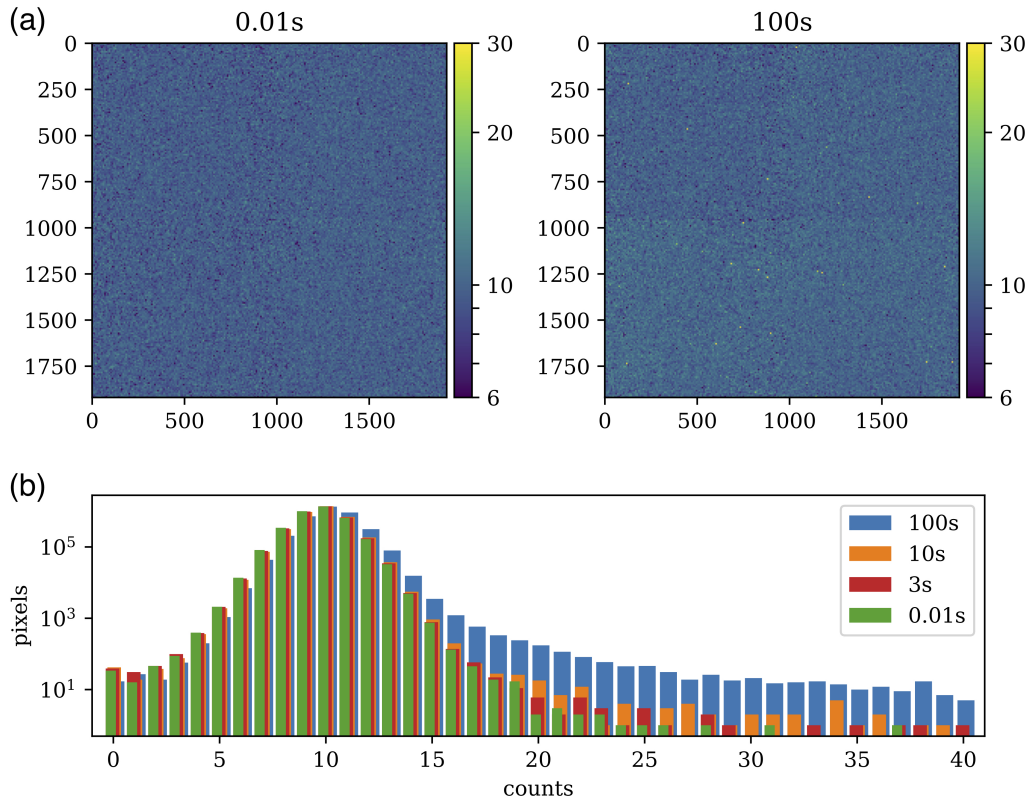


**Figure 3.26:** Time dependence of the dark current. (a) For the short 0.01 s exposure, the image is dominated by the readout noise. The white pixels in the 100 s image are zingers from the optical fibers (see below). (b) Histogram of pixel counts from readout and dark current for four exposure times. The exposure time most frequently used in this project was  $\sim 3$  s, where the dark current is negligible. The detector software adds a 10 ADU offset to allow plotting images on a logarithmic scale, and this offset is included in the plots.

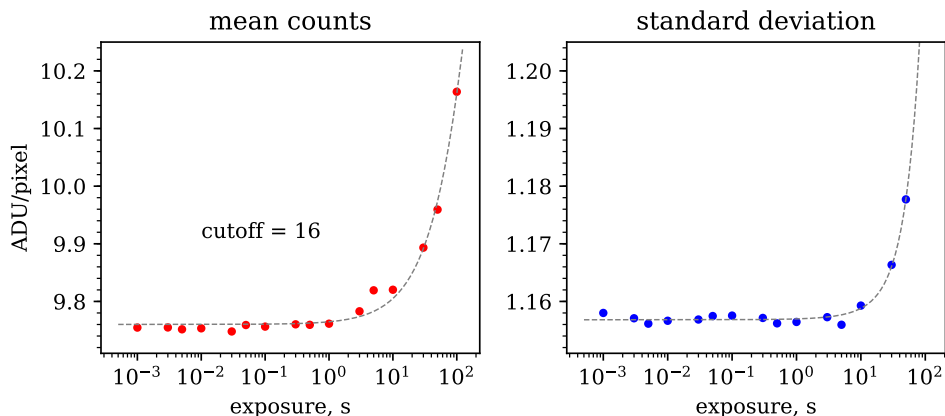


**Figure 3.27:** Dark current and standard deviation of an average pixel vs exposure time. To avoid including hot pixels and zingers, counts  $> 16$  ADU are neglected in the statistics. The actual software offset is 9.75. Dark current is insignificant for exposures up to 10 s.

If an image is acquired without exposing the detector to the X-ray beam, one should ideally see zero everywhere. The real pixel counts have a poissonian distribution. An offset

value of 10 counts is added to each pixel by the built-in software. We have investigated the effect of the dark current as a function of exposure time. We plotted the count distribution, average counts/pixel and standard deviation, for a series of dark images acquired for 1 ms – 100 s (figure 3.26). We wanted to determine at which acquisition time the average pixel count and standard deviation curves "take off". This exposure time is 10 s as shown in figure 3.27. The hot pixels that start to appear in the dark images are mainly due to the presence of zingers. Zingers are spots in the images from photons generated by radioactive thorium in the taper optics, or by cosmic rays passing through the detector.

When measuring a very weak signal  $dS$  on a huge background  $B$ , the counting noise is essentially  $\sqrt{B}$ . The signal-to-noise ratio ( $S/N$ ) in one image is then  $dS/\sqrt{B}$ . For a laser induced difference measurement with near identical backgrounds in the two images (laser ON and laser OFF images), the  $S/N$  ratio is:

$$S/N = \frac{dS}{\sqrt{2B}}.$$

When the difference is measured  $N$  times, the  $S/N$  ratio of the average image is:

$$S/N = \sqrt{N} \frac{dS}{\sqrt{2B}}.$$

The  $S/N$  ratio is then linear in  $dS$  and  $\sqrt{N}$ . That highlights the importance of maximising the signal  $dS$ ; i.e. maximising the number of excited molecules with the laser. Collecting many images is less efficient since the the  $S/N$  scales with  $\sqrt{N}$ . As for the pulse intensity  $I_0$ , the  $S/N$  ratio is also (only) proportional to  $\sqrt{I_0}$ . In practice the laser excitation might be difficult to increase due to radiation damage and jet instabilities at high laser power.

### Ketek Si drift diode

The Ketek AXAS-M1 detector was used for XES detection in the Johann setup. It is a silicon drift detector, which is a single element (0D) photon-counting energy dispersive detector. Si drift diodes (SDD) are sensitive to the X-ray energy and can accept high photon count rates up to  $10^6$  counts/s.

The  $\emptyset$  10 mm detection area is made of high purity silicon which is Peltier cooled. Each incoming X-ray photon produces ionisation in Si dependent on the energy. The charge drifts through a series of ring electrodes to the collection electrode where it is converted to voltage.

The Ketek detector can detect X-rays with photon energies in the range between 0.2 keV and 30 keV. The photon energy is resolved to a precision of typically 123 eV for Mn  $K\alpha$  photons ( $\sim 6$  keV). The detector is operated by the Mercury software. It allows to collect X-ray spectra, choose a region of interest (ROI), i.e. a range of energy channels corresponding to the Fe  $K\alpha$  or  $K\beta$  emission lines for example and sum up the photon counts in that ROI. The energy discrimination allows to filter out unwanted contributions from scattering from the sample, cosmic rays etc.

### Maxipix 5x1

The Maxipix detector was used to measure XES in the von Hámos setup. It is a hybrid pixel detector with a 2D detection area. The Maxipix is a photon counting detector. As such it has zero readout noise and is perfectly linear. It has a single energy threshold that can discriminate photon energies higher than the threshold. It has a  $71 \times 14$  mm detection area

from five  $256 \times 256$  pixel modules ( $1280 \times 256$  pixels total). The pixel size is 55 microns. There is a  $110 \mu\text{m}$  (2 pixel size) gap between the modules. The detector can collect 295 frames per second (fps) and can be gated down to  $1 \mu\text{s}$ . The quantum efficiency is 0.90 at 7 keV (reduced from 0.9999 from absorption in the  $80 \mu\text{m}$  Mylar window).

### 3.2.9 Laser/X-ray timing

In order to synchronise the beamline electronics, the N354 timing card is used. It receives two input signals: a sinusoidal signal from the RF clock of the storage ring (SR) at 352.2 MHz and a TTL pulse from the orbit clock at 355 kHz (the 992-nd sub-harmonic of the RF frequency). The latter is used as an absolute phase signal, a bunch marker, that puts a time tag on the single bunches in the SR. This allows to centre the choppers automatically on the single bunch in the  $7/8 + 1$  mode for example.

From these inputs, a number of frequency divided output signals are generated for triggering beamline equipment. The card runs at the RF clock frequency and uses a chain of dividers to generate clocks at lower frequencies classified into 3 groups (figure 3.28). The N354 also has a burst mode for  $N$  pulses.

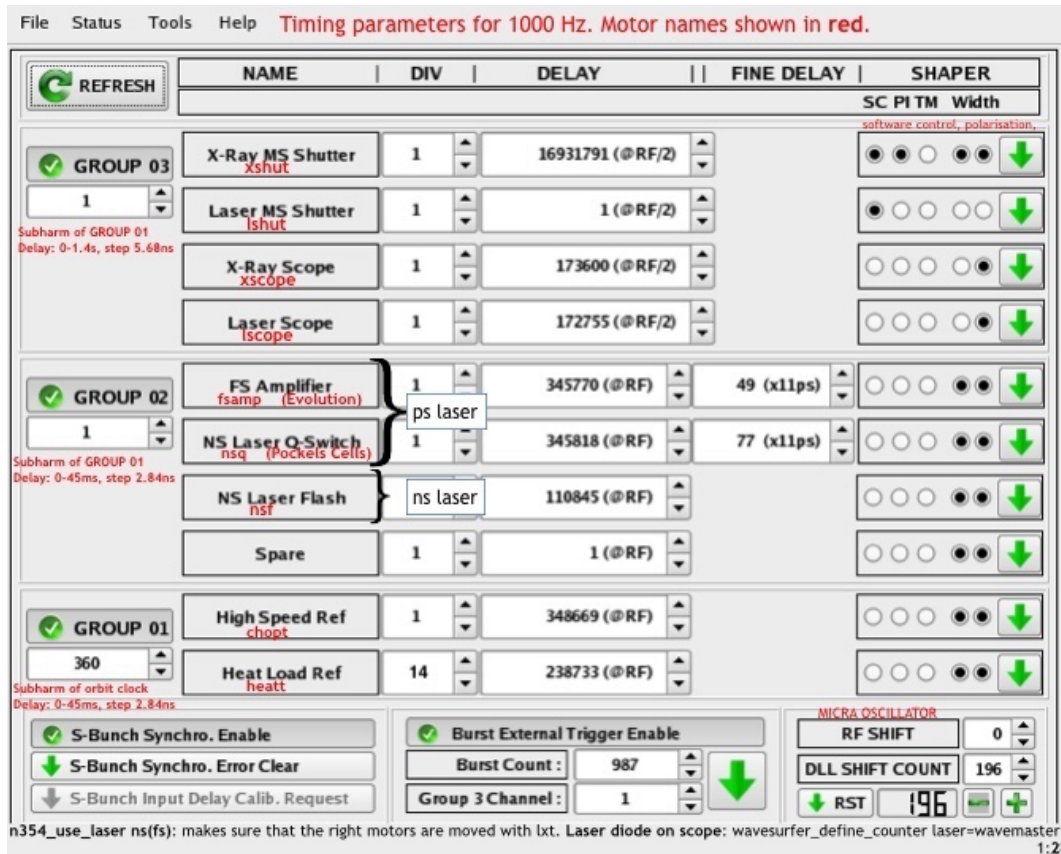


**Figure 3.28:** GUI for RF synchronisation (N354). The orbit frequency is divided and time shifted for the various instruments on the beamline.

As an example, group 1 has 2 channels for chopper synchronisation. First the orbit frequency is divided by 360 to get 986.3 Hz. The second channel is further divided by 14 to get the frequency of the Eybert chopper 70.45 Hz. The next column ("delay", figure 3.28) shows the time delay in units of 2.84 ns, the RF cycle, that is added to the chopper frequencies for the synchronisation on the single bunch.

The fs laser runs at 88.05 MHz with a phase that can be shifted very precisely with respect to the orbit clock. The RF phase shifter is 8 bit, which means that the smallest time delay step in the RF clock is  $2.84 \text{ ns}/2^8 = 11.1 \text{ ps}$ .

In order to check the time delay between the laser and the X-ray pulses, a GaAs detector is used that is sensitive to both X-rays and optical light. A scatterer is put on the sample position so that the scattered laser light hits the GaAs detection area. The X-rays hit the GaAs directly. The signal from the GaAs is recorded on the X-ray oscilloscope that is triggered by the TTL signal "xscope". The time delay of the laser pulse relative to the X-ray pulse is measured. The laser timing is then moved to the desired time delay (the X-ray pulse is not changed).

### 3.2.10 Laser system

#### Femtosecond laser

The Ti:sapphire laser produces 85 fs pulses at 800 nm that are synchronised to the RF/4 clock at 88.05 MHz. These pulses are very weak, nJ, and need amplification.

The oscillator pulses are very short in time. The field intensity is very high and to amplify the pulse you need to stretch it in time. The process is called chirp-pulse-amplification. The pulse enters the amplifier and is then chirped by a grating, (also called a stretcher) since the spectrum is distributed in space (dispersed). The oscillator pulse is stretched from 85 fs to  $\sim 100 \text{ ps}$ , i.e. by a factor of  $\sim 1000$ .

The stretched pulse goes into the 1 kHz pulsed amplifier, which is a cavity with a 20 W pump laser with green light. The green pump is sent onto a Ti:sapphire crystal, which is seeded by the stretched oscillator pulses to coherently emit and amplify the photons by stimulated emission. This process amplifies the oscillator pulses  $10^6$  times!

The amplified oscillator pulse leaves the cavity and goes back to the grating. The pulses are 100 ps long and need to be re-compressed to 1.2 ps. It has to be compressed by 2 reflections in the compressor grating. The amplified pulse has now 4 mJ at 800 nm.

#### TOPAS

The 1 kHz amplified laser produces 800 nm pulses which are rarely used in experiments. To change the wavelength we use a TOPAS which is an optical parametric amplifier (OPA).

Inside the TOPAS there is a nonlinear crystal. First, the 2<sup>nd</sup> harmonic of the fundamental is generated to give 400 nm laser pulses. Second, that beam is focused onto a sapphire crystal and due to self focusing, a white light spectrum is generated. The 400 nm beam and the white light spectrum are mixed in a non-linear crystal. By doing so, the wavelength can be tuned in the whole visible range and in the UV and IR.

The non-linear conversion has a very low efficiency. However, due to the very intense incoming 800 nm pulse ( $1.6 \cdot 10^{16}$  ph/pulse for 4 mJ pulses) it is still possible to efficiently excite the sample with TOPAS pulses in the 10-100  $\mu\text{J}$ /pulse range. The laser beam is linearly polarised and a waveplate/polariser combination can be used to reduce the power.

## 3.3 XES Spectrometers on ID09

There are two XES spectrometers on ID09 that use different measurement principles.

The Johann spectrometer uses a spherical analyser crystal that works as a monochromator. XES spectra are recorded by energy scans during which the analyser angle and detector position are moved synchronously to keep the diffracted beam on the detector.

The von Hámos uses angular dispersion on a fixed analyser to measure the spectrum. It has up to 16 cylindrical crystal analysers that focus the emitted X-rays into a line on a 2D detector with the energy varying along the line. The spectrum is measured in one exposure without moving any elements. The advantage of the dispersive setup is that the spectra don't need to be corrected for variations in the incident beam intensity. The time needed to collect a narrow range spectrum with the von Hámos is longer than that with the Johann spectrometer. The latter has a higher count rate (ph/eV/s) for a given energy, typically 10-100 times higher per eV, and provides higher energy resolution. It was used in this project for monitoring the intensity at a fixed energy as a function of time delay. In that way, the excited-state fraction is monitored with high intensity and precision. The two setups are described below in more detail.

### 3.3.1 Johann spectrometer

The Johann emission spectrometer was installed in 2014 with the aim to complement scattering experiments with site-specific information from transition metal complexes.

The Johann spectrometer uses a spherically bent crystal, positioned on the Rowland Circle, to monochromatise and focus the emission onto the Ketec SDD or Maxipix CCD. The geometry is shown in figure 3.29(a). The emission is collected at high Bragg angles, typi-

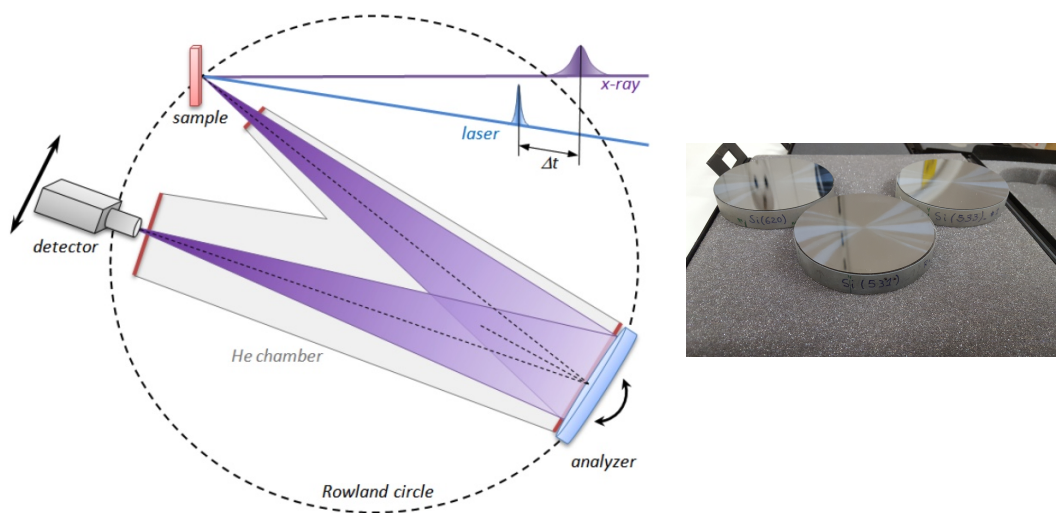


**Figure 3.29:** (a) Johann spectrometer for X-ray emission. The helium chamber is filled with He with a slight overpressure. (b) Spherical analysers for the Johann spectrometer,  $R = 100$  cm,  $\varnothing 10$  cm, Si(531), Si(533) and Si(620). (Courtesy Dmitry Khakhulin.)

cally  $70^\circ$ , in order to maximise the energy resolution. The diameter of the spherical analyser is 10 cm and the radius of curvature 100 cm. Three analyser crystals were used so far, Si(531), Si(533) and Si(620), see figure 3.29(b). Scans of the emission spectra are performed by scanning the analyser angle while translating the detector in a theta-2theta fashion. The advantage of the Johann geometry is that all incident rays have the same Bragg angle and as a result, the analyser can probe the emission spectrum at high resolution. Typically the energy resolution  $\Delta E/E$  is  $1.5 \cdot 10^{-4}$  for the  $K\beta$  line of Fe measured with Si(531).

Depending on the emission energy of the transition metal, the analyser can be changed to optimize the resolution at the emission energy. The analyser is focusing the emission into a stripe on the detector of about  $4 \text{ mmH} \times 10 \text{ mmV}$ . For that reason it is important to use a detector with a large active area like the  $1 \times 1$  Maxipix ( $28 \times 28 \text{ mm}^2$ ) or Ketec ( $\text{Ø}10 \text{ mm}$ ).

Since the X-ray path in the spectrometer is 2 m, absorption in air is significant below 10 keV. Therefore, a plexiglas helium chamber is used to enclose the beam path inside the Rowland circle. Due to leaks, the gas consumption is about 1 standard cylinder (50L) per day.

The  $[\text{Fe}(\text{phen})_3]^{2+}$  experiments used the pink beam from the U17 with the fundamental at 15 keV at closed gap (6 mm). The disadvantage of the pink beam is the contamination from the polychromatic scattered radiation. The detector should therefore have a high-energy threshold like the Ketec SDD and Maxipix detector.

### 3.3.2 Von Hámos spectrometer

The von Hámos (VH) spectrometer is designed for measuring X-ray emission spectra (XES) from 3d and 4d transition metals in the energy range 4-12 keV. In contrast to the Johann spectrometer, the von Hámos can measure a wide spectrum, typically 150 eV, in one exposure without scanning the Bragg angle of the analysers.

The VH spectrometer has 16 holders for cylindrical analyser crystals that are positioned in a  $4 \times 4$  matrix on a toroidal surface. They focus the emission in the horizontal plane (sagittally) while the vertical part propagates to the detector without focusing. The variation in the vertical angle on the analyser, the Bragg angle, probes the spectrum. Each analyser focuses the emitted X-rays into a line on the detector and the lines are normally overlapped into one line.

The first von Hámos spectrometer was built by Uwe Bergmann and Roberto Alonso-Mori at SLAC in 2012 [44] and the design was commercialised by JJXRAY in 2016. The VH spectrometer on ID09 was installed in October 2017. The time-resolved  $\text{K}\beta$  spectra from  $[\text{Fe}(\text{phen})_3]^{2+}$  presented in this thesis are the first time-resolved von Hámos spectra measured at ESRF.

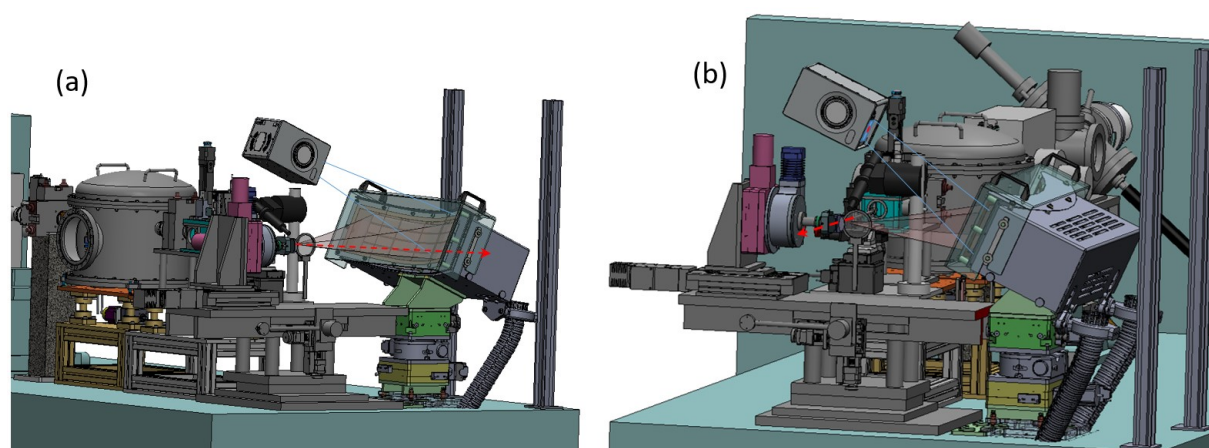


**Figure 3.30:** Von Hámos XES spectrometer on ID09/ESRF. (a) Up to 16 analysers focus & monochomatise the emission. The focus is an energy dispersive vertical line. The primary beam is shown in red. The Bragg angle can be varied between  $51.5\text{-}81.5^\circ$ . (b) Upstream view of the spectrometer. The Maxipix is seen above the sample. (Courtesy Laurent Eybert, ISDD, ESRF).



**Figure 3.31:** (a) 16 analysers mounted in the VH holder. When not used, the analysers are protected by a plexiglas screen. (b) Cylindrical Si(531) analyser with a radius of curvature 0.5 m. The analyser is 110 mm wide and 30 mm high. A 0.15 mm crystal wafer is bonded to the glass substrate.

The ID09 setup with the VH spectrometer, the diffractometer and the Maxipix detector is shown in figure 3.30. The banana shaped crystal holder and an analyser is shown in figure 3.31. The spectrometer is mounted at  $90^\circ$  from the incident beam at the height of the beam. The sample-spectrometer distance is  $\sim 500$  mm depending on the emission energy and analyser type. The background from elastic and Compton scattering is the lowest possible in this position. This is because the incident beam is 100% polarised in the horizontal plane. The polarisation factor for scattered radiation, elastic and inelastic, in the direction  $(2\theta, \phi)$  is proportional to the geometric polarisation factor

$$P = 1 - \sin^2 2\theta \cdot \cos^2 \phi.$$

Here  $2\theta$  is the deflection angle from the primary beam.  $\phi$  is the azimuthal angle which is zero along the polarisation direction  $y$ . In the direction  $(2\theta, \phi) = (90^\circ, 0^\circ)$ ,  $P = 0$ . We call this position the polarisation hole.

The analysers were made by Roberto Verbeni from the Optics Group at ESRF. Each analyser is 110 mm wide  $\times$  30 mm high and has a sagittal radius  $r_s = 0.5$  m. The crystals are made from a 0.15 mm silicon wafer bonded onto a cylindrical substrate made of quartz. Six Si(111), six Si(220) and one Si(531) analyser are available.

For these Si analysers, the energy range is typically 100-200 eV. That is wide enough to probe both  $K\beta$  and the VtC line simultaneously. For Fe, the  $K\beta$  and VtC emission are at 7058 and 7108 eV, respectively. The VtC line is just below the 1s ionisation energy of 7112 eV. The two lines were measured simultaneously with Si(440) analysers over an energy range of 156 eV.

Fe  $K\alpha$  and  $K\beta$  lines are separated by 660 eV. To measure them simultaneously, we used eight Si(333) and eight Si(440) crystals and offset them horizontally on the Maxipix with the roll motors. We used Si(333) for the  $K\alpha_1$  and  $K\alpha_2$  doublet at 6404 and 6391 eV and Si(440) for Fe  $K\beta$  at 7058 eV. The VH spectra from an Fe foil are shown in figure 3.32.

To reduce losses from absorption in air, the flight path has to be in helium inside a plastic bag. To estimate the importance of that, let's calculate the transmission in air. Using Beer-Lambert's law:

$$I(t) = I_0 \exp(-\mu t),$$

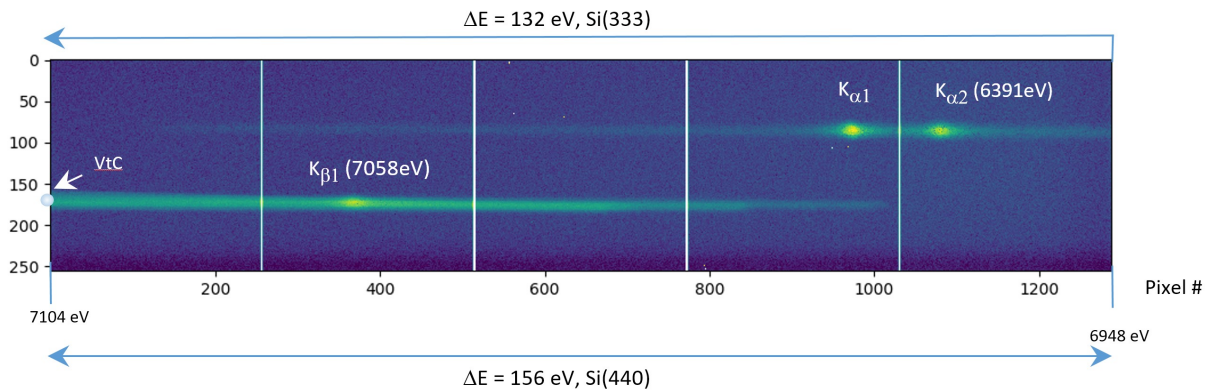


**Figure 3.32:** K emission from an Fe foil. The  $K\alpha$  lines were recorded with eight Si(333) crystals and  $K\beta$  with eight Si(440) crystals. The VtC emission is on the edge of the detector. The image is rotated  $90^\circ$  for convenience. The upper part of the detector is to the left. The energy range is 156 eV and 132 eV for Si(440) and Si(333), respectively.

where  $\mu$  is the absorption coefficient for air and  $t$  is the air path (1093 mm). Air has 78.1%  $N_2$ , 20.9%  $O_2$  and 0.9% Ar.  $\mu$  is calculated from the photoelectric cross sections for these atoms:

$$\mu = \sum_i n_i \sigma_i,$$

where  $n_i$  is the atom density and  $\sigma_i$  the absorption cross section.  $\sigma_i$  are tabulated in XOP. The result is shown in figure 3.33. At 7 keV,  $\mu = 1.53 \cdot 10^{-3} \text{ mm}^{-1}$ . With the 1093 mm flight path, the transmission is 18.6% at 7 keV. With a perfect He bag, the transmission is 100%, but in practice it is slightly lower due to air leaks.

### Sagittal focusing

The isotropic  $4\pi$  emission is focused by the cylindrical crystal analyser into an energy dispersive line as shown in figure 3.34. The horizontal divergence is focused at the magnification

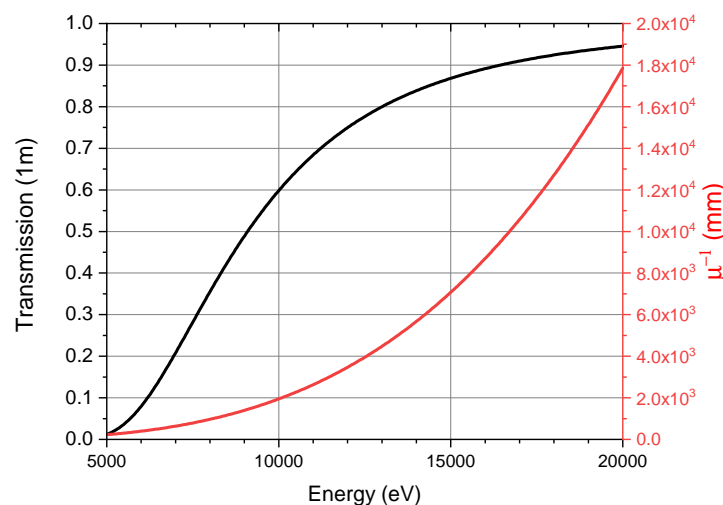


**Figure 3.33:** Absorption in air. The black curve shows the transmission after 1 m. The red curve is the inverse absorption coefficient  $\mu^{-1}$ .

$M = 1$ , i.e the line width on the detector is a 1:1 image of the sample in the beam direction. The length of the focused line is  $2 \times$  the analyser height,  $2 \times 30 = 60$  mm.

Let's first consider a  $2\pi$  cylindrical crystal with a vertical axis and the sample in the centre, see figure 3.34(a). In the horizontal plane, the  $2\pi$  emission is reflected back onto the sample. When adding the vertical direction, the 3D configuration is shown in figure 3.34(b). At a certain height in the cylinder, the incidence angle  $\theta$  is matching the emission energy and angles near  $\theta$  are diffracted onto a vertical line on the detector. The line is parallel with the analyser and  $2 \times$  the length. In 3.34(c), the cylinder is tilted  $90^\circ - \theta$  which brings the analyser into the polarisation hole. The detector is parallel to the analyser and the sample & detector fall on one line (the cylinder axis). The latter is important for calculating the energy resolution from the source size, see later. In beamline coordinates  $(x, y, z)$ , the positions are:

Sample:	$(x, y, z) = (0, 0, 0),$
Analyser centre:	$(x, y, z) = (0, r_s/\sin \theta_0, 0, 0),$
Detector centre:	$(x, y, z) = (0, 2r_s \cos \theta_0 \cot \theta_0, 2r_s \cos \theta_0).$

The sample-analyser distance is:

$$p = r_s / \sin \theta_0.$$

The sample, analyser and detector form an equilateral triangle that can be rotated to any angle around the sample. When the centre of the analyser is in the polarization hole, the background from elastic and inelastic scattering is minimised. The VH parameters for Fe  $K\beta$  at 7058 eV with Si(440) are shown in table 3.9.

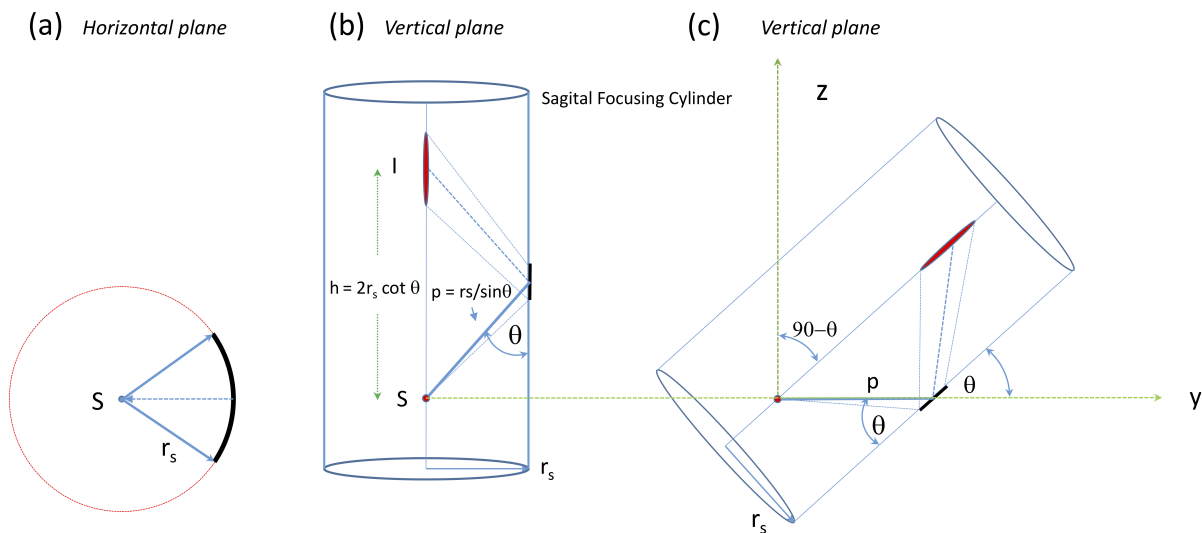


**Figure 3.34:** Focusing properties of a cylindrical crystal. (a) Focusing with a  $90^\circ$  Bragg angle in the horizontal plane. The source and focus coincide. (b) Focusing at the Bragg angle  $\theta$  with a vertical cylindrical crystal. The image  $I$  of the source  $S$  is a line. With  $M = 1$  horizontal focusing, the vertical footprint is  $2 \times$  the length of the analyser and the width is the thickness of the sample. (c) Focusing condition with the cylinder (analyser) rotated  $90^\circ - \theta$  into the polarisation hole to minimise the background. Note that the detector is parallel to the analyser and the detector window is pointing towards the sample.

$E_{K\beta}$ (eV)	$d(440)$ (Å)	$\theta_0$ (°)	$r_s$ (mm)	$p$ (mm)	dety (mm)	detz (mm)	$R_m$ (mm)
7058	0.9601	66.185	500	546.5	178.2	403.8	597.4

**Table 3.9:** Analyser and detector parameters for recording Fe  $K\beta$  emission with Si(440).

### Meridional focusing

In a horizontal row of the crystal holder, the 4 analysers form a fragmented circle with a radius  $r_s = 0.5$  m, see figure 3.35. In the columns, the rays from the centre of the analysers are directed to the same point on the detector. For that to happen, the analyser centres have to lie on the meridional focusing circle. The individual lines are then overlapped on the detector, not only for one but for all 4 columns. So the 16 analyser centres lie on a toroidal surface and form a segmented toroidal surface. The analysers can also be aligned onto one cylindrical surface and quadruple the energy range to  $4 \times 156.3 = 625.2$  eV for Si(440) at 7 keV. But that requires a big detector, i.e.  $4 \times 60 = 240$  mm long which is not practical.

The meridional focusing condition is:

$$R_m = \frac{2}{\sin \theta_0} \left( \frac{pq}{p+q} \right) = \frac{p}{\sin \theta_0} = \frac{r_s}{\sin^2 \theta_0}$$

with  $r_s = 500$  mm and  $\theta = 66.185^\circ$  we get  $R_m = 597.4$  mm. It is possible to show that with the upper and lower analysers at  $\pm 45$  mm from the spectrometer centre, the horizontal offset is  $h = 1.69$  mm and the crystal tilt  $\alpha = \pm 4.32^\circ$ , see figure 3.35(b).

### Detector energy scale

We will now calculate how the Bragg angle and energy varies along the detector coordinate  $z_d$ . The analyser is at the distance  $p$  from the source at the height of the primary beam. The

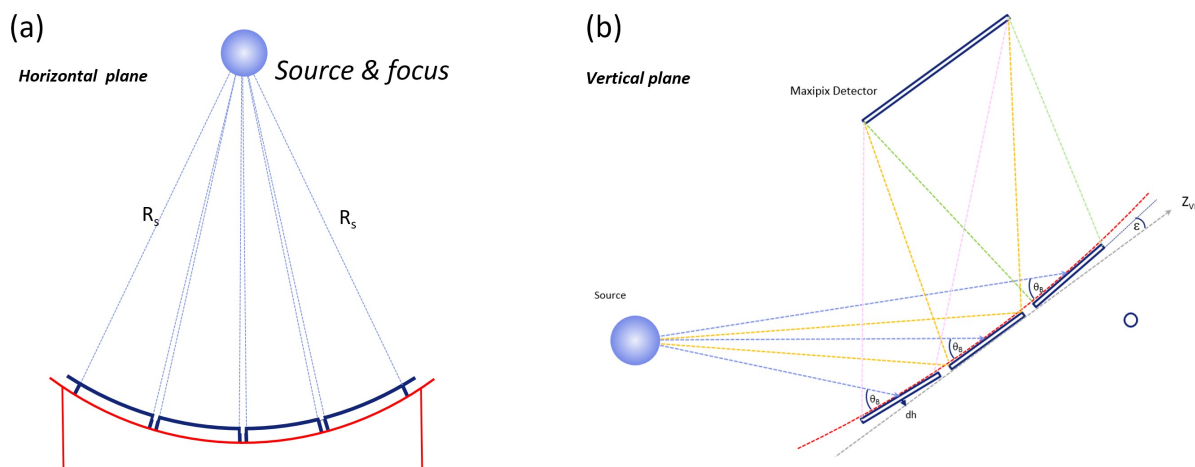


**Figure 3.35:** Focusing with a multi-crystal analyser. (a) Sagittal focusing with four crystals in a row. The crystal holder is shown in red and analysers in blue. (b) Meridional focusing from crystals in a vertical column. The centres of the crystals fall on a sphere of radius  $R_m$ . The crystal assembly form a segmented toroidal crystal and the vertical flatness of the analysers disperse the beam (and energy).

inclination angle is  $\theta_0$ , the Bragg angle for the centre of the emission energy. Bragg's law gives

$$2d_{hkl} \sin \theta_0 = \lambda,$$

where  $\lambda$  is the wavelength and  $d_{hkl}$  is the lattice spacing of the  $(hkl)$  reflection. The wavelength and energy are related as:

$$\lambda = (hc)/E,$$

where  $h$  is Planck's constant and  $c$  is the speed of light. Numerically:

$$\lambda[\text{\AA}] = 12.3984/E[\text{keV}].$$

The definitions of the  $z_a$  and  $z_d$  coordinates for the analyser and detector are shown in figure 3.36(a). They are related as  $z_d = 2 z_a$ . From figure 3.37 we derive the Bragg angle vs analyser position  $z_a$  as:

$$\theta(z_a) = \theta_0 - \frac{z_a \sin \theta_0}{(p + z_a \cos \theta_0)} \approx \theta_0 - \frac{\sin^2 \theta_0}{2p} z_a = \theta_0 - \frac{\sin^2 \theta_0}{r_s} z_a.$$

The approximation is accurate to  $\leq \pm 1.1\%$  for  $-15 \leq z_a \leq 15$  mm in the setup. The acceptance angle is:

$$\Delta\theta = \frac{\sin \theta_0}{p} \Delta z_a = \frac{\sin^2 \theta_0}{r_s} \Delta z_a.$$

With  $\Delta z_a = 30$  mm and Si(440) at 7058 eV,  $\Delta\theta = 2.87^\circ$ . The angle vs detector position is obtained from by substituting  $z_d = 2 z_a$ :

$$\theta(z_d) = \theta_0 - \frac{\sin \theta_0}{(2p + z_d \cos \theta_0)} z_d \approx \theta_0 - \frac{\sin -\theta_0}{2p} z_d = \theta_0 - \frac{\sin^2 \theta_0}{2r_s} z_d.$$

The energy scale  $E(z_d)$  is obtained from Bragg's law:

$$E(z_d) = hc \left[ 2d \sin \left( \theta_0 - \frac{\sin \theta_0}{(2p + z_d \cos \theta_0)} z_d \right) \right]^{-1}.$$

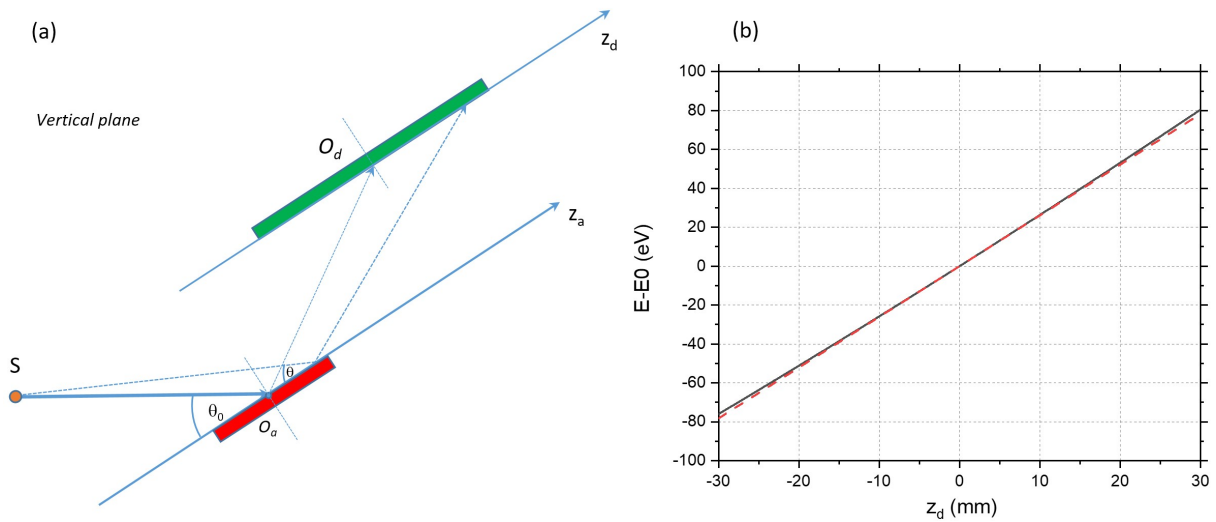


**Figure 3.36:** Energy dispersion on the detector. (a) Analyser and detector positions and their coordinates  $z_a$  and  $z_d$ . (b) Energy scale along the detector (black line) for Si(440) at  $E_0 = 7058$  eV, the Fe  $K_\beta$  line. The red line is the tangent at  $E_0$ . The energy range is 156.4 eV and the deviation from linearity is  $\pm 1.1\%$  at the extremities. The slope of the red line is 2.607 eV/mm.

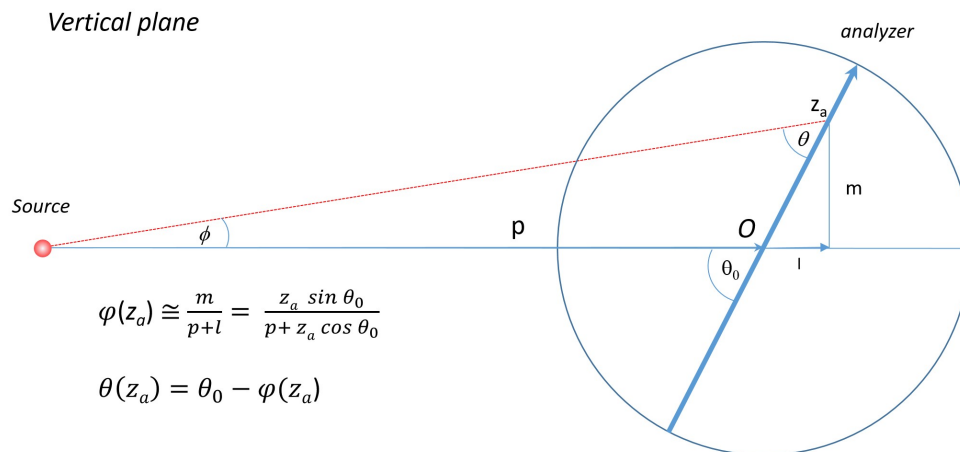


**Figure 3.37:** Bragg angle for a given position  $z_a$  on the analyser.

The  $E(z_d)$  curve for Fe  $K\beta$  is shown in figure 3.36(b). The curve is essentially linear over the 60 mm detector with a  $\pm 1.1\%$  deviation at the ends from the central tangent. The slope is 2.607 eV/mm in the centre. With a pixel size of 0.055 mm, the energy increment is 0.144 eV/pixel. The detector & analyser parameters are summarised in table 3.10 for the Maxipix detector.

$\Delta z_a$ (mm)	$\Delta z_d$ (mm)	$p$ (mm)	$d(440)$ (Å)	$\theta_0$ (°)	$\Delta\theta$ (°)	$E_0$ (eV)	$\Delta E$ (eV)	$dE/dz_d$ (eV/mm)	$dE/\text{pixel}$ (eV)
30	60	546.5	0.9601	66.18	2.87	7058	156.3	2.607	0.143

**Table 3.10:** Von Hámos parameters used for the  $K\beta$  emission spectrum of Fe. The radius of curvature of the crystals is  $r_s = 0.5$  m.

### Cylindrical analysers

It is well known that crystals in back-scattering geometry at Bragg angles near  $90^\circ$  have a small energy range  $\Delta E$  per unit angle (eV/deg). The effect is shown in the energy vs angle plot for different analysers ( $hkl$ ) in figure 3.38(b). Due to Bragg's law, the slope is zero at  $\theta_B = 90^\circ$  for all reflections ( $hkl$ ). For the energy range of interest here, 4-12 keV, back scattering reflections have high Miller indices ( $hkl$ ) and therefore small relative bandwidths  $\Delta E/E$ , see table in figure 3.38(a).

We will now calculate the slope of the curve. From Bragg's law we have:

$$E = (hc)/\lambda = \frac{1}{2d} \frac{hc}{\sin \theta}.$$

The differential is:

$$\frac{dE}{d\theta} = -\frac{1}{2d} hc \frac{\cos \theta}{\sin^2 \theta} = -\frac{1}{2d} \frac{hc}{\sin \theta} \cot \theta = -E \cot \theta.$$

Since  $\cot \theta \rightarrow 0$  for  $\theta \rightarrow 90^\circ$ ,  $dE/d\theta$  is small near  $90^\circ$ .

Bragg's law cannot predict the bandwidth of a diffracted polychromatic beam from a perfect crystal. For a perfect crystal, the bandwidth is calculated by Dynamical Diffraction Theory. The theory predicts that the reflected beam has a finite bandwidth  $\Delta E_{DW}$ , the

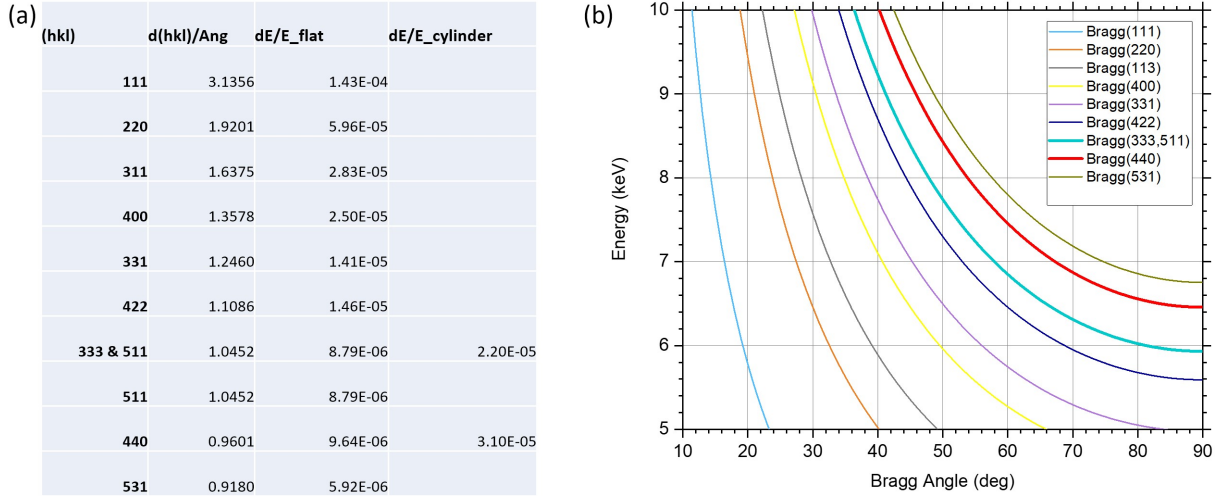


**Figure 3.38:** Properties of silicon analysers. (a) Si( $hkl$ ) bandwidths for flat and bent crystals. (b) Energy vs Bragg angle. The curves have zero slopes at  $90^\circ$ . When the slope  $dE/d\theta$  is small, the analyser “zooms in” on the energy scale.

Darwin Width, that depends on the number of lattice planes encountered before the incoming beam is extinct at the extinction depth a few microns into the bulk. The relative bandwidth,  $\Delta E_{DW}/E$ , is independent of energy. The amplitude, i.e. the reflectivity, is slightly lower than 1 due to absorption. We see in figure 3.38(a) that low-index reflections have large bandwidths,  $1.43 \cdot 10^{-4}$  for Si(111) and higher-index reflections, Si(440) for example, have smaller bandwidths,  $9.6 \cdot 10^{-6}$ . The effect is due to the shorter  $d$ -spacing for Si(440): when more planes are encountered by the incoming beam, the bandwidth is smaller.

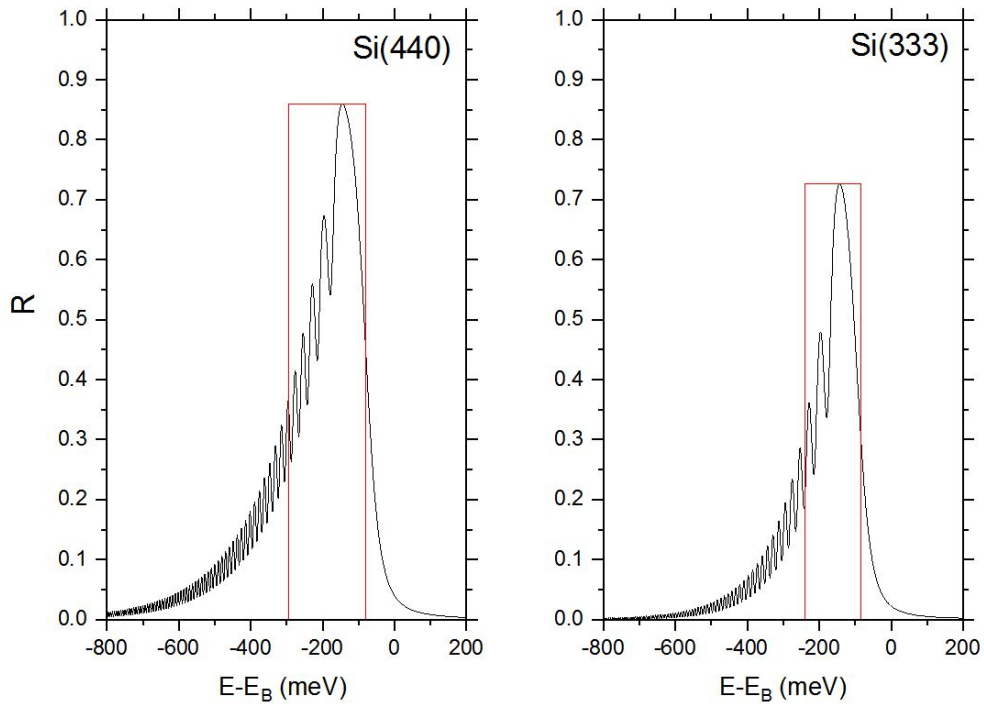


**Figure 3.39:** Reflectivity curves for cylindrically bent Si(440) and Si(333) at 7058 and 6400 eV for  $K\beta$  and  $K\alpha$ , respectively. The sagittal radius of curvature is  $r_s = 0.5$  m. The shift from zero in  $E - E_B$  is from the bending. The red boxes are used to simplify the calculation of the detector intensity. The reflectivity curves were calculated by Christoph Sahle, ID20, ESRF.

When a crystal is bent, the bandwidth increases due to dispersion in the lattice spacing and Bragg angle seen by the beam as it penetrates the bulk. Figure 3.39 shows the reflectivity for cylindrically bent Si(333) and Si(440) calculated by Christoph Sahle with the XRStools program based on Takagi-Taupin diffraction theory for bent crystals. The calculations were done for non-polarised X-rays for Si(440) and Si(333) at 7058 eV and at 6400 eV, respectively. The incidence angles are adjusted so that the flat crystals produce beams at 7058 and 6400 eV, hereafter labelled  $E_B$ . The small shift from zero of the peak in the reflectivity curves  $R(E - E_B)$ , about  $-0.2$  eV, is from the dispersion in lattice spacing and incidence angle. The red boxes in figure 3.39 have the same peak height and area as the bent crystals. The boxes will be used in the calculation of the VH intensity from one pulse. The crystal parameters are summarised in table 3.11.

Analyser	$E$ (flat)	$\Delta E$ (bent)	$R_{max}$	BW	$(\Delta E/E)$
Si(333)	6400 (K $\alpha$ )	-0.161	0.727	0.155	$2.2 \cdot 10^{-5}$
Si(440)	7058 (K $\beta$ )	-0.187	0.859	0.217	$3.1 \cdot 10^{-5}$

**Table 3.11:** Bandwidth and reflectivity of bent Si(330) and Si(440) analysers ( $r_s = 0.5$  m).

The increase in the bandwidth caused by bending is significant. For Si(440),  $\Delta E/E$  is  $9.6 \cdot 10^{-6}$  and  $3.1 \cdot 10^{-5}$  for the flat and bent crystal, respectively. The bent bandwidth is 3.2 times larger. An incoming ray at 7058 eV is monochromatised to  $\Delta E_{hkl} = 0.22$  eV by a bent Si(440) analyser. In the present experiment, the increase in bandwidth is an advantage: the beam is focused and the intensity (ph/eV) is increased. The loss in resolution is insignificant as we will see later.

The diffracting surface of the analysers has the dimensions  $l \times h = 110 \times 30$  mm<sup>2</sup> in the horizontal and vertical respectively and a radius of curvature is  $r_s = 0.5$  m. The space angle of the analyser is:

$$\Delta S \approx \frac{lh \sin \theta}{p^2}.$$

With the parameters from table 3.10,  $\Delta S = 10.11 \cdot 10^{-3}$  sr/analyser. With 16 analysers, the spectrometers intercepts 1.29% of the  $4\pi$  emission.

## Detector

The spectrometer has a Maxipix detector with five modules in a  $5 \times 1$  configuration. The detection area,  $71 \times 14$  mm<sup>2</sup>, is larger than the image which is typically  $60 \times 1$  mm<sup>2</sup>. The large field-of-view facilitates the alignment in both directions. There are  $1280 \times 256$  pixels with a 0.055 mm pixel size. As mentioned earlier, the detector is photon counting with zero noise and perfect linearity. The detector can record 295 frames per second (fps) and be gated to 1  $\mu$ s. The quantum efficiency is 0.90 at 7 keV (reduced from 0.9999 from absorption in the 80  $\mu$ m Mylar window).

We will now calculate the energy per pixel,  $\Delta E_{pix}$  in the centre of the detector. Let's calculate the differential

$$\frac{dE}{dz_d} = \frac{dE}{d\theta} \frac{d\theta}{dz_d} \approx \frac{\sin \theta_0 \cos \theta_0}{2r_s} E_0 = \frac{\sin 2\theta_0}{4r_s} E_0. \quad (3.1)$$

With the values in table 3.10, we get  $dE/dz_d = 2.607$  eV/mm for Si(440) at 7058 eV. With  $0.055$   $\mu\text{m}$  pixels, the pixel increment is  $\Delta E_{pix} = 0.143$  eV/pixel. Figure 3.36(b) shows the energy vs position. It can be approximated by a straight line to  $\pm 1.1\%$  over the 156.3 eV energy range. For completeness we repeat the detector energy range here:

$$\Delta E_{det} \approx \frac{\sin 2\theta_0}{2r_s} \Delta z_a E_0,$$

where  $\Delta z_a$  is the analyser length (30 mm) and  $E_0$  and  $\theta_0$  are the central energy and Bragg angle. For Si(440) at 7 keV,  $\Delta E_{det} = 156$  eV.

### Energy resolution

The spectrometer should resolve tiny shifts in energy between laser ON and laser OFF spectra in a pump-probe experiment. Since the laser ON spectrum is a mixture of excited and non-excited spectra, the spectrometer has to detect very small changes in the spectral amplitude. The resolution has the following contributions:

1. The intrinsic bandwidth of the bent crystal analyser
2. The detector's pixel resolution
3. The smearing from the finite source size  $\sigma_x$ ,  $\sigma_y$  and  $\sigma_z$ .
4. Alignment errors.

The total resolution is the convolution:

$$\Delta E_{VH} = \sqrt{(\Delta E)_{hkl}^2 + (\Delta E)_{pix}^2 + (\Delta E)_x^2 + (\Delta E)_y^2 + (\Delta E)_z^2 + (\Delta E)_{align}^2}.$$

We will discuss these terms below.

The first two contributions were discussed in the previous sections. As shown above, a bent Si(440) analyser monochromatises an incoming Fe  $K\beta$  ray at 7058 eV to  $\Delta E_{hkl} = 0.22$  eV (table 3.11). The pixel resolution is calculated from 3.1. With  $\theta_0 = 66.18^\circ$ ,  $E_0 = 7058$  eV, and  $r_s = 500$  mm, we get  $dE/dz_d = 2.607$  eV/mm or  $\Delta E_{pix} = 0.143$  eV per pixel. Spectral features below that step are not resolved.

Let's investigate how the source size affects the energy resolution and calculate the shift in the spectrum on the detector. We will show that it is most sensitive to the vertical source size. It is done by moving a point source from  $(0,0,0)$  to  $(\sigma_x, 0, 0)$ ,  $(0, \sigma_y, 0)$  and  $(0, 0, \sigma_z)$ .

1)  $\sigma_x$ . If we move a polychromatic point source from  $(0, 0, 0)$  to  $(\sigma_x, 0, 0)$ , the image is a line,  $(-\sigma_x, z_d)$  on the detector where  $z_d$  runs vertically from -30 to 30 mm. The focus swaps left and right on the image. The central energy  $E_0$  is imaged at  $(-\sigma_x, 0)$ . If we move the source to  $(-\sigma_x, 0, 0)$ , the image of  $E_0$  will move to  $(\sigma_x, z_d)$  on the detector. As a result, a source extending from  $-\sigma_x \leq x \leq \sigma_x$  and emitting at  $E_0$  is imaged into the transverse line  $-\sigma_x \leq x \leq \sigma_x$  at  $z_d = 0$ . This argument is valid if the focusing is aberration free, which is the case for the large incidence angle  $66.18^\circ$  in this study. **The thickness of the sample can thus be large without loss of energy resolution.**

For  $\sigma_y$  and  $\sigma_z$  displacements, it is sufficient to restrict the study to the  $(y, z)$  plane due to the cylindrical symmetry, see figure 3.40. The analyser  $z_a$ -axis is parallel to the detector's  $z_d$  axis at the (orthogonal) distance  $r_s$ . The central energy  $E_0$

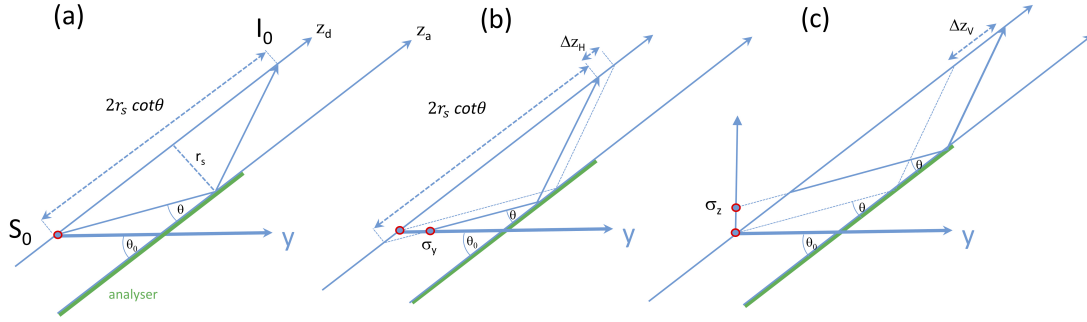


**Figure 3.40:** Energy resolution from the finite source size. (a) Point source. A ray striking the analyser at  $\theta$  arrives at the detector  $2r_s \cot \theta$  from the source. (b) Effect of the horizontal source size  $\sigma_y$ . A ray emitted at  $\sigma_y$  and striking the analyser at  $\theta$ , is detected  $\Delta z_H$  below the point source in (a). (c) The vertical source size: the ray emitted at  $\sigma_z$  and striking the analyser at  $\theta$ , is reflected  $\Delta z_V$  below the central point source. The displacements are calculated in the text.

strikes the analyser at  $\theta_0$ . A ray incident at  $\theta$  is reflected onto the detector  $2r_s \cot \theta$  from the source  $S_0$ .

2) When the source is displaced  $\sigma_y$ , the new  $\theta$  ray arrives at the distance  $2r_s \cot \theta + \Delta z_y$  on the detector:

$$\Delta z_y = \frac{\sin(\theta - \theta_0)}{\sin \theta} \sigma_y.$$

The shift is zero for  $\theta = \theta_0$ . The energy shift is obtained from the detector's energy gradient as:

$$\Delta E_y = \frac{\sin(\theta - \theta_0) \sin(2\theta_0)}{4r_s \sin \theta} E_0 \sigma_y.$$

$\Delta E_y$  is shown in figure 3.41(a). The shift is zero for  $E = E_0$  and less than 0.003 eV at the edge of the detector. The shift is insignificant compared to the other contributions in table 3.12. **Conclusion: opening the sample slits fully horizontally does not degrade the energy resolution.**

3) Let's consider  $\sigma_z$  as shown in figure 3.40(c). The displacement is:

$$\Delta z_z = \frac{1}{\sin \theta \cos(\theta - \theta_0)} \sigma_y,$$

and the energy shift is obtained from the detector gradient:

$$\Delta E_z = \frac{\sin 2\theta_0}{4r_s \sin \theta \cos(\theta - \theta_0)} E_0 \sigma_z.$$

$\Delta E_z$  is essentially flat vs energy as shown in figure 3.41(b). With a 0.06 mmV source,  $\Delta E_z$  is **0.17 eV, i. e. greater than the energy step on the detector, 0.14 eV/pixel.**

With several analysers, alignment errors have to be included in the instrumental resolution. As XES spectra are tricky to align due to the lack of sharp features, we estimate that the overlap can be done to an accuracy of 2 pixels,  $2 \times 0.143 = 0.286$  eV.

The final resolution of the von Hámos is thus  $< 1$  eV which is adequate for measuring the line width of 1s core emission in Fe. Atomic quantum calculations predict a linewidth 1.19 eV corresponding to a Heisenberg lifetime of 0.28 fs.

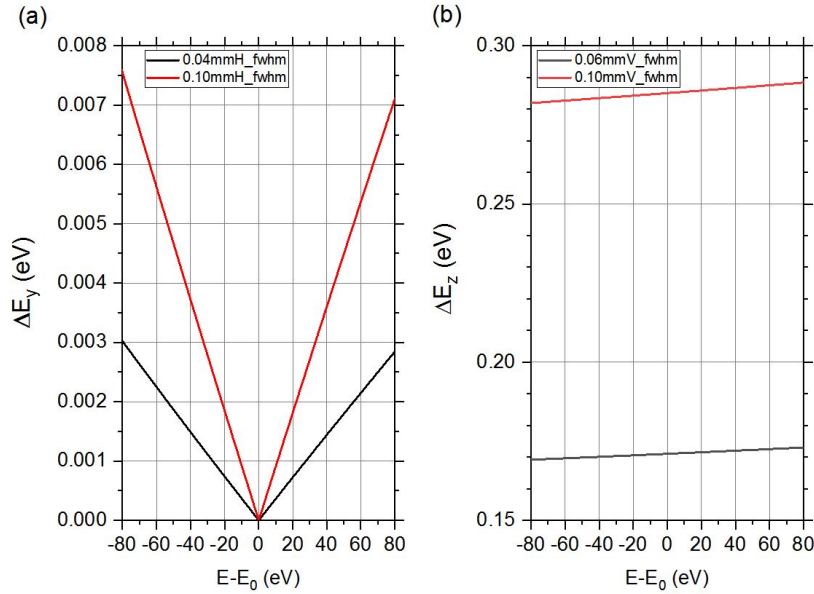


**Figure 3.41:** Energy resolution from the horizontal and vertical source size  $\sigma_y$  and  $\sigma_z$ . (a)  $\Delta E_y$  is small and zero in the centre (FWHM values). The black curve is the 0.04 mmH source in the experiment. (b)  $\Delta E_z$  is greater and quasi constant along the detector. The black curve is the 0.06 mmV source in the experiment (FWHM).

$\Delta E_{DW}$	$\Delta E_{pix}$	$\Delta E_x$	$\Delta E_y$	$\Delta E_z$	$\Delta E_{align}$	$\Delta E_{final}$
0.22	0.14	0.00	0.00	0.17	0.28	0.42

**Table 3.12:** Contributions to the energy resolution in the  $[\text{Fe}(\text{phen})_3]^{2+}$  K $\beta$  experiment at 7058 eV.

### 3.3.3 Von Hámos commissioning

The intensity of the K $\alpha$  and K $\beta$  lines is now calculated from the absorption of X-ray photons by Fe in the  $[\text{Fe}(\text{phen})_3]^{2+}$  solution at a concentration of 0.01 M in water. When an X-ray ionises Fe with the creation of a 1s core hole, the 1s hole is filled by a 2p, 3p or 3d electron with the emission of K $\alpha$ , K $\beta$  or VtC radiation respectively or the emission of Auger electrons. In Fe the quantum yield for photon or electron emission is 0.34 and 0.66, respectively. So the K-shell fluorescence yield is 34%. We will now calculate the absorption of photons above the 1s ionisation energy of 7112 eV from the U17 spectrum in figure 3.42(c). In addition to knowing the undulator spectrum, we need to calculate the energy dependent absorption coefficients for Fe and water,  $\mu_{Fe}$  and  $\mu_w$ , respectively.

#### Undulator intensity

The pink undulator spectrum was used with the fundamental at 15.0 keV, see figure 3.42(c). The FWHM of the fundamental is 2.4% and the size of the focused beam  $0.04 \times 0.06 \text{ mm}^2$ . The spectral intensity  $I_0(E)$ , in units of ph/eV/pulse, was calculated by Urgent/XOP with the emittance parameters of the ESRF. The reflectivity of the Pd coated mirror at 2.45 mrad incidence included and so was the absorption in beamline windows (1.0 mm C, 0.2 mm Be). The intensity was adjusted to give  $1 \cdot 10^9$  ph per pulse, the flux measured flux on the PD2 pindiode (8 mA bunch in 7/8+1 mode).

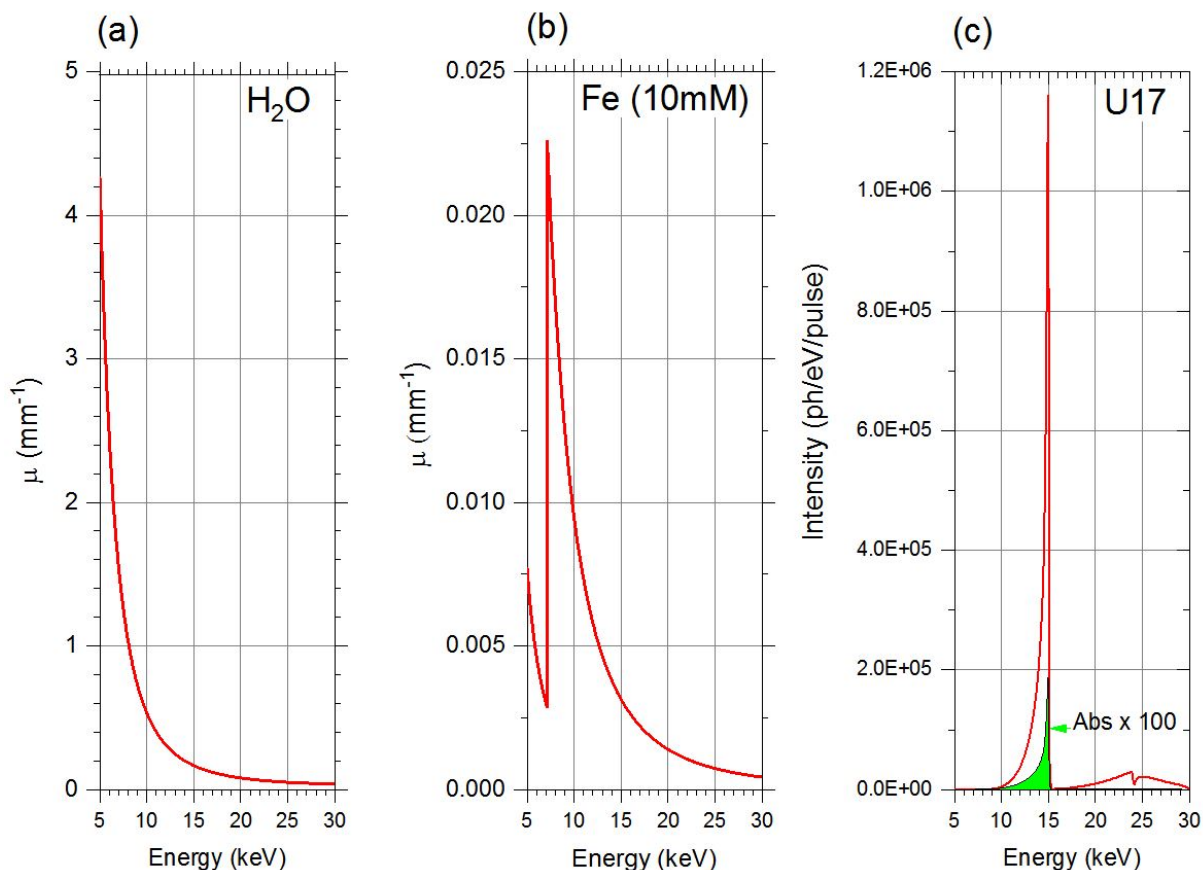


**Figure 3.42:** X-ray absorption for a 10 mM solution of  $[\text{Fe}(\text{phen})_3]^{2+}$  in water. (a) X-ray absorption coefficient for water. (b) X-ray absorption for a 10 mM gas of Fe atoms. Above the K-edge, the absorption is proportional to  $E^{-2.67}$ . (c) U17 spectrum (red) and the Fe absorption spectrum (green). The U17 intensity is scaled to  $1 \cdot 10^9$  ph/pulse. The bandwidth is 360 eV (2.4%).

### Sample concentration

The 0.01 M solution was injected by the  $45^\circ$  inclined sapphire nozzle which gives a 0.51 mm thick liquid sheet. The X-ray probed sample volume is  $V_0 = 0.04 \times 0.06 \times 0.51 \text{ mm}^3 = 1.22 \cdot 10^{-3} \text{ mm}^3$ . The number of Fe atoms in the beam is:

$$N_{\text{Fe}} = n_{\text{Fe}} V_0,$$

where  $n_{\text{Fe}}$  is the number density (Fe/ $\text{mm}^3$ ). The number density  $n$  and the molar concentration  $c$  are related as:

$$n = c \cdot \frac{N_a}{V_M},$$

where  $N_a$  is Avogadro number  $6.022 \cdot 10^{23} \text{ mol}^{-1}$  and  $V_M$  is a 1 litre volume ( $V_M = 1 \cdot 10^6 \text{ mm}^3$ ). From this we get  $n_{\text{Fe}} = 6.022 \cdot 10^{15} \text{ Fe}/\text{mm}^3$  and  $N_{\text{Fe}} = 7.35 \cdot 10^{12}$ . The molar concentration of water is 55.5 M with  $n_w = 3.34 \cdot 10^{19} \text{ H}_2\text{O}/\text{mm}^3$  and  $N_w = 4.078 \cdot 10^{16}$ . The mixing ratio Fe: $\text{H}_2\text{O}$  is 1:5548. The parameters are summarised in table 3.13.

### X-ray absorption

The U17 beam is attenuated according to Beer-Lambert's law:

$$I = I_0 \exp(-\mu t),$$

-	$c(M)$	$n$ (unit/mm <sup>3</sup> )	$N(V_0)$	$\mu^{-1}$ (mm, 7 keV)	$\mu^{-1}$ (mm, 15 keV)	$N_{abs}$
Fe	0.01	$6.02 \cdot 10^{15}$	$7.35 \cdot 10^{12}$	333	318	$2.85 \cdot 10^6$
H <sub>2</sub> O	55.5	$3.34 \cdot 10^{19}$	$4.08 \cdot 10^{16}$	0.66	6.63	$7.40 \cdot 10^7$

**Table 3.13:** Absorption parameters for the 0.01 M [Fe(phen)<sub>3</sub>]<sup>2+</sup> solution in water. The X-ray absorption  $N_{abs}$  is calculated for the 15 keV pink spectrum with  $1 \cdot 10^9$  photon/pulse and a 2.4% BW.

with

$$\mu = \mu_w + \mu_{Fe}.$$

$t$  is the sample thickness and  $\mu$  the total absorption.  $\mu$  depends on the atomic densities and the photoelectric cross sections  $\sigma_i$  as:  $\mu = \sum_i c_i \sigma_i$ , where the sum extends over the different atoms. The  $\sigma_i(E)$  functions were taken from the NIST data base in XOP.

For water,  $n_H = 6.68 \cdot 10^{19}$  H/mm<sup>3</sup>,  $n_O = 3.34 \cdot 10^{19}$  O/mm<sup>3</sup>.  $\mu_w$  is shown in figure 3.42(a). With  $\mu_w = 0.150$  mm<sup>-1</sup> at 15 keV, the absorption length  $\mu_w^{-1}$  is 6.6 mm. The intensity after the 0.509 mm sample is  $0.926I_0$ .

For Fe,  $n_{Fe} = 6.02 \cdot 10^{15}$  Fe/mm<sup>3</sup>.  $\mu_{Fe}$  is shown in figure 3.42(b). Note the sharp increase in  $\mu_{Fe}$  at the K edge at 7112 eV. With  $\mu_{Fe} = 2.92 \cdot 10^{-3}$  mm<sup>-1</sup> at 15 keV, the absorption length  $\mu_{Fe}^{-1}$  is 342 mm. That is 7.7 times longer than on the K edge at 7.112 keV.

How is the K emission absorbed by water? In the  $y$ -direction, towards the analysers, the sample is 0.04 mm thick. With a  $\mu_w$  of 1.46 mm<sup>-1</sup> at 7000 eV, the absorption is < 5.7% much lower than absorption in air in the spectrometer.

### Fluorescence intensity

The number of photons absorbed by the solution is calculated from Beer-Lambert's law. The transmitted (spectral) intensity after a sample thickness  $t$  is:

$$I(E) = I_0(E) \exp(-[\mu_w + \mu_{Fe}]t).$$

The (spectral) absorption from  $0 - t$ :

$$I_{abs}(E) = I_0(E)(1 - \exp(-[\mu_w + \mu_{Fe}]t))$$

The Fe part is the difference:

$$N_{abs}(Fe) = I_0(E) \{(1 - \exp(\mu_w + \mu_{Fe})t) - (1 - \exp)(-\mu_w t)\} = I_0 \exp(-\mu_w t) \{1 - \exp(\mu_{Fe} t)\}.$$

Energy integration gives the total number of Fe absorbed photons in the pink U17 beam:

$$N_{abs}(Fe) = \int I_0(e) \exp(-\mu_w t) \{1 - \exp(\mu_{Fe} t)\} dE.$$

Numerically:

$$N_{abs}(Fe) = 2.85 \cdot 10^6 \text{ Fe/pulse.}$$

The fraction of absorbing Fe atoms is small,  $2.85 \cdot 10^6 / 7.35 \cdot 10^{12} = 3.87 \cdot 10^{-7}$ , and the concentration is 3.87 nM. With 34.4% of the absorption events producing X-rays, the fluorescence source concentration is 1.24 nM. Moreover, in the pump-probe experiments, 15%

of  $[\text{Fe}(\text{phen})_3]^{2+}$  molecules are excited by the laser. The concentration contributing to the difference signal is therefore 0.18 nM.

$N_{abs}$  is linear in the pulse intensity  $I_0(E)$  and for a weakly absorbing solution it is also linear in the thickness  $t$ . The pulse intensity is limited by the maximum bunch charge in the storage ring, 10 mA, the signal can be increased with a thicker sample than used here, 0.51 mm. However the laser penetration is smaller than the X-ray penetration which would limit the gain in S/N. The solution is to rotate the liquid sheet by  $45^\circ$  around the  $z$ -axis and focus the laser into a line with a cylindrical lens. A second option for increasing the signal is to lower the X-ray energy. By lowering the energy from 15 keV to 12 keV,  $\mu_{Fe}$  increases by a factor 1.9.

At the FXE beamline at the EuXFEL, 9.2 keV was used in the first XES experiments on Fe complexes. Fe absorption at 9.2 keV is 2.6 times higher than at 15 keV and the pulse is 1000 times higher than at ESRF with  $10^{12}$  ph/pulse. Single shot spectra are still too weak so many pulses have to be accumulated on the detector. However the 10 Hz macro pulse structure at the EuXFEL is not great for accumulating images.

As mentioned above,  $2.85 \cdot 10^6$  photons are absorbed per pulse, and 34.4% of them emit K radiation. The energy and intensity of the  $K\alpha$ ,  $K\beta$  and  $VtC$  lines from the Krause Schofield data in XOP/DABA, are shown in table 3.14. Table 3.14 also shows the  $4\pi$  intensities for  $[\text{Fe}(\text{phen})_3]^{2+}$  in the last column. In the following we will calculate the K intensities on the detector.

Emission line	Energy (eV)	Relative intensity (%)	Intensity ( $4\pi$ , ph/pulse)
$K\alpha_2$	6391.0	29.7	$2.91 \cdot 10^5$
$K\alpha_1$	6404.0	58.1	$5.70 \cdot 10^5$
$K\beta_1$ & $K\beta_3$	7058.2	12.2	$1.20 \cdot 10^5$
$K_{VtC}$	7108.3	0.08	$7.84 \cdot 10^2$
Total		100	$9.80 \cdot 10^5$

**Table 3.14:** Fe K-edges and their intensities. The total  $4\pi$  intensities for  $[\text{Fe}(\text{phen})_3]^{2+}$  are shown in the last column. The calculation assumes  $1 \cdot 10^9$  ph/pulse at 15 keV, 0.01 M Fe concentration and a  $0.04 \times 0.06 \times 0.51$  mm<sup>3</sup> sample. The total K emission is  $9.80 \cdot 10^5$  per pulse.

## Detector intensity

The intensity on the detector will now be calculated from the isotropic  $4\pi$  intensities in table 3.14. The angle-energy distribution of the emission,  $\varepsilon(E, \theta, \phi)$  is the product of the isotropic angular emission times the normalised energy spectrum  $S(E)$  multiplied by the total intensity  $N_{abs}^*$ :

$$\varepsilon(E, \theta, \phi) = N_{abs}^* \frac{1}{4\pi} S(E).$$

$N_{abs}^*$  is the total number of K photons after Auger correction and  $S(E)$  is the spectral intensity in units of ph/eV/pulse.  $\theta$  is the Bragg angle and  $\phi$  the azimuthal angle. Integrating over all angles and energies gives the total source intensity in ph/pulse:

$$\iiint \varepsilon(E, \theta, \phi) d\theta d\phi dE = N_{abs}^*.$$

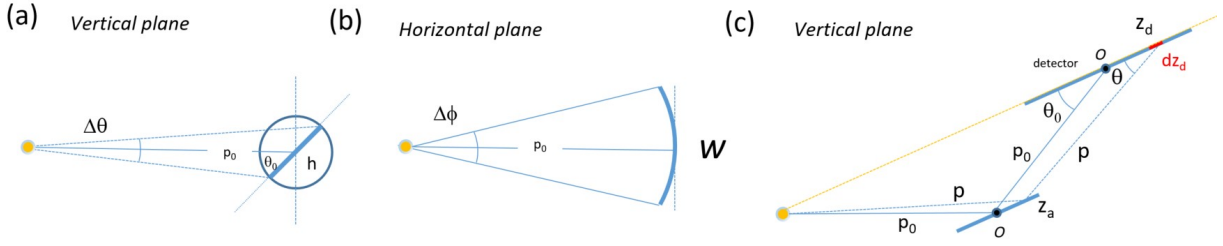


**Figure 3.43:** Angular acceptance of the analyser and detector. (a) Vertical analyser acceptance. (b) Horizontal analyser acceptance. (c) Angular acceptance of a pixel element  $dz_d$  at  $z_d$  on the detector. The incidence angle on the pixel  $dz_d$  is  $\theta$  and the source distance  $2p$ .

Let's start by calculating the solid angle of one analyser. With the symbols in figure 3.43, the vertical angular acceptance is:

$$\Delta\theta \simeq \frac{h \sin \theta_0}{p_0},$$

and the horizontal

$$\Delta\phi \simeq \frac{w}{p_0}.$$

The analyser dimensions are  $h = 30$  mm,  $w = 110$  mm. The central Bragg angle is  $\theta_0 = 66.18^\circ$  and the source-analyser distance  $p_0 = 546.5$  mm. That gives  $\Delta\theta = 50.2 \cdot 10^{-3}$  rad ( $2.88^\circ$ ) and  $\Delta\phi = 0.201$  rad ( $11.53^\circ$ ). The solid angle, i.e. the angular fraction on the unit sphere, is

$$\Delta\Omega = \frac{1}{4\pi} \Delta\theta \Delta\phi,$$

which is  $0.803 \cdot 10^{-3}$  sr per analyser. With 8 analysers in the  $[\text{Fe}(\text{phen})_3]^{2+}$  experiment, 0.64% of the emission is intercepted.

The intensity on a detector pixel element  $dz_d \times dz_d$  is now calculated. First we calculate the solid angle of the pixel and then the diffracted intensity from the analyser into that pixel. With the notation in figure 3.43, the Bragg angle in position  $z_d$  on the detector is:

$$\theta(z_d) = \theta_0 - \frac{\frac{1}{2}z_d \sin \theta_0}{p_0 + \frac{1}{2}z_d \cos \theta_0}.$$

The distance to the pixel is  $2p$ :

$$2p(z_d) = \sqrt{\left(p_0 + \frac{1}{2}z_d \cos \theta_0\right)^2 + \left(\frac{1}{2}z_d \sin \theta_0\right)^2}.$$

The space angle of the pixel is then:

$$d\theta_p = \frac{\sin \theta}{2p} dz_d,$$

and

$$d\phi_p = \frac{1}{2p} dz_d,$$

and the solid angle:

$$d\Omega_p = \frac{1}{4\pi} d\theta_p d\phi_p = \frac{1}{4\pi} \frac{\sin \theta}{4p^2} dz_d^2.$$

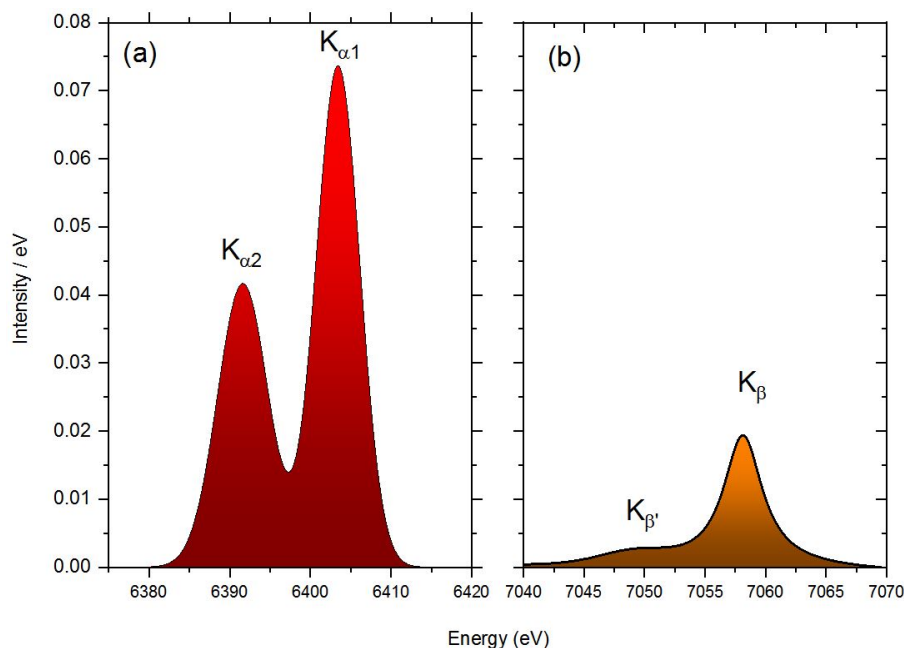


**Figure 3.44:** K emission from Fe. The sum of  $K\alpha$  and  $K\beta$  is normalised to 1. (a) The  $K\alpha$  intensity is 87.8% of the total intensity. (b) The  $K\beta$  intensity is 12.2% of the total intensity. The spectra are from  $[\text{Fe}(\text{terpy})_2]^{2+}$  and measured with the Johann spectrometer on ID09 (courtesy Dmitry Khakhulin).

Assuming that the horizontal divergence is focused into one superpixel on the detector, the intensity is:

$$dI_p(E_a) = N_{abs}^* \int R(E' - E_a) S(E') dE' \cdot d\Omega_p(E_a),$$

where  $S(E_a)$  is the normalised spectral density in figure 3.44 in ph/eV/pulse.

The integral can be calculated numerically or approximated using the box reflectivity in figure 3.39. The pixel intensity is:

$$dI_p(E_a) = DQE N_{abs}^* R_0 w_R S(E_a) d\Omega_p(E_a),$$

where DQE is the quantum efficiency of the detector at the XES energy,  $R_0$  the peak reflectivity and  $w_R$  the width. The solid angle  $d\Omega_p$  is not constant across the detector: it decreases by 6.6% from the low to high-end of the energy range. The calculated spectrum is shown in figure 3.45. In the top panel, the incident spectrum on one analyser is shown. The intensity is corrected for 7 keV absorption in water (transmission 0.679). The width of the line is 5.3 eV (FWHM). The Si(440) analyser reflectivity is shown in black. It accepts the pink XES spectrum in a 0.22 eV bandwidth. That is 24 times smaller than the width of the  $K\beta$  line. When the finite source size is included in the instrumental response, a sharp line is broadened to 0.42 eV, which is sufficient for resolving the structure in the  $K\beta$  spectrum.

The detected spectrum is shown in the lower panel of figure 3.45. Note the dramatic reduction before and after the analyser. That is unavoidable when measuring a full spectrum in one exposure. One analyser receives 65.4 ph/pulse from  $K\beta$  of which only 0.0101 ph/pulse are detected. The detected fraction is  $0.0101/65.4 = 1.54 \cdot 10^{-4}$ !

The calculated intensity, 0.0101 ph/pulse/analyser agrees with the observed one, 0.0106 ph/pulse, which is 5% higher. The agreement might be fortuitous but it indicates that the

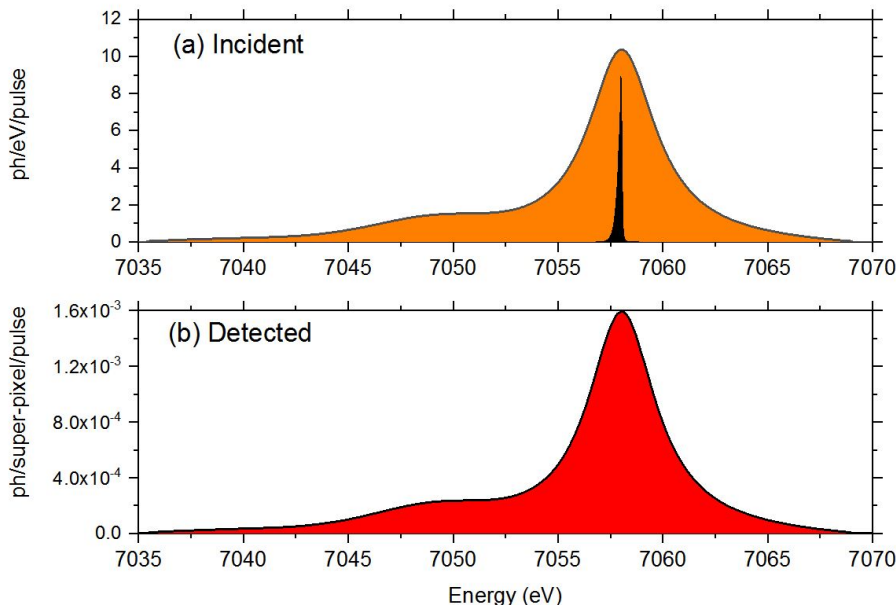


**Figure 3.45:** (a) Incoming spectrum from  $K\beta$  on one Si(440) analyser per pulse from a 10 mM  $[\text{Fe}(\text{phen})_3]^{2+}$  solution. The incoming flux on the analyser is 65.4 ph/pulse. The reflectivity of the analyser is shown in black. The position of the reflectivity is “walked” through the  $K\beta$  spectrum from dispersion in the Bragg angle. (b) Diffracted intensity on the detector. The horizontal pixels are summed into “superpixels” as if the sample was a point source. The integrated intensity is 0.0101 ph/pulse/analyser for  $1 \cdot 10^9$  ph/pulse at 15 keV. The measured intensity is 0.0106 ph/pulse, 5% higher.

beamline and the spectrometer are working as expected and that firm conclusions can be made from the experiments.

In passing we note that the spectral count rate (ph/BW) of the Johann spectrometer is greater than for one von Hámos analyser. We can get a quick estimate of the gain as follows. For the spherical analyser in the Johann spectrometer, the Bragg angle is constant over the crystal surface. Assuming that the bandwidth of the cylindrical and spherical analyser are the same, the Johann intensity is the area of the black reflectivity curve in figure 3.45(a). That curve has 1.70 ph/pulse with a detector DQE of 0.90. The Johann gain on the  $K\beta$  peak is  $1.7/0.0101 = 168$  for one Johann and one von Hámos analyser. With 16 von Hámos analysers, the Johann gain is 10.5. For monitoring population dynamics vs time, the Johann spectrometer is superior. The above comparison is slightly simplified since the Johann analyser is 1 m from the sample and has a radius of 100 mm. With these true dimensions, the Johann collects 1.49 ph/pulse with a corresponding gain in the count rate of 145 over the von Hámos. The parameters used in the intensity calculation are summarized in table 3.15.

The steps in the VH detection process are shown on a log scale in figure 3.47. We name it the “XES staircase” due to the dramatic reduction between the steps. For example the count rate from the HS state is 12.2 counts/sec with 8 analysers and running at 986.3 Hz.

We should finally mention a comparison with the intensity level at the FXE beamline at EuXFEL. In the recent  $[\text{Fe}(\text{bpy})_3]^{2+}$  experiment published in [45], the  $K\beta$  intensity was 2.5 ph/pulse/analyser with Si(531) analysers. The experiment was done with a 0.1 mm thick jet, 15 mM concentration and X-rays at 9.2 keV with  $1 \cdot 10^{11}$  ph/pulse. The intensity agrees qualitative with our predictions since the 100 fold gain in pulse intensity and the higher X-ray absorption at 9.2 keV would give a count rate for our sample of 3.7 ph/pulse/analyser.

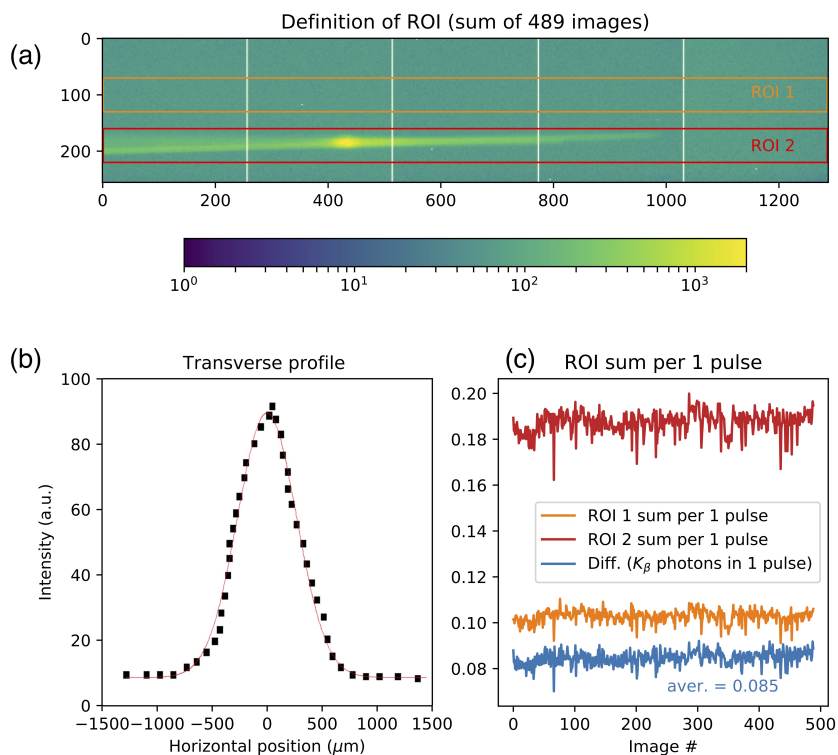


**Figure 3.46:**  $K\beta$  detection. (a) Image of the  $K\beta$  line. The image is the sum of 489 100-second exposures. (b) Focus of the  $K\beta$  line. The width is 0.60 mm, slightly bigger than the sample thickness 0.51 mm. (c) Extracting the total XES signal from the background. After background subtraction, ROI2-ROI1, the total  $K\beta$  intensity for 8 analysers is 0.085 ph/pulse.

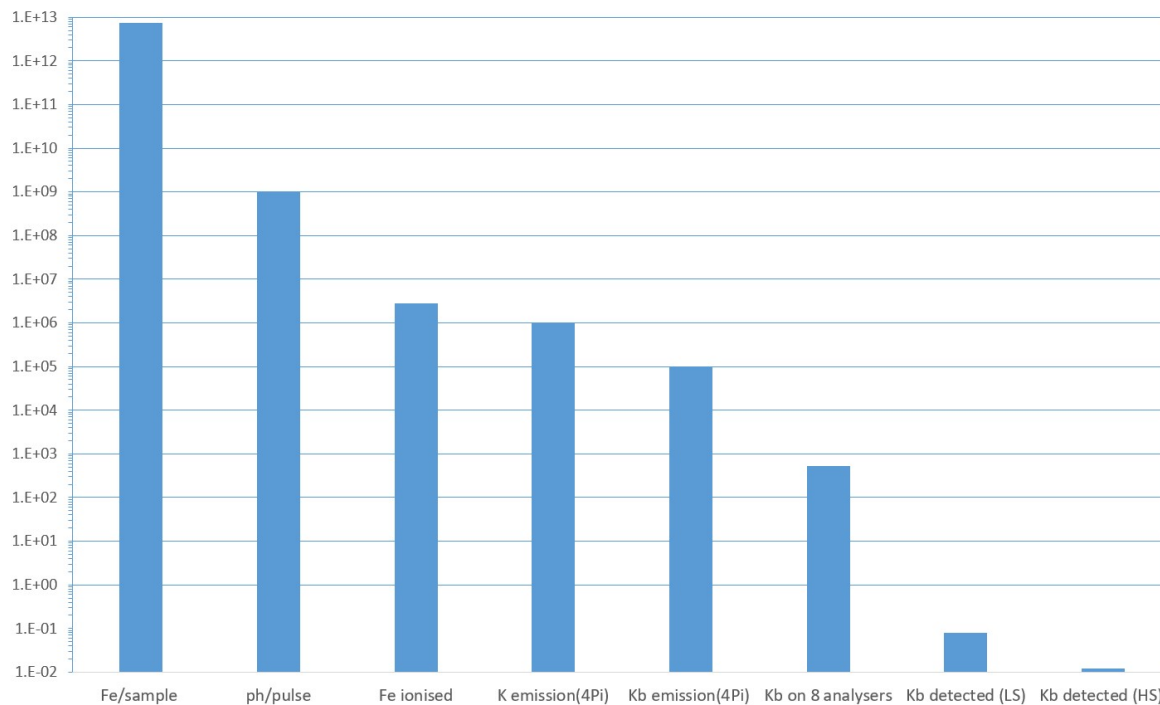


**Figure 3.47:** XES staircase for  $K\beta$  emission from  $[\text{Fe}(\text{phen})_3]^{2+}$  from the 15 keV beam with  $1 \cdot 10^9$  ph/pulse. The concentration of  $[\text{Fe}(\text{phen})_3]^{2+}$  is 10 mM and 8 Si(440) analysers are used. The HS occupancy is 15%.

Parameter	Value	Unit	Comment
Fe atoms in sample	$7.35 \cdot 10^{12}$		10 mM, volume = $0.06 \times 0.04 \times 0.509 \text{ mm}^3$
Fe atoms ionised	$2.85 \cdot 10^6$	atoms/pulse	15 keV pink beam, 2.4% BW and $1 \cdot 10^9$ ph/pulse
$4\pi$ K emission (excl. water abs.)	$9.80 \cdot 10^5$	K ph/pulse	34.4% X-rays, 65.6% Auger $e^-$
$4\pi$ $K\alpha$ emission (87.8%)	$8.61 \cdot 10^5$	$K\alpha$ /pulse	87.8% $K\alpha$ emission, no abs. corr.
$4\pi$ $K\beta$ emission (12.2%)	$1.20 \cdot 10^5$	$K\beta$ /pulse	12.2% $K\beta$ emission, no abs. corr.
$4\pi$ $K\alpha$ emission (incl. abs. in water)	$5.84 \cdot 10^5$	$K\alpha$ /pulse	Incl. water abs. at 6400 eV
$4\pi$ $K\beta$ emission (incl. abs. in water)	$8.12 \cdot 10^4$	$K\beta$ /pulse	Incl. water abs. at 7058 eV
Analyser solid angle of Si(440)	$8.03 \cdot 10^{-4}$	srad	Si(333) has $8.37 \cdot 10^{-4}$ srad
Incident $K\alpha$	469.3	$K\alpha$ ph/pulse	
Incident $K\beta$	65.2	$K\beta$ ph/pulse	
$K\alpha$ detection ratio Si(333)	$8.14 \cdot 10^{-5}$	per incoming $K\alpha$	Detector DQE 0.90
$K\beta$ detection ratio Si(440)	$1.54 \cdot 10^{-4}$	per incoming $K\beta$	Detector DQE 0.90
$K\alpha$ detected	0.0382	$K\alpha$ ph/pulse	
$K\beta$ detected	0.0101	$K\beta$ ph/pulse	
$K\alpha$ count rate	37.7	$K\alpha$ ph/s	986.3 Hz pulse rate from chopper
$K\beta$ count rate	10.0	$K\beta$ ph/s	986.3 Hz pulse rate from chopper

**Table 3.15:** Parameters for calculating the count rates of the  $K\alpha$  and  $K\beta$  emission in  $[\text{Fe}(\text{phen})_3]^{2+}$  for *one* cylindrical analyser in the von Hámos spectrometer. The simulation agrees to within 5% with the experiment.

# WAXS AND XES EXPERIMENTS ON $[\text{Fe}(\text{PHEN})_3]^{2+}$ IN WATER

$[\text{Fe}(\text{phen})_3]^{2+}$ , why is this metal complex of interest for the design of functional materials like solar cells? It is because metal complexes can capture visible light and generate an electric potential that can be used in solar cells. Classical solar cells are based on Si single-crystal wafers that work well with conversion efficiencies up to 23%, but they are expensive and only affordable for big industrial applications. In order to make smaller and cheaper solar cells, new technology has to be developed. One promising class of solar cells is dye-sensitised solar cells (DSSC). They are based on  $\text{TiO}_2$  nanoparticles covered by light capturing dye molecules. The principle is shown in figure 4.1. The dyes are transition metal complexes with a central 3d or 4d transition metal bound to organic ligands. These complexes efficiently absorb visible

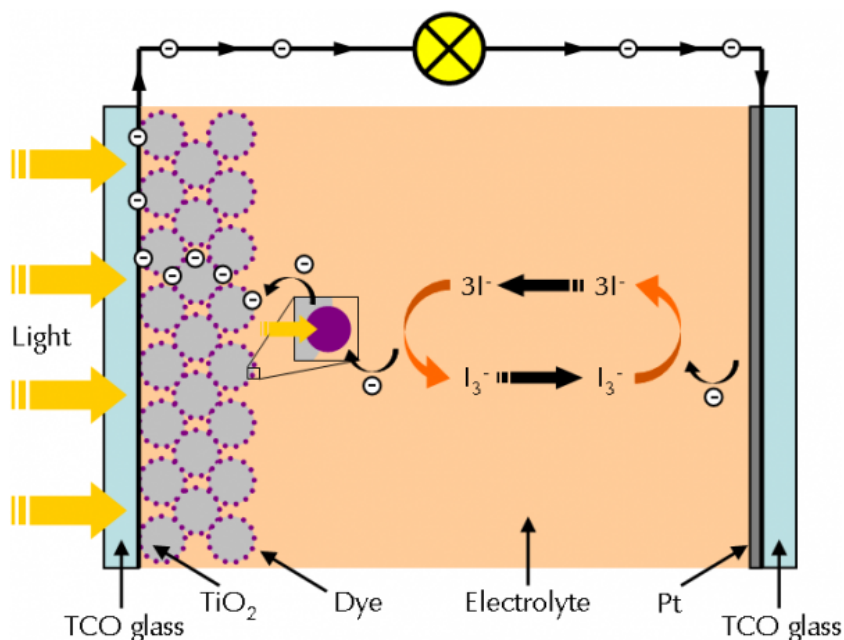


**Figure 4.1:** Principle of a solar cell with dye molecules coated on  $\text{TiO}_2$  nanoparticles. Upon the absorption of a photon, the 3d (or 4d) electron moves to the ligand in the MLCT state and most of the electrons are transferred to the  $\text{TiO}_2$  conduction band. The induced voltage can power an electric device. Finally the positively charged dye receives an electron from iodine  $\text{I}^-$  which terminates the cycle. Drawing from the company Gamry's web page.

light. Upon photon absorption, an electron is transferred from the metal 3d or 4d valence orbital to an unoccupied ligand orbital with a similar energy. This process is called metal-to-ligand charge transfer (MLCT) and the excited state of the molecule is called the MLCT state. Typical lifetimes of MLCT states are nanoseconds to microseconds for 4d metals like Ru and Os while it is sub picoseconds for 3d metals due to the weaker ligand field splitting [46]. After MLCT excitation, the molecule returns to the ground state either directly with the emission of light or by cascading through a sequence of states where the electron is localised on the metal. These states are called metal-centred states. The return to the GS can be radiative or non-radiative depending on the selection rules of the wave functions involved.

The efficiency of 3d and 4d metal complexes for the conversion of photon energy is very different. In Fe complexes, the charge separation in the MLCT states is extremely short, about 100 fs, because the electron is "captured" immediately by lower energy metal-centred states whereby charge separation is lost. In 4d metal complexes like  $[\text{Ru}(\text{bpy})_3]^{2+}$  and  $[\text{Os}(\text{bpy})_3]^{2+}$ , the MLCT lifetime is about 1 million times longer with lifetimes of 900 ns and 25 ns, respectively. The lifetime is longer since the molecule is trapped in the MLCT potential with no gateway to low energy metal centred states. The electron transferred to the ligand has time to further migrate to the semiconductor ( $\text{TiO}_2$ ) in the solar cell. Unfortunately 4d metals are rare and the high cost is detrimental for large scale applications in solar cells. As a result there is great interest in synthesising advanced organic complexes with Fe due to the high abundance of Fe and the much lower cost. Recent work by researchers in Villy Sundstrom's group at the University of Lund have managed to increase the energy of the metal centred states by synthesising ligands with a stronger ligand field. In the iron carbene complex  $[\text{Fe}(\text{btz})_3]^{2+}$  for example, the MLCT lifetime is 528 ps [47]. A schematic energy diagram comparing  $[\text{Fe}(\text{phen})_3]^{2+}$  with the Fe carbene complex is shown in figure 4.2. The energy of the metal centred triplet ( $S = 1$ ) and quintet states ( $S = 2$ ) in the carbene complex is so high

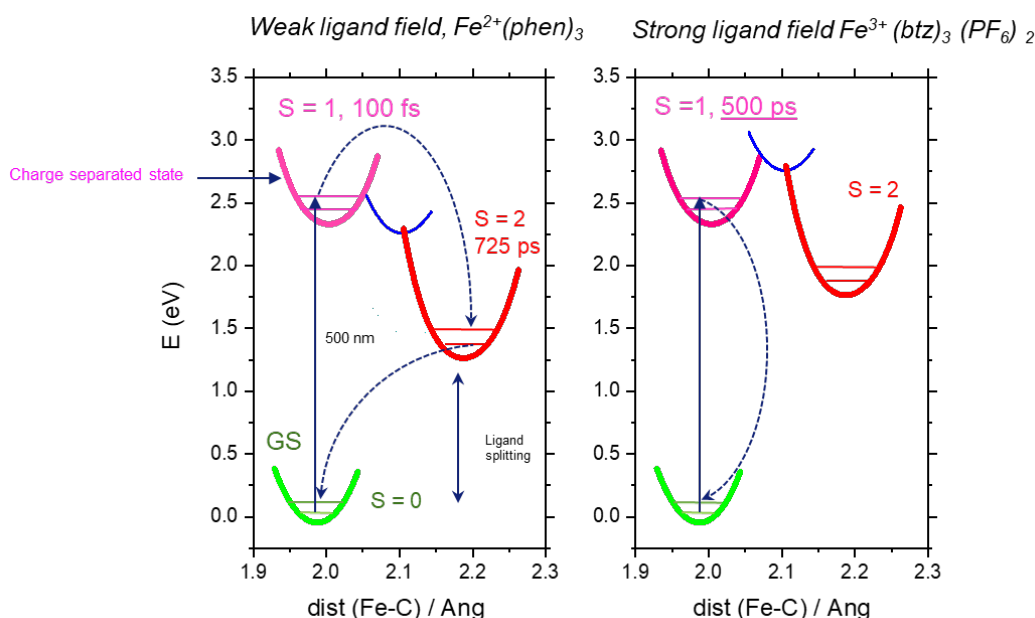


**Figure 4.2:** Simplified energy diagrams for weak and strong ligand field complexes. (a)  $[\text{Fe}(\text{phen})_3]^{2+}$ . (b) The Fe carbene complex  $[\text{Fe}(\text{btz})_3]^{2+}(\text{PF}_6)_2$ . The transit to the metal centred HS state ( $S = 2$ ) is blocked. The MLCT state decays to the GS with the emission of a photon. The MLCT state lifetime in acetonitrile  $\text{CH}_3\text{CN}$  is 528 ps, the longest lifetime for an MLCT Fe complex recorded so far.

that intersystem crossing from the MLCT potential is impossible. The MLCT state decays to the ground state in 528 ps in acetonitrile ( $\text{CH}_3\text{CN}$ ). For well separated states the decay rate is  $\propto 1/\Delta E$  as expressed by Fermi's Golden rule. The reader is referred to the excellent review by James McCusker for more details about the photophysics of transition metal complexes and their history [46].

The aim of the current study is to characterise the photocycle of  $[\text{Fe}(\text{phen})_3]^{2+}$  by time-resolved wide-angle X-ray scattering (WAXS), which measures structural changes and by X-ray emission spectroscopy (XES), which measures the spin state of  $\text{Fe}^{2+}$ . The experiments were performed with 100 ps X-ray pulses and the molecules were excited by 1.2 ps laser pulses. The photocycle is thus examined with 100 ps resolution. The experiments were done in aqueous solution of  $[\text{Fe}(\text{phen})_3]^{2+}$  at 10 mM concentration. As the molar concentration of water is 55.5 M, the solute/solvent mixing ratio is 1:5548. Compared with many other solution studies done on ID09, the low scattering power of Fe complexes ( $Z = 26$ ) is challenging since the intensity from pairs of atoms scales as  $Z_1 \cdot Z_2$ . As a result, the solute scattering signal is weak, typically  $1 \cdot 10^{-4}$  to  $1 \cdot 10^{-3}$  of the water background. The lifetime of  $[\text{Fe}(\text{phen})_3]^{2+}$  HS state was measured with the Johann spectrometer. The XES von Hámos spectrometer was used for the first time in this project to measure the spin and population of the HS state.

## 4.1 Structure and photocycle of $[\text{Fe}(\text{phen})_3]^{2+}$

The molecular structure of the  $[\text{Fe}(\text{phen})_3]^{2+}$  complex in the low spin ground state (LS,  $S = 0$ ) is shown in figure 4.3(a). The  $\text{Fe}^{2+}$  ion in the centre of the molecule is coordinated by six N atoms from three phenanthroline ligands that form three perpendicular planes in space. The six Fe-N distances are equal in the GS,  $1.99 \pm 0.01 \text{ \AA}$ . The coordination is only approximately octahedral due to ligand steric hindrance. In the high spin state (HS,  $S = 2$ ) Fe-N bonds are  $\sim 10\%$  longer and there is a small variation in the bond length as shown in figure 4.3(b). We will later explain the reason for the bond elongation. From Density Functional Theory (DFT) calculations by Latévi Max Lawson Daku, University of Geneva, the Fe-N bond lengths are predicted to be  $1.99 \text{ \AA}$  and  $2.18 \text{ \AA}$  for the LS and HS states, respectively. Note that these values are for the structure in aqueous solution and that they change slightly in other solvents.

In aqueous solution, the complex exhibits strong absorption in the MLCT band centred

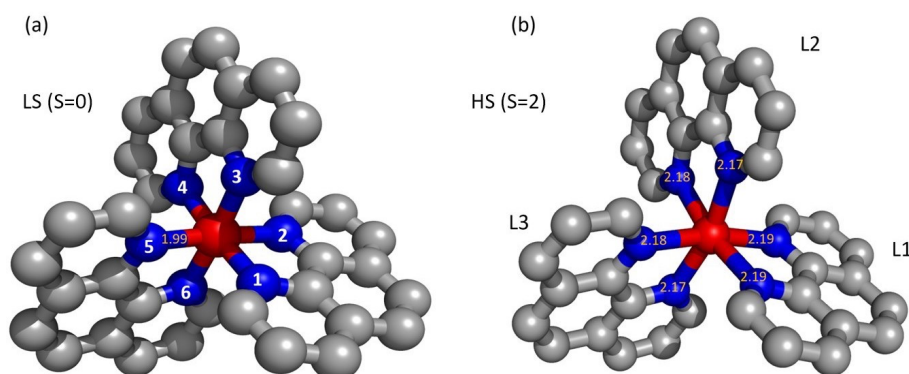


**Figure 4.3:**  $[\text{Fe}(\text{phen})_3]^{2+}$  in the LS (a) and HS state (b).  $\text{Fe}^{2+}$  is red, N blue and C grey (H atoms are omitted). The stoichiometry is  $\text{Fe}^{2+}(\text{N}_2\text{C}_{12}\text{H}_8)_3$ .  $\text{Fe}^{2+}$  has the configuration  $[\text{Ar}]3d^6$ . The HS state is distorted as seen by the slightly varying Fe-N bond distances.

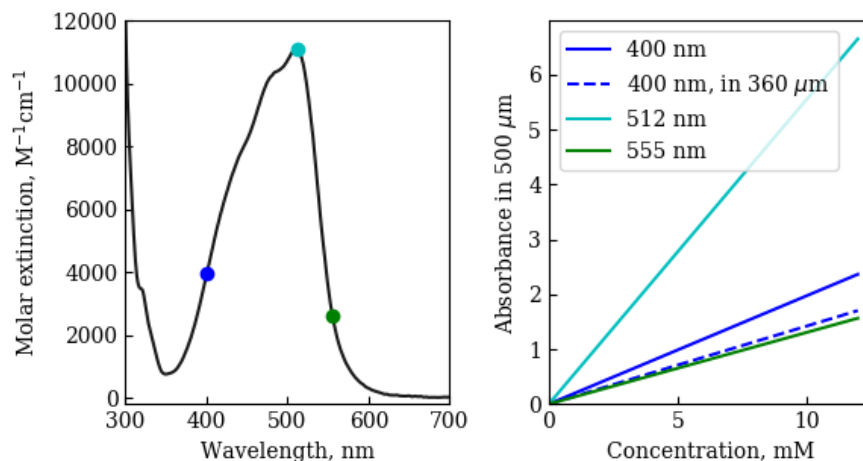


**Figure 4.4:** (a) Molar absorption of  $[\text{Fe}(\text{phen})_3]^{2+}$  in water measured with a NanoDrop OneC spectrometer. (b) Absorbance vs concentration for a  $500 \mu\text{m}$  liquid jet. For the 10 mM concentration used in this study,  $\mu^{-1} = 0.28 \text{ mm}$  at 400 nm.

at 512 nm. The Franck-Condon principle dictates that upon photon absorption, the molecule is excited vertically to the  $^1\text{MLCT}$  state. Due to intersystem crossing at lower energies the high spin state (HS) is formed swiftly, in less than 1 ps, which then decays to the GS in about 725 ps. The transit to the GS is non radiative and the vibrational energy is dissipated in the solvent in a few picoseconds. The absorption spectrum in water was measured with a NanoDrop OneC spectrometer in the PSCM lab of the ESRF/ILL, see figure 4.4(a). The MLCT absorption band lies between 390-600 nm with a maximum at 512 nm.

### 4.1.1 Ligand field splitting

To understand the  $[\text{Fe}(\text{phen})_3]^{2+}$  photocycle in detail, let's have a look at the 3d orbitals of  $\text{Fe}^{2+}$  alone and in presence of the ligand field of three (1,10)-phenanthroline ligands. The 3d orbitals are shown in figure 4.5. Isolated  $\text{Fe}^{2+}$  has the configuration  $[\text{Ar}]3d^6$  with all five 3d orbitals equal in energy. The six valence electrons are placed on these orbitals according to Hund's rule: spin repulsion in an orbital favours maximising the total spin, which gives 5 spin-up and one spin-down electron, i.e.  $S = 2$  (figure 4.6(a)). In octahedral coordination, the ligand field splits the equal 3d orbitals into two subsets with different energies, the lower energy  $t_{2g}$  ( $\pi$  bonding orbitals) and higher energy  $e_g$  ( $\pi^*$  antibonding orbitals). The energy gap  $\Delta$  between  $t_{2g}$  and  $e_g$  depends on the ligand field strength  $10Dq$  and the distance from the metal to its nearest neighbours (Fe-N). The spin-pairing energy, i.e. the energy it takes to put a spin up and spin down in the same orbital, competes with the energy splitting  $\Delta$  as follows. When  $P$  is smaller than  $\Delta$ , the six electrons pair up in  $t_{2g}$  with  $S = 0$ . If  $P$  is greater than  $\Delta$ , the energy is lowest with four electrons in  $t_{2g}$  and two in  $e_g$  resulting in  $S = 2$  [48]. The scheme is shown in figure 4.6.

Ligands like (phen)=(1,10)-phenanthroline or (bpy)=(2,2')-bipyridine have relatively strong ligand fields  $\Delta > P$ , and  $[\text{Fe}(\text{phen})_3]^{2+}$  and  $[\text{Fe}(\text{bpy})_3]^{2+}$  favour a low-spin configuration in solution at room temperatures. However, as the energy difference is not too big, the equilibrium can shift depending on factors like temperature, pressure, magnetic field, photoexcitation and solvent interaction. Such a phase transition is called spin-crossover (SCO). Octahedrally coordinated Fe(II) complexes form a big class of SCO compounds including  $[\text{Fe}(\text{terpy})_2]^{2+}$ ,  $[\text{Fe}(\text{phen})_2(\text{NCS})_2]^{2+}$  etc. As a rule of thumb, for each electron transferred

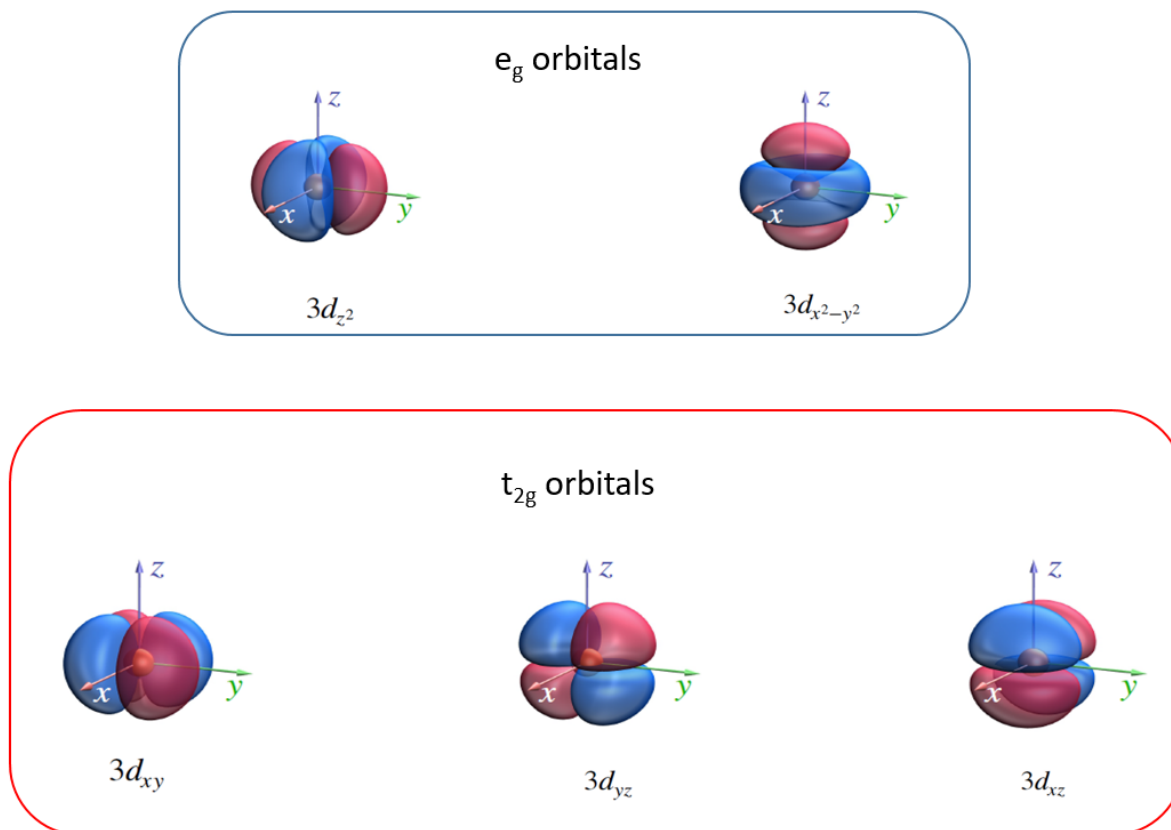


**Figure 4.5:**  $\text{Fe}^{2+}$  3d orbitals. The color shows the sign of the wavefunction, blue positive and red negative. Ligands are binding along the  $x$ ,  $y$  and  $z$  axis. The orbitals for the low energy level  $t_{2g}$  are  $3d_{xy}$ ,  $3d_{xz}$ , and  $3d_{yz}$ . They are fully spin up/spin down occupied in the LS state ( $S = 0$ ). The density of the  $t_{2g}$  orbitals on-axis is lower than for the  $e_g$  orbitals; the  $t_{2g}$  energy is therefore the lowest. The illustration was made using QChem5.2.

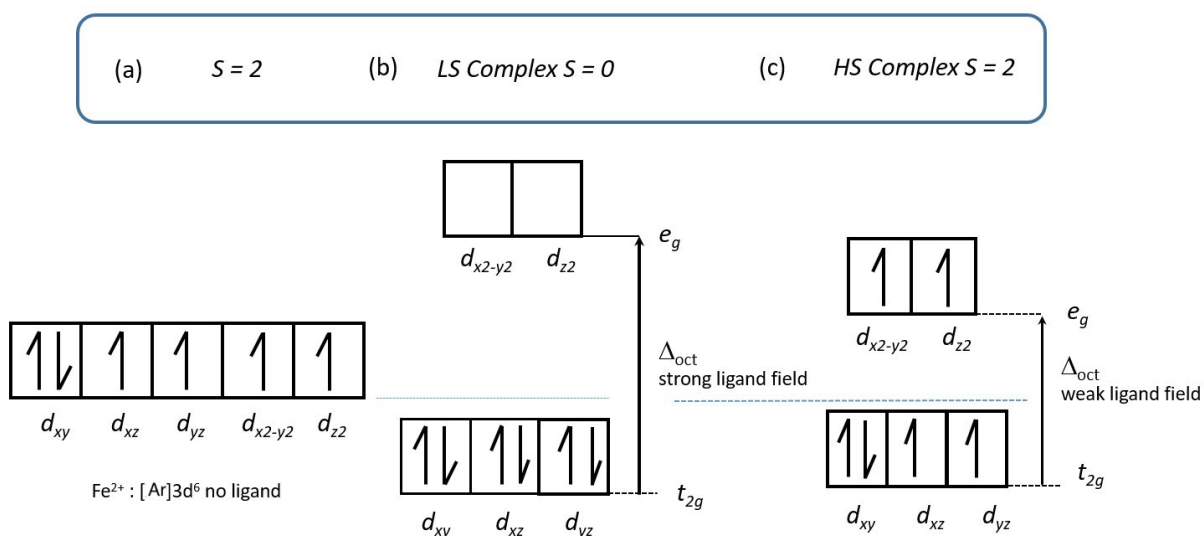


**Figure 4.6:**  $\text{Fe}^{2+}$  spin configurations. (a) Isolated  $\text{Fe}^{2+}$ , (b) a strong ligand field ( $\Delta > P$ ) forces the 3d electron into  $t_{2g}$  with  $S = 0$  (LS). (c) A weak ligand field ( $\Delta < P$ ) with  $S = 2$  (HS). Ab initio calculations by Marius Retegan, ESRF, predicts  $\Delta$  to 2.6 eV and 1.4 eV for the LS and HS states, respectively.

from a bonding to an antibonding orbital, the Fe-N bond length increases by  $\sim 0.1 \text{ \AA}$  [49]. That is clearly seen from the energy diagram for the singlet, triplet and quintet metal-centred states (figure 4.8(b)). Typically Fe-N (or Fe-O) distances in Fe(II) SCO compounds are about 1.9-2.0  $\text{\AA}$  in the low-spin state and 2.1-2.2  $\text{\AA}$  in the high-spin state.

## 4.1.2 Photo-excitation

When  $[\text{Fe}(\text{phen})_3]^{2+}$  is excited to the MLCT state, one of the 3d electrons is transferred to the lowest unoccupied orbitals of the ligand (nitrogen 2p orbitals). In less than 100 fs, the electron changes spin in the  $^1\text{MLCT} \rightarrow ^3\text{MLCT}$  intersystem crossing (ISC). After this, the system relaxes to the high-spin quintet state  $^5\text{T}_2$  via ISC, either directly in  $\sim 1$  ps or via the intermediate triplet state  $^3\text{T}_1$ , from which the transition to  $^5\text{T}_2$  takes  $\sim 100$  fs. The 3d electronic configuration in these states is shown in figure 4.7.

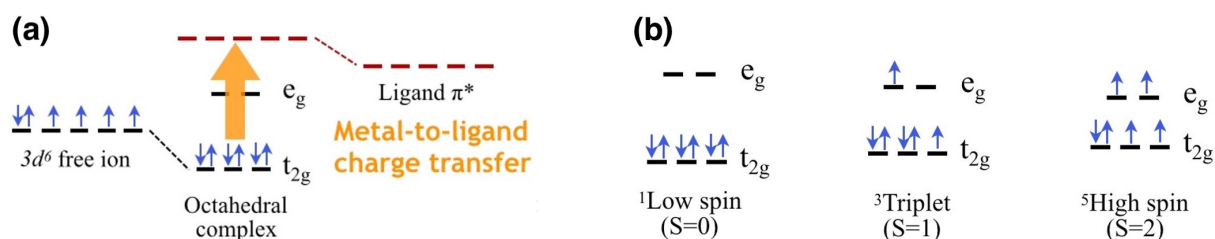


**Figure 4.7:** (a) Hybridisation of the 2p level of N with the  $e_g$  state of  $\text{Fe}^{2+}$ . The MLCT transition is shown by the orange arrow. (b) Filling of 3d orbitals in the singlet, triplet and quintet states for  $\text{Fe}^{2+}$ .

The photocycle of the  $[\text{Fe}(\text{phen})_3]^{2+}$  complex was studied theoretically by C. Sousa using density functional theory calculations (DFT) [49]. Energies of different excited states were optimised depending on the molecule configuration and transition probabilities between these states were predicted. Based on these transition cross sections, the  $[\text{Fe}(\text{phen})_3]^{2+}$  photocycle was predicted. The ground state and the excited states through which the system can relax are shown schematically in figure 4.8. The energy diagram shows the predicted potential energy surfaces (parabolic for small displacements) of the different states plotted against the reaction coordinate, Fe-N average bond length. Upon photo-excitation the complex is potentially passing all the presented states or skips some of them shown in parentheses:  $^1\text{A}_1 \rightarrow ^1\text{MLCT} \rightarrow (^3\text{MLCT}) \rightarrow (^3\text{T}_1) \rightarrow ^5\text{T}_2 \rightarrow ^1\text{A}_1$ . Note that the authors of this study indicate that both  $^1\text{MLCT}$  and  $^3\text{MLCT}$  have essentially the same Fe-N bond length because no antibonding orbital is occupied.

According to the transition optical absorption spectroscopy (TOAS) study of  $[\text{Fe}(\text{phen})_3]^{2+}$  in MeCN by J. Tribollet et al. [50], the Franck-Condon energy diagram assumes the Fe-N distance in the  $^3\text{MLCT}$  state similar to that of the metal-centred triplet  $^3\text{T}_1$  state. The authors report a rapid transition from  $^1\text{MLCT}$  to  $^3\text{MLCT}$  with a lifetime of  $< 100$  fs, after which the system decays in 220 fs directly into  $^5\text{T}_2$  state bypassing the triplet  $^3\text{T}_1$  state. The  $^3\text{MLCT}$  lifetime of 220 fs is very short and is comparable to the characteristic time of the Fe-N bond stretch of 160 fs, which means that the complex does not have enough time for vibrational cooling before the transition into the HS state (ISC). The vibrationally hot  $^5\text{T}_2$  state cools down in  $\sim 8.6$  ps in MeCN and relaxes back to the ground state in  $\sim 1.1$  ns. Using TOAS with 30 ps excitation at 540 nm the authors observed the ground state bleach and the appearance of a spectral feature at 340 nm that decayed in 1.1 ns (figure 4.9). The 340 nm

feature was assigned to the HS state  $^5\text{T}_2$  which was monitored via the high energy transition  $^5\text{T}_2 \rightarrow ^5\text{MLCT}$ .

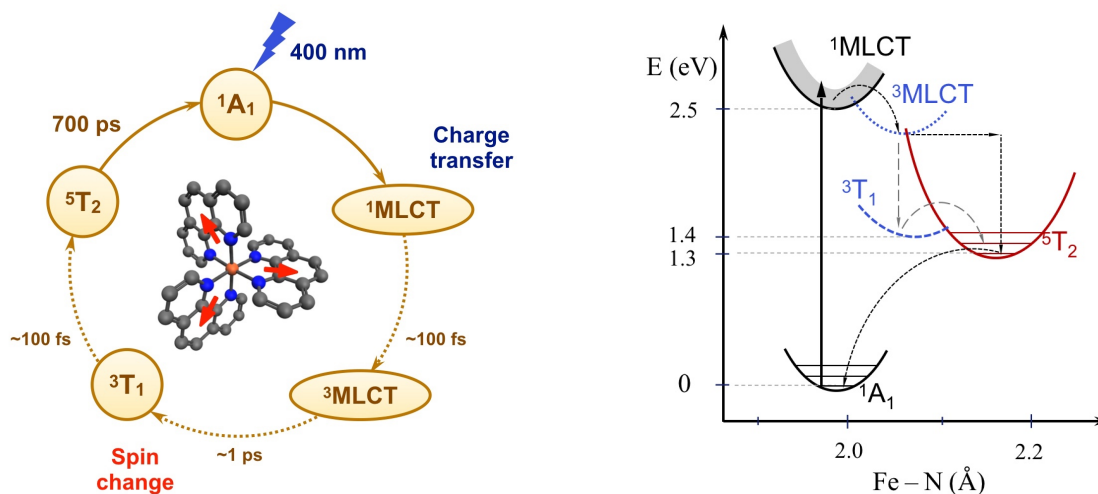


**Figure 4.8:** (a)  $[\text{Fe}(\text{phen})_3]^{2+}$  photocycle and lifetimes. (b) Energy bands from DFT. Upon photoexcitation the complex is likely to go through all the presented states or skip some of the states shown in parentheses as follows:  $^1\text{A}_1 \rightarrow ^1\text{MLCT} \rightarrow (^3\text{MLCT}) \rightarrow (^3\text{T}_1) \rightarrow ^5\text{T}_2 \rightarrow ^1\text{A}_1$ .

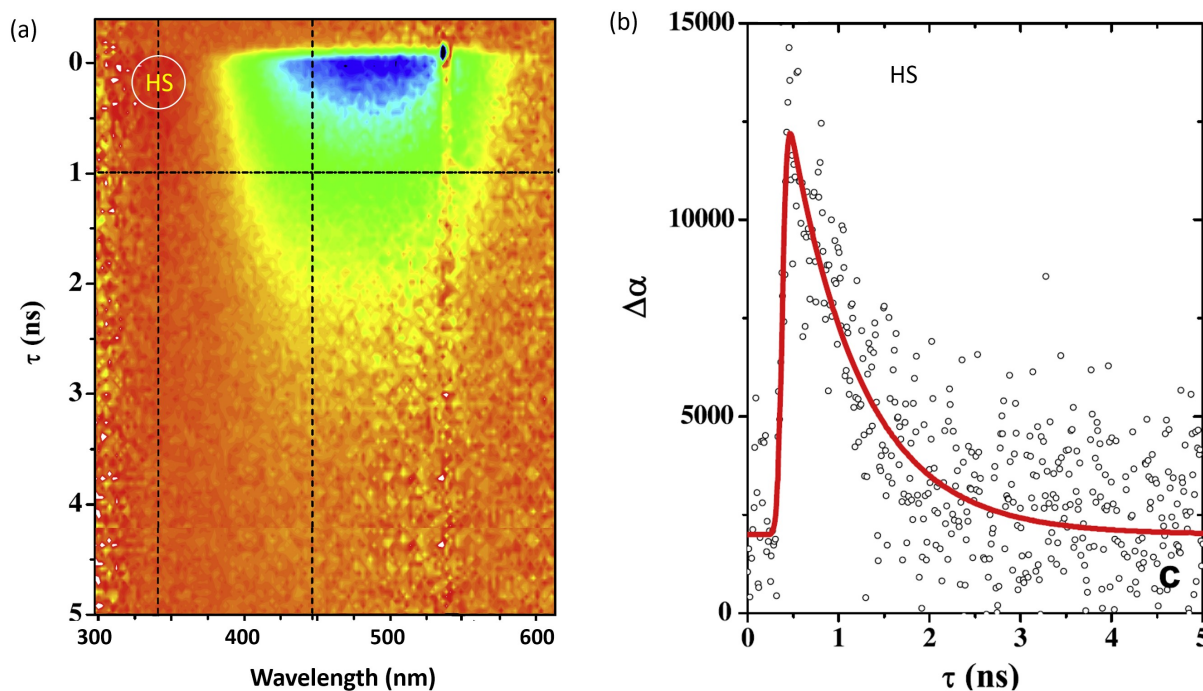


**Figure 4.9:** (a) Time-resolved absorption spectrum of  $[\text{Fe}(\text{phen})_3]^{2+}$  in acetonitrile ( $\text{CH}_3\text{CN}$ ). The solution is excited by 30 ps pulses at 540 nm and the absorption change is probed by a white light continuum. The depletion of the GS is seen in the blue negative area. The intensity code: blue < green < yellow < orange (0) < red. The formation of the HS state is shown in the circle at 340 nm. The 1.1 ns HS lifetime in  $\text{CH}_3\text{CN}$  is longer than the 0.73 ns lifetime in water. (b) Population decay of the HS state probed at 340 nm. Figure adapted from [50].

## 4.2 Laser excitation

The sample was bought as a 25 mM aqueous solution from Alfa Aesar and diluted to the desired concentration. The optical absorption of  $[\text{Fe}(\text{phen})_3]^{2+}$  was measured before and after the experiments to verify the absence of radiation damage and check the actual sample concentration. The UV-Vis absorption spectra were measured with the NanoDrop OneC UV-Vis spectrometer in the PSCM laboratory at ESRF and with the OceanOptics spectrometer in the ID09 sample preparation laboratory. The  $[\text{Fe}(\text{phen})_3]^{2+}$  extinction coefficient as a function of absorption wavelength is shown in figure 4.4 together with the optical density (OD) dependence of the sample concentration for various wavelengths and jet thickness. The extinction coefficient was derived from the spectra by normalising to the concentration and sample thickness (figure 4.4(a)). The measured spectra are in good agreement with the published absorption spectra of  $[\text{Fe}(\text{phen})_3]^{2+}$  in solution [51].

The concentration and excitation wavelength were chosen after a comparison with the parameters in the published works [52], [53] and varied later on. In the XAS work by S. Nozawa [52], the excitation of a 50 mM solution was done with 2 ps & 400 nm laser pulses. The optical density was  $\sim 6$  at 400 nm and the power density  $3.5 \text{ mJ/mm}^2$ . In the XAS study by H. Wang [53], a 250  $\mu\text{m}$  liquid jet with a 6 mM solution was excited at 515 nm (OD  $\sim 1.6$ ) by 760 fs long pulses with the power density  $0.27 \text{ mJ/mm}^2$ . Both experiments were done in a quasi-collinear geometry of the laser and X-ray beam.

In the present study, the time-resolved WAXS and XES experiments were done using  $[\text{Fe}(\text{phen})_3]^{2+}$  solutions with 3-10 mM concentrations. The sample was excited by 1.2 ps long laser pulses at 1 kHz, at various excitation wavelengths in the MLCT absorption band: 400 nm, 512 nm and 555 nm. The sample was circulated by a rotary pump and injected into the beam by a 0.36 mm nozzle from the Swiss company Kyburz Sapphire or by capillaries that were cut just above the beam. In general the jet thickness was in the range 360-500  $\mu\text{m}$ . These parameters covered the range of optical densities from 0.6 to 5 and are shown in table 4.1.

If the absorption of the laser beam obeys Beer-Lambert's law, i.e. the intensity is far from saturating the absorption, the maximum signal-to-noise ratio (S/N) in a laser ON/laser OFF difference measurement can be shown to be at OD about 0.6 for a weak signal on a large background. At this optical density, 25% of the beam is transmitted and thermal gradients in the sample are low. When the optical density is very high, 2-4, the beam is absorbed on the surface of the jet which might render it unstable. However, in some cases the choice of a high sample optical density is justified, in XES for example since that technique is insensitive to solvent hydrodynamics.

Beer-Lambert's law is only valid for low intensity beams when the number of photons is much lower than the number of chromophores. In time-resolved scattering experiments with X-rays however, the ratio of laser photons and chromophores is of the same order to increase the weak signal. If the laser bleaches the chromophores during the duration of the pulse, the first layers of the liquid become transparent and the pulse can penetrate further into the sample. Unfortunately this rarely happens in practice.

As the laser fluence is very high, non-linear multi-photon excitations might occur. This can be checked by a power titration: the excitation is done at increasing pulse energies and the signal is plotted as a function of pulse energy. If multi-photon excitation is absent, the dependence is linear. And if two-photon absorption is present, the signal will have a quadratic term at high pulse energies.

The 800 nm fundamental of the picosecond laser system was either sent through the breadboard for 2<sup>nd</sup> harmonic generation to obtain 400 nm pulses or through the TOPAS to

Inhouse run	WAXS			XES	
	IHCH-1217	IHCH-1265	IHCH-1305	IHCH-1321	IHCH-1456
$\lambda$ (nm)	512, 555	400	400	400	400
Jet ( $\mu\text{m}$ )	360	500	500	$360 \times \sqrt{2}$	$360 \times \sqrt{2}$
C (mM)	10	10, 3	10, 3	25	25, 10, 3
OD	3.8, 1	2, 0.6	2, 0.6	5	5, 2, 0.6
Power density (mJ/mm <sup>2</sup> )	0.8 – 1.3 1.3 – 3.5	0.4 – 2.5 0.3 – 1.3	0.3 – 3.6	2.3	0.5 – 1.5
Delays	100 - 700ps 100ps - 8ns	100ps - 3ns 100ps - 4ns	100ps, 3ns	100ps - 2ns	100ps
Bunch mode	7/8 + 1	16-bunch	7/8 + 1	7/8 + 1	7/8 + 1 (top-up)
SB current (mA)	2.0 – 8	5	2.0 – 8	1.1 – 8	7.5
X-ray beam	19 keV Ru	18 keV Ru	18 keV Ru	15 keV pink	15 keV pink
Primary slits (mm <sup>2</sup> H×V)	5 × 0.7	7 × 0.7	5 × 0.7	3 × 0.7	2 × 0.5
Focus at sample ( $\mu\text{m}^2$ H×V)	100 × 60	100 × 60	100 × 60	100 × 60	40 × 60
Exposure	20 s	3 s	4 s – 6 s	567 × 3 s	489 × 100 s
detx (mm)	45	39.75	36.5 – 40		
$q_{max}$ ( $\text{\AA}^{-1}$ )	10.7	10.6	10.8		

**Table 4.1:** Summary of experimental parameters for time-resolved WAXS and XES experiments on  $[\text{Fe}(\text{phen})_3]^{2+}$  in solution.

obtain other wavelengths by nonlinear frequency mixing. The residual 800 nm component from the 2<sup>nd</sup> harmonic crystal was removed with a reflecting mirror. The laser was operating at 1 kHz and its power was measured with the WaveMaster power meter from Coherent to obtain the desired pulse energy. The laser beam was guided to the sample by mirrors and focused by a lens with a  $f = 0.5$  m focal length. The laser was focused slightly downstream the sample to avoid ionisation in air which often occurs at high power densities.

To measure the laser spot size at the sample, a photodiode with a 10-30  $\mu\text{m}$  pinhole was mounted on the goniometer and placed in the cross-hair of the Basler camera of the sample microscope. The pinhole was scanned horizontally and vertically to measure the laser spot size. Sometimes a full mesh scan was made to map the laser profile in 2D. The laser was typically focused to a round spot of 200-250  $\mu\text{m}$  diameter.

The laser beam is polarised vertically and the pulse energy can be attenuated by changing the orientation of a wave plate in the laser path. The waveplate is motorised and calibrated at the beginning of the experiment. That makes it possible to adjust the laser pulse energy from the control hutch. For calibration, the laser power was measured after the wave plate for a sequence of wave plate orientations (figure 4.10). The pulse energy is finally measured at the sample position to correct for losses in mirrors and the focusing lens. Typically 60-70% of the power was transmitted to the sample.

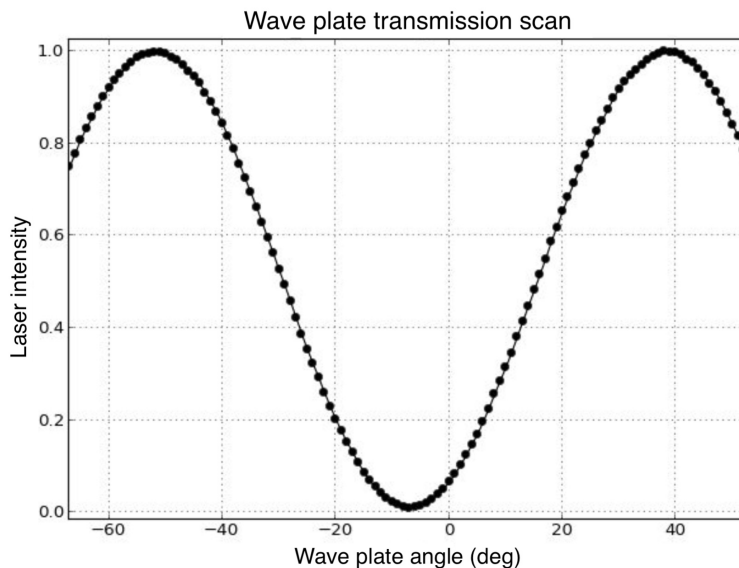


**Figure 4.10:** Scan of the laser intensity vs wave plate orientation. The laser intensity is varied by changing the angle of the wave plate.

The laser energy densities given in this section were calculated as the average density over the X-ray illuminated surface of the sample. For this, the laser profile was approximated by a 2D Gaussian and the fraction of pulse energy passing into the X-ray illuminated area was divided by that area. Table 4.1 summarises the energy densities used in all the experiments in this study. The datasets presented in the results were acquired at energy densities below the threshold of the non linear processes estimated from the power titration plots in figure 4.23. The power titrations were made as a check in the beginning of each WAXS, XES and TOAS experiment.

### 4.3 Sample delivery

The jet allows to refresh the sample for every pump-probe pulse pair, in our case, every millisecond. In addition, the problem of accumulating radiation damage and heat is greatly reduced. Finally irreversible reactions can be studied as well. The liquid sheet from a nozzle or the column of liquid from a cut capillary are exposed directly to the beam. The flow speed of a  $\varnothing$  0.5 mm capillary nozzle was measured and found to decrease in the course of the experiment. With the speed of the rotary pump at 16.5 rpm, the flow speed was initially 2.24 m/s, then 2.04 m/s after 2h and finally 1.84 m/s after 4h. The minimum flow speed is given by the speed needed for the jet to move out of the X-ray beam by the vertical size of the laser spot between two pulses 1 ms apart. With the 230  $\mu$ mV laser beam, the minimum speed is 0.23 m/s. The Swiss sapphire nozzle from Kyburz and the capillary jet are shown in figure 4.11.

### 4.4 Beamline configuration

In the XES and WAXS measurements shown below the synchrotron was operated in 16-bunch and 7/8 + 1 modes with a single bunch current of 2 – 8 mA. The U17 undulator gap was scanned to optimise the X-ray intensity with the Ru multilayers at 18 keV. The highest intensity was found with the U17 gap at 8.88 mm. The primary slits settings were from 7

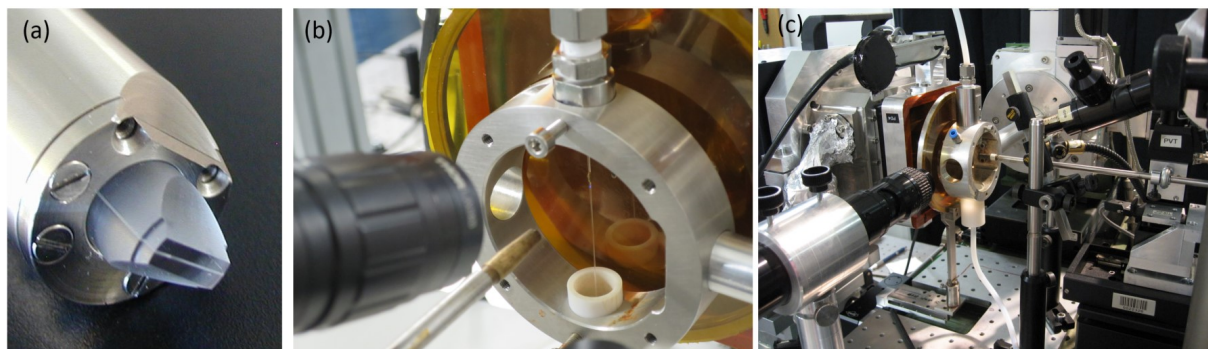


**Figure 4.11:** Jet systems for sample injection into the beams. (a) The Swiss sapphire nozzle (Kyburz) produces a flat 0.36 mm sheet of liquid. (b) Capillary nozzle produces a cylindrical column of liquid. The blue 400 nm laser beam is seen on the bare part of the liquid. (c) Collimator, sample cell, microscopes and the Rayonix detector.

$\times 0.7 \text{ mm}^2$  (H $\times$ V) in the 16-bunch mode down to  $2 \times 0.5 \text{ mm}^2$  in the 7/8 + 1 mode with long exposures, which gave a good compromise between high flux and a stable beam. The X-rays were focused with the old toroidal mirror to  $100 \times 60 \mu\text{m}^2$  (H $\times$ V). These parameters are summarised in table 4.1. Note that the Gaussian X-ray focus is cut by the sample slits so that the beam profile on the sample is a slit function with sharp edges.

To ensure single-pulse isolation from single bunches separated by 176 ns, the beam was sent through the 0.126 mm high tunnel in the rotor of the high-speed chopper 1.8 m from the focus. In a continuous beam, the rotor would chop out a 265 ns pulse with a trapezoidal profile in time (baseline). Single pulses were selected at 986.3 Hz which was also the frequency of the laser.

An intense beam with a symmetric energy spectrum with a 2.1% bandwidth at 18 keV was produced by the Ru/B<sub>4</sub>C multilayer monochromator 0.95 m upstream the sample. The intensity of the Ru beam was  $\sim 3 \cdot 10^8$  photons/pulse at 18 keV. The multilayer produces a symmetric spectrum from the asymmetric undulator spectrum and it removes higher harmonics as shown in figure 3.21. The pulse from the 8 mA single bunch is 120 ps long (FWHM).

The liquid jet was mounted on a horizontal translation stage gony that allowed to centre it on the beam. The beam position ( $y, z$ ) was determined by scanning a needle across the beam while monitoring transmitted intensity on the PD3 diode. The beam centre was marked with a cross-hair on the microscope.

The primary beam was stopped by a  $\text{\O} 1.6 \text{ mm}$  tungsten beamstop glued onto a circular kapton window. The beamstop can be seen after the sample cell in figure 4.11. The beamstop was moved as close as possible to the sample in order to minimise scattering in air.

The scattering was recorded on the  $170 \times 170 \text{ mm}^2$  Rayonix HS170 detector 40 mm from the liquid jet. With 18 keV X-rays, the detection area allowed to record a  $q$ -range of  $0.6 - 9.77 \text{ \AA}^{-1}$  for the inscribed cone on the square detector and up to  $10.67 \text{ \AA}^{-1}$  when the corners of the square are included. The sample-to-detector distance  $\text{detx}$  was refined by recording the diameter of the liquid peak as a function of  $\text{detx}$  as shown in figure 4.13(b). The beam centres were measured to ensure that the  $\text{detx}$  translation stage moved parallel to the beam. The jet was exposed to the pulsed beam for  $\sim 4 \text{ s}$  per image on average, for which the liquid peak intensity was  $\sim 30 \cdot 10^3 \text{ cts/pixel}$ . At that intensity, the response of the detector is linear.

## 4.5 WAXS measurements

The data collection was done using the waxscollect macros in SPEC (figure 4.12). Scattering patterns were acquired at different laser/X-ray time delays programmed to change in a loop. For each time delay a scattering pattern was recorded by exposing the detector to 1 kHz bursts of X-ray pulses for 3-6 s until 30-50% saturation. Then the image was read out and saved and the time delay changed to the next value in the sequence. The duty cycle, i.e. the fraction of time spent on data acquisition, was about 60-70%. The dead time is due to readout and saving of images and for changing motor settings. Positive time delays were interleaved by negative delays. The negative time delay corresponds to the X-ray probe pulse arriving before the laser and is used as a reference for the non-excited sample. The temperature profile of the jet is more uniform with the laser ON for all time delays. Sometimes the time delays were randomised to avoid systematic errors such as the storage ring current decay, sample concentration drift etc.

```

TIME-RESOLVED WAXS DATA COLLECTION (N354)
Angular settings:   from 0 to 1e-6 deg in steps of 1e-10 deg
Laser mode:        <on>
Time delay:        -3ns,100ps,185ps,340ps,630ps,-3ns,1.2ns,2.2ns,4ns,1us
File basename:     run01          Suffix: .edf
Description:       Dye 2 in ACN OD 1.0, wpo 10.4, 60uJ/pulse, detx=40
Log file:          run01.log
Path:              /data/id09/inhouse/Victoria/IHCH1305/dye2_ACN/run01

Current image: 8 of 100010 run01_0008, 7.9e-09 deg, time delay 2.2ns

Will take 100010 images. Estimated time: 11d 22h

Current iteration: 1 of 1

Waiting for burst mode to finish (remaining 7436 pulses)
duty cycle          78.58%
for read/save:     1.44%
for log:           0.83%
for spec(no log)  18.07%
--> ESC to cancel (wait for readout to finish)

```

**Figure 4.12:** Input parameters for waxscollect in SPEC. Nine positive time delays from 100 ps to 1  $\mu$ s are programmed in a loop that is repeated indefinitely. The non-excited reference is taken at -3 ns (the angular rotation in the first line is not used).

The sample-to-detector distance should be known as accurately as possible and is needed for calculating the scattering angle for a given pixel on the detector, which in turn determines  $q$ . An error in `detx` leads to a systematic error in the  $q$  scale and thus to an error in the Fe-N distance.

The Rayonix detector is moved on a motorised stage `detx` parallel to the incoming beam. The stage is pre-calibrated but when you mount a new sample, the sample-to-detector distance has to be checked. The sample-to-detector distance used in this work is 35-45 mm. The true sample-to-detector distance is measured from the radius of the liquid peak as a function of `detx`. Scattering patterns were recorded for several `detx` values. Each of the patterns has a ring from the maximum intensity, the liquid peak, as shown in figure 4.13. The ring radius depends linearly on the true distance to the sample. The ring radius and centre were fitted with the Fit2D software (figure 4.13(a)). The fitted values are plotted as a function of `detx` and the correction is found from the linear fit in figure 4.13(b). By measuring the ring centre vs `detx`, it is possible to check that the detector translation is truly parallel to the X-ray beam.

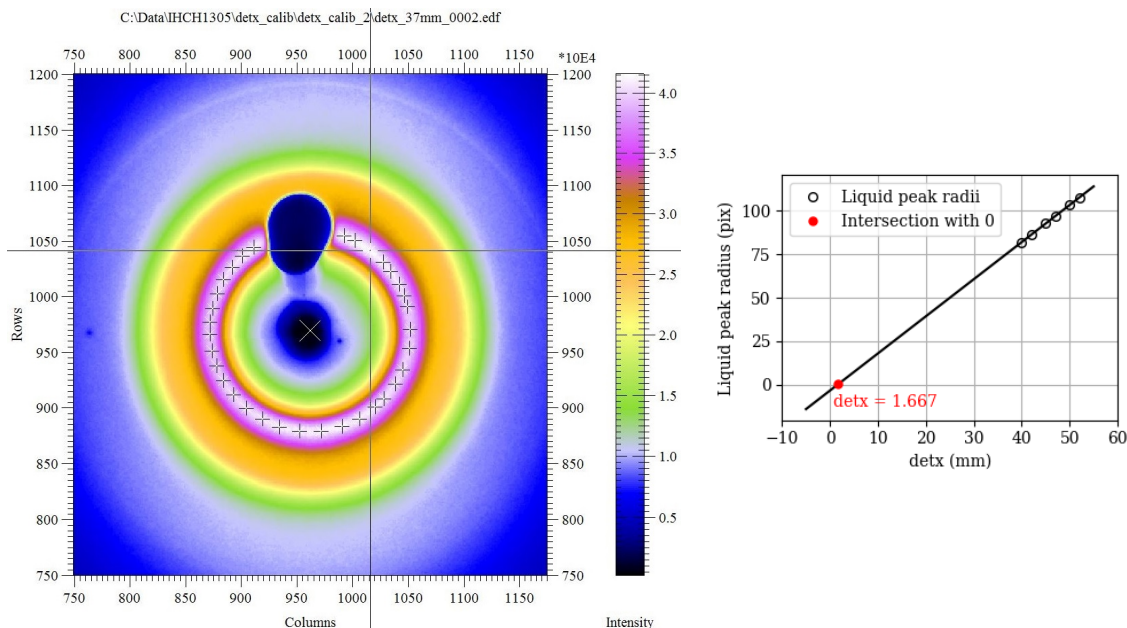


**Figure 4.13:** (a) Scattering pattern from water visualised by Fit2D. The black areas are shadows from the X-ray and laser beamstop (top). The liquid peak radius and the beam centre were calculated from 30 data points marked by crosses in the image. (b) The liquid-peak radius vs  $\text{detx}$  is fitted to a straight line. The true sample-detector distance is 1.667 mm smaller than  $\text{detx}$  before correction.

The first time-resolved WAXS experiment on  $[\text{Fe}(\text{phen})_3]^{2+}$  in aqueous solution was done in April 2017. Time-resolved difference scattering curves were obtained at a 100 ps time delay after excitation with 555 nm and 512 nm beams from the TOPAS. The decay of the time-resolved difference scattering signal was recorded at 100 ps – 8 ns time delays. For the 512 nm run, the difference signal was acquired at different laser fluences to check the signal linearity.

The 25 mM as-received solution was diluted to 10 mM. The solution was circulated by the closed loop rotary pump (gear pump) with the Swiss Kyburz Nozzle that makes a 360  $\mu\text{m}$  thick flat jet.

In the experiment, two laser wavelengths were chosen:  $\lambda_1 = 512$  nm for maximum absorption in the MLCT band and  $\lambda_2 = 555$  nm at the tail of the band for a more gentle and penetrating excitation with lower energy photons. These wavelengths were produced by the TOPAS laser. The optical density is  $\text{OD} = 4$  at 512 nm and  $\text{OD} = 0.7$  at 555 nm.

The experiment started with the laser tuned to  $\lambda = 555$  nm and focused to  $236 \times 222 \mu\text{m}^2$  (FWHM  $\text{H} \times \text{V}$ ). The number of  $[\text{Fe}(\text{phen})_3]^{2+}$  molecules in the  $100 \times 60 \times 360 \mu\text{m}^3$  volume of a 10 mM solution illuminated by the X-ray beam is  $N_{\text{mol}} = 1.3 \cdot 10^{13}$ . In order to estimate the total pulse energy in the experiment, let's calculate the laser pulse energy needed for the absorption to match that number. Approximating the laser beam with a 2D Gaussian ( $\sigma \cdot 2.355 = \text{FWHM}$ ), 9.5 % of the photons fall into the X-ray area of  $100 \times 60 \mu\text{m}^2$ . The OD 0.7 sample transmits  $0.1^{0.7} = 20\%$  of the photons, the rest is absorbed (neglecting reflection losses). The pulse should therefore have  $N_{\text{ph}} = N_{\text{mol}}/0.095/0.8 = 1.7 \cdot 10^{14}$  photons in this simplified model that assumes that  $[\text{Fe}(\text{phen})_3]^{2+}$  is bleached in the excited state during the 1.2 ps pulse. The associated pulse energy is 61  $\mu\text{J}$  and energy density 1.16  $\text{mJ}/\text{mm}^2$ . A similar calculation for 512 nm and  $\text{OD} = 4$  gives 53  $\mu\text{J}/\text{pulse}$  and 1  $\text{mJ}/\text{mm}^2$ .

The second time-resolved WAXS experiment was done in August 2017 on  $[\text{Fe}(\text{phen})_3]^{2+}$  in aqueous solution at two concentrations, 3 mM and 10 mM, using 400 nm laser excitation. The laser wavelength was changed to 400 nm to get a more stable beam since the TOPAS

beam was fluctuating in position and intensity at that time. This choice is non optimal since MLCT is excited into a higher vibrational state that transfers more heat to the solvent. For both concentrations the scattering was recorded with good statistics and the signal decay was followed up to 2 ns (+ a 1  $\mu$ s time delay for thermal calibration when the solvent expansion is completed). Various laser fluences were examined to check the linearity and choose the optimal power density.

The third experiment was done in October 2017 on  $[\text{Fe}(\text{phen})_3]^{2+}$  with 400 nm laser excitation. Aqueous solutions of 3 mM and 10 mM concentrations in water and in acetonitrile Me(CN) at 7 mM. The signals at 100 ps were studied as a function of laser fluences in order to complete the linearity study in the previous experiments. The MeCN solutions were also excited with 400 nm pulses at 1 mJ/mm<sup>2</sup>. Time-resolved data were recorded with good statistics and the signal decay followed to 3 ns. An example of the raw data is shown in figure 4.14.

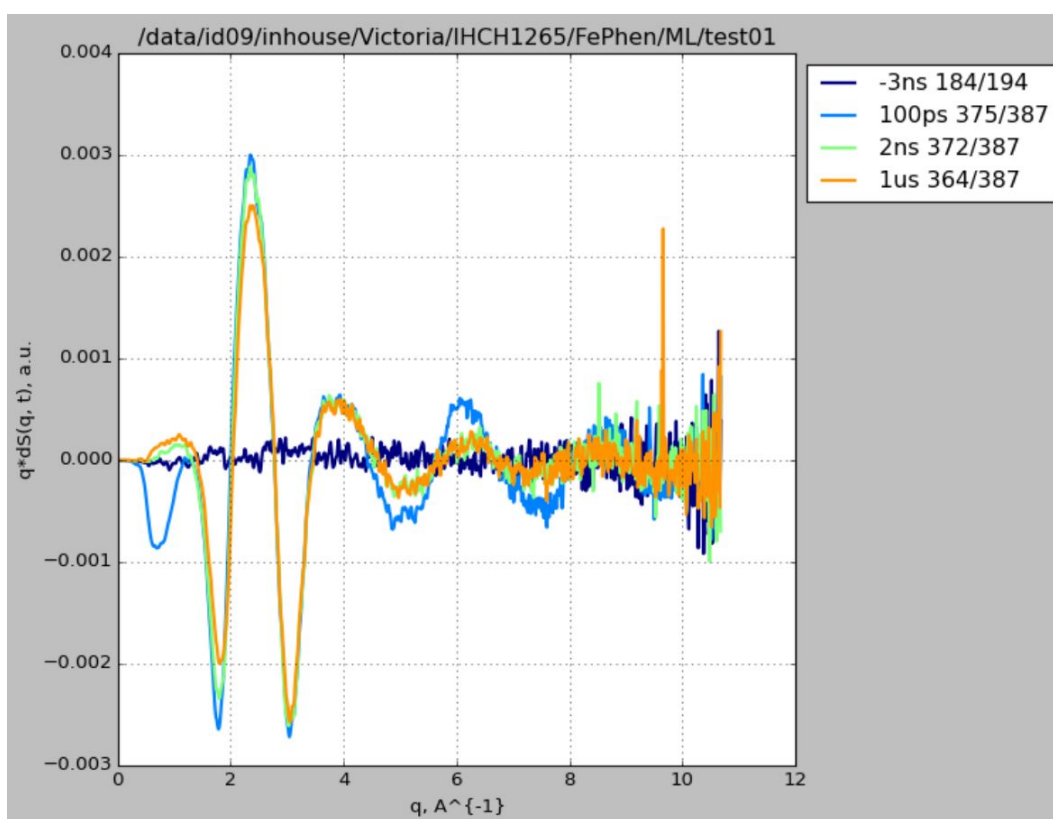


**Figure 4.14:** Difference scattering Laser ON - laser OFF for  $[\text{Fe}(\text{phen})_3]^{2+}$  in water after radial integration in the WAXSGUI. Each curve is the average of  $\sim 370$  images. For the blue 100 ps curve, the negative peak between  $0.5 - 1.5 \text{ \AA}^{-1}$  is from the  $0.19 \text{ \AA}$  Fe-N stretch in the HS state. Variations in the synchrotron current are compensated by scaling the laser ON and laser OFF curves' average intensity between  $5.5-8 \text{ \AA}^{-1}$  to 1 before subtraction.

## 4.6 Dye measurements

In each experiment, the difference curves were measured not only for the  $[\text{Fe}(\text{phen})_3]^{2+}$  solutions, but also for dye solutions in order to have the pure solvent response to laser heating taken with the same setup. We recall that the azobenzene-based dyes used for the solvent calibration undergo a trans-cis isomerisation upon photon absorption in the visible [32]. The

excited state lifetime is much shorter than the pump-probe experiment time resolution and therefore the solute structural change is not detected. The energy deposited by the laser is dissipated in the solvent from vibrational relaxation in tens of picoseconds as discussed earlier in the cooling of hot points. The solvent response caused by changes in solvent temperature, pressure and density is thus measured by scaling the amplitude to the water differentials shown in figure 2.14. The differential scattering at 100 ps  $dS(q, 100 \text{ ps})$  corresponds to the solvent response term caused by an isochoric temperature rise and  $dS(q, 1 \mu\text{s})$  is the solvent response after expansion at the temperature after the expansion.

In each experiment the air scattering was measured by stopping the liquid jet and taking an image with the same exposure time as for the sample. This allows to correct the scaling of ON and OFF curves as discussed later in this chapter.

## 4.7 WAXS scaling

The pixel intensities in the 2D images were azimuthally integrated into radial distribution functions (RDF) with corrections for the linear polarisation of the undulator, the geometric correction for the flat detector and the absorption in the sample and phosphor screen. The high  $q$  part of the RDFs is scaled to the atomic scattering for one unit-cell-molecule (UC) of the solution. That allows to put  $dS(q, t)$  on absolute scale,  $(\text{e.u.})^2/\text{UC}$ . When the scaled difference is compared with the theoretical change in scattering from *one* molecule transformation, the concentration of excited molecules is known. A spin-off of the scaling is that it automatically corrects for variations in the synchrotron current and drifts in the beam that could lower  $I_0$  through the slit in front of the jet.

In practice the scaling is done as follows. The molar mass of water is 18.02 g/mol and the density is 1000 g/liter at ambient conditions (300K, 1 atm). The molar concentration is then:

$$\frac{1000 \text{ g/l}}{18.02 \text{ g/mol}} = 55.48 \text{ mol/l} = 55.48 \text{ M}.$$

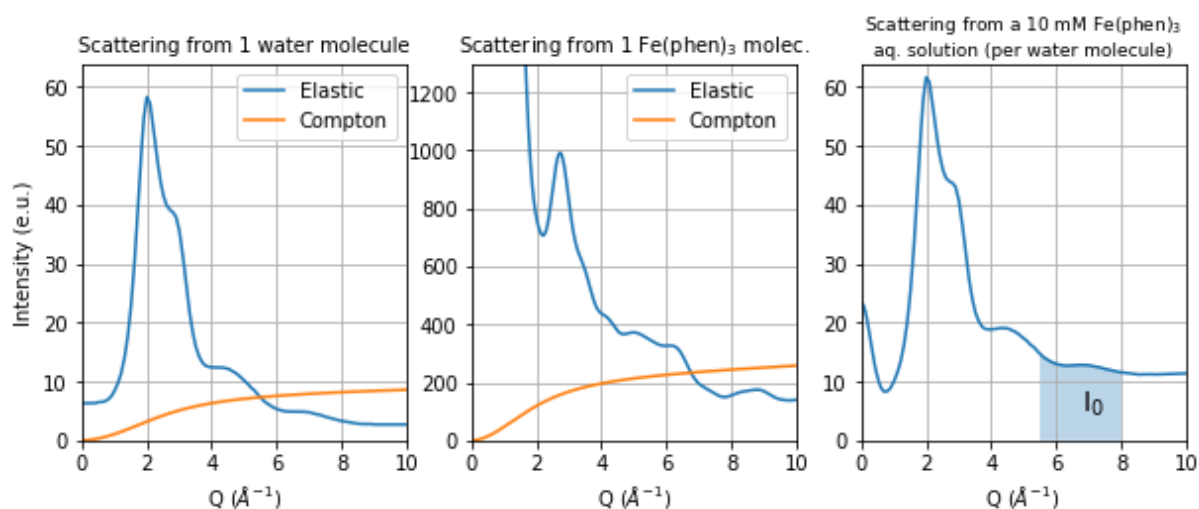


**Figure 4.15:** Elastic and Compton scattering for one water molecule (left), elastic and Compton scattering for one  $[\text{Fe}(\text{phen})_3]^{2+}$  molecule (centre) and total scattering from a 10 mM solution of  $[\text{Fe}(\text{phen})_3]^{2+}$  in water with a mixing ratio 1:5548 (right).

For a 10 mM  $[\text{Fe}(\text{phen})_3]^{2+}$  solution, the mixing ratio is:

$$r = \frac{0.01 \text{ M}}{55.48 \text{ M}} = 1.8 \cdot 10^{-4}.$$

In a 10 mM aqueous solution there are thus  $1.8 \cdot 10^{-4}$  solute molecules per water molecule. In other words, the solute-solvent mixing ratio is 1:5548.

Let's now describe how the scattering curves are scaled to absolute electron units (e.u.) per molecule. The Debye scattering from one unit-cell-molecule is calculated from the atomic positions in the unit-cell-molecule. At the highest  $q$  in this experiment,  $9 \leq q \leq 11 \text{ \AA}^{-1}$ , the Debye modulations are very weak so the scattering can be approximated by free atoms. There are 4 contributions: elastic and inelastic Compton scattering from water and the solute molecules. The scattered intensity for one unit-cell-molecule is:

$$S_{UC}(q) = S_{el}^{water} + S_C^{water} + r \cdot (S_{el}^{solute} + S_C^{solute}),$$

and these terms are shown in figure 4.15.

The radial integration and the detector corrections were done with the waxesGUI written by Marco Cammarata. The radial intensity for a 6 s exposure with a 2.1% BW pink beam is shown in figure 4.16. The scattering from air is shown in grey; it constitutes 15% of the total intensity in the  $I_1$   $q$  range and this was corrected before scaling. Let's note in passing that the air scattering, the detector background and the Compton scattering cancel out in difference  $dS(q, t)$ .

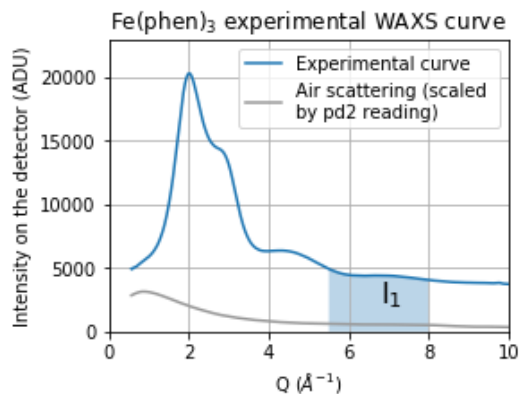


**Figure 4.16:** Radial intensity from a 10 mM  $[\text{Fe}(\text{phen})_3]^{2+}$  solution in water. The air scattering, measured separately, is shown in grey. In the  $I_1$  range, the air intensity is 15% of the total intensity. The data was taken at 18 keV with an exposure time of 6 s. The undulator was monochromatised by the 2.1% Ru multilayer with  $4 \times 10^{11}$  ph/s.

## 4.8 Solvent heating

The difference curves  $dS(q, t)$  have contributions from the change in structure in the LS  $\rightarrow$  HS transition and from the change in solvent temperature. The temperature is expected to rise in two steps. First, the ground state molecule is excited vertically to the  $^1\text{MLCT}$  state followed by a rapid transition to the vibrationally hot  $^5\text{T}_2^*$  state via  $^3\text{MLCT}$  in  $\sim 300$  fs. On this time scale the complex does not have enough time for vibrational cooling before the transition (ISC) to  $^5\text{T}_2$ . The vibrationally hot  $^5\text{T}_2^*$  state cools down in  $\sim 10$  ps [50]. The energy is released in vibrational relaxation from 3.1 to 1.3 eV at the bottom of the  $^5\text{T}_2$  potential. The second step is the HS  $\rightarrow$  LS decay from 1.3 to 0 eV in 725 ps. Since the solvent temperature is probed with 100 ps pulses, step 1 is smeared out to a 100 ps step-up function (erf).

The expected temperature rise can be calculated from the solvent heat capacity and excited solute concentration as shown in figure 4.17 for an aqueous solution with a 2.4 mM concentration of  $[\text{Fe}(\text{phen})_3]^{2+}$  molecules excited to  $^5\text{T}_2$ .

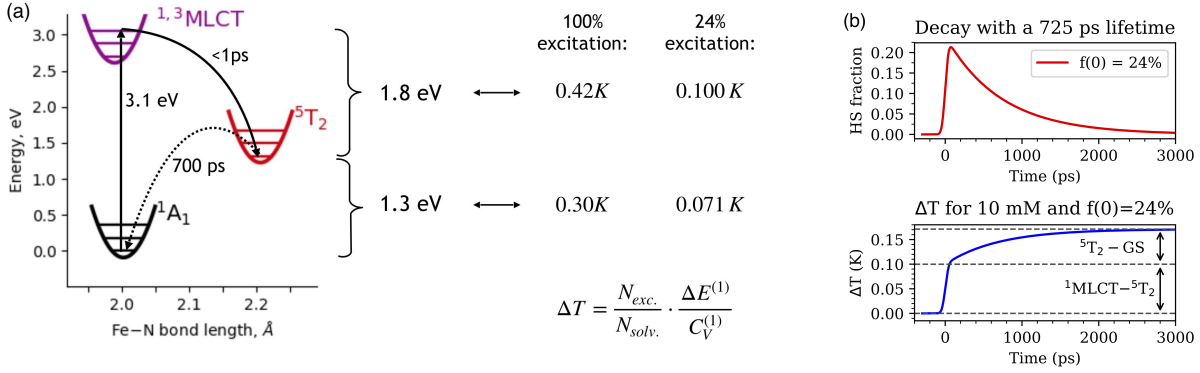


**Figure 4.17:** (a) The solvent temperature rises in two steps. Each excited  $[\text{Fe}(\text{phen})_3]^{2+}$  molecule releases 1.8 eV after vibrational cooling of the  $^5\text{T}_2$  state in the first step ( $< 100$  ps) and 1.3 eV after the return to the ground state in the second step (725 ps). The temperature rise depends on the mixing ratio of excited molecules in the solvent. (b) Excited solute decay (top) and solvent temperature rise (bottom) expected after 24% excitation of a 10 mM aqueous  $[\text{Fe}(\text{phen})_3]^{2+}$  solution. Note the duality between solute decay and temperature rise.

The difference scattering  $dS(q, t)$  is dominated by heating and although the shape of the isochoric water differential is known, the amplitude has to be determined carefully. As the temperature rises on the 0-10 ns time scale, the solvent amplitude increases with time but the shape of the curve is constant. In the nodal points of the  $\partial S(q)/\partial T|_V$  curve at 1.39, 2.23, 3.72 and 4.80  $\text{\AA}^{-1}$ , the signal is from the solute/cage alone. These solute amplitudes are used as initial values for separating the two components in the curve fitting.

Figure 4.18(a) shows the fitting of the WAXS dataset recorded on a 10 mM aqueous solution excited at 400 nm and 1.1 mJ/mm<sup>2</sup>. The experimental data  $q \cdot dS(q, 100 \text{ ps})$  are shown in black dots. The data are first fitted with a linear combination of the solvent heating  $\partial S(q)/\partial T|_V$  and solute structural change without including the cage term in the range  $2.5 \text{ \AA}^{-1} < q < 10.4 \text{ \AA}^{-1}$  where the cage is negligible. This gives the first approximation of the excited state fraction  $f(100 \text{ ps})$  and solvent temperature change  $\Delta T(100 \text{ ps})$ . In the next step the data are fitted in the whole  $q$  range and for all time delays with the cage term included. The cage term had to be downscaled by a factor 3, which will be discussed later in this chapter.

Figure 4.18(b) shows fitting of the solute+cage term to the dataset for a 10 mM solution excited at 400 nm & 1.2 mJ/mm<sup>2</sup> and probed at 100 ps – 2 ns delays. The HS fraction  $f(t)$  and solvent temperature change  $\Delta T(t)$  are refined as a function of time delay. The HS population is fitted as a convolution of an exponential decay with a Gaussian X-ray pulse:

$$S(\tau) = \frac{1}{\sqrt{2\pi}\sigma} \int_0^\infty dt e^{-\frac{t}{\tau_R}} e^{-\frac{(t-\tau)^2}{2\sigma^2}} = \frac{1}{2} \exp\left(\frac{\sigma^2 - 2\tau\tau_R}{2\tau_R^2}\right) \left\{ 1 - \text{erf}\left(\frac{\sigma^2 - \tau\tau_R}{\sqrt{2}\sigma\tau_R}\right) \right\},$$

where  $\tau$  is the laser/X-ray delay,  $\sigma$  the width of the Gaussian X-ray pulse in time, and  $\tau_R$  the HS decay time. The fit is shown in figure 4.19(a). The HS lifetime is found to be 725 ps and the HS fraction at the earliest measured delay is  $f(100 \text{ ps}) = 21.2\%$ , which can be extrapolated to  $f(0) = 24.3\%$ .

The measured solvent temperature is fitted as the sum of a Heaviside step function  $H(t)$  and an exponential rise broadened by a Gaussian X-ray pulse:

$$\Delta T(\tau) = \frac{1}{\sqrt{2\pi}\sigma} \int_{-\infty}^\infty dt e^{-\frac{(t-\tau)^2}{2\sigma^2}} \left\{ \Delta T_0 H(t) + \Delta T_1 H(t) [1 - e^{-t/\tau_R}] \right\}.$$

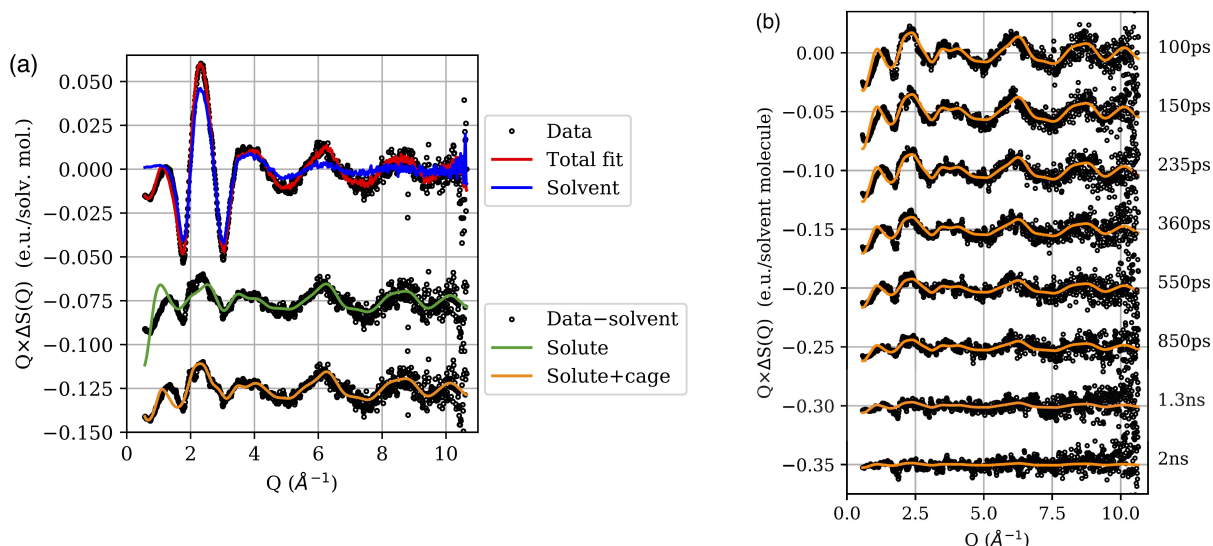


**Figure 4.18:** (a) Fitting of the difference scattering data. The experimental curve  $q \cdot dS(q, 100 \text{ ps})$  is shown in black dots. The solute contribution alone is shown in green offset by  $-0.075$  vs data corrected for solvent heating. The solute+cage is shown in orange offset by  $-0.125$ . (b) The solute and cage signal as a function of time. The orange lines show the best fit to the experimental data for the DFT calculated HS and LS structures. The fits use the downscaled MD cage term. The Fe-N distance increases by  $0.19 \text{ \AA}$  in the HS state. The HS state decays in  $725 \text{ ps}$  and the excess heat is taken up by water with an increase in temperature of  $0.33 \text{ K}$  after  $2 \text{ ns}$ . The excited HS fraction is  $21\%$  of the  $10 \text{ mM}$  solution at  $100 \text{ ps}$ .

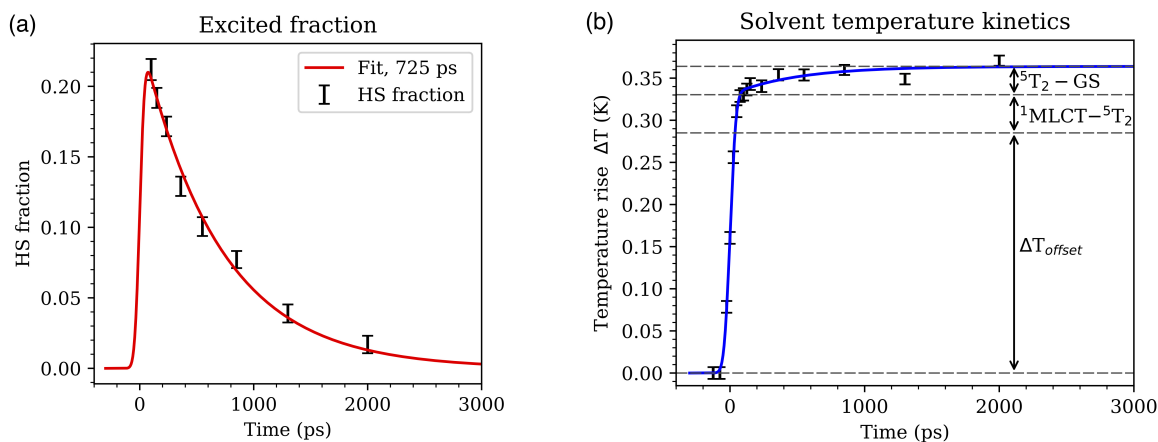


**Figure 4.19:** (a) The  $725 \text{ ps}$  decay of the  $\text{HS} \rightarrow \text{LS}$  state. The concentration of  $[\text{Fe}(\text{phen})_3]^{2+}$  is  $10 \text{ mM}$  and  $21\%$  of the molecules are laser excited at  $100 \text{ ps}$ . (b) Measured temperature profile from the  ${}^1\text{MLCT}$  decay to  ${}^5\text{T}_2$  (HS) followed by the return to the GS. In the early time range  $-75 \text{ ps}$  to  $75 \text{ ps}$ , the temperature is not corrected for the partial intensity in the  $100 \text{ ps}$  pulse that probes the excited state (laser slicing).

The fit is shown in figure 4.19(b). The first step at  $100 \text{ ps}$  is  $0.330 \text{ K}$  which is followed by a  $0.034 \text{ K}$  step from the  $\text{HS} \rightarrow \text{LS}$  decay in  $725 \text{ ps}$ . That gives a total experimental rise of  $0.364 \text{ K}$ . The expected temperature is shown in figure 4.17(b). It is calculated from the measured concentration of excited HS molecules at  $100 \text{ ps}$ ,  $2.1 \text{ mM}$ , and the two step-up functions are from the difference in the pulse and HS energy,  $3.1 - 1.3 = 1.8 \text{ eV}$  and the HS-LS difference,  $1.3 \text{ eV}$ . That accounts for a temperature rise of  $0.171 \text{ K}$ . The measured rise

is a factor  $0.364/0.171 = 2.1$  times greater! In the following we will discuss three scenarios for the anomalous temperature rise.

#### 4.8.1 Direct water heating

UV-vis absorption in water is extremely low for a 1.2 ps pump pulse at 400 nm. With the absorption coefficient  $\mu = 8 \cdot 10^{-3} \text{ m}^{-1}$  at 400 nm, the absorption length is 125 m. To check that the pump pulse does not heat water, the pump-probe experiment was performed on pure water to check for the possibility of multi-photon absorption at the power densities used in the solution experiment.  $dS(q, t)$  was found to be zero for all time delays. However from previous experiments on ID09 with 100 fs 267 nm laser pulses, multi-photon heating was observed in water using laser pulses with  $20 \mu\text{J}/\text{pulse}$  focused to  $200 \mu\text{m}$  ( $0.4 \text{ mJ}/\text{mm}^2$ ).

#### 4.8.2 Sequential excitations

Is it possible that the powerful 400 nm pulse is exciting some HS molecules a second time? That implies that the first part of the pulse produces the HS state and that these molecules are excited a second time later in the pulse. Let's first examine the energy scheme proposed by Tribollet et al. [50] and Sousa et al. [49] in figure 4.20. As  $^1\text{MLCT}$  molecules move to  $^5\text{T}_2$  (HS) in  $\sim 300$  fs and stay there for 725 ps on average, the  $^5\text{T}_2$  population is accumulating during the 1.2 ps pump pulse. The transit states  $^3\text{MLCT}$  and  $^3\text{T}_1$ , by contrast, are very short lived and less likely to interact with the pump pulse. So most likely the pump excites  $^5\text{T}_2$  to a vibrational state of  $^5\text{MLCT}$ . One might speculate that  $^5\text{MLCT}$  could transit to  $^1\text{MLCT}$  via intersystem crossing and restart the photocycle.

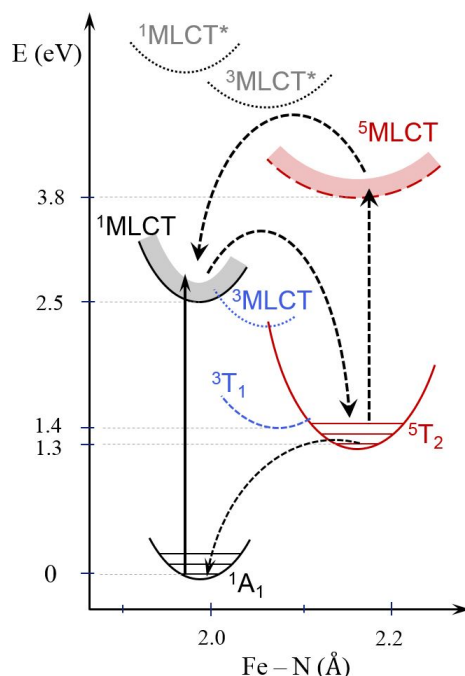


**Figure 4.20:** Energy scheme for  $[\text{Fe}(\text{phen})_3]^{2+}$  proposed by Tribollet and Sousa. The origin of the excess heat might be due to the  $^5\text{T}_2$  (HS)  $\rightarrow$   $^5\text{MLCT}$  transition that decays to  $^1\text{MLCT}$  by intersystem crossing. The time resolution of the experiments is insufficient to measure the structures involved. By contrast, the solvent temperature accumulates the energy from invisible transitions.

To prove that a secondary absorption process exists during the 1.2 ps pump pulse, we performed a transient optical absorption experiment in Mathias Bargheer's laboratory at the University of Potsdam. In the laser/laser pump-probe experiment, the change in the transmission was probed at 400 and 500 nm after 400 nm excitation. The pulse length of the pump and probe pulses was 150 fs. The result is shown in figure 4.21.

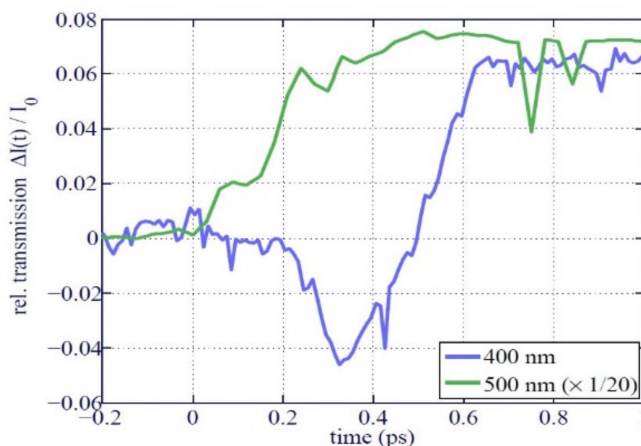


**Figure 4.21:** Transmission of a 2 mM solution of  $[\text{Fe}(\text{phen})_3]^{2+}$  excited at 400 nm and probed at 400 and 500 nm. The negative peak after 0.3 ps for the 400 nm probe is interpreted as the formation and decay of  $^5\text{MLCT}$ . The  $^5\text{MLCT}$  decays in 300 fs.

When the solution is probed at 500 nm near the  $^1\text{MLCT}$  absorption peak, the transmission increases between 0-1 ps from the depletion of the GS by the pump. For the 400 nm probe, a negative peak in the transmission appears after 250 fs and decays in 300 fs. This onset and decay are interpreted as the formation and decay of  $^5\text{MLCT}$ . The interpretation is consistent with the work by Tribollet et al. [50] who detected the HS state by a transient increase in absorption at 380 nm, as shown in figure 4.9. The Potsdam result shows that if the X-ray experiment was done with 500 nm pump pulses, double excitation would not occur. But the 500 nm pump was not available at the time of the experiment due to instability problems with the TOPAS.

### Power titration

If secondary excitation via the cycle  $^5\text{T}_2$  (725 ps)  $\rightarrow$   $^5\text{MLCT}$   $\rightarrow$   $^1\text{MLCT}$   $\rightarrow$   $^3\text{T}_1$   $\rightarrow$   $^5\text{T}_2$  (725 ps) is present and if the  $^5\text{T}_2 \rightarrow ^5\text{MLCT}$  absorption is higher than  $\text{GS} \rightarrow ^1\text{MLCT}$  absorption, the solvent temperature at 100 ps would be linear in pulse energy due to the recycling. Moreover the  $^5\text{T}_2$  population should saturate at higher pulse energies. To verify this hypothesis,  $dS(q, 100 \text{ ps})$  was measured as a function of the 400 nm pulse energy. The  $dS(q, 100 \text{ ps})$  curve is partitioned in four  $q$  areas according to their predominant solute or solvent contribution, see figure 4.23(a). The solute population is monitored by the negative area under the curve  $0.45\text{-}1.05 \text{ \AA}^{-1}$  from the Fe-N elongation where the solvent part is very small. The best solvent areas are  $2.1\text{-}2.6 \text{ \AA}^{-1}$  and  $2.85\text{-}3.3 \text{ \AA}^{-1}$  where the solute contribution is small which is seen in figure 4.14 due to the very small change in amplitude between 100 ps and 2 ns. The power titration is shown in figure 4.23(b). The three solvent amplitudes are essentially linear up to  $150 \mu\text{J}/\text{pulse}$  ( $2.19 \text{ mJ}/\text{mm}^2$ ). At the highest energy of  $175 \mu\text{J}/\text{pulse}$ , the laser was evaporating the surface of the liquid sheet so that measurement might not be reliable. The solute titration is linear up to about  $100 \mu\text{J}/\text{pulse}$  ( $1.46 \text{ mJ}/\text{mm}^2$ ) for then to saturate albeit slowly.

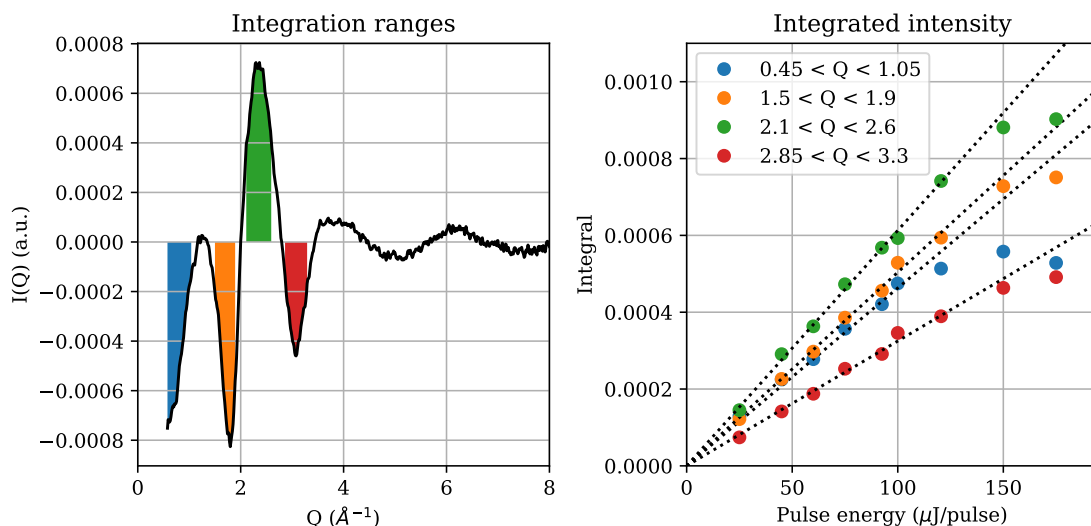


**Figure 4.22:** Power titration with colour coded integration ranges. The blue area is predominantly from Fe-N bond contraction in the solute and the orange, green and red are predominantly from the solvent heating. The solvent contributions are essentially linear in the pulse energy whereas the solute saturates above 100  $\mu\text{J}/\text{pulse}$  (1.46  $\text{mJ}/\text{mm}^2$ ).

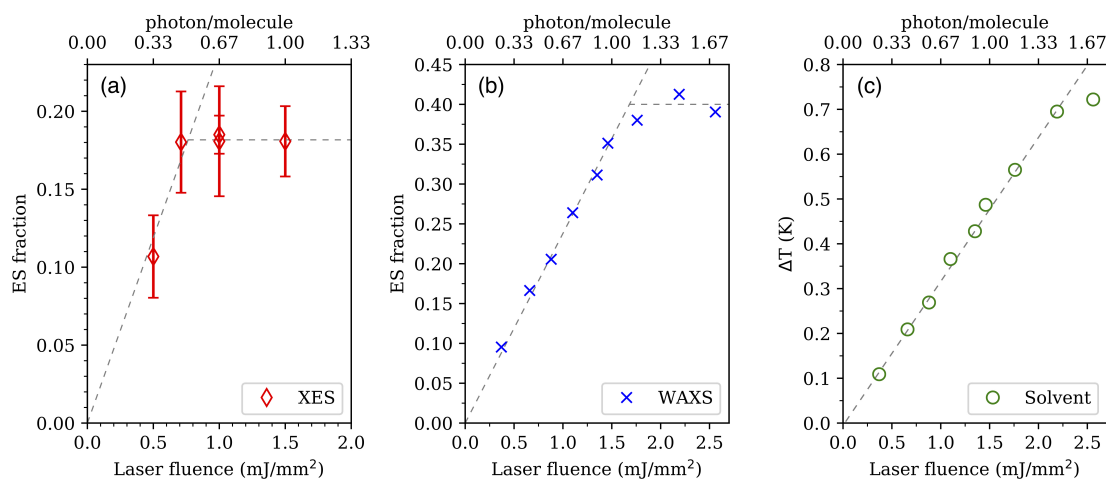


**Figure 4.23:** (a) Excited state fraction at 100 ps in a 10 mM solution from XES and (b) WAXS vs laser fluence. (c) Temperature rise in a 10 mM solution after 100 ps is linear as a function of laser fluence (WAXS).

The XES signal was measured separately in a 10 mM solution but the jet was inclined  $45^\circ$  to the laser beam. In spite of this, the integrated  $K\beta$  intensity saturates at lower pulse energy.

### 4.8.3 Ligand excitation

The static absorption measurements with the NanoDrop OneC spectrometer shows peaks, the MLCT peak at 512 nm and the peak at 250 nm which is assigned to ligand excitation, see figure 4.24. If the intensity of the 400 nm pump beam exceeds a certain threshold, two photons might combine to one at 200 nm at twice the energy. One might speculate that the laser could even trigger ligand dissociation followed by geminate recombination in the cage. The onset of two photon processes normally appears as a quadratic term in the signal vs pump power plot, but this behaviour was not observed.

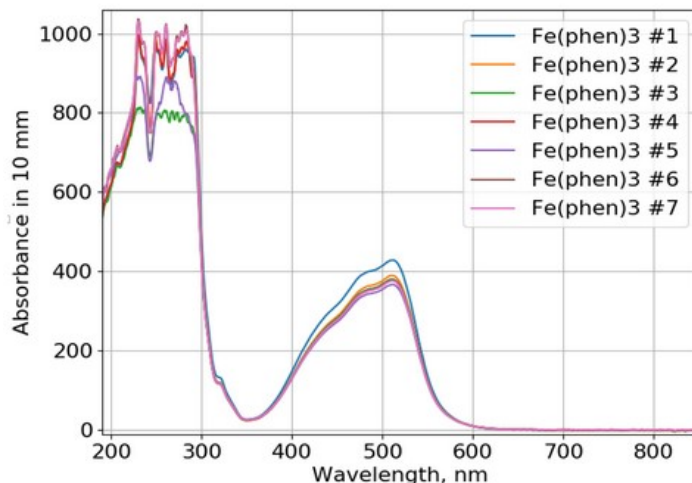


**Figure 4.24:** Optical absorption of  $[\text{Fe}(\text{phen})_3]^{2+}$  of seven samples measured with the NanoDrop OneC spectrometer in the PSCM laboratory at the ILL/ESRF.

Excess solvent heating was also reported by Denis Leshchev et al. for the  $[\text{Fe}(\text{btbip})_2]^{2+}$  complex which has a photocycle similar to  $[\text{Fe}(\text{phen})_3]^{2+}$  with a 260 ps HS lifetime [54]. With a temperature rise of 0.93 K after 1 ns, 32% is from an unknown heat source. The possibility of an invisible ultrafast decay  ${}^3\text{T}_1 \rightarrow \text{GS}$  channel that escapes detection with the 100 ps X-ray pulse at ESRF is discussed by the authors.

A second example of excess solvent heating is also reported by Sunhung Jun et al. [55] in a study of UV dissociation of  $\text{HgBr}_2$  that splits into  $\text{HgBr} + \text{Br}$  and  $\text{Hg} + \text{Br} + \text{Br}$ . These products are outside the cage after 100 ps and their structure is readily identified by their scattering signature. After diffusive recombination however, the temperature rises 0.54 K of which 0.13 K is attributed to the out-of-cage products. The extra 0.41 K comes from geminate recombination in the cage on the 10 ps time scale, which is invisible in 100 ps synchrotron experiments.

To conclude, on short time scales, the adiabatic temperature rise is sensitive to elusive ultrafast processes since the solvent temperature is accumulating the released energy on fast time scales  $< 10$  ns due to energy conservation.

## 4.9 LS and HS structures of $[\text{Fe}(\text{phen})_3]^{2+}$

The water temperature  $\Delta T(t)$  and the concentration of excited  $[\text{Fe}(\text{phen})_3]^{2+}$  molecules were presented in the previous section without detailing the structural model of the LS and HS states. The spatial coordinates of these structures were calculated by density functional theory (DFT) including corrections from the weak interaction with bulk water. The calculations were performed by Latévi Max Lawson Daku at Geneva University using different wavefunction approaches and symmetries. Two ground state and five excited state structures were optimised. The first LS structure was constrained to  $D_3$  point symmetry with all Fe-N distances equal and with ligands in orthogonal planes. In this geometry, the angles between the ligand central axes are  $120^\circ$  and the angles between the opposite Fe-N bonds are  $175.6^\circ \neq 180^\circ$ . In the second LS structure, Fe-N distances were set free ( $C_1$  point group symmetry). Five HS structures were calculated with two having  $D_3$  symmetry, two with  $C_2$  symmetry and finally one with  $C_1$  symmetry. The atomic positions  $(x, y, z)$  are listed in Appendix B with

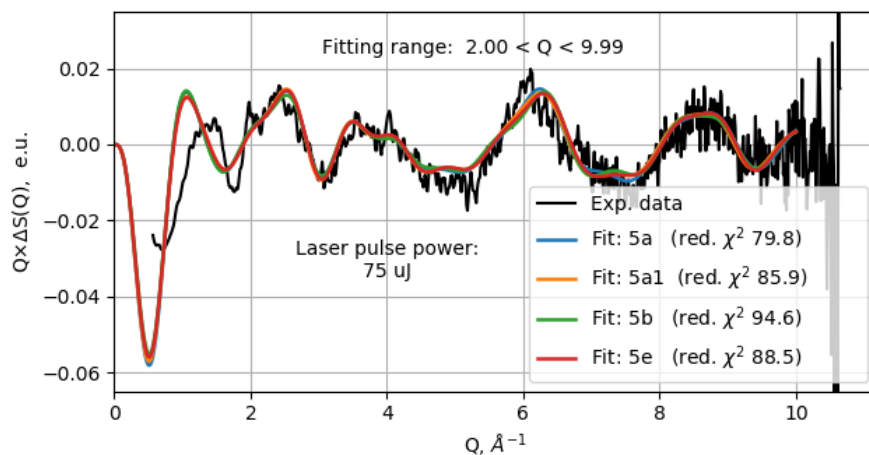


**Figure 4.25:** Comparison of 4 DFT models of the LS-HS transition against the experimental data at 100 ps. The cage is not included yet in the models. Model 5a in blue has the lowest  $\chi^2$  for  $q$  above  $2.5 \text{ \AA}^{-1}$ . The negative peak in the models at  $\sim 0.5 \text{ \AA}^{-1}$  is from the  $0.19 \text{ \AA}$  Fe-N bond elongation.

Fe-N distances and angles. The fits for four of the models are shown in figure 4.25. The difference in the Debye functions for these structures are very small indeed and they all fit the experimental data very well. The anisotropic expansion of the Fe-N distance in the HS state is not resolved by X-ray scattering due to the random orientation of the solutes. The experiment only probes average bond distances. Neglecting the cage term, model 5a has the lowest  $\chi^2$  for  $q > 2.0 \text{ \AA}^{-1}$  where the cage term is negligible. The high  $q$  data is consistent with a Fe-N bond length of  $1.99 \text{ \AA}$  in the LS and  $2.18 \text{ \AA}$  in the HS state.

This result is in fair agreement with the time-resolved X-ray absorption fine structure (XAFS) study by Nozawa et al. [52]. They find the Fe-N bondlength to be  $1.98(1) \text{ \AA}$  in the LS and  $2.15(2) \text{ \AA}$  in HS corresponding to a bond elongation of  $0.17 \text{ \AA}$  compared with  $0.19 \text{ \AA}$  in this study. When Nozawa's errors are included, the two studies agree. The 3D image of the 5a structure in the HS state is shown in figure 4.26 with DFT bond lengths and ligand angles.

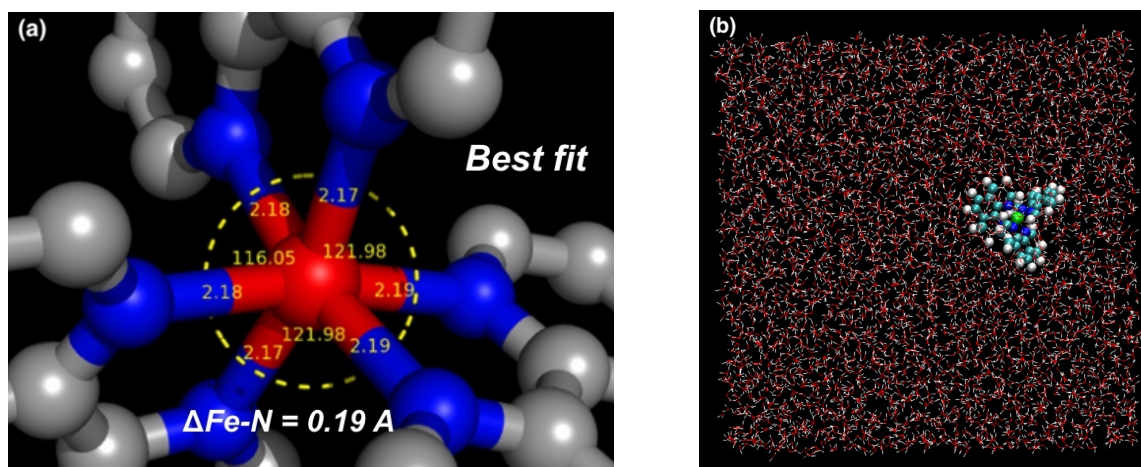


**Figure 4.26:** (a) Best model of the HS state of  $[\text{Fe}(\text{phen})_3]^{2+}$  with a zoom of the Fe-N bonds. The angles between the central axes of the ligands are also shown. (b) MD box with one  $[\text{Fe}(\text{phen})_3]^{2+}$  molecule and 4096  $\text{H}_2\text{O}$  molecules. The box length is  $49.6 \text{ \AA}$ . The simulations were made using MOLLY and the TIP4P model for water.

## 4.10 MD simulations of cage terms

Including the cage term to the DFT structures is important for matching the low  $q$  model to the experimental data. The cage is calculated from the  $g_{ij}(r)$  functions, where  $i$  is an atom in the solute and  $j$  is an atom in the solvent. That describes the packing of water molecules around the LS and HS structures. Rather unexpectedly the Fe..O distance, which is a good measure of the Fe distance to water, is contracting 1.0 Å for the first peak in the HS state in spite of the 0.19 Å expansion of the Fe-N bonds. Specifically the calculation predicts the Fe..O distance to decrease from 5.4 Å in LS to 4.4 Å in HS as shown in figure 4.27. This can be explained by the complex being more open to the solvent in the expanded HS state. In smaller molecules like Br<sub>2</sub> and I<sub>2</sub> by contrast, the excited states A/A' of Br<sub>2</sub><sup>\*</sup> and I<sub>2</sub><sup>\*</sup> are 15% longer and the cage radius follows accordingly. Ultrafast cage dynamics was also studied by T. Brandt van Driel et al. for [Ir<sub>2</sub>(dimen)<sub>4</sub>]<sup>2+</sup> in acetonitrile. They found that the contraction of the Ir-Ir distance in the excited state orients and attracts the N atom in acetonitrile which leads to a reduction in the effective cage radius [56].

The MD simulations for [Fe(phen)<sub>3</sub>]<sup>2+</sup> in water were done in collaboration with Qingyu Kong at the Soleil Synchrotron in Orsay using MOLDY. The Lennard-Jones potential for water was described by the TIP4P/2005 model [57]. In the simulations, one [Fe(phen)<sub>3</sub>]<sup>2+</sup> molecule is placed in a cubic box with a size of 49.6 Å with 4096 H<sub>2</sub>O molecules. The simulations were performed at 300 K with a water density of 1.013 kg/m<sup>3</sup>. The trajectories were tracked from 0-200 ps in time steps of 0.5 fs for both states. The atom-atom distribution  $g_{Fe-O}(r)$ , a measure of the cage radius, is shown in figure 4.27.

The first coordination Fe..O peak contracts from 5.4 Å in LS to 4.4 Å in HS. The contraction is also significant for the second and third peaks. The splitting of the 4.4 Å HS peak is most likely a computational artefact due to insufficient sampling. Another possible reason is the symmetry distortion in the HS state. The HS-LS difference distribution is shown in green. The positive creation peaks from the contraction in the HS state are side-by-side with negative annihilation peaks from LS. The cage term is shown in figure 4.28. Note the upturn in the cage term at low  $q$ , the signature of a smaller cage radius in HS.

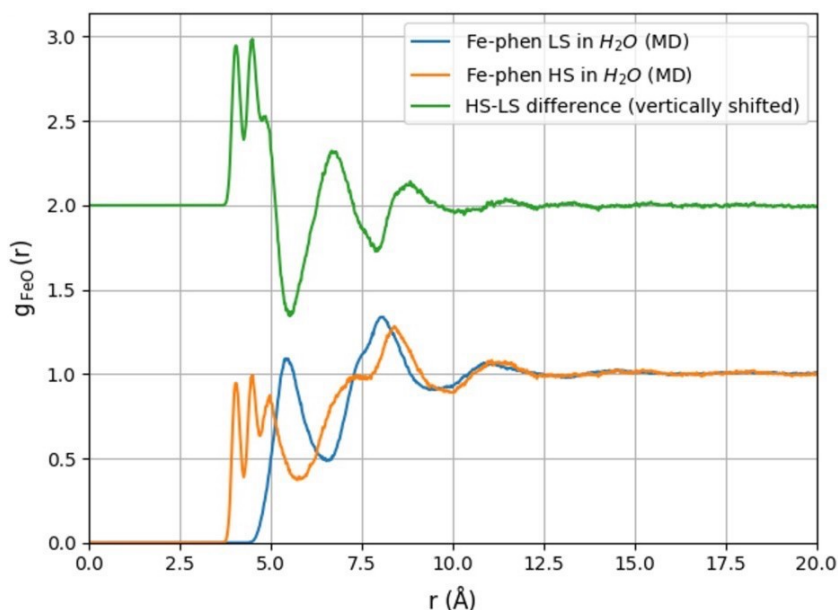


**Figure 4.27:** Fe..O distributions in the LS and HS states. Four water shells are visible in both structures. The first water shell is at 5.4 Å and 4.4 Å in the LS and HS structure, respectively.

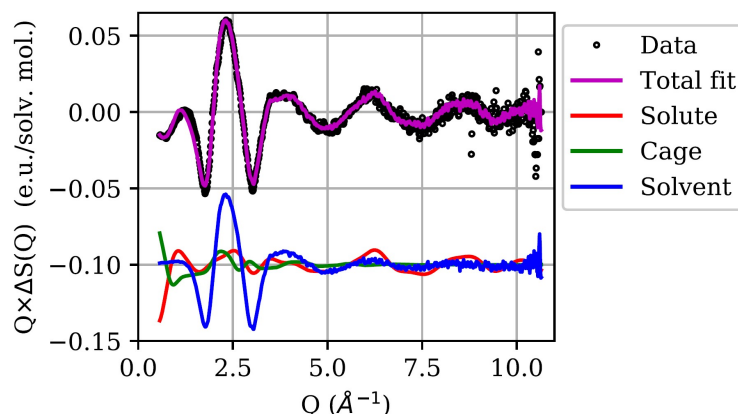


**Figure 4.28:** Contributions to the scattering  $q \cdot dS(q, 100 \text{ ps})$ . The top panel shows the total theoretical signal in purple. The dominating heat signal is blue, the HS-LS Debye function is red and the HS-LS cage term is green. The best fit is obtained by reducing the cage amplitude to 33% which corresponds to a smaller Fe..O contraction, from 5.4 to 5.1 Å, in the transition LS  $\rightarrow$  HS.

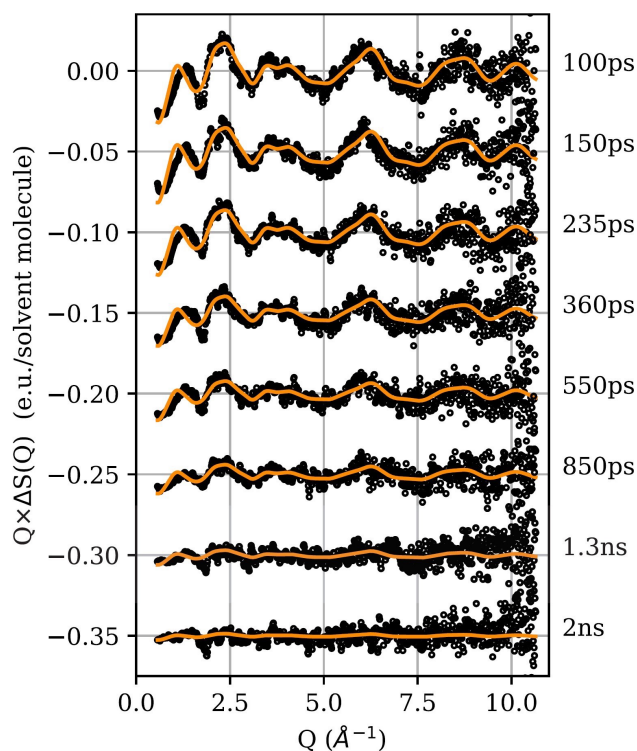


**Figure 4.29:** The solute and cage signal as a function of time. The red lines show the best fit to the experimental data for the DFT calculated HS and LS structures. The fits use the downscaled MD cage term. The Fe-N distance increases by 0.19 Å in the HS state. The HS state decays in 725 ps and the excess heat is taken up by water with an increase in temperature of 0.33 K after 2 ns. The excited HS fraction is 21% of the 10 mM solution.

As mentioned the fits become perfect by reducing the cage *amplitude* to 33% of the MD value for all the experimental curves in the time range 0 – 2 ns as shown in figure 4.29.

What do we learn from having to downscale the cage term to the 33% level? The question can be phrased differently: what is the relation between the change in cage radius  $dr$  and  $dS_{\text{cage}}(q)$ ? Some insight can be gained by considering the Fe..O distribution as a Dirac function at  $r = 5.4 \text{ Å}$  and calculate the change in  $dS(q)$  vs  $dr$ . The diatomic Debye function for the

hypothetical Fe-O bond is:

$$S(q) = \sum_{i,j} f_i f_j \frac{\sin(q r_{ij})}{(q r_{ij})} = f_{Fe}^2(q) + f_O^2(q) + 2f_{Fe}(q)f_O(q) \frac{\sin(q r)}{(q r)}.$$

For a bond increase  $r \rightarrow r + dr$ ,  $dS(q)$  is approximated to first order as:

$$dS(q) = \frac{dS}{dr} \cdot dr = 2f_{Fe}(q)f_O(q) \frac{q^2 r \cos(qr) - q \sin(qr)}{(qr)^2} \cdot dr.$$

For a small change in the bond length  $dr$ ,  $dS(q)$  is proportional to  $dr$ . The scale factor depends on  $q$  but it is nearly constant for  $q < 2.0 \text{ \AA}^{-1}$ , where the cage term is strongest as shown in figure 4.30. The figure shows  $dS(q)$  for an Fe-O bond at  $5.4 \text{ \AA}$  that contracts to  $5.3 \text{ \AA}$  ( $dr -0.1 \text{ \AA}$ ),  $4.9 \text{ \AA}$  ( $dr -0.5 \text{ \AA}$ ) and  $4.4 \text{ \AA}$  ( $dr -1.0 \text{ \AA}$ ). The exact Debye functions are shown by thick lines and the approximation is shown with broken lines. The linear approximation is perfect for a  $dr$  of  $-0.1 \text{ \AA}$  for all  $q$ . For  $-0.5 \text{ \AA}$  and  $-1.0 \text{ \AA}$  contractions, the approximation is fair for  $q < 2$  where the cage term dominates. In conclusion we estimate the Fe..O contraction for water in the HS state to be  $0.33 \text{ \AA}$  from the reduction in  $dS(q)$  amplitude  $< 2.5 \text{ \AA}^{-1}$ . A similar cage contraction is also reported for  $[\text{Fe}(\text{bpy})_3]^{2+}$  by Haldrup et al. [39]

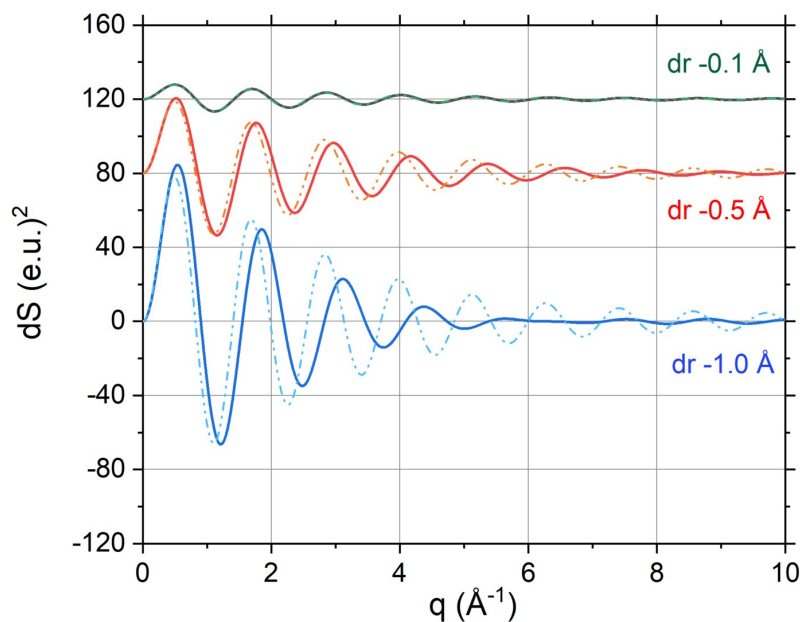


**Figure 4.30:** Simulated scattering from changes in the Fe..O distance ( $dr$ ). The full curves are  $dS(q)$  for the Debye function of a virtual Fe-O bond that contracts by 0.1, 0.5 and 1.0  $\text{\AA}$ . The broken-line curves are their linear equivalents.

This simple simulation highlights a fundamental problem in X-ray scattering: how to differentiate between a small structural change and a change in population. If the experiment measures the decay from the blue to the green curve shown above, it can be interpreted as either a bond contraction or a change in population with an ultrafast transition to the GS that is not resolved by the 100 ps X-ray pulse.

## 4.11 Lifetime measurements with Johann Spectrometer

The spin of transition metal complexes is determined by the electron configuration of the  $3d$  or  $4d$  shell. Valence-to-core (VtC) transitions are probing the hybridisation of the  $3d$  or

4d electrons with the ligand so they provide very useful information about the metal-ligand bonds. VtC emission is very weak however, two orders of magnitude weaker than  $K\beta$ . As mentioned in the theory chapter, the  $K\alpha$  and  $K\beta$  lines in 3d metals are due to  $2p \rightarrow 1s$  and  $3p \rightarrow 1s$  transitions after the creation of a 1s core hole from the absorption of an X-ray photon. The two lines are sensitive to the metal spin state due to the exchange interaction of the 2p and 3p orbitals with the 3d orbitals. When the spin state changes, the relative change in  $K\beta$  is bigger than that in  $K\alpha$ , but  $K\alpha$  is 8 times more intense. Usually the  $K\beta$  is used to probe the spin states of the metal because each spin state, i.e. a singlet, doublet, triplet and quintet, has a unique  $K\beta$  spectrum as we will see shortly. The  $K\beta$  was also used to probe the spin kinetics in this project although  $K\alpha$  is a more common choice.

The first time-resolved XES measurements on  $[\text{Fe}(\text{phen})_3]^{2+}$  in aqueous solution were done with the Johann spectrometer in order to measure unambiguously the lifetime of the excited HS complex in water without interference from solvent heating. For comparison we also measured the spin kinetics of  $[\text{Fe}(\text{phen})_3]^{2+}$  and  $[\text{Fe}(\text{dmp})_3]^{2+}$  in acetonitrile, where (dmp)=3,4-dimethylphenanthroline is a ligand similar to (1,10)-phenanthroline.

The analyser crystal used for  $K\beta$  is a Si(531) spherical crystal with a 1 m radius of curvature. The  $d$ -spacing is 0.9179 Å corresponding to a Bragg angle of  $73.1145^\circ$  for Fe- $K\beta$  at 7057.98 eV. The analyser was mounted on a motorised stage with one rotation and two translations 500 mm from the sample. The Silicon Drift Diode (SDD) was positioned on the Rowland circle and its position pre-aligned using a laser pointer that scattered the beam from an iron tip on the goniometer at the sample position. The  $K\beta$  emission was found from a Bragg scan and the angle set to  $73.1145^\circ$ . The analyser Bragg angle and the SDD position were scanned such that the SDD receives the diffracted beam at all  $\theta$  angles ( $\theta - 2\theta$  scan). The X-ray beam was sent onto the iron tip at the sample position and the emission was recorded on the SDD. Using the strong emission from the solid sample allowed us to optimise the focusing distances and refine the analyser angle from the peak of the Fe- $K\beta$  line. As the take-off angle for the diffracted beam from the analyser is deflected by  $2 \times$  Bragg angle, the SDD detector has to move in synchrony with the Bragg angle to be centred on the deflected beam. Finally absorption in air was reduced by a He chamber. With a flight path of 2 m at 7 keV, the gain in intensity is a factor 8. The Swiss sapphire nozzle was used with a 360  $\mu\text{m}$ -thick flat jet tilted  $\sim 45^\circ$  with respect to the incoming X-ray beam.

The second harmonic ( $\lambda = 400$  nm) of the picosecond laser was used to excite the sample. The laser beam dimension was  $185 \times 210 \mu\text{m}^2$  (FWHM) and the laser was directed onto the sample almost collinearly with the X-ray beam (the angle between the pump and the probe beams was  $\sim 15^\circ$ ). The laser power was 120 – 155  $\mu\text{J}$ /pulse corresponding to a power density of 2.5 – 3.25  $\text{mJ}/\text{mm}^2$ .

In order to efficiently use the Johann spectrometer to measure time-resolved spectral changes, we made a quick measurement of  $K\beta$  from the non-excited LS state and the excited mixture of LS and HS states. This allows to choose the energy at which the difference between the two spectra is highest and move the analyser to that Bragg angle. The spin relaxation kinetics was then measured by recording the decay of the laser excited signal as a function of the laser/X-ray delay. The spin kinetics is shown in figure 4.31.

The difference signal was measured for a series of time delays between the laser and the X-ray pulses, including negative values. The data points are well sampled around time zero in order to refine the actual arrival time of the pump pulse. The measured intensity was fitted against the expression for an exponential decay convoluted with a Gaussian X-ray pulse. In this expression, the laser pulse is assumed to be a Dirac function in time which is a good assumption given that the X-ray pulse is  $\sim 100$  ps. The expression for the time dependent

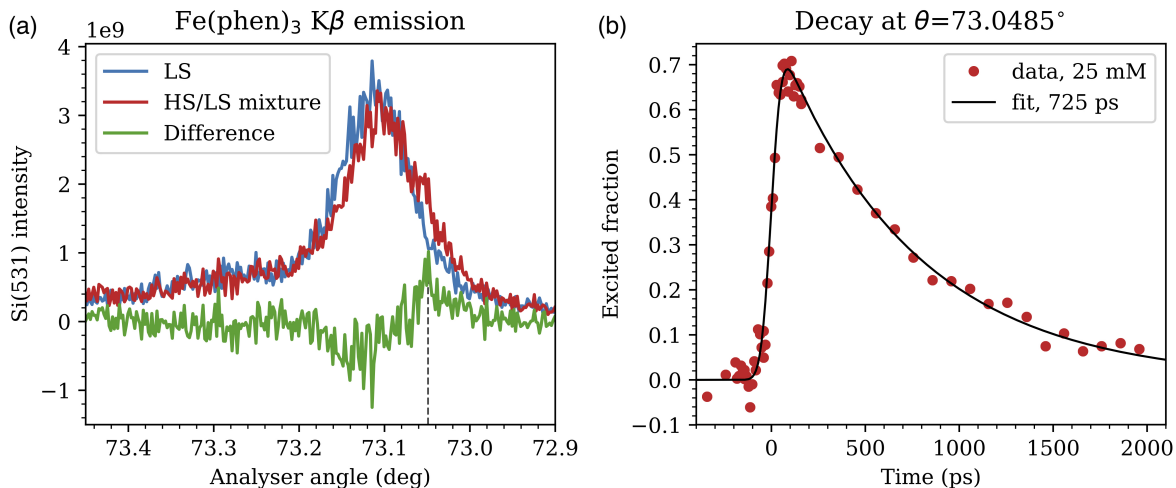


**Figure 4.31:** Lifetime of  $[\text{Fe}(\text{phen})_3]^{2+}$  in water measured by time-resolved XES in Johann geometry. (a)  $K\beta$  spectra of the non excited LS state and the excited LS+HS mixture. The data are recorded 100 ps after excitation. (b) HS population vs time measured at the analyser angle shown in dashed line in (a). The refined X-ray pulse length is 83 ps at the average single bunch current 2.9 mA, which is in agreement with the streak camera measurements shown in figure 3.6.

signal is:

$$S(\tau) = \frac{1}{\sqrt{2\pi}\sigma} \int_0^\infty dt e^{-\frac{t}{\tau_R}} e^{-\frac{(t-\tau)^2}{2\sigma^2}} = \frac{1}{2} e^{\frac{\sigma^2 - 2\tau\tau_R}{2\tau_R^2}} \left\{ 1 - \text{erf} \left( \frac{\sigma^2 - \tau\tau_R}{\sqrt{2}\sigma\tau_R} \right) \right\},$$

where  $\tau$  is the laser/X-ray delay,  $\sigma$  the width of the Gaussian X-ray pulse in time, and  $\tau_R$  the HS decay time. The fit not only gives the HS state lifetime, it also gives the offset in time zero and the X-ray pulse width. The fitted X-ray pulse width 83 ps is slightly shorter than the nominal 88 ps pulse for the average 2.9 mA single bunch current as measured by the streak camera. The HS lifetimes for  $[\text{Fe}(\text{phen})_3]^{2+}$  and its modified ligand sister compounds are shown in table 4.2.

Complex	Solvent	Concentration	Scanned delays	Lifetime
$[\text{Fe}(\text{phen})_3]^{2+}$	Water	25 mM	−500 ps − 3 ns	725 ps
$[\text{Fe}(\text{phen})_3]^{2+}$	Me(CN)	7 mM	−1 ns − 4 ns	1225 ps
$[\text{Fe}(\text{dmp})_3]^{2+}$	Me(CN)	6 mM	−1 ns − 5 ns	670 ps
$[\text{Fe}(\text{dmbp})_3]^{2+}$	Water	10 mM	−140 ps − 6 ns	830 ps
$[\text{Fe}(\text{dmbp})_3]^{2+}$	Me(CN)	10 mM	−140 ps − 6 ns	1.2 ns

**Table 4.2:** Refined lifetimes of HS–LS relaxation of  $\text{Fe}^{2+}$  complexes in solution measured by time-resolved XES in Johann geometry. The 1225 ps lifetime of  $[\text{Fe}(\text{phen})_3]^{2+}$  in MeCN is in agreement with [50].

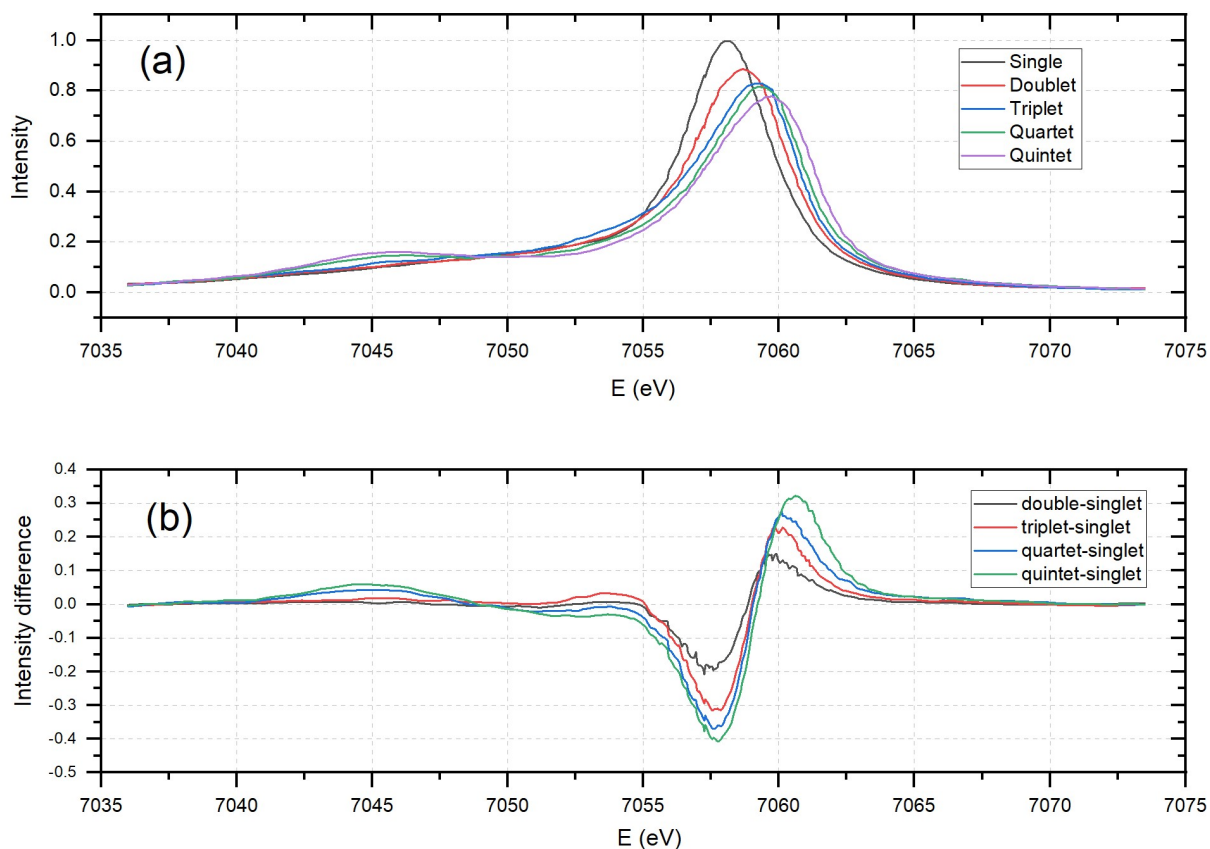


**Figure 4.32:** (a) Line shape of  $K\beta$  emission from  $\text{Fe}^{2+}$  in octahedral symmetry from the principal spin states in solution. The positions of the peaks are linear in the spin. (b) Difference spectra relative to the singlet state. The spectra are taken from W. Zhang, [7]

## 4.12 Spin state detection with von Hámós Spectrometer

In order to measure the line shape of  $K\beta$  from  $[\text{Fe}(\text{phen})_3]^{2+}$ , we performed time-resolved spectral XES measurements with the von Hámós spectrometer. As we shall see in the following, this allowed to unambiguously identify the spin of the laser excited state 100 ps after excitation and the degree of excitation.

Since the excited sample is a mixture of excited and non-excited  $[\text{Fe}(\text{phen})_3]^{2+}$  molecules, the spectrum of the excited state is a linear combination of the pure ground and excited state spectrum.

To determine the spin and excitation degree, we used the spectra published by Zhang et al. [7] and Haldrup et al. [39]. These spectra were taken from samples in solution, namely  $[\text{Fe}(\text{bpy})_3]^{2+}$  and  $[\text{Fe}(\text{phen})_2(\text{NCS})_2]^{2+}$ , and were measured with a von Hámós spectrometer. The spectra and the difference spectra are shown in figure 4.32.

The X-ray emission was generated by exposing a 10 mM solution of  $[\text{Fe}(\text{phen})_3]^{2+}$  in water to the 15 keV pink beam from the U17 undulator. The 7/8+1 filling mode was used with a single bunch current of 8 mA. The primary slits 27 m from the undulator were opened to  $2.0 \times 0.5 \text{ mmH} \times \text{mmV}$  and the single bunch isolated by the high-speed chopper at a pulse rate of 986.3 Hz. The intensity and spectral bandwidth of the beam was  $1 \times 10^9 \text{ ph/pulse}$  and 4.0%, respectively. The solution sample was delivered by the 0.36 mm Swiss Sapphire Nozzle and the jet was rotated  $45^\circ$  to increase the thickness to 0.51 mm. The XES signal was monochromatised by 8 cylindrical Si(440) analysers and the diffracted signal was recorded by the  $5 \times 1$  Maxipix detector. The line image from the individual analysers were carefully

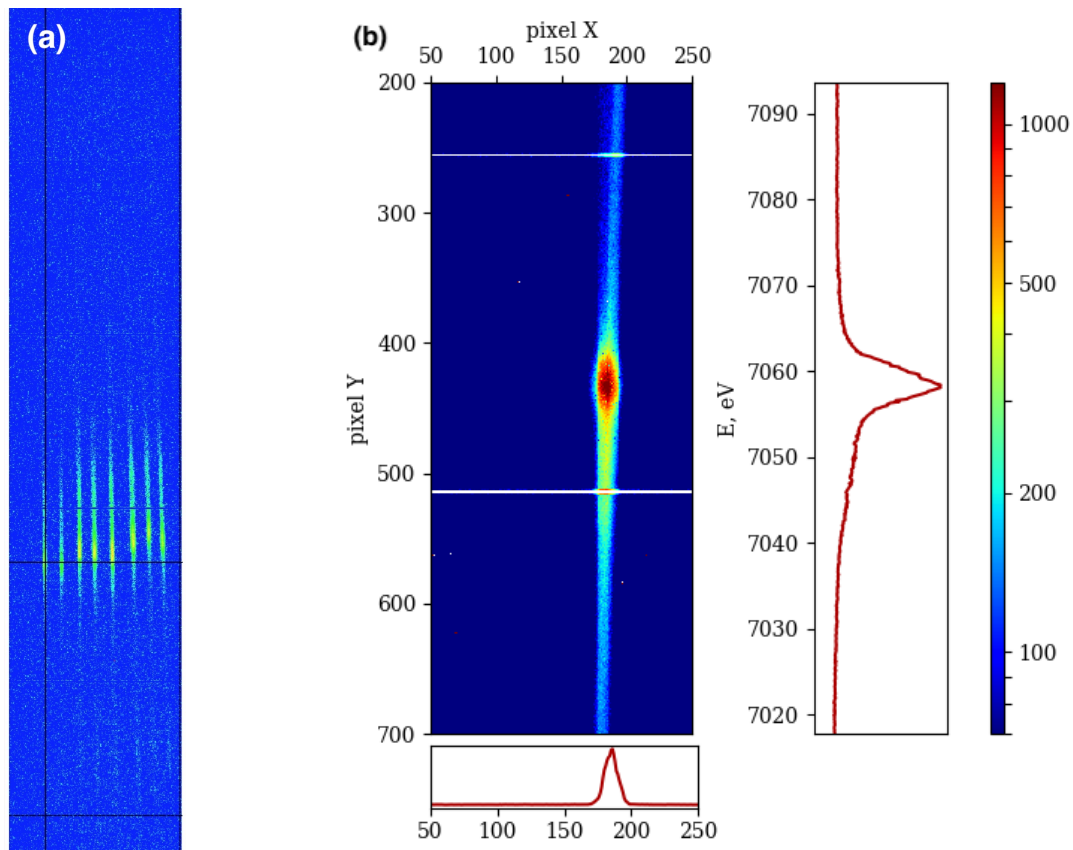


**Figure 4.33:** (a) Fe  $K\beta$  from a solid sample focused on the Maxipix by eight Si(440) analysers before overlap. (b) Image of the  $K\beta$  line from photo-excited  $[\text{Fe}(\text{phen})_3]^{2+}$  100 ps after excitation. The energy scale is vertical. The spectrum is a mixture of 82% LS and 18% HS states from incomplete laser excitation. The width of the line is 0.60 mm in fair agreement with the 1:1 sagittal focusing of the sample.

overlapped using the pitch and roll motors on the back of the analyser crystals. The images from the eight analysers are shown in figure 4.33. The detector was exposed for 100 s for the ON and OFF images with a laser/X-ray delay of 100 ps. About 250 laser ON and 250 laser OFF spectra were summed to increase the S/N ratio. The summed  $K\beta$  image for the laser ON part is shown in figure 4.33(b). To further increase the S/N ratio, horizontal pixels were summed. The image is then reduced to a 1D spectrum with 1280 superpixels along the energy axis. The laser ON and OFF spectra and their difference are shown in figure 4.34.

Recall that the  $K\beta$  spectrum is probing the  $3p \rightarrow 1s$  transition and the change in energy and shape is induced by the change in  $3d$  spin. The ON spectrum is shifted slightly to higher energy. With the increase in spin, the  $3p$  degeneracy is lifted by the  $3d$  exchange interaction. It is seen by the appearance of the  $K\beta'$  feature on the low energy side of the main peak. The difference spectrum ON-OFF is fitted against Zhang's reference spectra as shown in figure 4.35 which clearly indicates that the 100 ps state is a pure  $S = 2$  HS state. The amplitude of the difference shows that 18% of the LS population is in the HS state. The analysis shows that the HS spectrum is shifted by 1.7 eV which is easily resolved by the 0.5 eV spectrometer resolution.

When the excitation degree  $\alpha$  is known, the pure HS spectrum is calculated as:

$$HS = \frac{S_{ON} - (1 - \alpha)S_{OFF}}{\alpha},$$

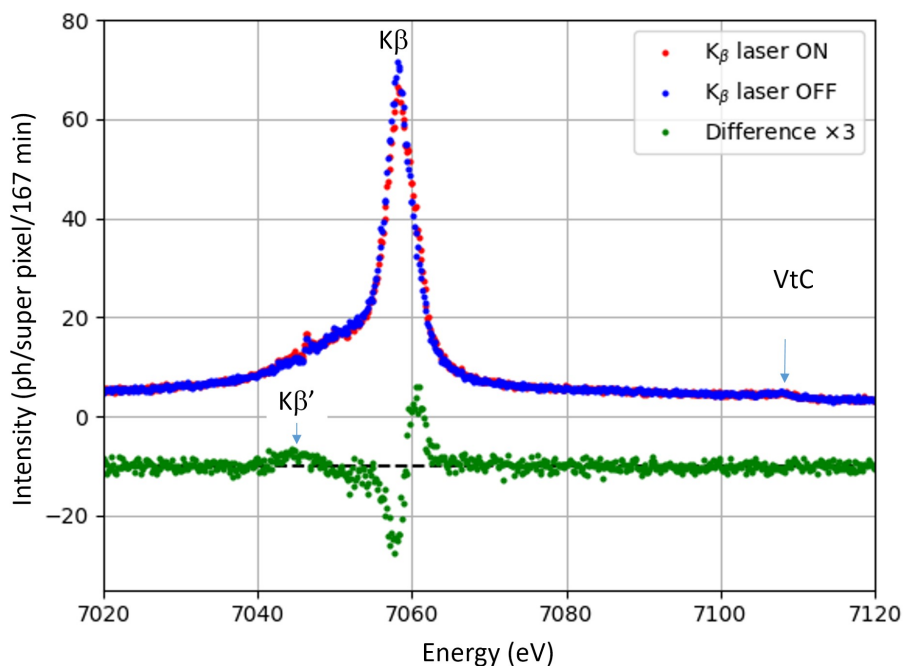


**Figure 4.34:**  $K\beta$  spectra of laser excited (ON) and non-excited (OFF)  $[\text{Fe}(\text{phen})_3]^{2+}$  in water. The time delay is 100 ps. The ON-OFF difference is shown in green. The amplitude of the green spectrum is proportional to the excitation degree. The shape is the pure signature of the HS $\rightarrow$ LS transition since non excited solutes cancel out in the difference. The 100 ps state is a pure  $S = 2$  and the excitation degree is 18%.

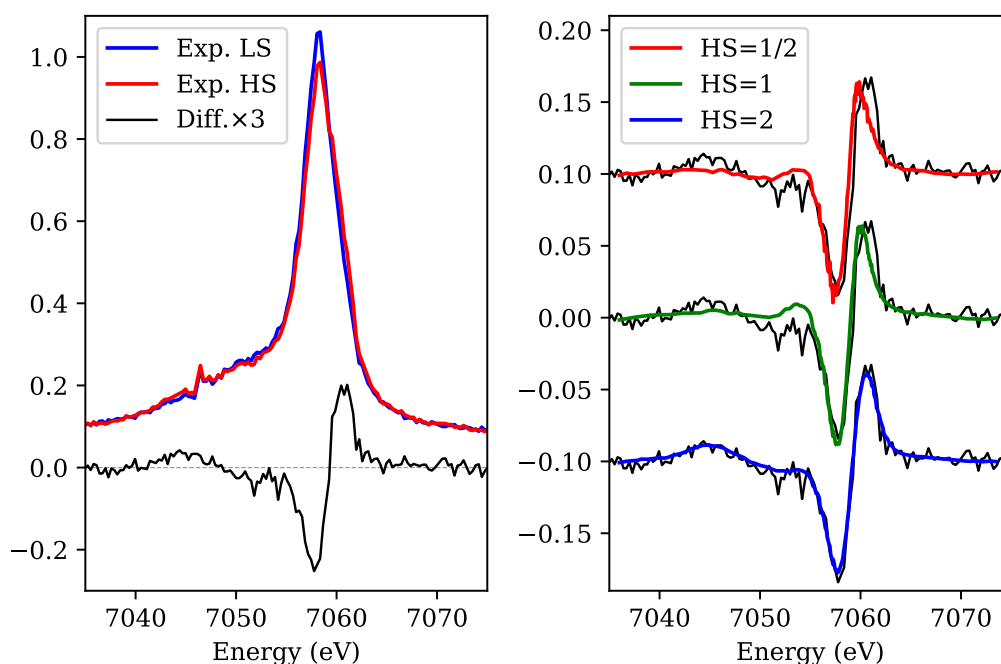


**Figure 4.35:** Fingerprinting the spin state of the 100 ps excited state by fitting the difference spectrum laser ON - laser OFF to Zhang's reference spectra. The  $S = 2$  quintet state is fitting the experimental data perfectly.

where  $S_{ON}$  and  $S_{OFF}$  are the measured spectra. The LS and HS spectra were also compared with predictions from semi-empirical multiplet calculation by Marius Retegan in figure 4.36.

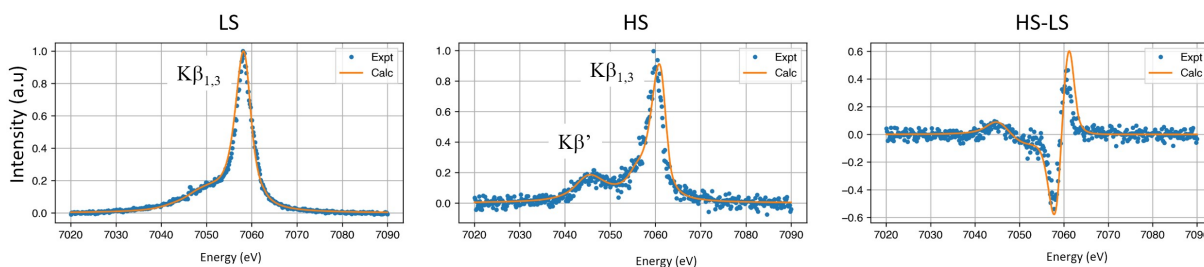


**Figure 4.36:** Measured and calculated  $K\beta$  spectra of  $[\text{Fe}(\text{phen})_3]^{2+}$ . The exchange splitting of the  $K\beta'$  and  $K\beta_{1,3}$  is 15 eV. The theoretical curves were calculated by Marius Retegan using the Crispy® software [58].

In the calculation, the parameters were adjusted to match the measured Fe-N bondlengths in the two states. The calculated spectra are shifted by 53 eV and broadened by a 1.6 eV Lorentzian to match the data. The agreement is very good. Note how the HS spectrum is split into  $K\beta'$  and  $K\beta_{1,3}$  due to exchange splitting of the 3p level. The spectra resemble closely those reported by Gyorgy Vanko in  $[\text{Fe}(\text{terpy})_2]^{2+}$  [37].

The VtC is a ligand transition hybridised with the 3d levels. The VtC is seen as the weak bump at 7107.5 eV in figure 4.34. The amplitude is  $\sim 100$  times lower than  $K\beta$ . A zoom of the VtC is shown in figure 4.37 with a simplified excitation scheme.

The laser ON and OFF VtC spectra were fitted with a Lorentzian with peak positions at 7107.30 eV (OFF) and 7107.54 eV (ON). Assuming that the ON spectrum is 82% LS and 18% HS, the extrapolated shift in HS energy is 1.33 eV. That shift is comparable with the  $t_{2g}$  and  $e_g$  gaps 2.31 eV and 1.28 eV, respectively, predicted by Marius Retegan. The low intensity of the VtC peak does not resolve  $t_{2g}$  and  $e_g$  in the HS state with the intensity on ID09. If the pump-probe experiment could run at 1 MHz, the splitting in the VtC band would be resolved as predicted by theory. The theoretical VtC line for the LS and HS states of  $[\text{Fe}(\text{phen})_3]^{2+}$  are shown in figure 4.37.

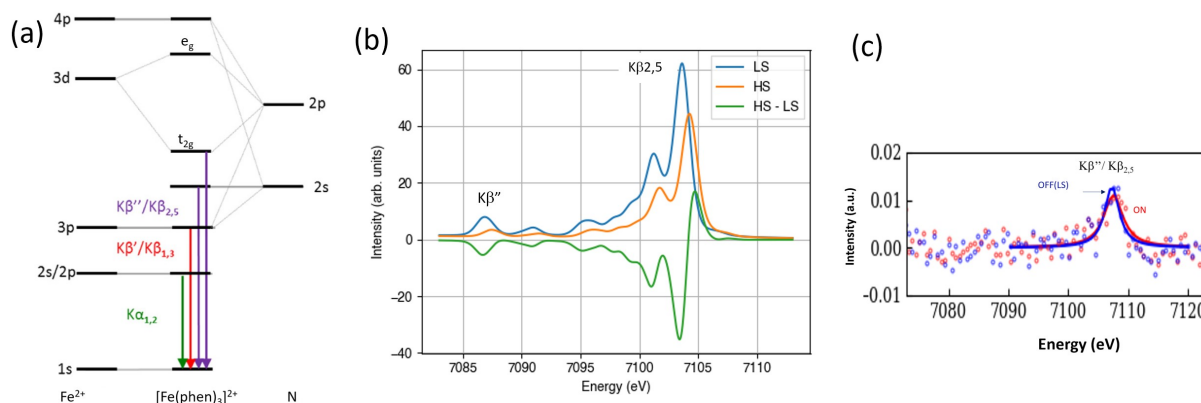


**Figure 4.37:** (a) The energy levels for isolated  $\text{Fe}^{2+}$  are shown to the left. The energy levels of an isolated N are shown to the far right. In the middle, the hybridised levels of the  $[\text{Fe}(\text{phen})_3]^{2+}$  molecule are shown with  $K\alpha$  transitions in green,  $K\beta$  in red and VtC in purple.  $K\beta_{2,5}$  probes the  $t_{2g}$  state. (b) Calculated VtC spectra in  $[\text{Fe}(\text{phen})_3]^{2+}$ .  $K\beta_{2,5}$  is shifted by +0.61 eV in the HS state. (c) Measured VtC spectra with Lorentzian fits in the LS and HS states. The ON state is shifted +0.24 eV in the 18% HS state (+1.33 eV at 100%). The VtC amplitude is 100 times weaker than  $K\beta$ .

# CONCLUSIONS

---

---

The PhD project was aimed at studying the photocycle of the metal complex  $[\text{Fe}(\text{phen})_3]^{2+}$  in aqueous solution by time-resolved X-ray emission spectroscopy (TRXES), X-ray scattering (TRWAXS) and optical spectroscopy to gain a deeper understanding of the interplay between electronic and structural changes in the molecule. The X-ray experiments were done using the 100 ps pump-probe setup on beamline ID09 at the ESRF. Fluorescence XES spectra provide unique information about the valence and spin state of metal atoms and ions and scattering probes atom-atom distribution  $g_{\alpha\beta}(r)$  for pairs of atoms. The TRWAXS signal has contributions from the solute of interest, the cage and the bulk solvent and it is not straightforward to separate them. If the lifetime of a given emission line from a metal is known from time-resolved XES,  $K\beta$  at 7058 eV in the case of  $[\text{Fe}(\text{phen})_3]^{2+}$ , that parameter can be fixed in the analysis of the TRWAXS data, which is making the structural model more reliable.

In an optical/X-ray pump-probe experiment with synchrotron radiation, the time resolution is limited by the X-ray pulse length of 100 ps (FWHM). It is a hard limit due to the dispersion in energy and space of the electrons in a bunch in a circular synchrotron. The instrumental time resolution in this study is determined by the convolution of the 100 ps X-ray pulse with the 1.2 ps laser pulse and their relative jitter of 2 ps. As a result, the time resolution is essentially given by the 100 ps X-ray pulse. In the LS  $\rightarrow$  HS and HS  $\rightarrow$  LS transitions, the atoms change position on the time scale of molecular vibrations, i.e. in 10 fs to 100 fs, so synchrotron experiments are blind to these position changes in time. By contrast the 725 ps lifetime of the HS state allows to determine the structure of this quasi stationary state and its population as a function of time. With ultrashort pulses from free electron lasers, the femtosecond time scale can now be explored and the coherent motions in photochemical reactions have been resolved in some cases like for PtPOP [? ].

To achieve 100 ps resolution with synchrotron radiation, the experiments have to be done by the tedious pump-probe method with laser & X-ray pulses running in tandem at the highest possible frequency. The laser frequency used in this work is 1 kHz, much lower than the X-ray frequency from the synchrotron. The X-ray frequency had to be lowered to match the 1 kHz laser to the X-ray pulses by the use of a mechanical high-speed chopper. In lowering the X-ray frequency, the average X-ray intensity is reduced dramatically. In 16-bunch mode for example, the X-rays are running at 5.68 MHz. When the frequency is reduced to 1 kHz, the intensity (ph/s) drops by a factor 5680. To make best use of the few X-ray pulses available at 1 kHz, it is important to have the maximum number of photons per pulse which is done by using the raw undulator spectrum, the pink beam, which can produce up to  $5 \cdot 10^9$  ph/pulse in 4-bunch mode at the ESRF. XES is pink-beam compatible when the undulator fundamental is well above the absorption edge of the metal. Pink beam WAXS also works for medium resolution work when the  $q$  range is limited to  $0 - 8 \text{ \AA}^{-1}$ . For the wider  $q$  range used in this study,  $0 - 10.6 \text{ \AA}^{-1}$ , the undulator fundamental has to be monochromatised to have a

well-defined central energy. The undulator spectrum is made symmetric with a Ru multilayer with a 2.1% BW at the expense of losing a factor of 5 in flux. The wider  $q$  range from the Ru monochromator is a great advantage for separating the solvent heating from the solute/cage signal and for fitting multiple pathways in a reaction.

The photocycle of  $[\text{Fe}(\text{phen})_3]^{2+}$  was studied previously by time-resolved optical spectroscopy and X-ray absorption (XAS). These works have established that the strong ligand field of (1,10)-phenanthroline favours a LS ( $S = 0$ ) ground state of  $[\text{Fe}(\text{phen})_3]^{2+}$  with all six 3d electrons paired in spin-up/spin-down blocks in the  $t_{2g}$  level. The  $e_g$  orbitals are empty. Calculations with Crispy<sup>®</sup> show that  $t_{2g}$  and  $e_g$  are split by 2.31 eV in LS. In the HS state,  $t_{2g}$  and  $e_g$  are split by 1.28 eV and each level has two unpaired electrons that add up to  $S = 2$ .

The LS and HS structures were calculated by DFT with no symmetry constraints ( $C_1$ ), and also with the molecular symmetry constrained to  $D_3$  and to  $C_2$ . In the LS state, the six Fe-N distances are 1.99 Å. In the HS state the structure is distorted and the bond lengths vary slightly by  $\pm 0.01$  Å around an average of 2.18 Å due to steric hindrance.

The  $[\text{Fe}(\text{phen})_3]^{2+}$  photocycle proceeds as follows. Upon absorption of a visible photon around 512 nm, the LS state is excited vertically to the Franck-Condon state  $^1\text{MLCT}$  by electron transfer to the ligand. The Fe-N bond length in  $^1\text{MLCT}$  is 1.99 Å as in the GS. The  $^1\text{MLCT}$  state is charge separated, and for solar cell applications that lifetime should be as long as possible to increase the chance of the electron being captured by a semiconductor.  $[\text{Fe}(\text{phen})_3]^{2+}$  is unusable for solar cells since the  $^1\text{MLCT}$  state is destabilised by the intersystem crossing with the lower lying  $^3\text{MLCT}$  state which in turn also crosses the HS  $^5\text{T}_2$  state. Optical studies show that the decay cascade  $^1\text{MLCT} \rightarrow ^3\text{MLCT} \rightarrow ^5\text{T}_2$  is completed in  $\sim 320$  fs.

The structure of the HS state was probed in the time range -100 ps to 2 ns by high resolution TRWAXS. The laser induced  $dS(q, t)$  has contributions from the solute, cage and solvent. The solvent term, which dominates the scattering, is caused by the change in temperature from the formation and decay of the HS state. On the nanosecond time scale, the solvent heating is adiabatic and isochoric. The shape of the solvent spectrum was measured separately with a dye and the amplitude calibrated to a MD simulation for water. The initial amplitude of the solvent term in the fitting is determined from the solute nodal points of the Debye function  $dS(q)$ . Overall the solute signal is in perfect agreement with the DFT structures with a Fe-N bond elongation of 0.19 Å in the HS state.

The temperature rise from the  $^1\text{MLCT} \rightarrow \text{HS}$  decay is 0.045 K and 0.034 K for the HS  $\rightarrow$  GS decay. The excited fraction of  $[\text{Fe}(\text{phen})_3]^{2+}$  molecules is 21% of the 10 mM solution at 100 ps after laser excitation. The increase in the pressure in the solvent is highest after about 2 ns where the pressure increase reaches 0.8 bar (8 m under water) for then to reach ambient pressure after 70 ns.

In the discussion of the temperature steps mentioned above, we assume that the solution is in local thermal equilibrium. From the thermodynamic expression of the cooling of a hot point in a fluid medium, we estimate the time it takes for a 2.1 mM concentration of excited molecules for the temperature to become locally homogeneous. With an excited solute-solute distance of 92 Å at 2.1 mM, the thermal wave front takes 82 ps to move to the midpoint at 46 Å, which is faster than the time resolution of the experiment.

The two temperature steps mentioned above are consistent with the solvent amplitude of  $dS(q)$  in the LS  $\rightarrow ^1\text{MLCT} \rightarrow ^3\text{MLCT} \rightarrow ^5\text{T}_2 \rightarrow \text{LS}$  cycle with 400 nm excitation and a 2.1 mM HS state concentration. The initial sharp step of 0.28 K is unexpected and we discussed the potential explanations for this anomaly. Our optical/optical measurements indicate that the HS state is coupling to an excited "ghost state" HS\* when pumped at 400 nm. We think that the most likely explanation for the temperature offset is sequential excitation of the HS

state. It works like this: the powerful 400 nm pump pulse excites some fraction of the HS molecules to HS\*. That state intersects  $^1\text{MLCT}$  and the molecules return to HS a second time. If the round time is shorter than the 1.2 ps pump pulse, the molecule might even be excited again. In any event, the excess heat should vanish at low laser powers. Unfortunately that is not easy to verify experimentally since the solute signal also vanishes at low powers. Anomalous temperature offsets were also observed for other molecules like  $[\text{Fe}(\text{btbip})_2]^{2+}$  and  $\text{HgBr}_2$ . In the latter case, the anomaly is caused by in-cage geminate recombination of Br with HgBr that is so fast that it escapes detection with 100 ps synchrotron pulses. In any case, even the fastest relaxation processes can't escape detection by the solvent thermometer.

The packing of water molecules around the LS and HS structures is clearly reduced in the low  $q$  part of  $dS(t, q)$  that deviates significantly from the gas phase Debye function. The cage is positive in the low  $q$  limit which shows that the cage radius is smaller in the HS state in spite of the 10% Fe-N bond elongation. The interpretation is that the expanded HS structure leaves more space for the nearest water molecule to get closer to  $\text{Fe}^{2+}$ . The spectral shape of the deviation is consistent with MD but MD overestimates the amplitude. A simple Debye simulation of the Fe..O signal shows that MD overestimates the change in the cage radius by a factor 3. As a result, the first coordination shell of water is 5.4 Å and 5.1 Å from  $\text{Fe}^{2+}$  in the LS and HS state, respectively.

The spin dynamics was probed by time-resolved XES on the  $\text{K}\beta$  line of  $\text{Fe}^{2+}$  centred at 7058 eV. The Johann spectrometer, in which the full incident beam on the analyser is monochromatised at the same energy due to the spherical shape, was employed to measure the time cause of the spin change in the LS→HS transition. The  $\text{K}\beta$  spectrum was scanned with the laser ON and laser OFF and the analyser angle moved to the position of maximum counts in the difference spectrum. At that position, the spectrometer is very sensitive to the change of spin. The spin population decay was fitted to a single exponential with a time constant of 725 ps. The onset around time zero in the fit includes the X-ray pulse profile, assumed here to be Gaussian, and time zero. The fit gives an 83 ps X-ray pulse in good agreement with the streak camera measurement of 88 ps. The  $\text{K}\beta$  and the VtC lines were measured with the von Hámos spectrometer over an energy range of 150 eV around 7058 eV using eight Si(440) analysers. The energy resolution of the spectrometer is 0.5 eV, which is enough for resolving the 1.7 eV splitting of the  $\text{K}\beta'$  and  $\text{K}\beta_{1,3}$  lines in the HS state. The splitting is caused by the exchange splitting of the 3p level from the polarised 3d electrons in the HS state. The spectral shape of the excited state at 100 ps was compared with references for doublet, triplet and quintet states from other  $\text{Fe}^{2+}$  complexes with different ligands. The quintet reference fits the 100 ps difference curve perfectly. Finally the VtC peak was observed at 7107.5 eV and it is 100 times weaker than  $\text{K}\beta$ . A tentative fit to the OFF and ON laser data indicates that the VtC peak is shifted +0.24 eV in the HS state. VtC probes the ligand bonding to  $\text{Fe}^{2+}$  and the energy position and spin contains valuable information about the nature of the ligand bond. Finally the Crispy® suite of programs for multiplet calculations in different spins states is a very powerful tool for predicting spectral shapes and shifts in energy of different spin states.

In view of the weak signal from the von Hámos spectrometer, 0.010 ph/pulse/analyser from  $\text{K}\beta$ , the focusing and monochromatisation by the analysers were studied carefully to make sure that the spectrometer is working correctly. The intensity of the  $4\pi$  fluorescence was calculated from the X-ray absorption in the dilute sample and the monochromatisation of the  $\text{K}\alpha$  and  $\text{K}\beta$  spectra by the bent analysers was examined. The intensity on the detector was then calculated from the solid angle of the pixels on the detector. The calculated intensity is 5% from the measured one, which is satisfactory in view of the many steps in the process. A striking observation is that the concentration of X-ray emitting ions is very low compared

with the 10 mM levels used in TRWAXS: 1.3 nM and 0.26 nM for the LS and HS emission, respectively (20% HS excitation). To improve the count rates significantly, future experiments should run faster than 1 kHz. If XES is stimulated by a monochromatic beam and the signal detected by a time gated detector, there is no need to chop the beam and the experiment could run at 354.4 kHz, the single bunch frequency in the  $7/8 + 1$  mode. Alternatively if the pink beam is used with a 250 gain in ph/pulse, the maximum frequency of the choppers and heatload and radiation damage on the sample become an issue. Simple simulations show that 40 kHz is the upper limit for pink beam experiments. With a 40 fold gain in count rate, the VtC emission would be detected in a few minutes and it would be possible to collect many more time delays per day at the beamline.

3D EMISSION ENERGIES

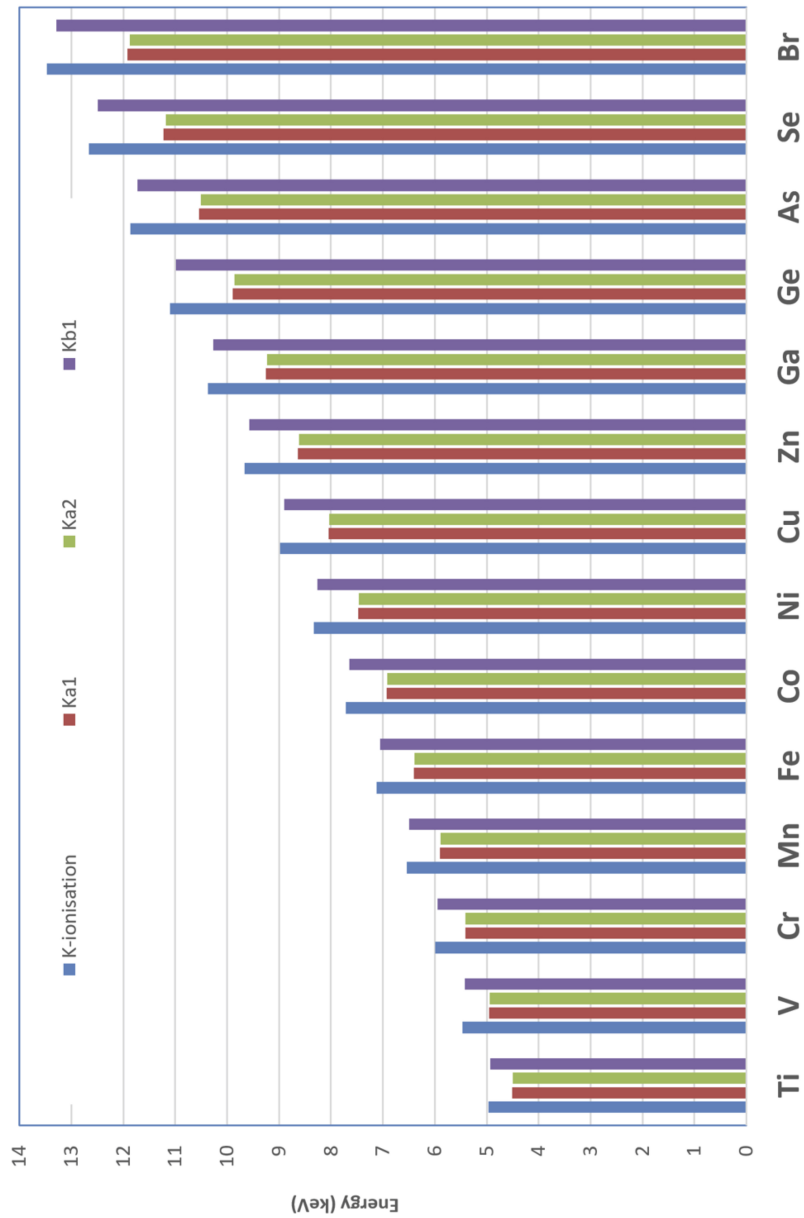
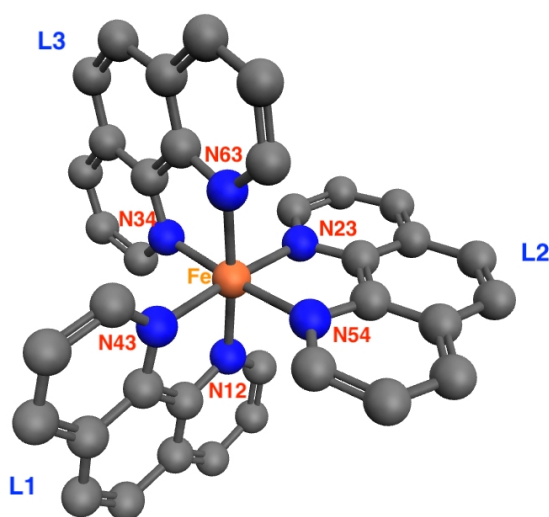


Figure A.1: Ionisation and emission energies for 3d elements.



## DFT STRUCTURE COORDINATES



**Figure B.1:**  $[\text{Fe}(\text{phen})_3]^{2+}$  structure with assigned numbers of N atoms and ligands.  $\text{Fe}^{2+}$  is red, N blue and C grey (H atoms are omitted). There are 67 atoms and the stoichiometry is  $\text{Fe}^{2+}(\text{N}_2\text{C}_{12}\text{H}_8)_3$ . Nitrogens are numbered according to the order of atoms listed in the DFT-refined HS structure "5a" ( $C_2$  symmetry) which fits WAXS data best. For structures with  $C_1$  and  $D_3$  symmetry the N positions are slightly different but within the same decade. The key distances and angles characterising the structures are listed in table B.1.

Bond or angle	Structure						
	LS ( $D_3$ )	HS 5a	HS 5b	HS 5a1	HS 5e	LS ( $C_1$ )	HS ( $C_1$ )
Fe–N <sub>12</sub>		2.1915	2.1711			1.9909	2.1916
Fe–N <sub>43</sub>						1.9901	2.1916
Fe–N <sub>23</sub>	1.9906	2.1848	2.1828	2.2021	2.1815	1.9907	2.1847
Fe–N <sub>63</sub>						1.9904	2.1846
Fe–N <sub>34</sub>		2.1720	2.1959			1.9900	2.1720
Fe–N <sub>54</sub>						1.9917	2.1720
N <sub>12</sub> –Fe–N <sub>63</sub>		169.2516°	167.0438°			175.6428°	169.2523°
N <sub>23</sub> –Fe–N <sub>43</sub>	175.5649°	169.2516°	167.0438°	168.0395°	168.5497°	175.3810°	169.2557°
N <sub>34</sub> –Fe–N <sub>54</sub>		166.0177°	169.5491°			175.6174°	165.9873°
L <sub>12</sub>		121.9763°	118.8830°			119.7863°	121.9927°
L <sub>23</sub>	120°	116.0473°	122.2341°	120°	120°	120.0424°	116.0060°
L <sub>13</sub>		121.9763°	118.8830°			120.1712°	122.0013°

**Table B.1:** Key parameters for  $[\text{Fe}(\text{phen})_3]^{2+}$  structures calculated by DFT. Fe–N distances are given in Å.  $L_{12}$ ,  $L_{23}$  and  $L_{13}$  are the angles between the central axes of the corresponding ligands.

No.	Atom	$x$ (Å)	$y$ (Å)	$z$ (Å)	No.	Atom	$x$ (Å)	$y$ (Å)	$z$ (Å)
1	Fe	0.000000	0.000000	0.000000	41	H	4.771713	-2.069009	2.750493
2	C	3.863931	-1.708463	2.274078	42	H	6.114935	-0.743575	0.985976
3	C	3.948180	-0.860410	1.144610	43	H	6.114935	0.743575	-0.985976
4	C	5.177175	-0.412274	0.546901	44	H	4.771713	2.069009	-2.750493
5	C	5.177175	0.412274	-0.546901	45	N	1.495310	0.774377	-1.061574
6	C	3.948180	0.860410	-1.144610	46	H	-1.834307	0.520111	2.499747
7	C	3.863931	1.708463	-2.274078	47	H	-3.609299	-0.816433	3.618965
8	C	-2.097800	-0.463810	2.130317	48	H	-4.177670	-3.097920	2.750493
9	C	-3.097235	-1.230529	2.755981	49	H	-3.701422	-4.923902	0.985976
10	C	-3.411538	-2.492031	2.274078	50	H	-2.413513	-5.667476	-0.985976
11	C	-2.719227	-2.989019	1.144610	51	H	-0.594043	-5.166929	-2.750493
12	N	1.495310	-0.774377	1.061574	52	H	1.367583	1.328500	2.499747
13	C	-2.945627	-4.277428	0.546901	53	H	1.097598	3.533961	3.618965
14	C	-2.231547	-4.689702	-0.546901	54	H	-0.594043	5.166929	2.750493
15	C	-1.228953	-3.849429	-1.144610	55	H	-2.413513	5.667476	0.985976
16	C	-0.452393	-4.200494	-2.274078	56	N	-0.077025	-1.682165	-1.061574
17	C	0.647229	2.048654	2.130317	57	H	-3.701422	4.923902	-0.985976
18	C	0.482948	3.297548	2.755981	58	H	-4.177670	3.097920	-2.750493
19	C	-0.452393	4.200494	2.274078	59	H	2.511701	2.717528	-3.618965
20	C	-1.228953	3.849429	1.144610	60	H	0.466724	1.848612	-2.499747
21	C	-2.231547	4.689702	0.546901	61	H	1.097598	-3.533961	-3.618965
22	C	-2.945627	4.277428	-0.546901	62	H	1.367583	-1.328500	-2.499747
23	N	-1.418286	-0.907788	1.061574	63	H	-3.609299	0.816433	-3.618965
24	C	-2.719227	2.989019	-1.144610	64	H	-1.834307	-0.520111	-2.499747
25	C	-3.411538	2.492031	-2.274078	65	N	-1.418286	0.907788	-1.061574
26	C	2.614287	2.067020	-2.755981	66	C	1.450572	-1.584843	2.130317
27	C	1.450572	1.584843	-2.130317	67	C	2.614287	-2.067020	2.755981
28	C	2.727766	-0.425296	0.570417					
29	C	2.727766	0.425296	-0.570417					
30	C	0.482948	-3.297548	-2.755981					
31	C	0.647229	-2.048654	-2.130317					
32	C	-1.732200	-2.149666	0.570417					
33	C	-0.995565	-2.574962	-0.570417					
34	N	-0.077025	1.682165	1.061574					
35	C	-3.097235	1.230529	-2.755981					
36	C	-2.097800	0.463810	-2.130317					
37	C	-0.995565	2.574962	0.570417					
38	C	-1.732200	2.149666	-0.570417					
39	H	0.466724	-1.848612	2.499747					
40	H	2.511701	-2.717528	3.618965					

Table B.2: Atomic positions ( $x, y, z$ ) of the LS  $[\text{Fe}(\text{phen})_3]^{2+}$  structure with  $D_3$  symmetry

No.	Atom	$x$ (Å)	$y$ (Å)	$z$ (Å)	No.	Atom	$x$ (Å)	$y$ (Å)	$z$ (Å)
1	Fe	0.000000	0.000000	0.076457	41	H	-2.969021	-1.685902	5.095724
2	C	-2.469070	-1.403661	4.172524	42	H	2.969021	1.685902	5.095724
3	C	-1.237814	-0.706570	4.231306	43	N	1.190887	0.663859	1.792230
4	C	-0.593713	-0.339322	5.461890	44	H	-2.670161	0.341068	-1.754227
5	C	0.593713	0.339322	5.461890	45	H	-3.797155	-0.962788	-3.563217
6	C	1.237814	0.706570	4.231306	46	H	-2.813456	-3.156666	-4.279217
7	C	2.469070	1.403661	4.172524	47	H	-0.986415	-4.890994	-3.983265
8	C	-2.269331	-0.613925	-2.081297	48	H	1.053219	-5.647438	-2.807351
9	C	-2.896295	-1.353167	-3.099649	49	H	2.822722	-5.239006	-1.036225
10	C	-2.350579	-2.564499	-3.493792	50	H	-2.565537	1.579441	1.236564
11	C	-1.175615	-3.036460	-2.862483	51	H	-3.727580	3.743134	0.760429
12	N	-1.190887	-0.663859	1.792230	52	H	-2.822722	5.239006	-1.036225
13	C	-0.543378	-4.282349	-3.198609	53	H	-1.053219	5.647438	-2.807351
14	C	0.584577	-4.700975	-2.548698	54	N	1.099099	-1.854689	-0.187916
15	C	1.177877	-3.907486	-1.508344	55	H	0.986415	4.890994	-3.983265
16	C	2.337669	-4.295857	-0.797222	56	H	2.813456	3.156666	-4.279217
17	C	-2.193478	2.254399	0.471694	57	H	3.965359	2.249202	2.866719
18	C	-2.841018	3.470891	0.196298	58	H	2.752782	1.553632	0.785436
19	C	-2.337669	4.295857	-0.797222	59	H	3.727580	-3.743134	0.760429
20	C	-1.177877	3.907486	-1.508344	60	H	2.565537	-1.579441	1.236564
21	C	-0.584577	4.700975	-2.548698	61	H	3.797155	0.962788	-3.563217
22	C	0.543378	4.282349	-3.198609	62	H	2.670161	-0.341068	-1.754227
23	N	-1.158855	-1.031911	-1.461647	63	N	1.158855	1.031911	-1.461647
24	C	1.175615	3.036460	-2.862483	64	C	-2.349472	-1.329190	1.768946
25	C	2.350579	2.564499	-3.493792	65	C	-3.022784	-1.716090	2.942461
26	C	3.022784	1.716090	2.942461	66	H	1.073688	0.613072	6.398296
27	C	2.349472	1.329190	1.768946	67	H	-1.073688	-0.613072	6.398296
28	C	-0.627575	-0.355125	2.996686					
29	C	0.627575	0.355125	2.996686					
30	C	2.841018	-3.470891	0.196298					
31	C	2.193478	-2.254399	0.471694					
32	C	-0.609160	-2.225823	-1.839840					
33	C	0.580824	-2.663679	-1.160981					
34	N	-1.099099	1.854689	-0.187916					
35	C	2.896295	1.353167	-3.099649					
36	C	2.269331	0.613925	-2.081297					
37	C	-0.580824	2.663679	-1.160981					
38	C	0.609160	2.225823	-1.839840					
39	H	-2.752782	-1.553632	0.785436					
40	H	-3.965359	-2.249202	2.866719					

**Table B.3:** Atomic positions ( $x, y, z$ ) of the HS(5a)  $[\text{Fe}(\text{phen})_3]^{2+}$  structure with  $C_2$  symmetry

No.	Atom	$x$ (Å)	$y$ (Å)	$z$ (Å)	No.	Atom	$x$ (Å)	$y$ (Å)	$z$ (Å)
1	Fe	0.000000	0.000000	-0.013589	41	H	-2.955338	-1.708066	4.989554
2	C	-2.455120	-1.425594	4.066608	42	H	2.955338	1.708066	4.989554
3	C	-1.232004	-0.717711	4.123047	43	N	1.169918	0.691694	1.679505
4	C	-0.591641	-0.342680	5.353455	44	H	-2.650649	0.272918	-1.831117
5	C	0.591641	0.342680	5.353455	45	H	-3.838616	-1.123760	-3.538248
6	C	1.232004	0.717711	4.123047	46	H	-2.931714	-3.393868	-4.091239
7	C	2.455120	1.425594	4.066608	47	H	-1.144287	-5.153155	-3.700834
8	C	-2.281548	-0.712180	-2.101749	48	H	0.925120	-5.853867	-2.542850
9	C	-2.942546	-1.503629	-3.057641	49	H	2.789866	-5.327916	-0.904192
10	C	-2.438077	-2.757451	-3.361033	50	H	-2.656449	1.511167	1.107815
11	C	-1.264386	-3.216927	-2.716561	51	H	-3.798466	3.703295	0.716753
12	N	-1.169918	-0.691694	1.679505	52	H	-2.789866	5.327916	-0.904192
13	C	-0.666854	-4.497254	-2.976983	53	H	-0.925120	5.853867	-2.542850
14	C	0.477806	-4.884498	-2.336454	54	N	1.117867	-1.879510	-0.213584
15	C	1.123218	-4.024387	-1.383536	55	H	1.144287	5.153155	-3.700834
16	C	2.320536	-4.366786	-0.709604	56	H	2.931714	3.393868	-4.091239
17	C	-2.245299	2.235678	0.410678	57	H	3.937956	2.291455	2.756936
18	C	-2.880262	3.471104	0.186006	58	H	2.724002	1.610865	0.680920
19	C	-2.320536	4.366786	-0.709604	59	H	3.798466	-3.703295	0.716753
20	C	-1.123218	4.024387	-1.383536	60	H	2.656449	-1.511167	1.107815
21	C	-0.477806	4.884498	-2.336454	61	H	3.838616	1.123760	-3.538248
22	C	0.666854	4.497254	-2.976983	62	H	2.650649	-0.272918	-1.831117
23	N	-1.177012	-1.122088	-1.469723	63	N	1.177012	1.122088	-1.469723
24	C	1.264386	3.216927	-2.716561	64	C	-2.325917	-1.368410	1.661720
25	C	2.438077	2.757451	-3.361033	65	C	-3.000537	-1.749169	2.834012
26	C	3.000537	1.749169	2.834012	66	H	1.070410	0.618616	6.289980
27	C	2.325917	1.368410	1.661720	67	H	-1.070410	-0.618616	6.289980
28	C	-0.619533	-0.364010	2.888357					
29	C	0.619533	0.364010	2.888357					
30	C	2.880262	-3.471104	0.186006					
31	C	2.245299	-2.235678	0.410678					
32	C	-0.656856	-2.348808	-1.768439					
33	C	0.552829	-2.753740	-1.098166					
34	N	-1.117867	1.879510	-0.213584					
35	C	2.942546	1.503629	-3.057641					
36	C	2.281548	0.712180	-2.101749					
37	C	-0.552829	2.753740	-1.098166					
38	C	0.656856	2.348808	-1.768439					
39	H	-2.724002	-1.610865	0.680920					
40	H	-3.937956	-2.291455	2.756936					

Table B.4: Atomic positions ( $x, y, z$ ) of the HS(5b)  $[\text{Fe}(\text{phen})_3]^{2+}$  structure with  $C_2$  symmetry

No.	Atom	$x$ (Å)	$y$ (Å)	$z$ (Å)	No.	Atom	$x$ (Å)	$y$ (Å)	$z$ (Å)
1	Fe	0.000000	0.000000	0.000000	41	H	5.035128	-1.883619	2.850660
2	C	4.112796	-1.564459	2.371701	42	H	6.340199	-0.681882	1.030926
3	C	4.172963	-0.784842	1.190555	43	H	6.340199	0.681882	-1.030926
4	C	5.403439	-0.377137	0.570583	44	H	5.035128	1.883619	-2.850660
5	C	5.403439	0.377137	-0.570583	45	N	1.732677	0.735440	-1.142903
6	C	4.172963	0.784842	-1.190555	46	H	-1.850723	0.231475	2.646913
7	C	4.112796	1.564459	-2.371701	47	H	-3.571790	-1.174324	3.805544
8	C	-2.129227	-0.743586	2.257094	48	H	-4.148826	-3.418739	2.850660
9	C	-3.094200	-1.540476	2.902010	49	H	-3.760627	-5.149833	1.030926
10	C	-3.411259	-2.779556	2.371701	50	H	-2.579573	-5.831715	-1.030926
11	C	-2.766175	-3.221471	1.190555	51	H	-0.886301	-5.302358	-2.850660
12	N	1.732677	-0.735440	1.142903	52	H	1.125825	1.487036	2.646913
13	C	-3.028329	-4.490947	0.570583	53	H	0.768900	3.680423	3.805544
14	C	-2.375109	-4.868084	-0.570583	54	H	-0.886301	5.302358	2.850660
15	C	-1.406789	-4.006313	-1.190555	55	H	-2.579573	5.831715	1.030926
16	C	-0.701537	-4.344015	-2.371701	56	N	-0.229428	-1.868263	-1.142903
17	C	0.420649	2.215758	2.257094	57	H	-3.760627	5.149833	-1.030926
18	C	0.213009	3.449894	2.902010	58	H	-4.148826	3.418739	-2.850660
19	C	-0.701537	4.344015	2.371701	59	H	2.802890	2.506099	-3.805544
20	C	-1.406789	4.006313	1.190555	60	H	0.724898	1.718511	-2.646913
21	C	-2.375109	4.868084	0.570583	61	H	0.768900	-3.680423	-3.805544
22	C	-3.028329	4.490947	-0.570583	62	H	1.125825	-1.487036	-2.646913
23	N	-1.503249	-1.132822	1.142903	63	H	-3.571790	1.174324	-3.805544
24	C	-2.766175	3.221471	-1.190555	64	H	-1.850723	-0.231475	-2.646913
25	C	-3.411259	2.779556	-2.371701	65	N	-1.503249	1.132822	-1.142903
26	C	2.881192	1.909418	-2.902010	66	C	1.708578	-1.472172	2.257094
27	C	1.708578	1.472172	-2.257094	67	C	2.881192	-1.909418	2.902010
28	C	2.938919	-0.394595	0.603736					
29	C	2.938919	0.394595	-0.603736					
30	C	0.213009	-3.449894	-2.902010					
31	C	0.420649	-2.215758	-2.257094					
32	C	-1.811189	-2.347881	0.603736					
33	C	-1.127730	-2.742476	-0.603736					
34	N	-0.229428	1.868263	1.142903					
35	C	-3.094200	1.540476	-2.902010					
36	C	-2.129227	0.743586	-2.257094					
37	C	-1.127730	2.742476	0.603736					
38	C	-1.811189	2.347881	-0.603736					
39	H	0.724898	-1.718511	2.646913					
40	H	2.802890	-2.506099	3.805544					

**Table B.5:** Atomic positions ( $x, y, z$ ) of the HS(5a1)  $[\text{Fe}(\text{phen})_3]^{2+}$  structure with  $D_3$  symmetry

No.	Atom	$x$ (Å)	$y$ (Å)	$z$ (Å)	No.	Atom	$x$ (Å)	$y$ (Å)	$z$ (Å)
1	Fe	0.000000	0.000000	0.000000	41	H	5.011513	-1.846573	2.872301
2	C	4.088800	-1.536721	2.388119	42	H	6.314204	-0.670189	1.038592
3	C	4.147237	-0.772202	1.198595	43	H	6.314204	0.670189	-1.038592
4	C	5.377562	-0.370665	0.574670	44	H	5.011513	1.846573	-2.872301
5	C	5.377562	0.370665	-0.574670	45	N	1.705621	0.733452	-1.145430
6	C	4.147237	0.772202	-1.198595	46	H	-1.834831	0.248717	2.656462
7	C	4.088800	1.536721	-2.388119	47	H	-3.524471	-1.174888	3.832654
8	C	-2.107275	-0.728362	2.268011	48	H	-4.104935	-3.416811	2.872301
9	C	-3.056425	-1.534191	2.921414	49	H	-3.737502	-5.133166	1.038592
10	C	-3.375239	-2.772644	2.388119	50	H	-2.576701	-5.803355	-1.038592
11	C	-2.742366	-3.205512	1.198595	51	H	-0.906577	-5.263384	-2.872301
12	N	1.705621	-0.733452	1.145430	52	H	1.132810	1.464651	2.656462
13	C	-3.009786	-4.471773	0.574670	53	H	0.744753	3.639725	3.832654
14	C	-2.367776	-4.842438	-0.574670	54	H	-0.906577	5.263384	2.872301
15	C	-1.404872	-3.977714	-1.198595	55	H	-2.576701	5.803355	1.038592
16	C	-0.713560	-4.309365	-2.388119	56	N	-0.217622	-1.843837	-1.145430
17	C	0.422857	2.189134	2.268011	57	H	-3.737502	5.133166	-1.038592
18	C	0.199564	3.414037	2.921414	58	H	-4.104935	3.416811	-2.872301
19	C	-0.713560	4.309365	2.388119	59	H	2.779718	2.464838	-3.832654
20	C	-1.404872	3.977714	1.198595	60	H	0.702020	1.713368	-2.656462
21	C	-2.367776	4.842438	0.574670	61	H	0.744753	-3.639725	-3.832654
22	C	-3.009786	4.471773	-0.574670	62	H	1.132810	-1.464651	-2.656462
23	N	-1.487998	-1.110385	1.145430	63	H	-3.524471	1.174888	-3.832654
24	C	-2.742366	3.205512	-1.198595	64	H	-1.834831	-0.248717	-2.656462
25	C	-3.375239	2.772644	-2.388119	65	N	-1.487998	1.110385	-1.145430
26	C	2.856861	1.879846	-2.921414	66	C	1.684417	-1.460772	2.268011
27	C	1.684417	1.460772	-2.268011	67	C	2.856861	-1.879846	2.921414
28	C	2.912875	-0.389147	0.605465					
29	C	2.912875	0.389147	-0.605465					
30	C	0.199564	-3.414037	-2.921414					
31	C	0.422857	-2.189134	-2.268011					
32	C	-1.793449	-2.328050	0.605465					
33	C	-1.119426	-2.717198	-0.605465					
34	N	-0.217622	1.843837	1.145430					
35	C	-3.056425	1.534191	-2.921414					
36	C	-2.107275	0.728362	-2.268011					
37	C	-1.119426	2.717198	0.605465					
38	C	-1.793449	2.328050	-0.605465					
39	H	0.702020	-1.713368	2.656462					
40	H	2.779718	-2.464838	3.832654					

Table B.6: Atomic positions ( $x, y, z$ ) of the HS(5e)  $[\text{Fe}(\text{phen})_3]^{2+}$  structure with  $D_3$  symmetry

No.	Atom	$x$ (Å)	$y$ (Å)	$z$ (Å)	No.	Atom	$x$ (Å)	$y$ (Å)	$z$ (Å)
1	Fe	-0.000197	0.000139	0.077427	41	H	-2.968197	-1.686357	5.097166
2	C	-2.468650	-1.403665	4.173900	42	H	2.969802	1.685386	5.096328
3	C	-1.237151	-0.706992	4.232424	43	N	1.191478	0.663221	1.793035
4	C	-0.592643	-0.340212	5.462886	44	H	-2.670361	0.341912	-1.753005
5	C	0.594607	0.338781	5.462732	45	H	-3.796040	-0.960228	-3.564067
6	C	1.238296	0.706384	4.232090	46	H	-2.811343	-3.152718	-4.282221
7	C	2.469729	1.403150	4.173205	47	H	-0.984303	-4.887429	-3.986650
8	C	-2.269134	-0.612648	-2.080880	48	H	1.054356	-5.644967	-2.810170
9	C	-2.895360	-1.350861	-3.100381	49	H	2.822809	-5.238199	-1.037308
10	C	-2.349144	-2.561631	-3.495585	50	H	-2.565635	1.580250	1.237036
11	C	-1.174554	-3.034119	-2.863990	51	H	-3.728351	3.743200	0.758893
12	N	-1.191519	-0.662949	1.793335	52	H	-2.824515	5.237266	-1.039604
13	C	-0.541919	-4.279503	-3.201076	53	H	-1.054936	5.644675	-2.811183
14	C	0.585591	-4.698779	-2.550776	54	N	1.098725	-1.854549	-0.187202
15	C	1.178213	-3.906289	-1.509313	55	H	0.984988	4.887998	-3.986060
16	C	2.337552	-4.295288	-0.797828	56	H	2.812719	3.153807	-4.280459
17	C	-2.193924	2.254568	0.471414	57	H	3.966313	2.248011	2.867328
18	C	-2.841820	3.470591	0.194912	58	H	2.753768	1.552163	0.786138
19	C	-2.338926	4.294656	-0.799605	59	H	3.726417	-3.744035	0.761244
20	C	-1.178988	3.906018	-1.510325	60	H	2.564428	-1.580481	1.238228
21	C	-0.585993	4.698666	-2.551457	61	H	3.797008	0.961108	-3.562442
22	C	0.542235	4.279896	-3.200833	62	H	2.670331	-0.341577	-1.752337
23	N	-1.158871	-1.031003	-1.461082	63	N	1.158686	1.031244	-1.460888
24	C	1.175017	3.034679	-2.863340	64	C	-2.350370	-1.327798	1.770333
25	C	2.350100	2.562501	-3.494235	65	C	-3.023147	-1.715191	2.943955
26	C	3.023582	1.715207	2.943104	66	H	1.074675	0.612401	6.399120
27	C	2.350262	1.328169	1.769685	67	H	-1.072216	-0.614238	6.399408
28	C	-0.627395	-0.355065	2.997707					
29	C	0.628030	0.354726	2.997550					
30	C	2.840320	-3.471165	0.196709					
31	C	2.192791	-2.254809	0.472582					
32	C	-0.608843	-2.224561	-1.840119					
33	C	0.580866	-2.662857	-1.161135					
34	N	-1.099442	1.854566	-0.187819					
35	C	2.896126	1.351638	-3.099064					
36	C	2.269313	0.613091	-2.080158					
37	C	-0.581490	2.662778	-1.161765					
38	C	0.608723	2.224785	-1.840062					
39	H	-2.754421	-1.551340	0.786907					
40	H	-3.965893	-2.248006	2.868457					

**Table B.7:** Atomic positions ( $x, y, z$ ) of the LS  $[\text{Fe}(\text{phen})_3]^{2+}$  structure with  $C_1$  symmetry

No.	Atom	$x$ (Å)	$y$ (Å)	$z$ (Å)	No.	Atom	$x$ (Å)	$y$ (Å)	$z$ (Å)
1	Fe	-0.003748	0.007666	0.000230	41	H	5.197672	-0.075741	2.748108
2	C	4.219985	-0.088573	2.273767	42	H	5.936652	1.644870	0.969251
3	C	3.974642	0.720708	1.139284	43	H	5.370278	3.008738	-1.011170
4	C	4.942012	1.595202	0.533161	44	H	3.619965	3.720876	-2.772602
5	C	4.627943	2.351645	-0.564947	45	N	1.078952	1.297262	-1.060434
6	C	3.318606	2.299791	-1.157653	46	H	-1.908835	-0.227932	2.490217
7	C	2.916572	3.047956	-2.289515	47	H	-3.019286	-2.151917	3.610744
8	C	-1.763989	-1.237094	2.123278	48	H	-2.642970	-4.474911	2.749124
9	C	-2.383407	-2.333330	2.749856	49	H	-1.482764	-5.971054	0.992380
10	C	-2.175605	-3.617806	2.271459	50	H	-0.002335	-6.153822	-0.976923
11	C	-1.340129	-3.805638	1.145162	51	H	1.472480	-4.984048	-2.743797
12	N	1.672410	-0.130248	1.065598	52	H	0.739679	1.759783	2.502996
13	C	-1.040727	-5.080850	0.551721	53	H	-0.370700	3.680439	3.628472
14	C	-0.219643	-5.182267	-0.540055	54	H	-2.565927	4.525074	2.763183
15	C	0.372685	-4.017298	-1.139657	55	H	-4.438328	4.277897	1.001661
16	C	1.224594	-4.038419	-2.269047	56	N	0.581693	-1.572033	-1.062189
17	C	-0.204802	2.142271	2.134639	57	H	-5.335907	3.094332	-0.972617
18	C	-0.844174	3.225437	2.763930	58	H	-5.058605	1.237547	-2.746744
19	C	-2.058212	3.692136	2.284045	59	H	1.278025	3.468097	-3.629034
20	C	-2.636142	3.068789	1.152916	60	H	-0.285420	1.899702	-2.493848
21	C	-3.888609	3.451091	0.558602	61	H	2.389033	-2.820302	-3.616650
22	C	-4.386284	2.794937	-0.536184	62	H	1.772178	-0.684015	-2.502890
23	N	-0.960421	-1.381140	1.058076	63	H	-3.639902	-0.630846	-3.628193
24	C	-3.673257	1.701145	-1.138990	64	H	-1.483729	-1.172616	-2.510269
25	C	-4.115864	0.978527	-2.272215	65	N	-1.660933	0.295726	-1.063909
26	C	1.621491	2.908322	-2.764724	66	C	1.939663	-0.889187	2.139500
27	C	0.727278	2.027117	-2.130264	67	C	3.199886	-0.889462	2.763939
28	C	2.679288	0.657690	0.568092					
29	C	2.354231	1.440238	-0.575116					
30	C	1.730971	-2.842291	-2.753703					
31	C	1.392196	-1.627890	-2.130563					
32	C	-0.760483	-2.647511	0.569973					
33	C	0.086577	-2.752174	-0.568607					
34	N	-0.728319	1.525538	1.063768					
35	C	-3.331443	-0.054835	-2.761386					
36	C	-2.111914	-0.372732	-2.136707					
37	C	-1.923178	1.989294	0.574768					
38	C	-2.435799	1.313381	-0.567616					
39	H	1.129915	-1.503650	2.514550					
40	H	3.352417	-1.523818	3.631536					

Table B.8: Atomic positions ( $x, y, z$ ) of the HS  $[\text{Fe}(\text{phen})_3]^{2+}$  structure with  $C_1$  symmetry



# TRANSITION OPTICAL ABSORPTION SPECTROSCOPY (TOAS) MEASUREMENTS

The experimental setup is shown in figure C.1. The sample is excited by an intense monochromatic laser pump pulse of 398 nm and probed by a weak polychromatic laser pulse. The duration of the pump and probe pulses is  $\sim 150$  fs, and the time resolution of the experiment is thus  $\sim 250$  fs.

At the output of the laser the beam has 0.35 W of power and the wavelength is 795 nm. The beamsplitter (BS) divides the 795 nm laser beam into an intense pump and a much weaker probe pulse.

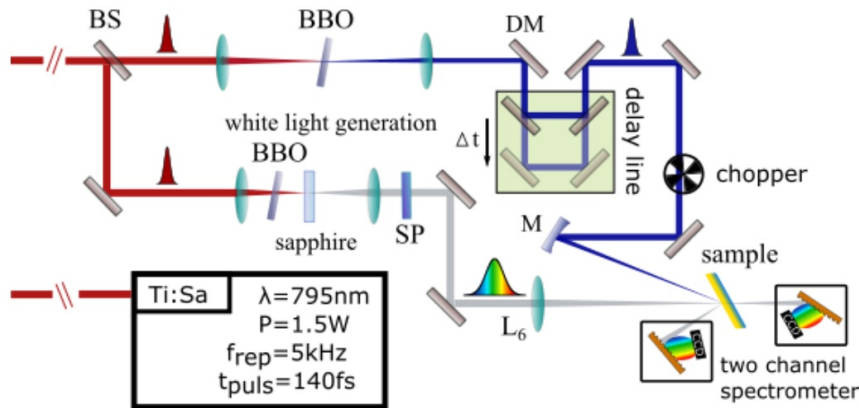


**Figure C.1:** The setup of the laser pump/laser probe TOAS experiment.

The probe beam is focused onto the Ti sapphire crystal, and the high electromagnetic field generates a continuous spectrum from 400 nm to 750 nm. The remaining near-infrared 795 nm component is blocked by a short pass filter (SP). The white light probe pulses are focused onto the sample and the reflection and transmission are measured simultaneously by a two-channel spectrometer.

The near-infrared pump pulses are focused onto a BBO crystal (beta Barium borate  $\text{BaB}_2\text{O}_4$ ) to generate the second harmonic of 398 nm. The second harmonic is reflected by a dichroic mirror (DM) and enters the motorised delay stage, where the time delay between the

---

pump and the probe pulses can be changed with in  $\sim$  fs steps within a few ns range. After the delay stage, the pump pulses are modulated with a frequency of 2.5 kHz by a mechanical chopper synchronised to the 5 kHz repetition rate of the probe. The probe thus measures a sequence of spectra transmitted by the excited and unexcited sample.

The sample diluted to 2 mM was circulated in a 360  $\mu\text{m}$ -thick flat liquid jet. The pump pulse was focused onto a  $85 \times 85 \mu\text{m}^2$  (FWHM) circular spot on the sample. The sample was circulated at a rate of 1 mm/ms, which means that between the two consequent probe pulses at 5 kHz the sample was fully refreshed (moved by 200  $\mu\text{m}$  in 200  $\mu\text{s}$ ).

The laser output power was tuned between  $\sim 4 - 25$  mW. At 5 kHz repetition rate this corresponds to  $1 - 5 \mu\text{J}/\text{pulse}$ . As almost all the power was put into the pump pulse, the excitation fluence was  $\sim 0.1$  to  $0.6 \text{ mJ}/\text{mm}^2$  for the given focusing.

---

# SIMULATIONS OF SINGLE-PULSE LAUE DIFFRACTION FROM PROTEINS WITH RADIATION FROM SYNCHROTRON AND XFEL SOURCES

---

In my first year I studied the feasibility of doing Laue serial crystallography with the ID09 beam parameters from the old ESRF source and new EBS source. In the simulations micro-crystals of Myoglobin are exposed to single pulses from the U17 undulator on ID09. The diffracted intensities are calculated for different focus and crystal sizes for random orientations of the crystals. The background from water scattering, elastic and inelastic, is included which allows to estimate the resolution limit  $d_{min}$  as a function of the crystal size.

## D.1 Introduction

Macromolecular crystallography is a powerful tool for structure determination that has been used to define structures of tens of thousands of protein molecules and molecular complexes to atomic resolution. However, understanding the relationship between protein structure and their function requires dynamics information, which is much more challenging.

In large biological systems, reactions typically proceed via a series of intermediates with lifetimes and duration of the overall reaction from femtoseconds to seconds or even longer. Time-resolved crystallography requires the synchronised initiation of the reaction in a significant fraction of the sample, and the triggering event must be faster than the process of interest. For light-dependent systems, the activation is done by a pump laser pulse and the space-average structure of the intermediates is probed by an X-ray pulse after a certain time delay. By varying the time delay after reaction initiation, the structural changes and reaction kinetics are recorded in a so-called “molecular movie”. The time resolution is defined by the convolution of the temporal profiles of the pump and probe pulses and of the jitter in the time delay between these pulses. For monochromatic synchrotron radiation, the X-ray pulse intensity is rather low, which requires longer exposure times for a single diffraction pattern acquisition, thus affecting the time resolution. The time resolution can be boosted by either increasing the X-ray flux, as in case of ultra-brilliant X-ray free-electron lasers (XFEL) with 10<sup>12</sup> photons in a 100 fs pulse, or by taking advantage of Laue diffraction with a polychromatic synchrotron beam. This technique is utilizing the “pink” X-ray beam naturally emitted

by insertion devices at synchrotron sources to record diffraction patterns from stationary single crystals, and the time resolution has increased over the last 20 years from milliseconds to nanoseconds and more recently, to 100 ps, the limit imposed by the 100 ps X-ray pulse, with up to 1010 photons per pulse.

Each of these methods has advantages and drawbacks. XFEL radiation is essentially monochromatic (bandwidth 0.2%) so the number of observable diffraction spots per pattern is limited. Also, the edges of the spectrum are very sharp so many of the diffraction intensities are only partially recorded. In contrast, the wider bandwidth (1-5%) of a pink beam speeds up the data collection simply because a complete data set is collected with fewer images. Furthermore, the intensities are fully recorded by the smooth undulator spectrum (fundamental). However, for both the XFEL and Laue method, the high X-ray flux produces significant radiation damage, and this problem becomes even worse when the experiment is conducted at biologically relevant temperatures in order not to freeze out molecular motions. The importance of the ultrashort XFEL pulse is obvious here, as the diffraction pattern is obtained before the crystal is destroyed, and the data is free from radiation damage. The 100 ps synchrotron pulse is too long to avoid this undesirable effect.

Another advantage of XFELs over synchrotrons is that even sub-micron crystal sizes are sufficient to get good quality diffraction data. Classical Laue diffraction experiment requires single crystals of one to several hundred micron size mounted on the tip of a goniometer. Diffraction patterns are collected at different crystal orientations in order to record enough reflection intensities  $I(h,k,l)$  to reconstruct the electron density of the studied structure. However, many proteins are not able to form crystals of sufficient size, and most reactions in crystals are effectively irreversible due to radiation damage, slow return to the ground state or the reaction itself is irreversible. Serial Laue crystallography aims to overcome these problems by combining single images from multiple crystals, the approach widely used at XFELs. This would allow using smaller crystals and the lower intensity of synchrotron sources compared to XFELs would be partially compensated by the broader bandwidth and thus the greater number of observable reflections. Moreover, sacrificing the time resolution in synchrotron studies for studying slower processes with super pulses, i.e. trains of multiple 100 ps pulses, would increase the beam intensity and thus the signal to noise ratio.

Serial Laue crystallography approach could be tested on the ID09 beamline of the ESRF. In order to estimate the optimal crystal size for such an experiment, as well as the diffraction data quality and the number of diffraction patterns from randomly oriented crystals needed to get a complete dataset, a calculation predicting the Laue intensities from carboxymyoglobin crystals on a liquid background was made. The calculation required specification of the sample, source and detector parameters. The main input parameters are presented in the following chart (figure D.1). These parameters are described in the next sections of the present report.

The ID09 parameters that have been used as default for the Laue simulations are presented in table D.1

## D.2 Myoglobin structure

Myoglobin is a small monomeric hemoprotein whose physiological importance is principally related to its ability to bind molecular oxygen. Its single polypeptide chain with molecular weight of  $\sim 17$  kDa consists of 153 amino acids. Myoglobin is the first protein for which a 3D structure was determined by X-ray crystallography by Max Perutz and John Kendrew in 1958, resulting in a Nobel Prize in chemistry 4 years later. The structure topology is a

Beamline parameters	Detector parameters
Spectrum & intensity: fig. 3.9; $3 \cdot 10^9$ ph	Distance to sample 100 mm
Focus size (H×V): $75 \times 45 \mu\text{m}^2$	Pixel array: $3840 \times 3840$
Slit size (H×V): $7 \times 0.7 \text{ mm}^2$	Pixel size: $44.27 \mu\text{m}$
Pulse length: 100 ps	Binning mode: $2 \times 2$
Mirrors and attenuators: Pd mirror, 1 mm C filters	Point spread function: $100 \mu\text{m}$
	Quantum efficiency: $\sim 0.7$ at 15.2 keV

**Table D.1:** ID09 parameters used for the Laue simulations

so-called ‘globin fold’ represented by eight  $\alpha$ -helices connected through the turns with a heme prosthetic group (figure D.2 (a)).

The latter consists of four pyrrolic groups building up a porphyrin ring and an iron atom located in its center (figure D.2 (b)). The iron ion has six coordination sites, meaning that it can interact with six ligands. Four of them are nitrogen atoms of the four pyrroles in the heme plane, and two additional bonds might form on the sides of the heme plane. In myoglobin, the heme plane is situated between two histidine residues, His64 and His93, being referred to as distal and proximal histidine, respectively (figure D.2 (c)). The fifth coordination site is occupied by the imidazole side chain of His93, which stabilizes the heme group and pulls the iron ion slightly ( $\sim 0.4 \text{ \AA}$ ) out of the porphyrin plane.

This describes myoglobin in its oxygen free form known as deoxymyoglobin. Having an unoccupied 6th coordinate position of the iron atom, myoglobin can reversibly bind molecular oxygen as well as some other similar ligands. This ligand molecule is stabilized by hydrogen bonding interaction with the distal histidine residue, and the iron atom is partially pulled back to the heme plane (figure D.2 (c)).

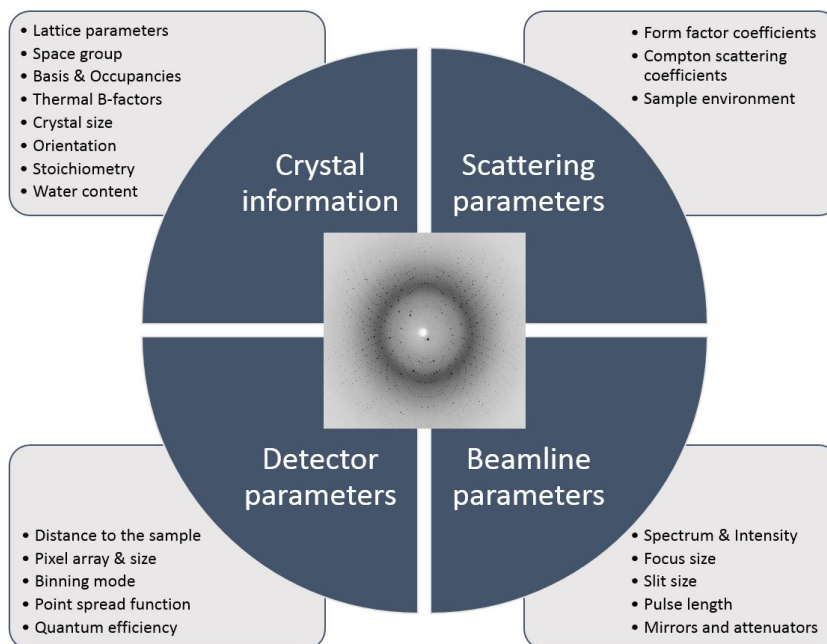


**Figure D.1:** Input parameters for calculating Laue diffraction patterns

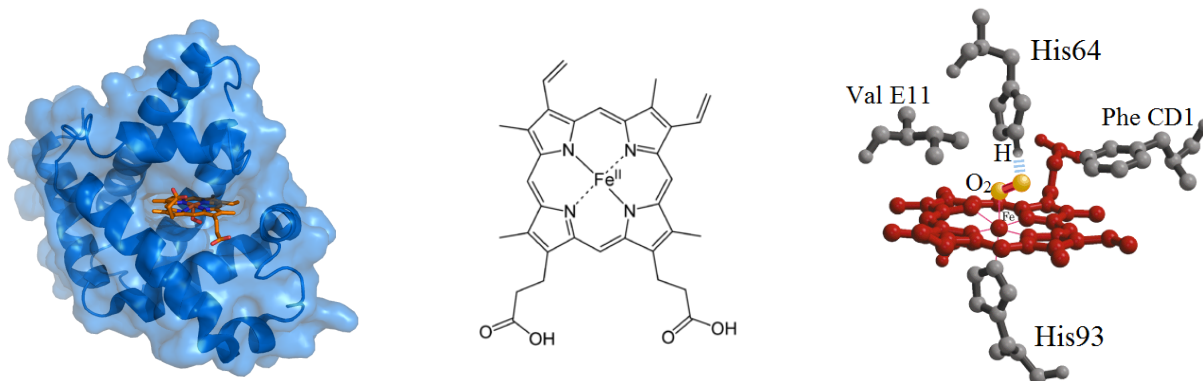


**Figure D.2:** (a) Globin fold structure of myoglobin. (b) Heme structure. (c) Heme coordination in oxymyoglobin

Since the initial discovery of its structure over 50 years ago, myoglobin has been widely studied and, thus, is an ideal model system and a benchmark for computer simulations. Moreover, as the iron-ligand bond can be broken upon photodissociation, it has been employed to investigate conformational relaxation processes in proteins. Carbon monoxide binds to the heme iron atom in a way similar to the oxygen binding, but the binding is stronger, so MbCO is more stable and more easily photolyzed. This makes it a perfect model for time-resolved studies.

### D.3 Diffraction pattern predictions

The Laue diffraction patterns were predicted for carboxymyoglobin (MbCO) crystals of cubic shape and linear size from 5 to 60  $\mu\text{m}$ . The model crystal structure data were taken from the Protein Data Bank (PDB), where the structure can be found by its reference 1A6G. It has monoclinic symmetry and belongs to the space group  $P2_1$ , meaning that the three lattice constants are different ( $a \neq b \neq c$ ) and the angle  $\beta$  between  $a$  and  $c$  is different from  $90^\circ$ . Usually the unit cell is defined so that  $\beta > 90^\circ$ . The unit cell parameters for the chosen structure are given in figure D.3. The reciprocal space lattice is also monoclinic. The crystals were supposed to be surrounded by a 200  $\mu\text{m}$ -thick layer of water to account for the main source of background. This information needed for the calculations is shortly presented in table D.2)

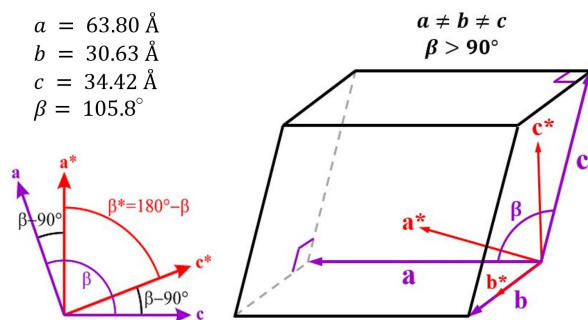


**Figure D.3:** Unit cell parameters for the model MbCO crystals. Space group  $P2_1$  (monoclinic lattice).

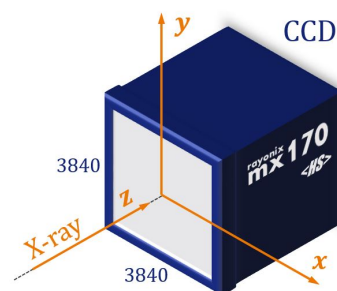


**Figure D.4:** Definition of the laboratory frame of reference.

Crystal information		Scattering parameters
Lattice parameters:	see fig. D.3	Form factor coefficients:
Space group:	P2 <sub>1</sub> (monoclinic)	Taken from the International tables for crystallography [59]
Basis & occupancies:	PDB structure 1A6G	Compton scattering coefficients:
Thermal B-factors:	information from PDB	Calculated as described in [29]
Crystal size:	5 – 60 μm	Sample environment:
Orientation:	random (Euler angles)	200 μm-thick water sheet, scattering data from [60]
Stoichiometry:	C <sub>774</sub> N <sub>210</sub> O <sub>222</sub> S <sub>5</sub> Fe	
Water content:	35%	

**Table D.2:** Sample parameters used for diffraction pattern prediction

The simulation started with calculating the diffraction peak positions as they would appear in the coordinate system of the CCD detector (laboratory frame of reference Oxyz). The incident beam is parallel to the Oz axis and perpendicular to the detector plane (xOy) (figure D.4).

The crystal was introduced as a fractional coordinate system of its monoclinic Bravais lattice in real space at a fixed orientation to the lab frame. This orientation was defined by three Euler angles ( $\psi, \theta, \phi$ ) between the axes Oz and O'z' of the Cartesian coordinate system (O'x'y'z') associated with the crystal fractional coordinates (u,v,w) as

$$\begin{bmatrix} x' \\ y' \\ z' \end{bmatrix} = \begin{bmatrix} a & b \cos \gamma & c \cos \beta \\ 0 & b \sin \gamma & c \cdot \frac{\cos \alpha - \cos \beta \cos \gamma}{\sin \gamma} \\ 0 & 0 & \frac{V}{ab \sin \gamma} \end{bmatrix} \begin{bmatrix} u \\ v \\ w \end{bmatrix},$$

where  $V = abc\sqrt{1 - \cos^2 \alpha - \cos^2 \beta - \cos^2 \gamma + 2 \cos \alpha \cos \beta \cos \gamma}$  is the unit cell volume. In the case of monoclinic space group  $V = abc \sin \beta$  and

$$\begin{aligned} x' &= au + cw \cos \beta, \\ y' &= bv, \\ z' &= \frac{V}{ab}w = cw \sin \beta. \end{aligned}$$

Assuming sample-to-detector distance is 100 mm, the position of any reflection on the detector can be easily calculated using the conventional definition of polar coordinates in (xOy) if the scattered beam vector is known.

When a single crystal is illuminated by the X-ray beam, the scattered radiation appears as discrete diffraction peaks. It is well known from X-ray crystallography theory that each diffraction peak is a Bragg reflection from the family of direct crystal lattice planes. For a fixed position of the crystal, the wavelength of the reflections are selected by Bragg's law:

$$2d \sin \theta = n \cdot \lambda,$$

where  $d$  is the distance between the atomic planes,  $\theta$  is the angle of X-ray incidence with respect to that family of lattice planes (Bragg angle),  $\lambda$  is the wavelength of the incident

X-ray beam, and  $n$  is the order of the reflection (integer). Bragg's law has an equivalent in terms of reciprocal lattice vectors: the Laue condition requires that the change in wave vector upon scattering  $\mathbf{K} = \mathbf{k}' - \mathbf{k}$  is a vector in reciprocal lattice.

There is a simple geometrical representation of this condition called the Ewald construction (figure D.5 (a)). Given an incident wave vector  $\mathbf{k}$  pointing from the origin of the reciprocal space, a sphere of radius  $k$  is drawn around its tip (so that it passes through the origin). This sphere determines all possible directions of the reflected wave vector  $\mathbf{k}'$ . If there are reciprocal lattice points lying on the surface of the sphere, the scattering vector  $\mathbf{K} = \mathbf{k}' - \mathbf{k}$  fulfils the Bragg condition, and the corresponding diffraction peak is observed. The integer coordinates  $(h,k,l)$  of these scattering vectors, in reciprocal lattice units, are the Miller indices of the direct crystal lattice planes perpendicular to these scattering vectors.

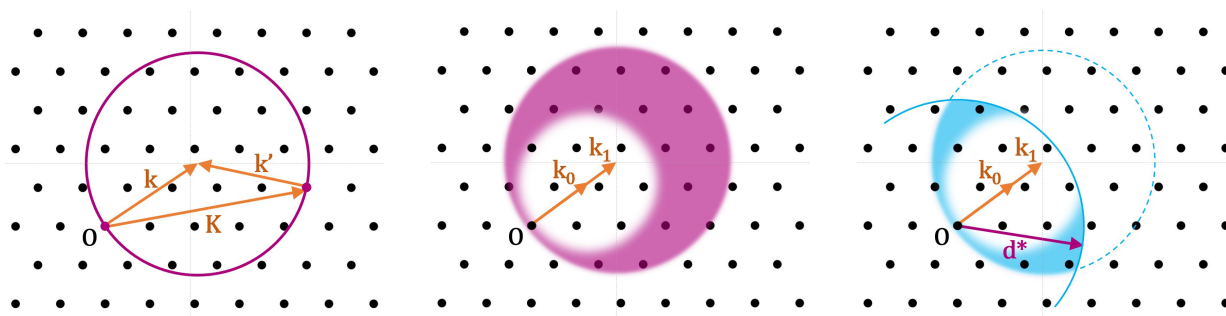


**Figure D.5:** (a) Ewald construction (representation of the Laue condition). (b) Ewald construction for a polychromatic case. (c) Resolution limit shown with the Ewald construction

The example above describes the condition for perfectly monochromatic radiation. If the X-ray beam contains wavelengths from  $\lambda_1$  to  $\lambda_2$ , the sphere transforms into the region between the two spheres with corresponding radii  $k_0$  and  $k_1$ , as shown in figure D.5 (b). Bragg peaks will then be observed for all reciprocal lattice vector between these two spheres.

How many crystal lattice planes will give rise to observable reflections? The limiting factor is the resolution limit i.e. the size of the smallest observable feature in the structure. If the distance between two objects is smaller than the resolution, they are not resolved and appear as a single entity. The smallest distance  $d_{min}$  between crystal lattice planes producing observable Bragg reflections is defining the resolution limit. Theoretically, it is restrained by the X-ray wavelength, but in practice it depends on the crystal quality: more perfect crystals diffract to higher resolution (lower  $d_{min}$ ). An example of how the resolution affects the accuracy of electron density map refinement is illustrated in (figure D.6, [61]).

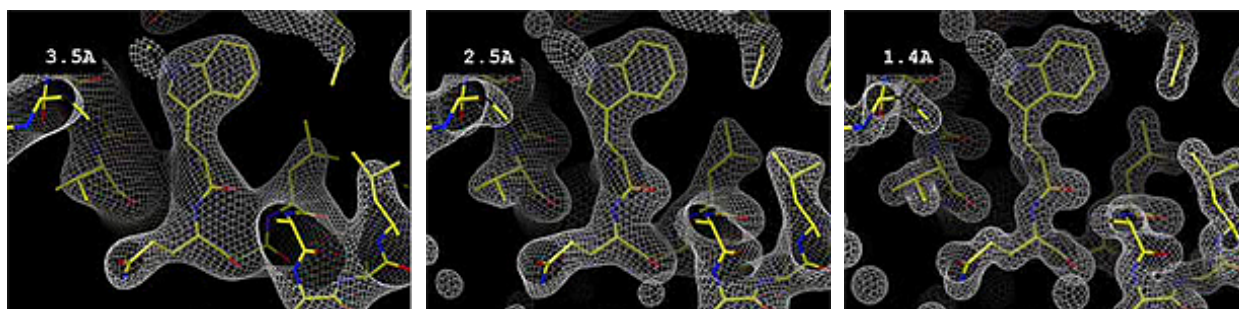


**Figure D.6:** Electron density map accuracy dependent on resolution. Snapshots from the movie by James Holton [61]

The d spacing between the crystal lattice planes is related to the Miller indices (h,k,l) and is calculated for a monoclinic lattice as

$$\frac{1}{d^2} = \frac{1}{\sin^2 \beta} \cdot \left( \frac{h^2}{a^2} + \frac{k^2 \sin^2 \beta}{b^2} + \frac{l^2}{c^2} - \frac{2hl \cos \beta}{ac} \right),$$

where  $a, b, c$  and  $\beta$  are the corresponding monoclinic unit cell parameters. The resolution limit puts another restriction on the observable reflections which can be illustrated with the Ewald construction. The reciprocal lattice parameters can be calculated from the real space parameters. If, for instance, the simulated diffraction image has to include reflections down to  $d_{min} = 1.2 \text{ \AA}$  resolution, they correspond to the reciprocal lattice points inside the sphere of radius  $d^* = 2\pi/d_{min}$  centred on the origin of the reciprocal lattice (figure D.5 (c)). The criteria for observable reflections can be described analytically as follows.

Having defined a fractional coordinate system of the crystal's monoclinic Bravais lattice at a certain angle to the incoming X-ray beam, we can draw the reciprocal lattice points, the Ewald construction and the resolution limit. Assume a scattering vector  $\mathbf{K} = \mathbf{k}' - \mathbf{k}$  with coordinates  $\mathbf{K} = \{h, k, l\}$  in the monoclinic coordinate system of the crystal that can be expressed, using the Euler angles of the unit cell in reciprocal space, into laboratory Cartesian coordinates  $\{K_x, K_y, K_z\}$ . Given that the incident beam  $\mathbf{k}$  is parallel to z, i.e.  $k_{min} = \{0, 0, k_{min}\}$  and  $k_{max} = \{0, 0, k_{max}\}$ , the Ewald Sphere confinement can be expressed by 3 inequalities:

$$\begin{aligned} K_x^2 + K_y^2 + (K_z - k_{min})^2 &\geq k_{min}^2; \\ K_x^2 + K_y^2 + (K_z - k_{max})^2 &\leq k_{max}^2; \\ \frac{1}{d_{min}^2} &> \frac{1}{\sin^2 \beta} \cdot \left( \frac{h^2}{a^2} + \frac{k^2 \sin^2 \beta}{b^2} + \frac{l^2}{c^2} - \frac{2hl \cos \beta}{ac} \right). \end{aligned}$$

Another inequality can be added in order to remove backscattering events:

$$K_x^2 + K_y^2 > K_z^2.$$

Given all the sphere radii, it is straightforward to find maximum and minimum coordinates of the reciprocal lattice points that lie inside the selected volume. Making a list of all possible Miller indices combinations that have to be checked, one can scan and select the scattering vectors applying the criteria above. Calculating the polar and azimuthal angles for the given scattering vectors allows to plot the diffraction pattern in the detector plane at a given distance from the crystal.

Figure D.7 shows the positions of the diffraction peaks from a crystal with  $P2_1$  monoclinic space group symmetry and unit cell parameters as was specified above for model MbCO crystals. The pattern was calculated for a 100 mm sample-to-detector distance with a resolution limit of 1.2  $\text{\AA}$ . The range from 9.8 to 15.5 keV is the region where the U17 flux is  $>1\%$  of its maximum flux at 15.2 keV.

While the space group symmetry of a crystal defines the diffraction pattern geometry, the basis of the lattice is responsible for diffraction peak intensities. Even very small changes in the protein structure inside the unit cell can be tracked with time resolved X-ray crystallography. Every atom in the unit cell is contributing to the sum of complex components – the structure factor:

$$F(\mathbf{K}) = \sum_{j=1}^n f_j(\mathbf{K}) e^{i\mathbf{K}\mathbf{r}_j} \cdot e^{-q^2 \langle u^2 \rangle / 3},$$

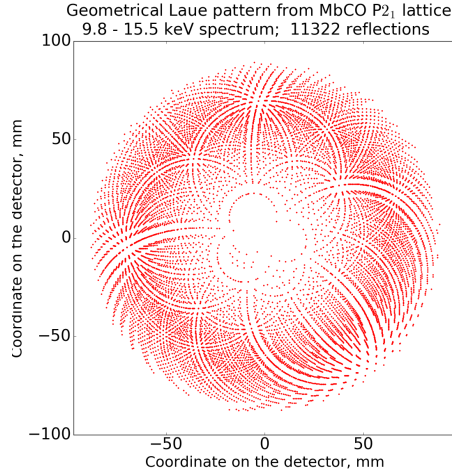


**Figure D.7:** Diffraction peak positions for a model MbCO crystal recorded on the Rayonix detector 100 mm from the crystal

where atomic form factors  $f_j(\mathbf{K})$  for an atom of type  $j$  are tabulated functions of the scattering vector  $\mathbf{K}$  and  $\mathbf{r}_j$  is the atomic coordinate in the unit cell;  $e^{-q^2\langle u^2 \rangle/3}$  is the Debye-Waller factor for each atom where  $q = 4\pi \sin \theta/\lambda$  and  $\langle u^2 \rangle$  is a mean square displacement of the atom. Debye-Waller factor values for each atoms are usually tabulated in the Protein Data Bank for each structure.

The intensity of the diffraction spot is then calculated as:

$$I_L(\mathbf{K}) = \left( \frac{e^2}{mc^2} \right)^2 \frac{dI(\lambda)}{d\lambda} \lambda^4 \frac{1}{2 \sin \theta} \frac{V}{V_0} \cdot PAD \cdot |F(\mathbf{K})|^2,$$

where  $e^2/mc^2 = r_0$  – Thompson scattering length,  $dI/d\lambda$  – intensity per unit  $\lambda$  per  $m^2$ ,  $\theta$  – Bragg angle,  $V$  – sample volume,  $V_0$  – unit cell volume,  $P, A, D$  – correction factors for polarization, absorption and quantum efficiency of the detector, respectively:  $P(\theta, \phi) = 1 - \sin^2 \theta \sin^2 \phi$ ,  $D \sim 0.7$ ,  $A$  was supposed  $\sim 1$ ,  $\|F(\mathbf{K})\|^2$  – structure factor of a given reflection. This formula can also be written in terms of energy rather than wavelength:

$$I_L(\mathbf{K}) = \left( \frac{e^2}{mc^2} \right)^2 \frac{dI(E)}{dE} \frac{(hc)^3}{E^2} \frac{1}{2 \sin \theta} \frac{V}{V_0} \cdot PAD \cdot |F(\mathbf{K})|^2.$$

The U17 flux is shown in figure 3.9 with  $3 \cdot 10^9$  ph/pulse in a 5% bandwidth at 15.2 keV.

The calculated diffraction images also include the background on the detector. The crystals are supposed to be surrounded by a 200- $\mu\text{m}$  thick sheet of water perpendicularly to the X-ray beam. The contributing terms are elastic scattering from water and Compton scattering from water and the crystal atoms.

The intensity of the elastic X-ray scattering from water was estimated based on the experimental data reported in [3]. The Compton intensities were calculated theoretically using the approach described in [2] to calculate the coherent and incoherent scattered X-ray intensities. The background intensity per unit space angle was recalculated into the background intensity for each detector pixel according to the following idea. The intensity scattered into the space-angle element  $d\Omega = \sin \theta d\theta d\phi$  is expressed as:

$$\frac{dI(\theta, \phi)}{d\Omega} = I_0 r_0^2 \cdot PAD \cdot I(q)$$

with  $I_0$  [ph/ $m^2$ /s] and  $q = 4\pi \sin \theta/\lambda$ . The space-angle of a  $dl \times dl$  pixel-element on a flat CCD detector at a distance  $d$  from the sample (figure 2.19) is calculated as:

$$d\Omega = \left( \frac{\cos \theta}{d} \right)^2 \cos \theta dl^2 = \frac{\cos^3 \theta}{d^2} dl^2.$$

Calculating  $d\Omega$  for each  $2 \times 44.3 \mu\text{m}$  pixel of the Rayonix detector 100 mm from the sample, we can obtain the background intensity for each pixel as:

$$dI(\theta, \phi) = I_0 r_0^2 \cdot PAD \cdot I(q) \cdot d\Omega.$$

The detector is supposed to operate in a  $2 \times 2$  pixel binning mode, and the intensities are calculated for a  $1920 \times 1920$  matrix.

The intensity of each Laue spot is assumed to be distributed over the detector plane as a 2D Gaussian function. The center of the Gaussian is defined by (x, y) coordinates in the detector plane, and the dispersion is given by the point-spread function of the CCD, which is  $100 \mu\text{m}$  for the Rayonix HS170. The Cartesian (x, y) coordinates are transformed into the integer (i, j) coordinates to find the corresponding detector pixel. The intensity of the pixel is calculated as the 2D Gaussian integrated over the pixel area. As the pixel size *2times*  $44.3 \mu\text{m}$  is less than the point-spread function of the detector, the contribution of each Laue reflection is calculated not only for a single “central” pixel, but also for the surrounding pixels. By considering an area of  $5 \times 5$  pixels one can account for 94.7% of the reflection intensity. This was calculated by integrating over the pixel area in 2D the Gaussian profile of the intensity. The integral is:

$$\iint_{-a}^a \frac{1}{2\pi\sigma_x\sigma_y} \exp\left(-\frac{x^2}{2\sigma_x^2}\right) \exp\left(-\frac{y^2}{2\sigma_y^2}\right) dx dy = (\text{erf}(\alpha))^2,$$

$$\alpha = \frac{a}{\sigma\sqrt{2}}, \quad \sigma = \sigma_x = \sigma_y,$$

where  $a$  is the integration limit of  $5/2$  size of the  $2 \times 44.3 \mu\text{m}$  pixel shown in figure D.8 in comparison to  $2\sigma$  and  $3\sigma$ .

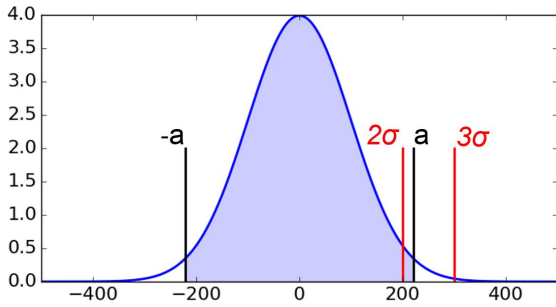


**Figure D.8:** Chosen Gauss function integration limit in comparison to  $2\sigma$  and  $3\sigma$ .

Figure D.9 represents the results of combining the matrices containing diffraction and background intensities. As the background is mainly caused by water elastic scattering, it is similar for crystals of different size. In contrast, the number of observable reflections and the resolution thus depend on the crystal size. According to Bragg’s law,  $2d \sin \theta = n\lambda$ , which means that small  $d$  reflections, the high resolution reflections, appear at high scattering angles.

One approach to define the resolution limit for a given crystal size is to calculate the  $d$  spacing for each observable reflection in the pattern and hereby determine the smallest. A reflection is considered observable when the pixel intensity from diffraction is 2 times higher than the background from the total diffuse scattering in the pixel. The background noise is calculated as the variance of the background, i.e. the square root of the intensity of the background. Figure D.9 shows the Laue patterns and figure D.10 their resolution limits for  $20 \mu\text{m}$  and  $40 \mu\text{m}$  crystals. In all the simulations, the focal size is  $75 \times 45 \mu\text{m}$  (H×V).

Figure D.10 (a) shows the distribution of reflection intensities as a function of  $d$  spacing between the lattice planes. Low resolution reflections at smaller angles (higher  $d$  values) are

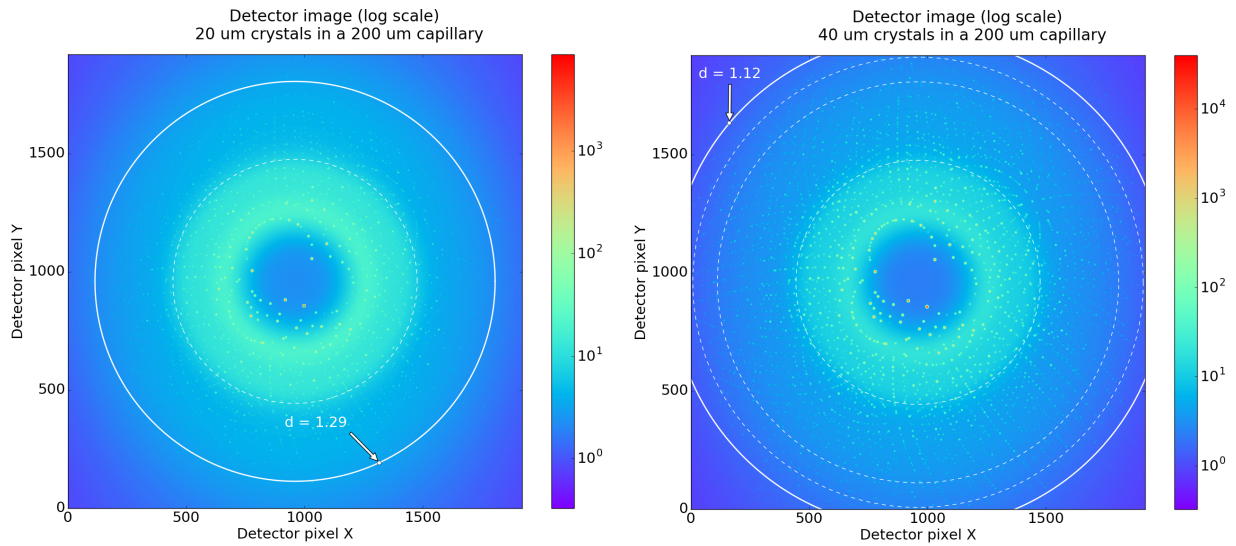


**Figure D.9:** Prediction of single-pulse Laue patterns and their resolution limits for 20  $\mu\text{m}$  & 40  $\mu\text{m}$  crystals of MbCO. The calculations include the background from a 0.2 mm thick sheet of water. The pulse intensity is  $2 \times 10^9$  ph/pulse

rarely seen and present only a small part of all the reflections. This "low resolution hole" can be explained by the Ewald construction (figure D.5 (c)) as the region between the two spheres for a spectrum with 5% bandwidth is extremely thin near the reciprocal space origin and thus intersects with very few reciprocal lattice points. The high resolution reflections (corresponding to small  $d$  values) tend to have low intensities due to the atomic form factors and the Debye-Waller factor.

The signal to noise of a Laue reflection is calculated as follows. Due to the finite crystal size and the point spread function of the detector, a diffraction peak is smeared out and distributed over a  $5 \times 5$  pixel matrix. The background noise from the diffuse scattering in

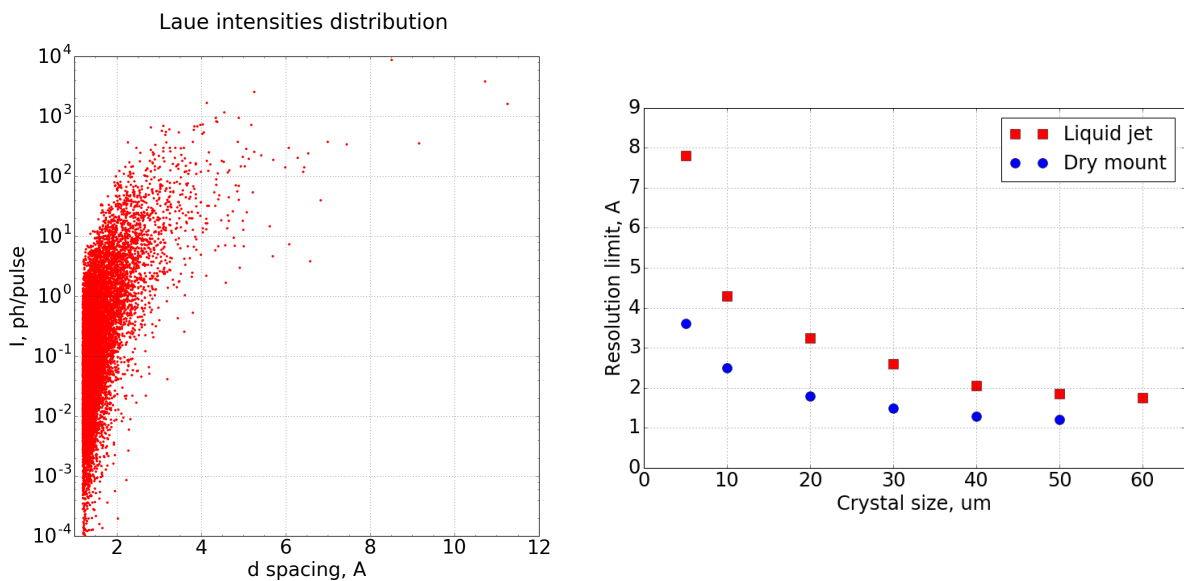


**Figure D.10:** (a) Reflection intensity distribution over  $d$  spacing values and (b) statistically calculated resolution limit for modelled MbCO diffraction patterns

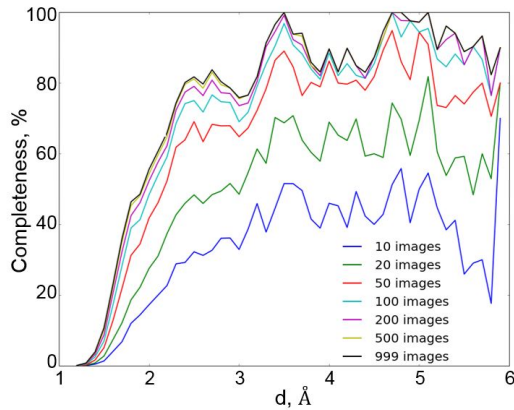


**Figure D.11:** Dataset completeness study for a 20  $\mu\text{m}$  MbCO crystal.

that super pixel is calculated as the variance in that intensity which, for Poisson statistics, is the square root of the intensity. This defines the signal to noise ratio of a reflection.

In this study, the resolution limit is defined as the  $d$  value where the average S/N curve reaches 2. The average was calculated taking into account all the reflections with intensity  $> 1$ . Lower intensities would not be observed as the images are supposed to be read out after each single pulse exposure. For better statistics, the average curve was calculated from a combination of 1000 diffraction patterns from equally sized crystals tilted at different random angles to the beam. The obtained resolution limit is shown in figure D.10 (b) as a function of crystal size. This approach gives larger values of the resolution limits than the values obtained by direct observation of all the reflections and finding a particular "best" one, as the average value would always be higher than the minimum.

Taking a diffraction pattern snapshot from a crystal positioned at a fixed angle to the beam gives information from a small fraction of the unique reflections. To get more complete data, many crystals orientations need to be exposed to the beam. In case of serial crystallography, the crystals appear at random angles with respect to the X-Ray beam, which is here an advantage for the data collection and interpretation. What is the number of random diffraction patterns needed to reconstruct the electron density? One could calculate, for each  $d$  spacing, which part (in %) of all the reflections is actually observed within a dataset of 1, 10, 20, 50, ..., 1000 images. The results of such a study for 20  $\mu\text{m}$  MbCO crystals are shown in figure D.11. A good value of completeness, about 80%, is obtained with  $\sim 100$  images.

## D.4 Serial Laue crystallography experiments on ID09

The first serial crystallography experiment on ID09 was done in collaboration with Ilme Schlichting and Marco Cammarata, who used an approach to translate a 300  $\mu\text{m}$ -thick quartz capillary filled with crystals in mother liquor. Each capillary contained about 100 lysozyme crystals of  $\sim 100 \times 30 \mu\text{m}$  size or carboxyhemoglobin crystals of  $\sim 70 \times 40 \mu\text{m}$  size. The sample to detector distance was  $\sim 200$  mm, and the capillaries were exposed, at each translation point, to a 20  $\mu\text{s}$ -long train of pink X-ray pulses with  $E_f = 15.2$  keV containing  $\sim 2.1 \cdot 10^{11}$  photons. The carboxyhemoglobin crystals did not produce reasonable diffraction data maybe due to poor crystal quality, but the diffraction patterns from lysozyme crystals were much better and could be indexed. The indexing was done in collaboration with the former ID09 PhD student Friedrich Schotte using this indexing program TREX which is running on the ID09 computers figure D.12 (a). This example shows one of the best images obtained during the experiment. The crystal diffracted to 2.4  $\text{\AA}$  resolution, and the image contains 207

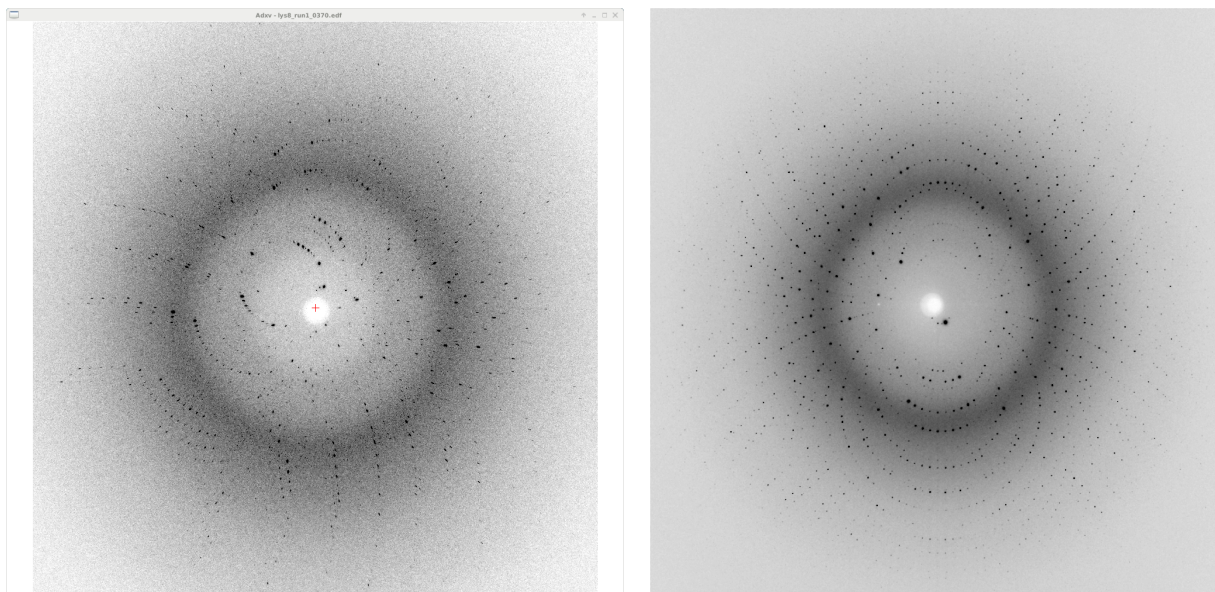


**Figure D.12:** Laue diffraction patterns taken on ID09. (a) Laue diffraction pattern from a large ( $100 \times 30 \mu\text{m}$ ) single lysozyme crystal sealed in a  $300 \mu\text{m}$ -thick quartz capillary in mother liquor. (b) Laue diffraction pattern from a large ( $300 \times 150 \mu\text{m}$ ) single crystal of trypsin surrounded by mother liquor in a  $300 \mu\text{m}$ -thick quartz capillary.

diffraction spots with  $S/N > 2$ .

In the beginning of the year 2017 there was another Laue crystallography experiment on ID09. Large ( $\sim 150 \times 300 \mu\text{m}$ ) trypsin crystals were mounted in a  $300 \mu\text{m}$  thick capillary filled with mother liquor. Exposures also contained about  $2.1 \times 10^{11}$  photons per diffraction pattern, the crystal was rotated and the datasets were recorded for different crystal orientations with a step of  $3^\circ$ . The sample to detector distance was 180-240 mm. The collected datasets are of very good quality (figure D.12 (b)) with a 1.7-2.0 Å resolution limit.

The experiment was also done on  $100 \times 100 \mu\text{m}$  thaumatin crystals under similar conditions. The obtained diffraction patterns are of lower quality, they diffract to lower resolution and contain fewer diffraction spots but still can be indexed.

# BIBLIOGRAPHY

---

---

1. M. Cammarata, M. Levantino, F. Schotte, P. A. Anfinrud, F. Ewald, J. Choi, A. Cupane, M. Wulff, and H. Ihee, "Tracking the structural dynamics of proteins in solution using time-resolved wide-angle X-ray scattering," *Nature Methods*, vol. 5, no. 10, pp. 881–886, 2008.
2. A. H. Zewail, "The birth of molecules," *Scientific American*, vol. 263, no. 6, pp. 76–83, 1990.
3. A. H. Zewail, "Femtochemistry: Atomic-scale dynamics of the chemical bond," *The Journal of Physical Chemistry A*, vol. 104, no. 24, pp. 5660–5694, 2000.
4. T. R. M. Barends, L. Foucar, A. Ardevol, K. Nass, A. Aquila, S. Botha, R. B. Doak, K. Falahati, E. Hartmann, M. Hilpert, M. Heinz, M. C. Hoffmann, J. Kofinger, J. E. Koglin, G. Kovacsova, M. Liang, D. Milathianaki, H. T. Lemke, J. Reinstein, C. M. Roome, R. L. Shoeman, G. J. Williams, I. Burghardt, G. Hummer, S. Boutet, and I. Schlichting, "Direct observation of ultrafast collective motions in CO myoglobin upon ligand dissociation," *Science*, vol. 350, pp. 445–450, oct 2015.
5. Q. Y. Kong, M. G. Laursen, K. Haldrup, K. S. Kjær, D. Khakhulin, E. Biasin, T. B. van Driel, M. Wulff, V. Kabanova, R. Vuilleumier, S. Bratos, M. M. Nielsen, K. J. Gaffney, T. C. Weng, and M. H. J. Koch, "Initial metal–metal bond breakage detected by fs X-ray scattering in the photolysis of  $\text{Ru}_3(\text{CO})_{12}$  in cyclohexane at 400 nm," *Photochemical & Photobiological Sciences*, vol. 18, no. 2, pp. 319–327, 2019.
6. H. T. Lemke, C. Bressler, L. X. Chen, D. M. Fritz, K. J. Gaffney, A. Galler, W. Gawelda, K. Haldrup, R. W. Hartsock, H. Ihee, J. Kim, K. H. Kim, J. H. Lee, M. M. Nielsen, A. B. Stickrath, W. Zhang, D. Zhu, and M. Cammarata, "Femtosecond X-ray absorption spectroscopy at a hard X-ray free electron laser: application to spin crossover dynamics," *The Journal of Physical Chemistry A*, vol. 117, pp. 735–740, jan 2013.
7. W. Zhang, R. Alonso-Mori, U. Bergmann, C. Bressler, M. Chollet, A. Galler, W. Gawelda, R. G. Hadt, R. W. Hartsock, T. Kroll, K. S. Kjær, K. Kubiček, H. T. Lemke, H. W. Liang, D. A. Meyer, M. M. Nielsen, C. Purser, J. S. Robinson, E. I. Solomon, Z. Sun, D. Sokaras, T. B. van Driel, G. Vankó, T.-C. Weng, D. Zhu, and K. J. Gaffney, "Tracking excited-state charge and spin dynamics in iron coordination complexes," *Nature*, vol. 509, pp. 345–348, may 2014.
8. A. Plech, M. Wulff, S. Bratos, F. Mirloup, R. Vuilleumier, F. Schotte, and P. A. Anfinrud, "Visualizing chemical reactions in solution by picosecond X-ray diffraction," *Physical Review Letters*, vol. 92, no. 12, p. 125505, 2004.
9. K. Pande, C. D. M. Hutchison, G. Groenhof, A. Aquila, J. S. Robinson, J. Tenboer, S. Basu, S. Boutet, D. P. DePonte, M. Liang, T. A. White, N. A. Zatsepin, O. Yefanov, D. Morozov, D. Oberthuer, C. Gati, G. Subramanian, D. James, Y. Zhao, J. Koralek, J. Brayshaw, C. Kupitz, C. Conrad, S. Roy-chowdhury, J. D. Coe, M. Metz, P. L. Xavier, T. D. Grant, J. E. Koglin, G. Ketawala, R. Fromme, V. Srajer, R. W. Henning, J. C. H. Spence, A. Ourmazd, P. Schwander, U. Weierstall, M. Frank, P. Fromme, A. Barty, H. N. Chapman, K. Moffat, J. J. Van Thor, and M. Schmidt, "Femtosecond structural dynamics drives the trans/cis isomerization in photoactive yellow protein," *Science*, vol. 352, pp. 725–729, may 2016.
10. S. Techert, F. Schotte, and M. Wulff, "Picosecond X-ray diffraction probed transient structural changes in organic solids," *Physical Review Letters*, vol. 86, no. 10, pp. 2030–2033, 2001.

11. S. E. Canton, K. S. Kjær, G. Vankó, T. B. van Driel, S.-i. Adachi, A. Bordage, C. Bressler, P. Chabera, M. Christensen, A. O. Dohn, A. Galler, W. Gawelda, D. Gosztola, K. Haldrup, T. Harlang, Y. Liu, K. B. Møller, Z. Németh, S. Nozawa, M. Pápai, T. Sato, T. Sato, K. Suarez-Alcantara, T. Togashi, K. Tono, J. Uhlig, D. A. Vithanage, K. Wärnmark, M. Yabashi, J. Zhang, V. Sundström, and M. M. Nielsen, “Visualizing the non-equilibrium dynamics of photoinduced intramolecular electron transfer with femtosecond X-ray pulses,” *Nature Communications*, vol. 6, p. 6359, may 2015.
12. H. Ravishankar, M. N. Pedersen, M. Eklund, A. Sitsel, C. Li, A. Duelli, M. Levantino, M. Wulff, A. Barth, C. Olesen, P. Nissen, and M. Andersson, “Tracking  $\text{Ca}^{2+}$  ATPase intermediates in real time by x-ray solution scattering,” *Science Advances*, vol. 6, no. 12, p. eaaz0981, 2020.
13. N. Slater, “Classical motion under a Morse potential,” *Nature*, vol. 180, no. 4598, pp. 1352–1353, 1957.
14. E. J. Baran, “Mean amplitudes of vibration of the halogen molecules,” *Zeitschrift für Naturforschung A*, vol. 58, no. 1, pp. 36–38, 2003.
15. J. H. Lee, M. Wulff, S. Bratos, J. Petersen, L. Guerin, J.-C. Leicknam, M. Cammarata, Q. Kong, J. Kim, K. B. Moller, and H. Ihee, “Filming birth of molecules and solvent rearrangement,” *Journal of the American Chemical Society*, vol. 135, no. 8, pp. 3255–3261, 2013.
16. V. Srajer, T.-y. Teng, T. Ursby, C. Pradervand, Z. Ren, S.-i. Adachi, W. Schildkamp, D. Bourgeois, M. Wulff, and K. Moffat, “Photolysis of the carbon monoxide complex of myoglobin: nanosecond time-resolved crystallography,” *Science*, vol. 274, no. 5293, pp. 1726–1729, 1996.
17. F. Schotte, M. Lim, T. A. Jackson, A. V. Smirnov, J. Soman, J. S. Olson, G. N. Phillips Jr., M. Wulff, and P. A. Anfinrud, “Watching a protein as it functions with 150-ps time-resolved X-ray crystallography,” *Science*, vol. 300, no. 5627, pp. 1944–1947, 2003.
18. D. Bourgeois, B. Vallone, F. Schotte, A. Arcovito, A. E. Miele, G. Sciara, M. Wulff, P. Anfinrud, and M. Brunori, “Complex landscape of protein structural dynamics unveiled by nanosecond Laue crystallography,” *Proceedings of the National Academy of Sciences of the United States of America*, vol. 100, no. 15, pp. 8704–8709, 2003.
19. L. X. Chen, W. J. Jäger, G. Jennings, D. J. Gosztola, A. Munkholm, and J. P. Hessler, “Capturing a photoexcited molecular structure through time-domain X-ray absorption fine structure,” *Science*, vol. 292, no. 5515, pp. 262–264, 2001.
20. M. Saes, C. Bressler, R. Abela, D. Grolimund, S. L. Johnson, P. A. Heimann, and M. Chergui, “Observing photochemical transients by ultrafast X-ray absorption spectroscopy,” *Physical Review Letters*, vol. 90, no. 4, p. 047403, 2003.
21. K. H. Kim, J. G. Kim, S. Nozawa, T. Sato, K. Y. Oang, T. W. Kim, H. Ki, J. Jo, S. Park, C. Song, T. Sato, K. Ogawa, T. Togashi, K. Tono, M. Yabashi, T. Ishikawa, J. Kim, R. Ryoo, J. Kim, H. Ihee, and S.-i. Adachi, “Direct observation of bond formation in solution with femtosecond X-ray scattering,” *Nature*, vol. 518, pp. 385–389, feb 2015.
22. M. Harmand, R. Coffee, M. R. Bionta, M. Chollet, D. French, D. Zhu, D. M. Fritz, H. T. Lemke, N. Medvedev, B. Ziaja, S. Toleikis, and M. Cammarata, “Achieving few-femtosecond time-sorting at hard X-ray free-electron lasers,” *Nature Photonics*, vol. 7, pp. 215–218, mar 2013.
23. J. C. Kendrew, G. Bodo, H. M. Dintzis, R. G. Parrish, H. Wyckoff, and D. C. Phillips, “A three-dimensional model of the myoglobin molecule obtained by X-ray analysis,” *Nature*, vol. 181, no. 4610, pp. 662–666, 1958.
24. T.-Y. Teng, V. Šrajer, and K. Moffat, “Photolysis-induced structural changes in single crystals of carbon-monooxy myoglobin at 40 K,” *Nature structural biology*, vol. 1, no. 10, pp. 701–705, 1994.
25. K. Moffat and R. Henderson, “Freeze trapping of reaction intermediates,” *Current opinion in structural biology*, vol. 5, no. 5, pp. 656–663, 1995.
26. D. Bourgeois, T. Ursby, M. Wulff, C. Pradervand, A. Legrand, W. Schildkamp, S. Labouré, V. Srajer, T. Y. Teng, M. Roth, and K. Moffat, “Feasibility and realization of single-pulse Laue diffraction on macromolecular crystals at ESRF,” *Journal of Synchrotron Radiation*, vol. 3, no. 2, pp. 65–74, 1996.

27. R. F. Tilton Jr, I. D. Kuntz Jr, and G. A. Petsko, "Cavities in proteins: structure of a metmyoglobin xenon complex solved to 1.9 Å," *Biochemistry*, vol. 23, no. 13, pp. 2849–2857, 1984.
28. B. E. Warren, *X-ray Diffraction*. Courier Corporation, 1990.
29. F. Hajdu, "Revised parameters of the analytic fits for coherent and incoherent scattered X-ray intensities of the first 36 atoms," *Acta Crystallographica Section A*, vol. 28, no. 3, pp. 250–252, 1972.
30. G. Pálinkás, "Analytic approximations for the incoherent X-ray intensities of the atoms from Ca to Am," *Acta Crystallographica Section A*, vol. 29, no. 10, pp. 10–12, 1973.
31. M. Wulff, S. Bratos, A. Plech, R. Vuilleumier, F. Mirloup, M. Lorenc, Q. Kong, and H. Ihee, "Recombination of photodissociated iodine: A time-resolved X-ray-diffraction study," *The Journal of Chemical Physics*, vol. 124, p. 034501, 2006.
32. K. S. Kjær, T. B. Van Driel, J. Kehres, K. Haldrup, D. Khakhulin, K. Bechgaard, M. Cammarata, M. Wulff, T. J. Sørensen, and M. M. Nielsen, "Introducing a standard method for experimental determination of the solvent response in laser pump, X-ray probe time-resolved wide-angle X-ray scattering experiments on systems in solution," *Physical Chemistry Chemical Physics*, vol. 15, no. 36, pp. 15003–15016, 2013.
33. L. D. Landau and E. M. Lifshitz, "Fluid Mechanics," *New York*, vol. 61, 1959.
34. M. Cammarata, *Time resolved X-ray scattering as a tool to study transient species in solution*. PhD thesis, Palermo University, 2006.
35. A. H. Narten and H. A. Levy, "Liquid water: Molecular correlation functions from X-ray diffraction," *The Journal of Chemical Physics*, vol. 55, no. 5, pp. 2263–2269, 1971.
36. M. Chergui and E. Collet, "Photoinduced structural dynamics of molecular systems mapped by time-resolved X-ray methods," *Chemical Reviews*, vol. 117, pp. 11025–11065, aug 2017.
37. G. Vankó, A. Bordage, M. Pápai, K. Haldrup, P. Glatzel, A. M. March, G. Doumy, A. Britz, A. Galler, T. Assefa, D. Cabaret, A. Juhin, T. B. van Driel, K. S. Kjær, A. Dohn, K. B. Møller, H. T. Lemke, E. Gallo, M. Rovezzi, Z. Németh, E. Rozsályi, T. Rozgonyi, J. Uhlig, V. Sundström, M. M. Nielsen, L. Young, S. H. Southworth, C. Bressler, and W. Gawelda, "Detailed Characterization of a Nanosecond-Lived Excited State: X-ray and Theoretical Investigation of the Quintet State in Photoexcited  $[\text{Fe}(\text{terpy})_2]^{2+}$ ," *The Journal of Physical Chemistry C*, vol. 119, pp. 5888–5902, mar 2015.
38. P. Glatzel and U. Bergmann, "High resolution 1s core hole X-ray spectroscopy in 3d transition metal complexes – electronic and structural information," *Coordination chemistry reviews*, vol. 249, no. 1-2, pp. 65–95, 2005.
39. K. Haldrup, G. Vankó, W. Gawelda, A. Galler, G. Doumy, A. M. March, E. P. Kanter, A. Bordage, A. Dohn, T. B. van Driel, K. S. Kjær, H. T. Lemke, S. E. Canton, J. Uhlig, V. Sundström, L. Young, S. H. Southworth, M. M. Nielsen, and C. Bressler, "Guest–host Interactions investigated by time-resolved X-ray spectroscopies and scattering at MHz rates: solvation dynamics and photoinduced spin transition in aqueous  $[\text{Fe}(\text{bipy})_3]^{2+}$ ," *The Journal of Physical Chemistry A*, vol. 116, pp. 9878–9887, oct 2012.
40. U. Bergmann, C. R. Horne, T. J. Collins, J. M. Workman, and S. P. Cramer, "Chemical dependence of interatomic X-ray transition energies and intensities – a study of Mn  $K\beta$  and  $K\beta_{2,5}$  spectra," *Chemical physics letters*, vol. 302, no. 1-2, pp. 119–124, 1999.
41. A. M. March, T. A. Assefa, C. Boemer, C. Bressler, A. Britz, M. Diez, G. Doumy, A. Galler, M. Harder, D. Khakhulin, Z. Németh, M. Pápai, S. Schulz, S. H. Southworth, H. Yavaş, L. Young, W. Gawelda, and G. Vankó, "Probing transient valence orbital changes with picosecond valence-to-core X-ray emission spectroscopy," *The Journal of Physical Chemistry C*, vol. 121, pp. 2620–2626, feb 2017.
42. M. Altarelli, F. Schlachter, and J. Cross, "Making ultrabright X-rays," *Scientific American*, vol. 279, no. 6, pp. 66–73, 1998.

43. M. S. del Río and R. J. Dejus, "XOP v2. 4: recent developments of the X-ray optics software toolkit," in *Advances in Computational Methods for X-Ray Optics II*, vol. 8141, p. 814115, International Society for Optics and Photonics, 2011.
44. R. Alonso-Mori, J. Kern, D. Sokaras, T.-C. Weng, D. Nordlund, R. Tran, P. Montanez, J. Delor, V. K. Yachandra, J. Yano, and U. Bergmann, "A multi-crystal wavelength dispersive X-ray spectrometer," *Review of Scientific Instruments*, vol. 83, p. 073114, jul 2012.
45. D. Khakhulin, F. Otte, M. Biednov, C. Bömer, T.-K. Choi, M. Diez, A. Galler, Y. Jiang, K. Kubicek, F. A. Lima, A. Rodriguez-Fernandez, P. Zalden, W. Gawelda, and C. Bressler, "Ultrafast X-ray photochemistry at European XFEL: Capabilities of the femtosecond X-ray experiments (FXE) instrument," *Applied Sciences*, vol. 10, no. 3, p. 995, 2020.
46. J. K. McCusker, "Electronic structure in the transition metal block and its implications for light harvesting," *Science*, vol. 363, no. 6426, pp. 484–488, 2019.
47. P. Chábera, K. S. Kjaer, O. Prakash, A. Honarfar, Y. Liu, L. A. Fredin, T. C. B. Harlang, S. Lidin, J. Uhlig, V. Sundström, R. Lomoth, P. Persson, and K. Wärnmark, "Fe<sup>II</sup> hexa N-heterocyclic carbene complex with a 528 ps metal-to-ligand charge-transfer excited-state lifetime," *The Journal of Physical Chemistry Letters*, vol. 9, pp. 459–463, 2018.
48. A. Hauser, "Ligand field theoretical considerations," in *Spin Crossover in Transition Metal Compounds I. Topics in Current Chemistry*, vol. 233, pp. 49–58, Springer-Verlag, 2004.
49. C. Sousa, C. de Graaf, A. Rudavskiy, and R. Broer, "Theoretical study of the light-induced spin crossover mechanism in [Fe(mtz)<sub>6</sub>]<sup>2+</sup> and [Fe(phen)<sub>3</sub>]<sup>2+</sup>," *The Journal of Physical Chemistry A*, vol. 121, pp. 9720–9727, dec 2017.
50. J. Tribollet, G. Gallé, G. Jonusauskas, D. Deldicque, M. Tondusson, J. F. Letard, and E. Freysz, "Transient absorption spectroscopy of the iron(II) [Fe(phen)<sub>3</sub>]<sup>2+</sup> complex: Study of the non-radiative relaxation of an isolated iron(II) complex," *Chemical Physics Letters*, vol. 513, no. 1-3, pp. 42–47, 2011.
51. A. G. Bonn, *Towards photoinduced charge accumulation in purely molecular D6 metal complexes with oligo-triarylamine donors*. PhD thesis, University of Basel, 2015.
52. S. Nozawa, T. Sato, M. Chollet, K. Ichiyanagi, A. Tomita, H. Fujii, S.-i. Adachi, and S.-y. Koshihara, "Direct probing of spin state dynamics coupled with electronic and structural modifications by picosecond time-resolved XAFS," *Journal of the American Chemical Society*, vol. 132, pp. 61–63, jan 2010.
53. H. Wang, C. Yu, X. Wei, Z. Gao, G.-L. Xu, D.-R. Sun, Z. Li, Y. Zhou, Q.-J. Li, B.-B. Zhang, J.-Q. Xu, L. Wang, Y. Zhang, Y.-L. Tan, and Y. Tao, "Development of picosecond time-resolved X-ray absorption spectroscopy by high-repetition-rate laser pump/X-ray probe at Beijing Synchrotron Radiation Facility," *Journal of Synchrotron Radiation*, vol. 24, pp. 667–673, may 2017.
54. D. Leshchev, T. C. B. Harlang, L. A. Fredin, D. Khakhulin, Y. Liu, E. Biasin, M. G. Laursen, G. E. Newby, K. Haldrup, M. M. Nielsen, K. Wärnmark, V. Sundström, P. Persson, K. S. Kjær, and M. Wulff, "Tracking the picosecond deactivation dynamics of a photoexcited iron carbene complex by time-resolved X-ray scattering," *Chemical Science*, vol. 9, no. 2, pp. 405–414, 2018.
55. S. Jun, J. H. Lee, J. Kim, J. Kim, K. H. Kim, Q. Kong, T. K. Kim, M. Lo Russo, M. Wulff, and H. Ihee, "Photochemistry of HgBr<sub>2</sub> in methanol investigated using time-resolved X-ray liquidography," *Physical Chemistry Chemical Physics*, vol. 12, no. 37, pp. 11536–11547, 2010.
56. T. B. van Driel, K. S. Kjær, R. W. Hartsock, A. O. Dohn, T. Harlang, M. Chollet, M. Christensen, W. Gawelda, N. E. Henriksen, J. G. Kim, K. Haldrup, K. H. Kim, H. Ihee, J. Kim, H. Lemke, Z. Sun, V. Sundström, W. Zhang, D. Zhu, K. B. Møller, M. M. Nielsen, and K. J. Gaffney, "Atomistic characterization of the active-site solvation dynamics of a model photocatalyst," *Nature Communications*, vol. 7, p. 13678, dec 2016.
57. J. L. F. Abascal and C. Vega, "A general purpose model for the condensed phases of water: TIP4P/2005," *The Journal of chemical physics*, vol. 123, no. 23, p. 234505, 2005.

58. M. Retegan, "Crispy: v0.7.3," jun 2019. [Online]. Available: <https://dx.doi.org/10.5281/zenodo.1008184>. [Accessed 27-June-2019].
59. E. Prince, ed., *International Tables for Crystallography C*. Kluwer Academic Publishers, 3 ed., 2004.
60. G. L. Hura, J. M. Sorenson, R. M. Glaeser, and T. Head-Gordon, "A high-quality X-ray scattering experiment on liquid water at ambient conditions," *Journal of chemical physics*, vol. 113, no. 20, pp. 9140–9148, 2000.
61. J. Holton, "Molecular movies." [Online]. Available: <https://bl831.als.lbl.gov/~jamesh/movies/>.